EUROPEAN COMMISSION

Community research

PEBS

(Contract Number: FP7 249681)

DELIVERABLE (D-N°: 3.2-1)

Design and predictive modelling of the HE-E test

Author(s): O. Czaikowski, B. Garitte, I. Gaus, A. Gens, U. Kuhlmann, K. Wieczorek

Reporting period: 01/03/10 – 28/02/11

Date of issue of this report: 24/04/12

Start date of project: 01/03/10 Duration: 48 Months

Project co-funded by the European Commission under the Seventh Euratom Framework Programme for Nuclear Research &Training Activities (2007-2011)		
Dissemination Level		
PU	Public	
RE	Restricted to a group specified by the partners of the [PEBS] project	
CO	Confidential, only for partners of the [PEBS] project	

EURATOM

nagra.

Arbeitsbericht NAB 12-03

Design and predictive modelling of the HE-E test

PEBS Deliverable D3.2-1

April 2012

O. Czaikowski, B. Garitte, I. Gaus, A. Gens,
U. Kuhlmann, K., Wieczorek

KEYWORDS
Long Term Performance of Engineered Barrier Systems (PEBS), THM modelling, HE-E experiment, heater test

**Nationale Genossenschaft
für die Lagerung
radioaktiver Abfälle**

Hardstrasse 73
CH-5430 Wettingen
Telefon 056-437 11 11

www.nagra.ch

Nagra Working Reports concern work in progress that may have had limited review. They are intended to provide rapid dissemination of information. The viewpoints presented and conclusions reached are those of the author(s) and do not necessarily represent those of Nagra.

List of contents

List of tables

List of Figures

1 Introduction

Design calculations for the HE-E experiment are performed by three modelling teams: GRS, CIMNE and TKConsult. The design calculations are based on coupled thermo-hydraulic modeling and thermo-hydro-mechanical modeling. However the stress redistribution induced by the excavation (and the potential associated damage) were not directly taken into account.

In order to assess the range of possible modelling outcomes a large part of the conceptualisation was left to the initiative of the modellers. This included the initial saturation state in the OPA around the tunnel at the start of the experiment, the choice of the two-phase flow parameters and the description of the dependency of the thermal conductivity on the water saturation in the bentonite, the sand/bentonite mixture and the Opalinus Clay. This report describes the first phase of the HE-E modeling: the design modeling (Figure 1.1)

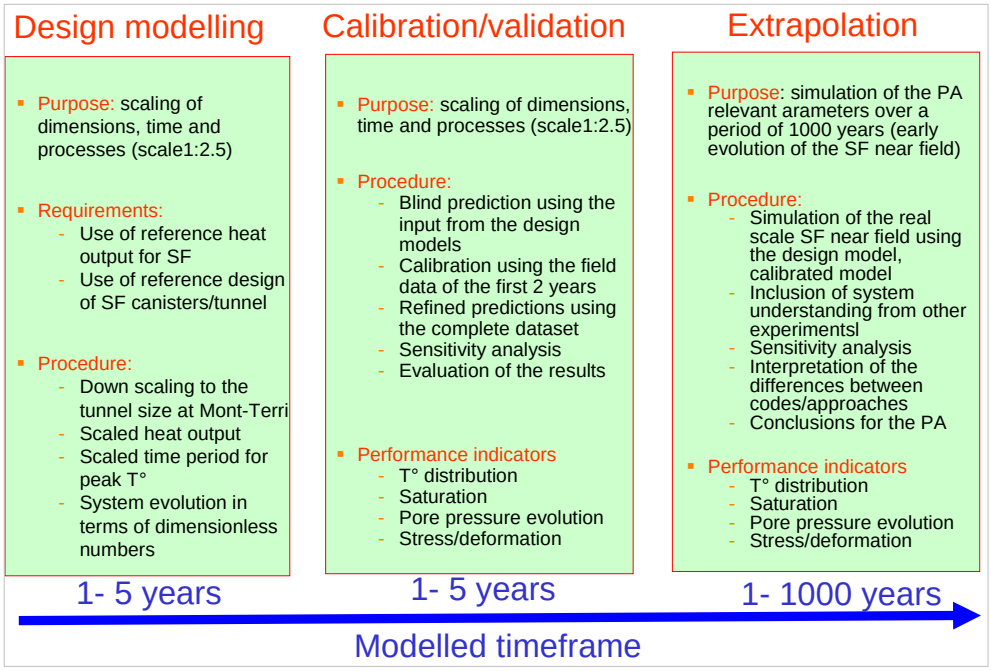

Figure 1.1 Modelling framework developed for the HE-E experiment within the PEBS project

1.1 Objectives of the design calculations

The objectives of the design calculations are:

- to predict design specific parameters regarding the heating system (maximum power needed)
- to predict the temperature profile radially and along the axis of the experiment in the bentonite but also in the OPA host rock and make suggestions for the emplacement of the temperature sensors
- to assess the resaturation state in the engineered barriers and in the host rock and make suggestions for the emplacement of the humidity sensors in the engineered barrier and the extra piezometers in the host rock
- to test the impact/difference of the two heating strategies that were proposed.

1.2 Geometry and boundary conditions for the design calculations

The dimensions of the experiment used for the design calculations are shown in Fig. 1.2 (for a more detailed description see Gaus (Ed.) (2011).

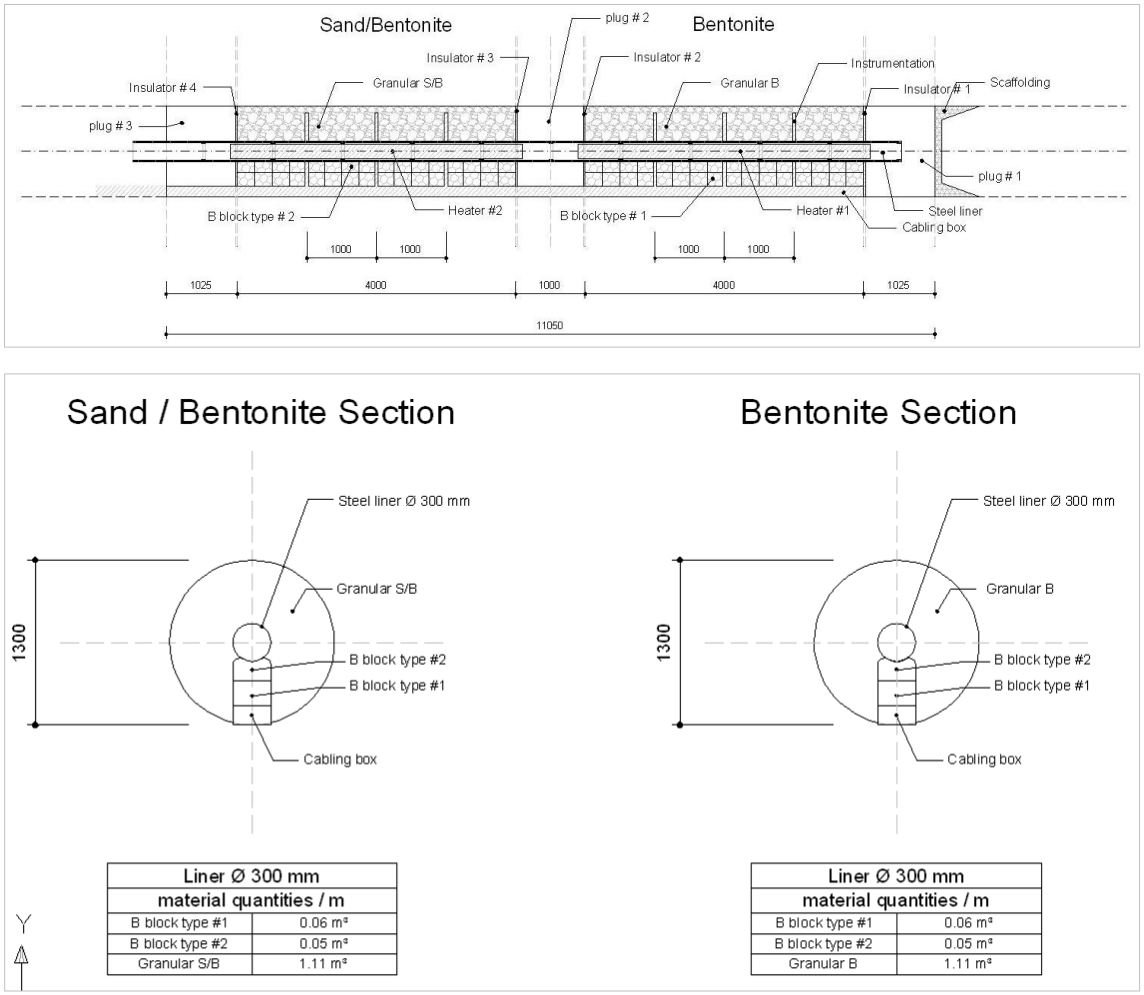

Figure 1.2 Dimensions of the HE-E experiment used for the design modelling.

A set of parameters describing the thermal and hydraulic parameters in the engineering materials (concrete, insulators), bentonite, the sand bentonite mixture and the host rock was proposed. These parameters were recommended in case more specific literature was not able to provide a more suitable value. The following literature was proposed as a basis for identifying the parameters of the OPA and the EDZ parameters in the models:

- Gens, A., Vaunat, J., Garitte, B. & Wileveau, Y. (2007). In situ behaviour of a stiff layered clay subject to thermal loading: observations and interpretation. Géotechnique 57, No. 2, 207–228
- Rösli U. (2010). VE Experiment: Long Term Monitoring Data Report - Phase 15 1 July 2009 – 30 June 2010. Mont Terri Project Technical Report TN 2010-12
- Mayor, J.C., Velasco M. (2008). The Ventilation Experiment Phase II (Synthesis Report). DELIVERABLE (D-N°:4.3.18) NF-PRO Project Work Package: WP 4.3.

Two heating strategies were proposed and tested by the modellers (the indicated temperatures are the temperatures at the liner surface):

Strategy 1	Initial temperature of 10°C, reaching 90°C after 3 months, 105°C after 6 months, 120°C after 1 years and 135°C after 3 years.
Strategy 2	Initial temperature of 10°C, then gradual temperature increase to reach 135°C after 1 year, then constant temperature of 135°C for the two following years.

Based on the outcomes of the results from the VE experiment and the data monitoring report (Rössli, 2010), the modellers estimated the initial saturation of the OPA in the tunnel.

The initial water content in the engineered materials is:

- Initial emplacement water content of the pellets: 5 %
- Initial emplacement water content of the bentonite blocks: 10 %
- Initial emplacement water content of the sand/bentonite: 6 %

The initial water pressure in Mont Terri the OPA is hydrostatic; the water pressure at the level of the top of the experiment corresponds to a column of 175-200 m. The tunnel itself is at atmospheric pressure.

Prior to the start of the modeling a Modellers dataset was distributed to the three modelling teams. This dataset is included in Appendix A.

2 Scoping calculations using TOUGH2 (TK Consult)

2.1 Introduction

The HE–E experiment is intended to investigate the early non-isothermal resaturation period of a backfilled SF/HLW emplacement tunnel and its impact on the thermo-hydro-mechanical behaviour. The objectives are:

1. to provide the experimental data base required for the validation of existing thermo-hydraulic models of the early resaturation phase;
2. to provide experimental data bases for model calibration, and
3. to upscale thermal conductivity of the partially saturated buffer from laboratoryto field scale (pure bentonite and bentonite-sand mixtures).

The experiment HE-E will be performed in the VE microtunnel of the Mont Terri Rock Laboratory and is aimed at improving the understanding of the thermal evolution of the near field around a SF/HLW waste container, during the very early phase after emplacement in a 1:2 scale in-situ configuration. Special interest is on the temperature evolution in the buffer and the thermal impact on the clay rock close to the tunnel.

This document describes the dataset for the scoping calculations of the HE-E experiment, the implementation of the HE-E experiment, and intermediate results. The results of the different simulation cases will assist in the planning of the experiment, and are the basis for the modelling prediction and validation part of the experiment.

A technical description of the experiment is given in greater detail in *Appendix A*. The dimensions of the different components in the VE microtunnel are shown in Figure 2.1.

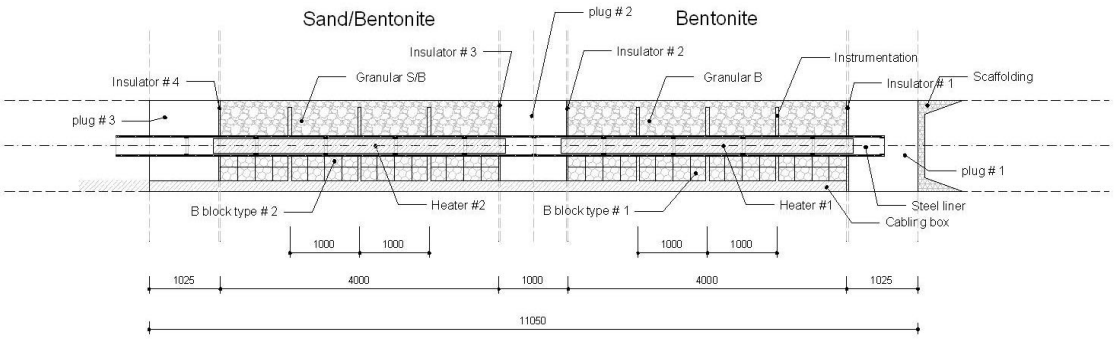

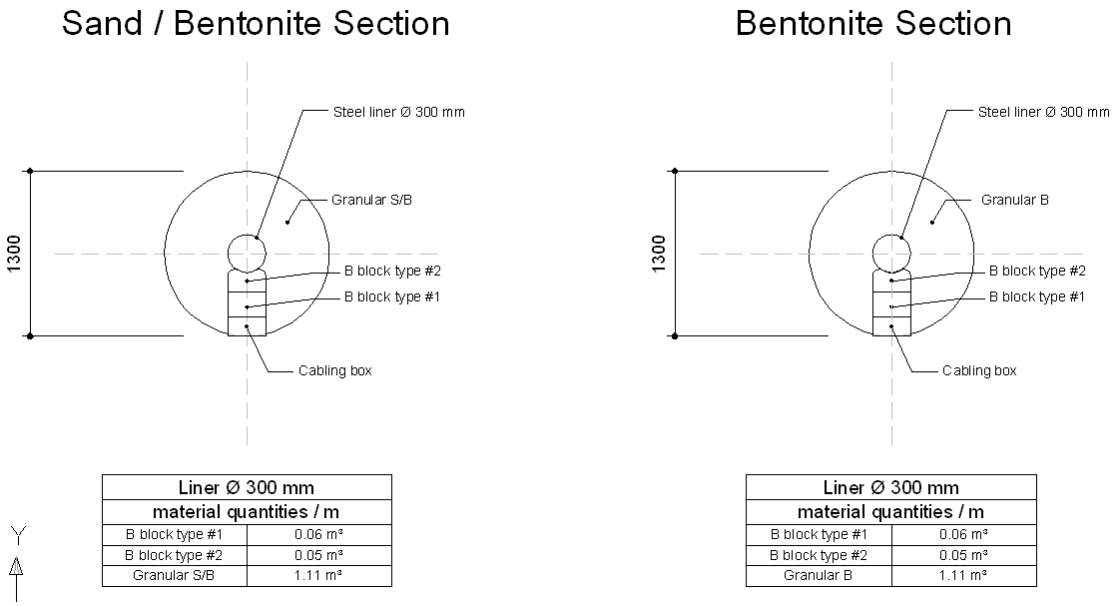

Figure 2.1 Current dimensions of the planned HE-E experiment (lengths in mm)

2.2 Model Implementation

2.2.1 Model Geometry

The configuration of the VE-micro tunnel with the different components associated with the HE-E experiments (Fig. 1.2) is implemented in a 3D numerical model implemented with the two-phase flow code TOUGH2 (Pruess et al. 1999). The geometry is implemented as an integrated-finite difference (IFD) mesh, using the visualization tool mView (Calder and Avis, 2007) shown in Figure 2.2.

The dimensions of the different materials are reproduced in the model, except for the bentonite blocks and the cabling box, which follow the segments of the radial geometry. In addition, the relatively thin isolators were represented with a 5-times greater thickness to avoid discretization problems. The thermal conductivity was adjusted accordingly to yield the same effective thermal conductance across the isolator.

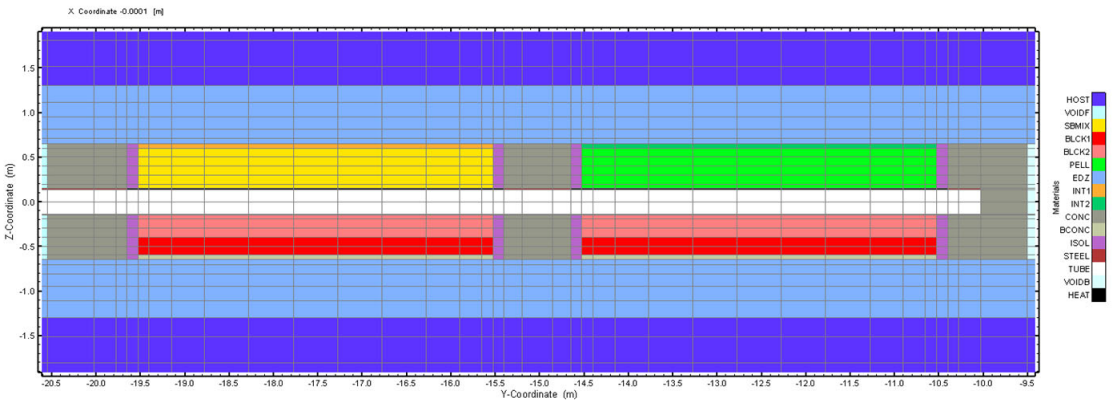

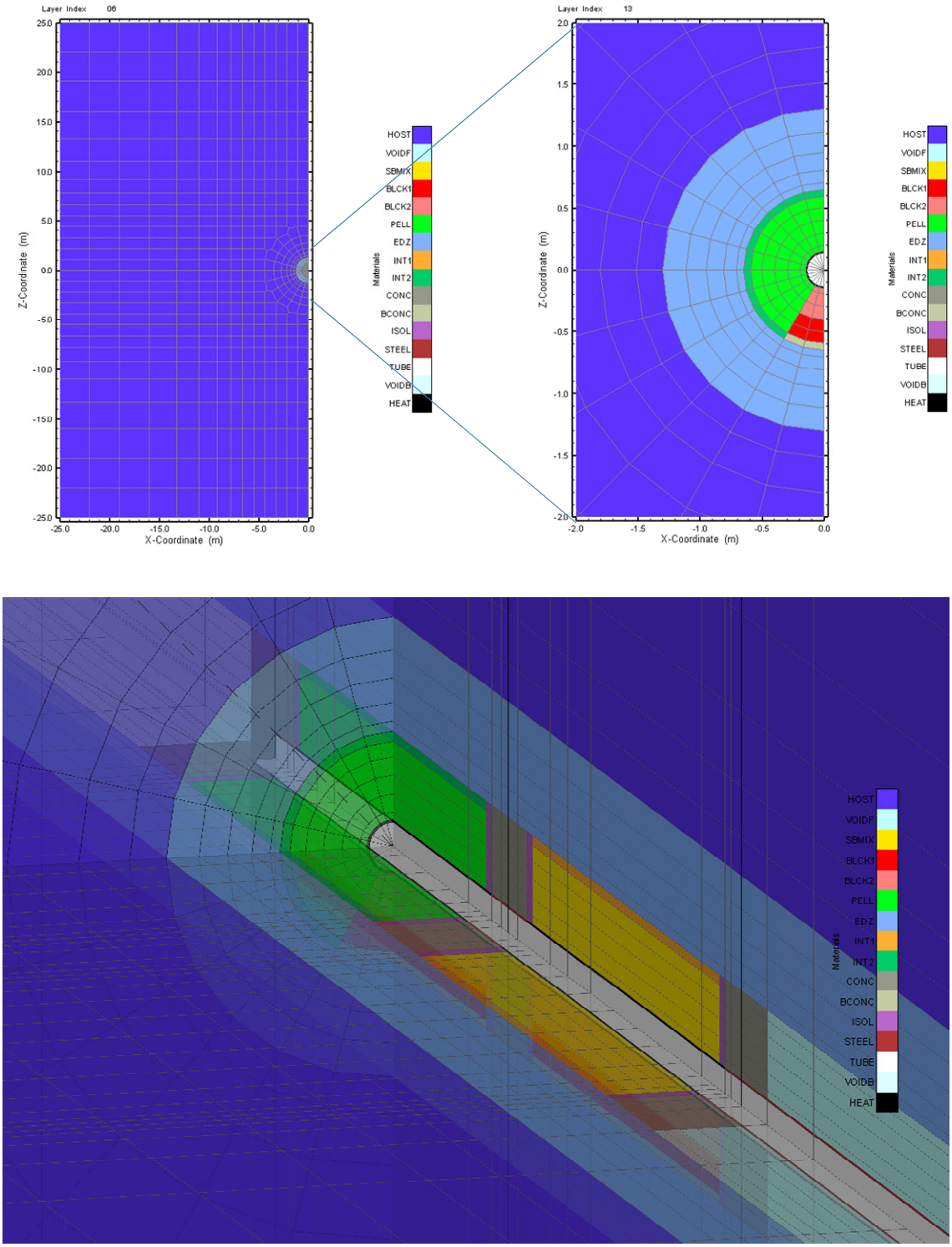

Figure 2.2 Mesh discretization along the tunnel axis (top), perpendicular to the tunnel (middle), and 3D representation (bottom)

2.2.2 Input Parameters

The input parameters are summarized in Table 2.1.

Table 1 Input parameters for the base case model scenario.

	OPA	EDZ	Bentonite blocks	Bentonite pellets	Sand/bentonite mix	Concrete (plugs)	Insulator	Steel
Permeability: k(m2)	1.0E-20	1.0E-18	2.5E-21	3.5E-20	1.0E-19	1.0E-20	1.0E-20	1.0E-50
Porosity ϕ	0.12	0.14	0.475	0.475	0.41	0.15	0.002	0.001
Pore compressibility: Cp [1/Pa]	1.7E-09	1.7E-09	2.0E-09	2.0E-09	2.0E-09	6.7E-10	6.93E-10	0
Van Genuchten: Po [Pa]	3.0E+06	1.0E+06	3.0E+07	1.8E+07	2.5E+05	1.5E+07	1.5E+07	1.0E+08
Van Genuchten; n	1.67	1.67	1.82	1.82	2.5	1.49	1.49	2
Residual Water Saturation: S_{wr}	0.3	0.3	0.01	0.01	(0.3) 0.01	0.01	0.01	0.01
Residual Gas Saturation: S_{gr}	0.01	0.01	0.001	0.001	0.01	0	0	0
Thermal expansion Tx [1/K]	3.47E-05	3.47E-05	1.5E-05	1.5E-05	1.5E-05	1.5E-05	1.5E-05	1.5E-05
Thermal conductivity Wet: Tcw [W/m K]	2.5	1.5	1.35	1.35	1.35	1.35	0.035	52
Dry: Tcd [W/m K]	2.5	1.5	0.4	0.4	0.4	0.4	0.035	52
Specific Heat: Sh [J/kg C]	946.5	1068	964	964	920	964	1400	1.0E+20
Initial saturation (Sw)			0.21	0.11	0.13	0.04	0.04	0.01

* Specific Heat of Steel set to high value to maintain constant temperatures

~ Linear relation between wet and dry thermal cond. Values

2.2.3 Heating Strategies

Two heating strategies are examined which will be evaluated for implementation of the actual experiment, which includes:

S1	Initial temperature of 10°C , reaching 90°C after 3 months, 105°C after 6 months, 120°C after 1 years and 135°C after 3 years.
S2	Initial temperature of 10°C, then gradual temperature increase to reach 135°C after 1 year, then constant temperature of 135°C for the two following years.

The prescribed temperatures for the different strategies are represented by prescribing heat generation rates as a function of time in such a way that they produce the target temperatures. The corresponding heat generation rates were computed as follows:

$$Q_h = (1-\phi)\rho\ C\ V\ dT/dt$$

where Q_h is the heat generation rate (J/s), ϕ is the porosity, ρ is the grain density, C is the specific heat capacity of the heater element (J/kg C), V is the element volume (m^3), and dT/dt is the rate of temperature change over time (C/s). In order to maintain a constant temperature following the temperature increases, the heat capacity was set at a very large value. This value

was used to compute the heat generation rate as a function of time for the different temperature increases over time.

2.2.4 Initial Conditions

The initial saturation conditions in the Opalinus Clay surrounding the VE tunnel are somewhat unclear. The tunnel has been actively ventilated during the VE test and also afterwards ventilation took place. The indications are that the near field is relatively dry indicating a significant desaturation of the EDZ.

An initial phase was simulated accounting for long-term ventilation of the VE tunnel assuming a relative humidity of 60%, which corresponds to a capillary suction pressure of 6.7E+7 Pa.

The initial pressure in the Opalinus Clay is assumed to be hydrostatic corresponding to a hydraulic head of 175 m at the VE tunnel. In the open tunnel, atmospheric pressure conditions are prescribed. The outer boundaries were assumed to be no-flow boundaries.

Following the ventilation period, the installation of the different components of the HE – E experiment is assumed to be instantaneous at the initial emplacement saturation of the different bentonite materials (sand/bentonite, bentonite pellets, and bentonite blocks). In addition, the two sections are separated by a concrete block and isolators, which are used to separate the installation from the open tunnel segments (Figure 2.1). The initial emplacement saturation for the different materials is summarized in Table 2.1.

2.2.5 Reference Case and Sensitivity Analysis

The reference case is based on the input parameters given in Table 2.1 and was performed for both heating strategies.

In addition, a series of sensitivity runs were performed to evaluate the following aspects:

- impact of the thermal properties
- the heating strategy
- initial saturation condition of the VE tunnel
- two phase flow properties
- permeability of the OPA
- conceptualisation of the bentonite

A summary of the different simulation cases is given in Table 2.2.

Table 2 Summary of the Different Simulation Cases

Case	Specification	Parameters (varied during sensitivity runs)
S1R0	heating strategy 1	Base-Case Parameter (Table 1): k(opa) =1.E-20m2, K(EDZ)=1.E-18m2 Tc(bentonite)=Tc+SQRT(Sw)*(Tcw-Tcd) Tc(opa)=2.5 (isotropic) vG=Po(opa)=3 MPa krg=van Genuchten
S2R0	heating strategy 2	
S1R1	Increase k(opa)	k(opa) =1.E-19m2, K(EDZ)=1.E-17m2
S1R2	Decrease k(opa)	k(opa) =1.E-21m2, K(EDZ)=1.E-19m2
S1R3	Tc(Sw)	Tc(bentonite)=Tc+Sw*(Tcw-Tcd)
S1R4	Initial saturation (bentonite)	Sw(BB)=0.5, Sw(Pellets)=0.1, SBmix=0.1
S1R5	Tc(opa) anisotropy	Tc(hor.)=2.5, Tc(vert.)=1.55
S1R6	vG-Po(opa)	vG-Po(opa)=9MPa
S1R7	TPF(bent.)	krg=Corey
S1R8	Slr(sbmix)	Increase Slr(sand/bent.)=0.3
S1R9	Tc(bent)=const.	Tc(bent)=1.35 W/m K

2.2.6 Performance Measures for Comparison between the Models

The simulation results are presented in the following format for comparison between the models:

- pressures versus time, pressure profile at given times (1, 2 , 3, 5 years)
- temperatures versus time, temperature profile at given times (1, 2 , 3, 5 years)
- saturation versus time, saturation profile at given times (1, 2 , 3, 5 years)

The observation points for the time series, indicated in Figure 2.3, include:

- Top OPA/bentonite interface of the experiment/middle of each section (bentonite and sand/bentonite)
- Bottom OPA/bentonite interface of the experiment/middle of each section (bentonite and sand/bentonite)
- Horizontal OPA/bentonite interface of the experiment/middle of each section (bentonite and sand/bentonite)

Further illustrations include 2D spatial distribution at certain times to characterise the relevant phenomena associated with heating and resaturation of the different bentonite materials.

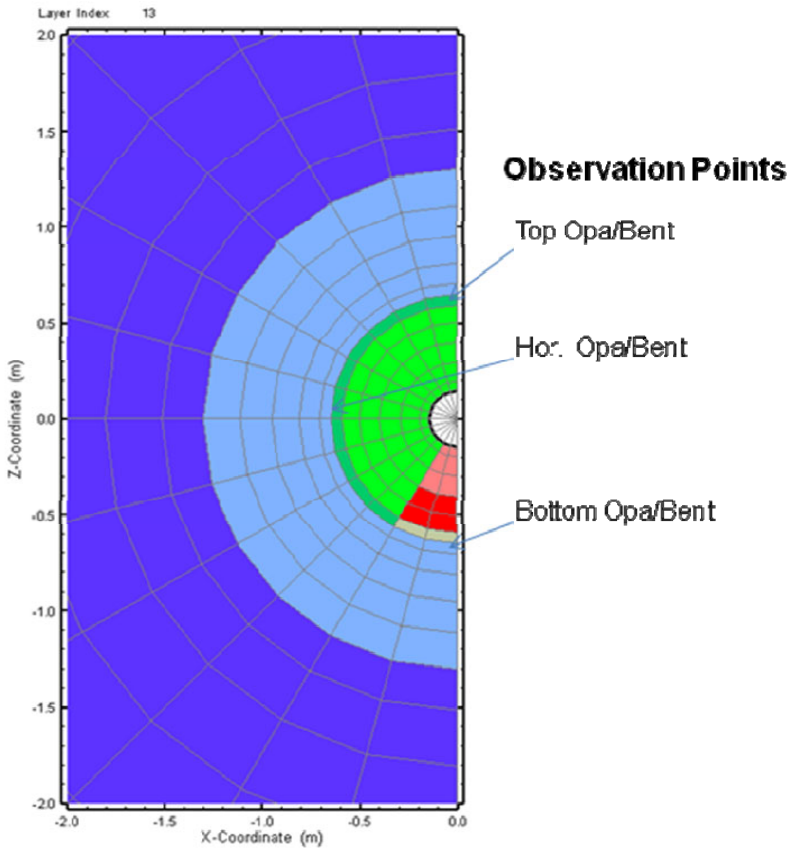

Figure 2.3 Observation points for time-series plots

2.3 Simulation Results

2.3.1 Initial Conditions (Ventilation)

The results of the simulations associated with the ventilation of the open tunnel are shown in vertical profiles of pressure and saturation at different times (Figures 2.4 and 2.5) for the base case using the host rock properties in Table 2.1. The pressure profiles show the expansion of the cone of the depression around the open tunnel. The associated desaturation is limited largely to the EDZ, reaching a gas saturation of as high as 60% at the tunnel wall. The simulated results after 10 years of ventilation will be used as initial conditions for the simulation of the heating phase described in Section 2.3.2.

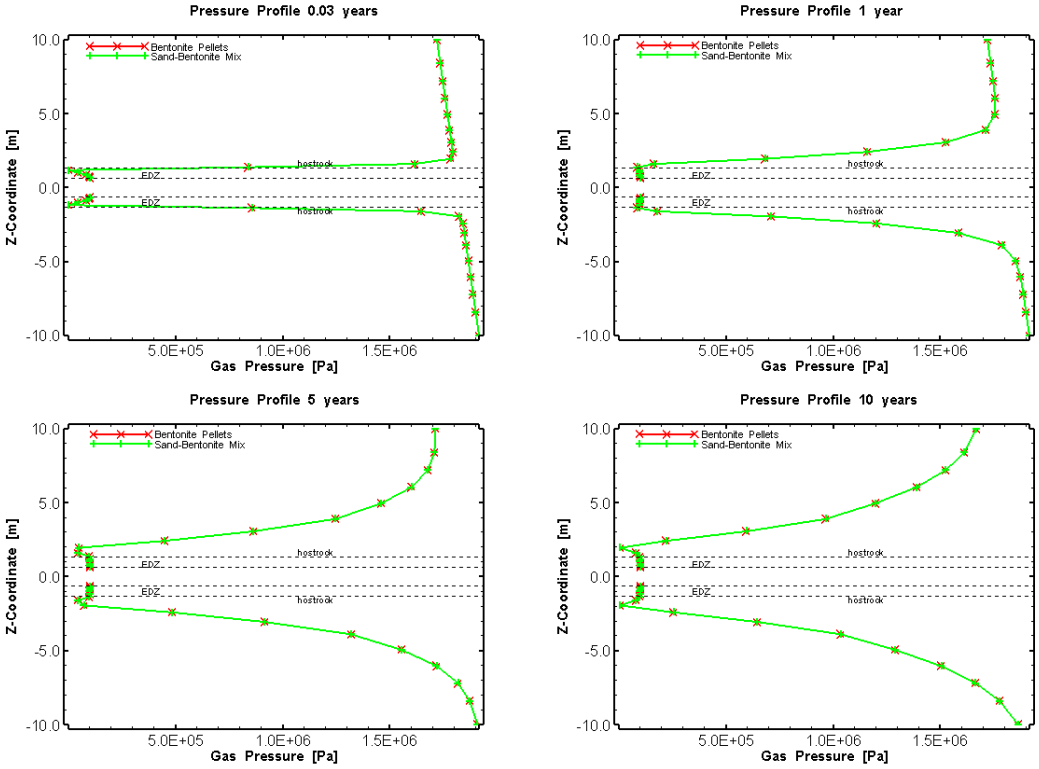

Figure 2.4 Simulated gas pressures along a vertical profile associated with ventilation in the open tunnel at different times.

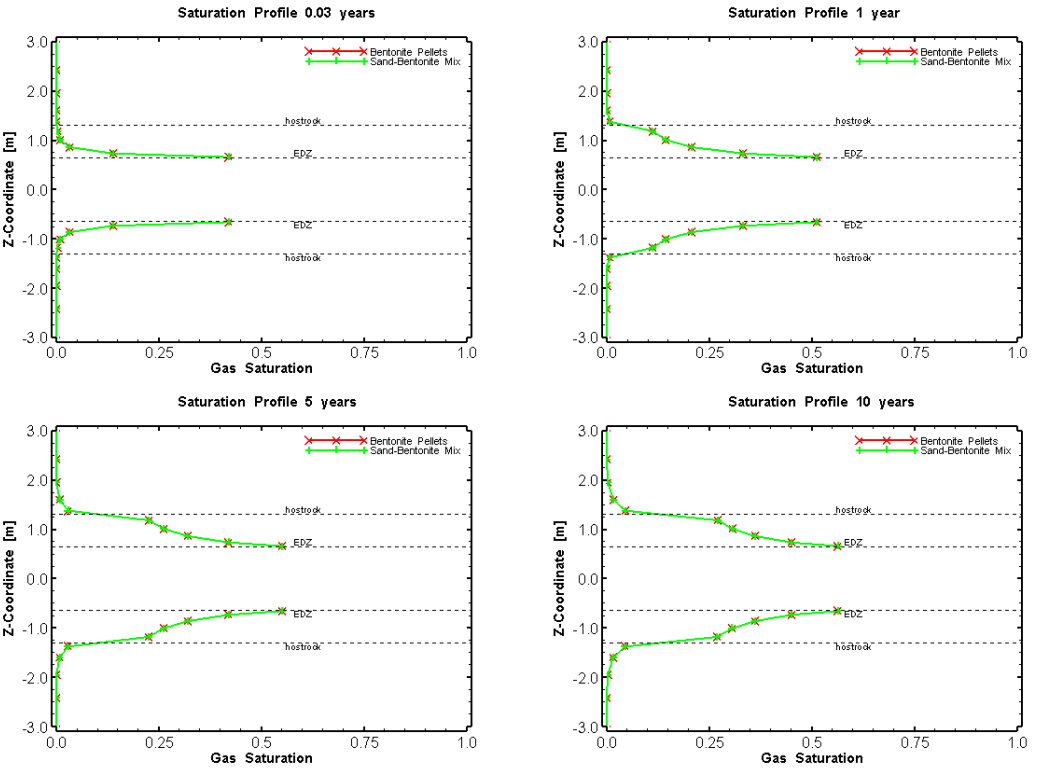

Figure 2.5 Simulated of gas saturations along a vertical profile associated with ventilation in the open tunnel at different times (close-up around the tunnel).

For the Sensitivity Cases R1 with increased k(OPA) and Case R2 with decreased k(OPA), the ventilation simulation produced different results in terms of the pressure and saturation distribution in the EDZ and Opalinus Clay. The results of these simulations are shown in Figures 2.6, 2.7, 2.8, and 2.9.

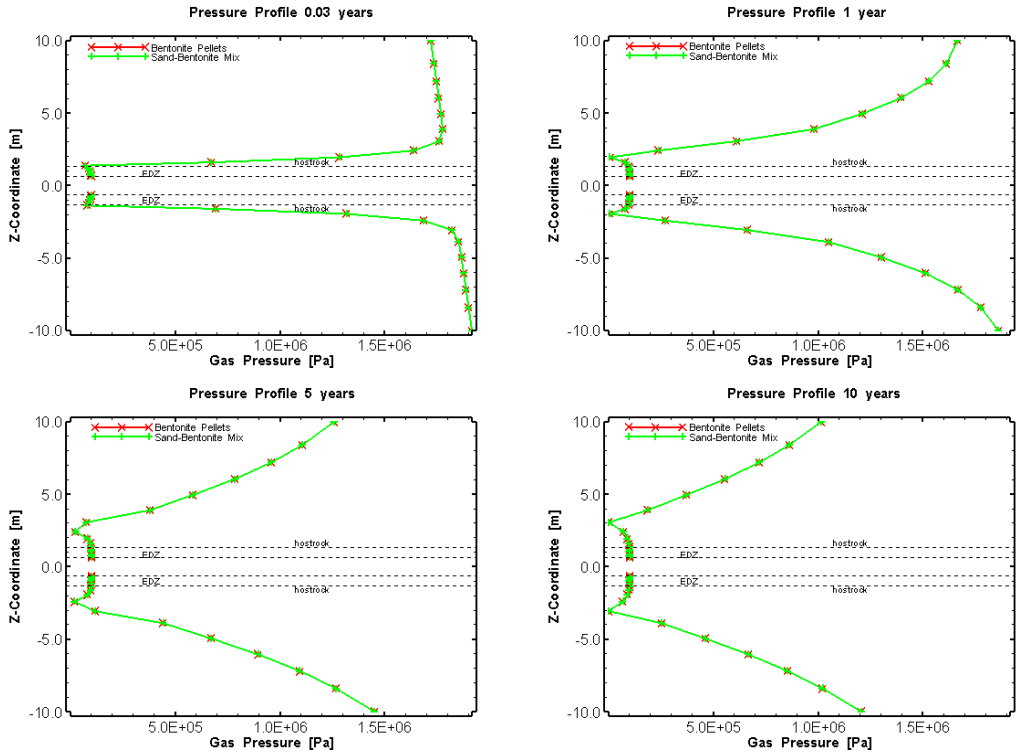

Figure 2.6 Case R1: Simulated gas pressures along a vertical profile associated with ventilation in the open tunnel at different times.

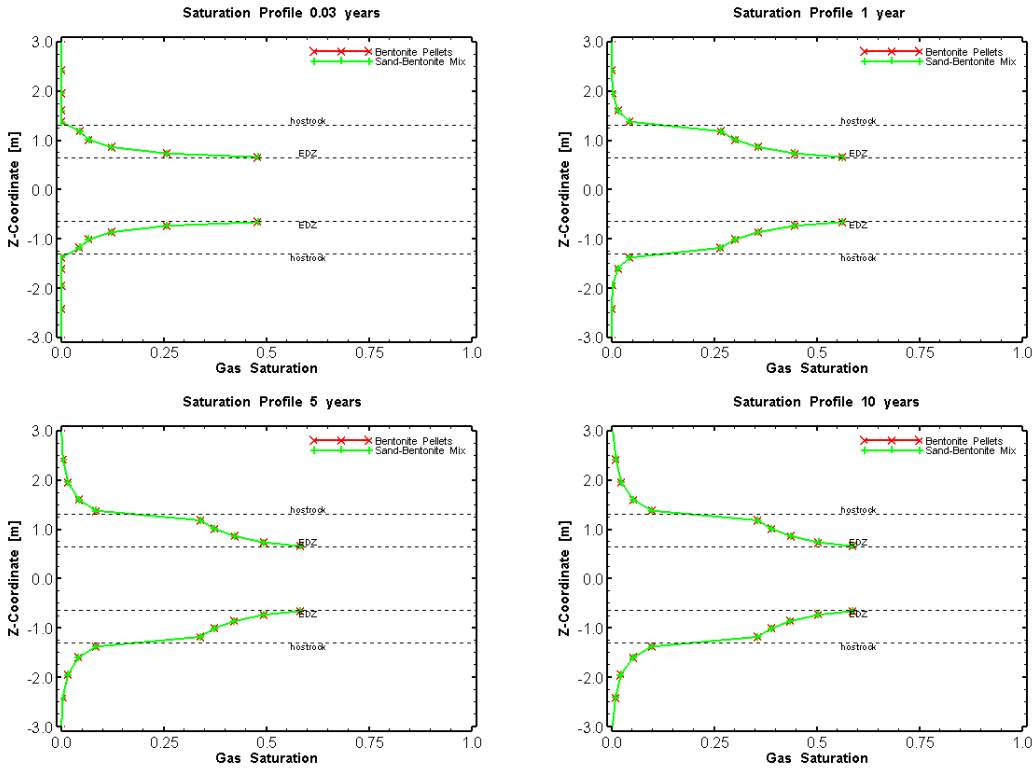

Figure 2.7 Case R1: Simulated gas saturations along a vertical profile associated with ventilation in the open tunnel at different times (close-up around the tunnel).

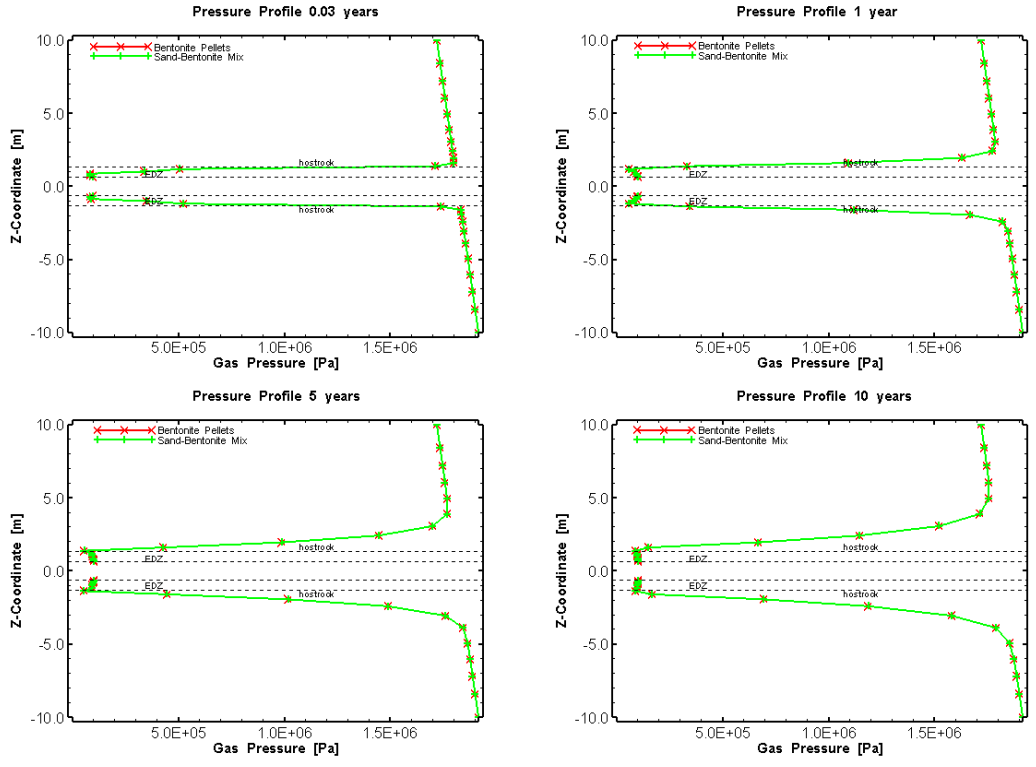

Figure 2.8 Case R2: Simulated gas pressures along a vertical profile associated with ventilation in the open tunnel at different times.

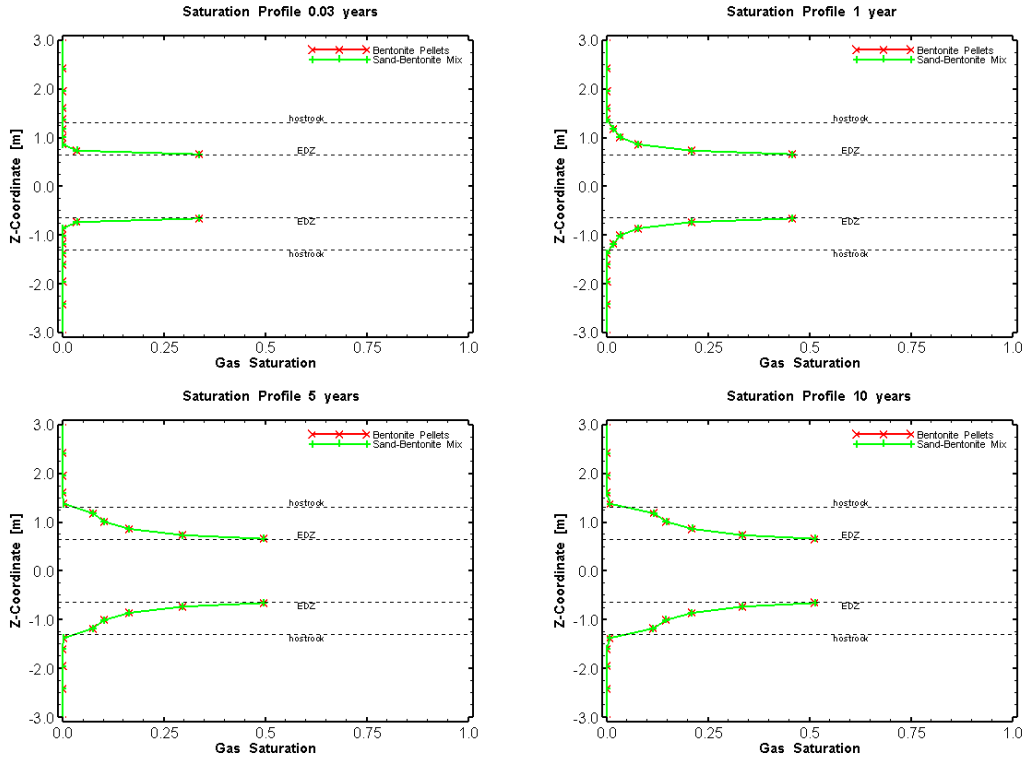

Figure 2.9 Case R2: Simulated gas saturations along a vertical profile associated with ventilation in the open tunnel at different times (close-up around the tunnel)

2.3.2 Base Case Simulations

The results of the simulations associated with heating and resaturation are presented according to the specifications described in Section 2.6. For the base-case simulation additional detailed plots of spatial distributions of temperatures and saturations are used to provide insight into the coupled heat- and two-phase flow.

Heating Strategy 1: The first heating strategies starts at an initial temperature of 10°C , reaching 90°C after 3 months, 105°C after 6 months, 120°C after 1 years and 135°C after 3 years.

The time histories of temperatures, pressures, and saturation are shown in Figure 2.10 and 2.11. The vertical profiles of temperature, pressure, and saturation at different times are given in Figures 2.12 and 2.13.

The temperature histories for both the bentonite pellets and the sand/bentonite indicate temperature increases to near 60ºC corresponding to the maximum prescribed temperature of 135 ºC of the heater element. The pressures at the observation locations indicate an increase to near 150 kPa. The pressures in the sand/bentonite section peak after 3 years followed by a gradual decline, whereas the pressures in the bentonite pellets continue to increase over 5 years. The pressure decline in the sand/bentonite is due to hydraulic dissipation associated with the higher permeability compared to the bentonite pellets. The simulated gas saturations indicate significant different responses between the sand/bentonite and the pellets with the gas saturations at the upper and lateral edge of the bentonite pellets decreasing do about 65% after 5

years. In the sand/bentonite, the gas saturation essentially remains the same. At the bottom edge, which is in the EDZ next to the element representing the cable box, the gas saturations decrease to 34% for the pellet section and 30% for the sand/bentonite section (Fig. 2.11).

The corresponding vertical temperature profiles are the same between sand/bentonite and pellets and are largely symmetric with only a slight difference around the cable box at the bottom of the bentonite blocks. The pressure profiles show distinct differences between the sand/bentonite and pellets in the upper part after two years. The pressure in the sand/bentonite actually decreased to a near constant profile above the heater element. The simulated pressure increase in the heater element is caused by thermal expansion for which a low porosity of 0.1% was assumed and negligible permeability (k=1.E-50m^2). The corresponding saturation profiles indicate that the gas saturations in the pellets decrease above the heater element, whereas in the sand/bentonite the saturation remained near the initial emplacement saturation, but decreased noticeably in the adjacent EDZ. In the bentonite blocks beneath the heater element, the saturations are the same. The high saturation in the bottom element at the contact between the EDZ remained constant, due to the negligible permeability assigned to the cable box.

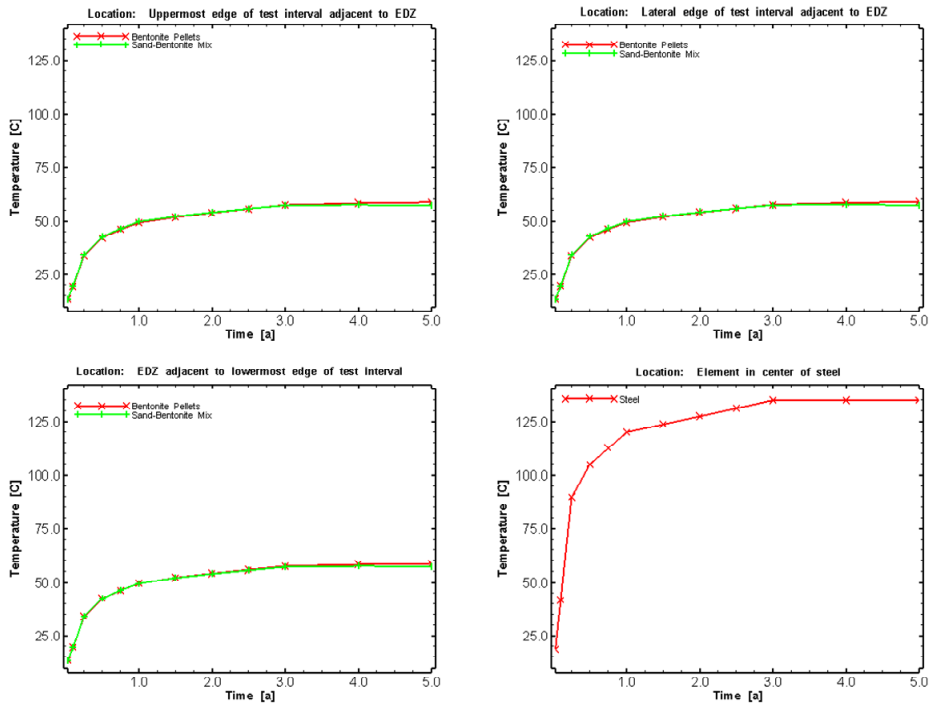

Figure 2.10 Case S1R0: Temperature histories at the different observation points, in addition to the prescribed temperature in the heater (lower right).

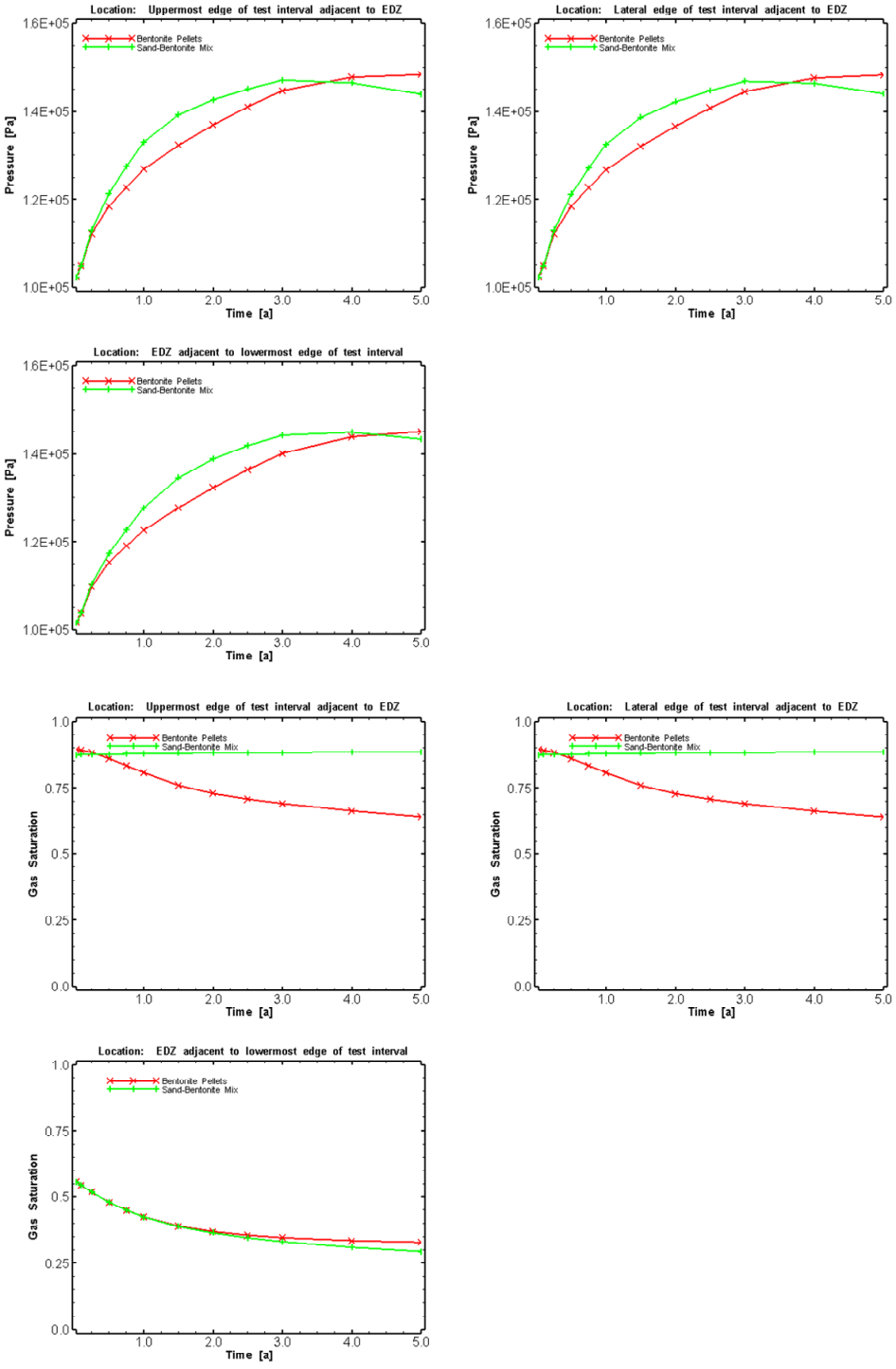

Figure 2.11 Case S1R0: Time histories of pressures (top) and saturation (bottom) at the different observation points.

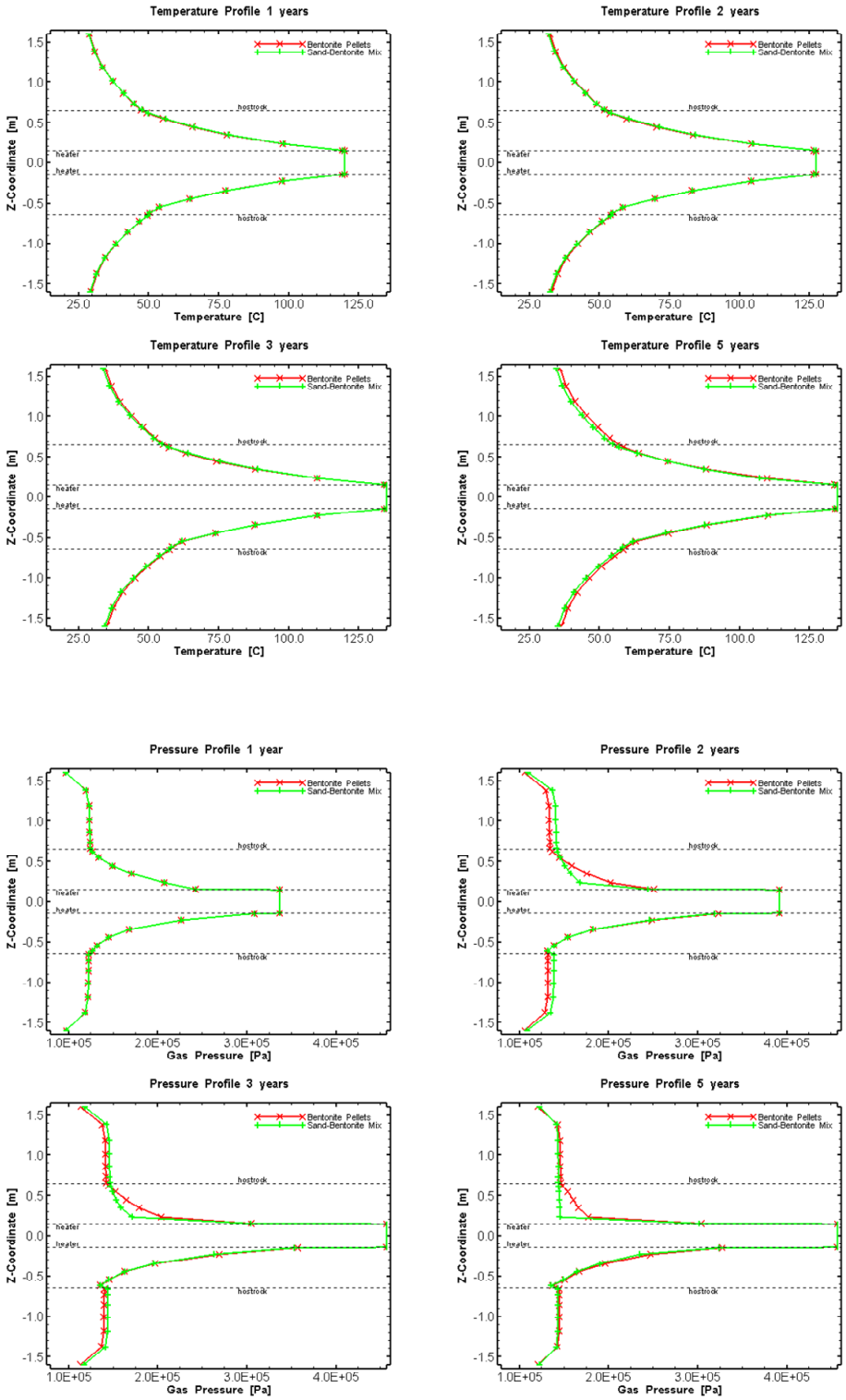

Figure 2.12 Case S1R0: Simulated vertical profiles of temperatures (top) and pressures (bottom) at different times.

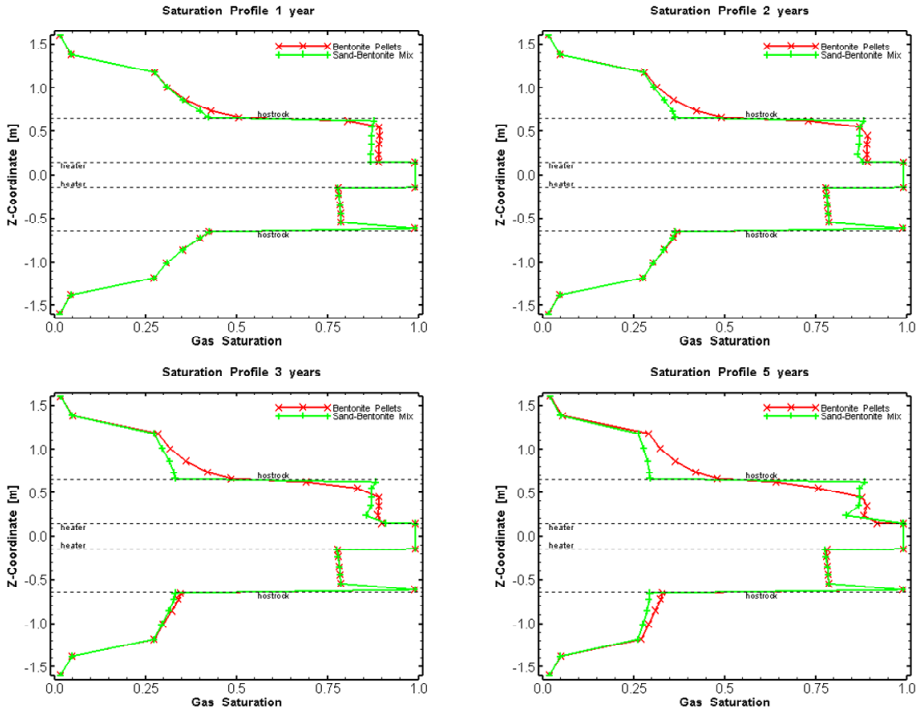

Figure 2.13 Case S1R0: Simulated vertical profiles of gas saturations at different times

The detailed spatial distributions of temperatures and gas saturations along the tunnel axis are shown in Figures 3.14 and 3.15, respectively. The simulations indicate a relatively rapid transport of heat into the surrounding clay, whereby the bentonite backfill creates a relatively steep gradient from a peak temperature of 135 ºC at the heater to about 60 ºC at the outer edge of the bentonite. The saturation in the bentonite shows relatively little change particularly for the sand/bentonite section, which was also shown in the history plots (Fig. 2.11). This is counterintuitive, because the sand/bentonite is characterized by a much greater permeability ($k=1.E\text{-}19m^2$) compared to that of the bentonite pellets ($3.5E\text{-}20m^2$). However, the capillary strength parameters P_0 is significantly lower for the sand/bentonite (2.E+5Pa) compared to that for the bentonite pellets (1.8E+7Pa). As a result, the liquid pressure gradient for water flow from the surrounding Opalinus Clay is nearly two orders of magnitude lower, resulting in relatively little water flow into the sand/bentonite.

The vertical sections perpendicular to the tunnel axis of gas saturations through the sand/bentonite section and through the bentonite pellets are shown in Figures 2.16 and 2.17, respectively. The results indicate some water flow in the sand/bentonite, but negligible changes in saturations, whereas the bentonite pellets do indicate a noticeable change in gas saturations. The bentonite blocks at the bottom of the heater show relatively little change from the initial emplacement saturation. This is due partly to the impermeable cable box at the bottom of the bentonite blocks restricting water inflow from the EDZ only via the sand/bentonite and the pellets. As the initial emplacement saturation of the blocks is higher (Sw=0.21) than those of the pellets (Sw=0.11) and of the sand/bentonite (Sw=0.13), the capillary pressure gradient is reduced.

In the immediate vicinity of the heater, the gas saturation is increased in the bentonite blocks below the heater and in the sand/bentonite above the heater. This is caused by evaporation of the pore water where the temperatures exceed the boiling point. The water vapour is transported away by diffusion and condenses at short distance, where the temperature falls below 100 ºC, which is indicated by a small decrease in gas saturation along the profiles (Fig. 3.10).

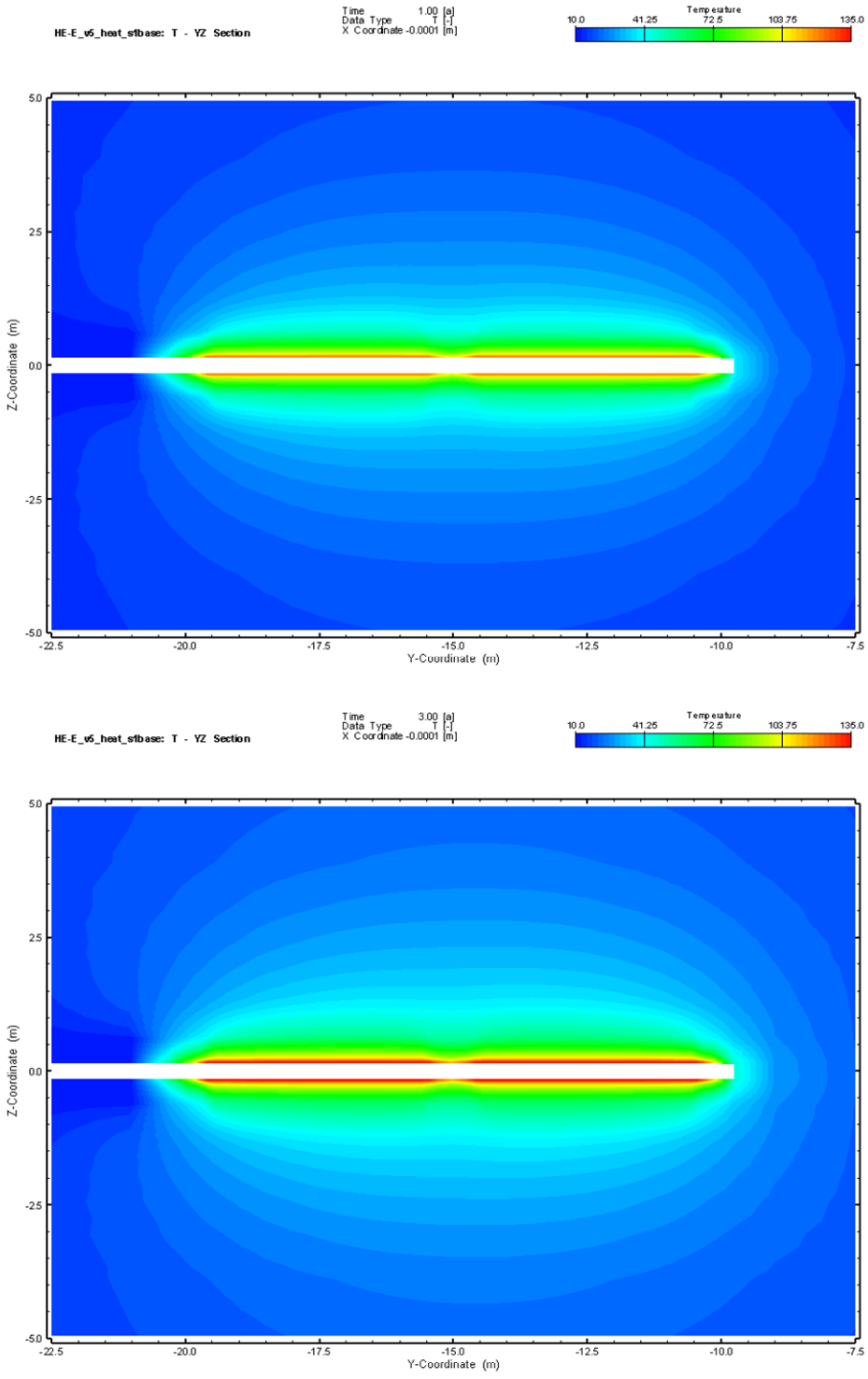

Figure 2.14 Case S1R0: Simulated distribution of temperatures along the tunnel axis after 1 yr (top) and after 3 yrs (bottom)

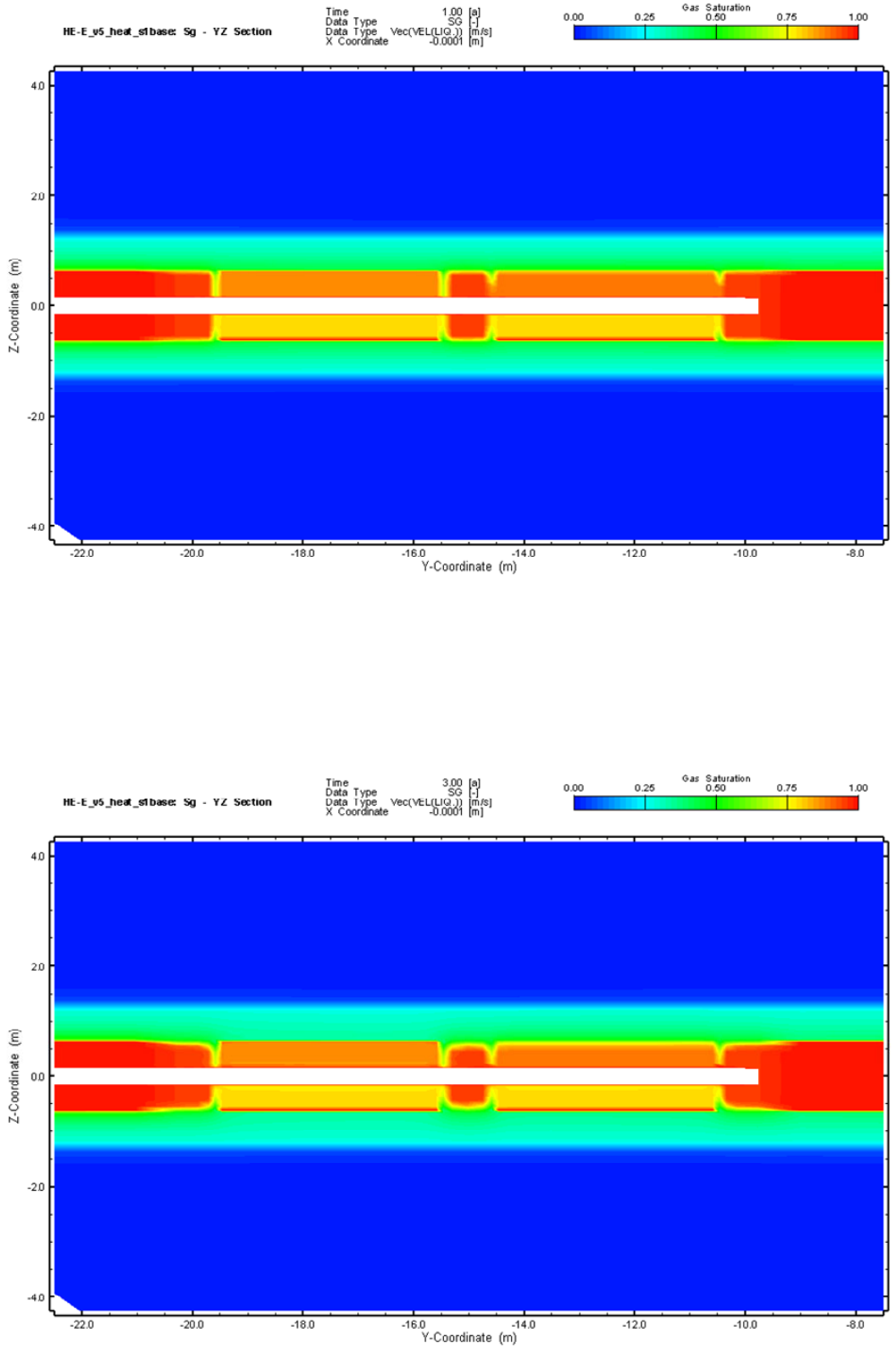

Figure 2.15 Case S1R0: Simulated distribution of gas saturations along the tunnel axis after 1 yr (top) and after 3 yrs (bottom)

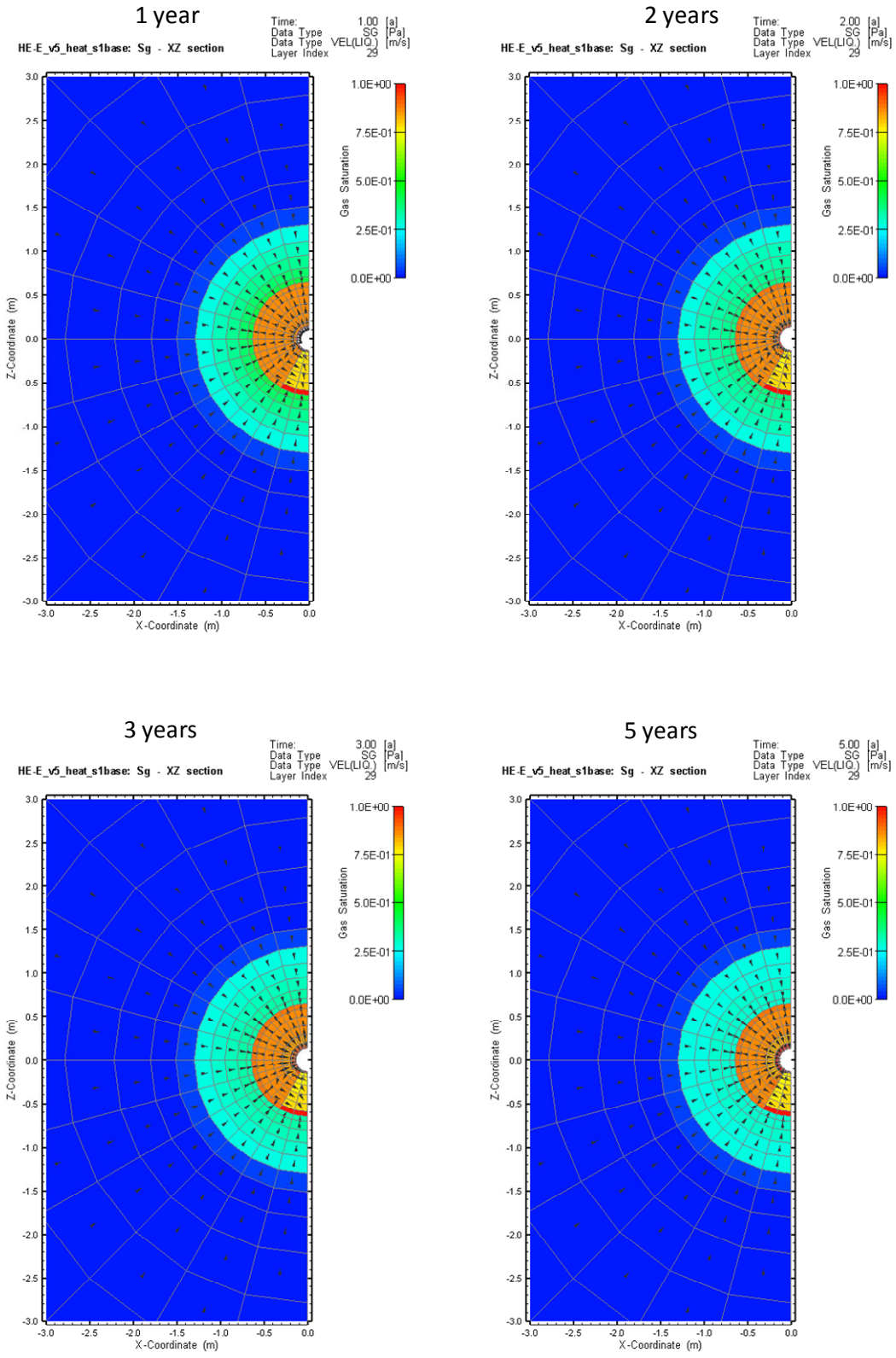

Figure 2.16 Case S1R0: Simulated distribution of gas saturations perpendicular to the tunnel axis in the sand/bentonite section at different times (arrows indicate the water fluxes).

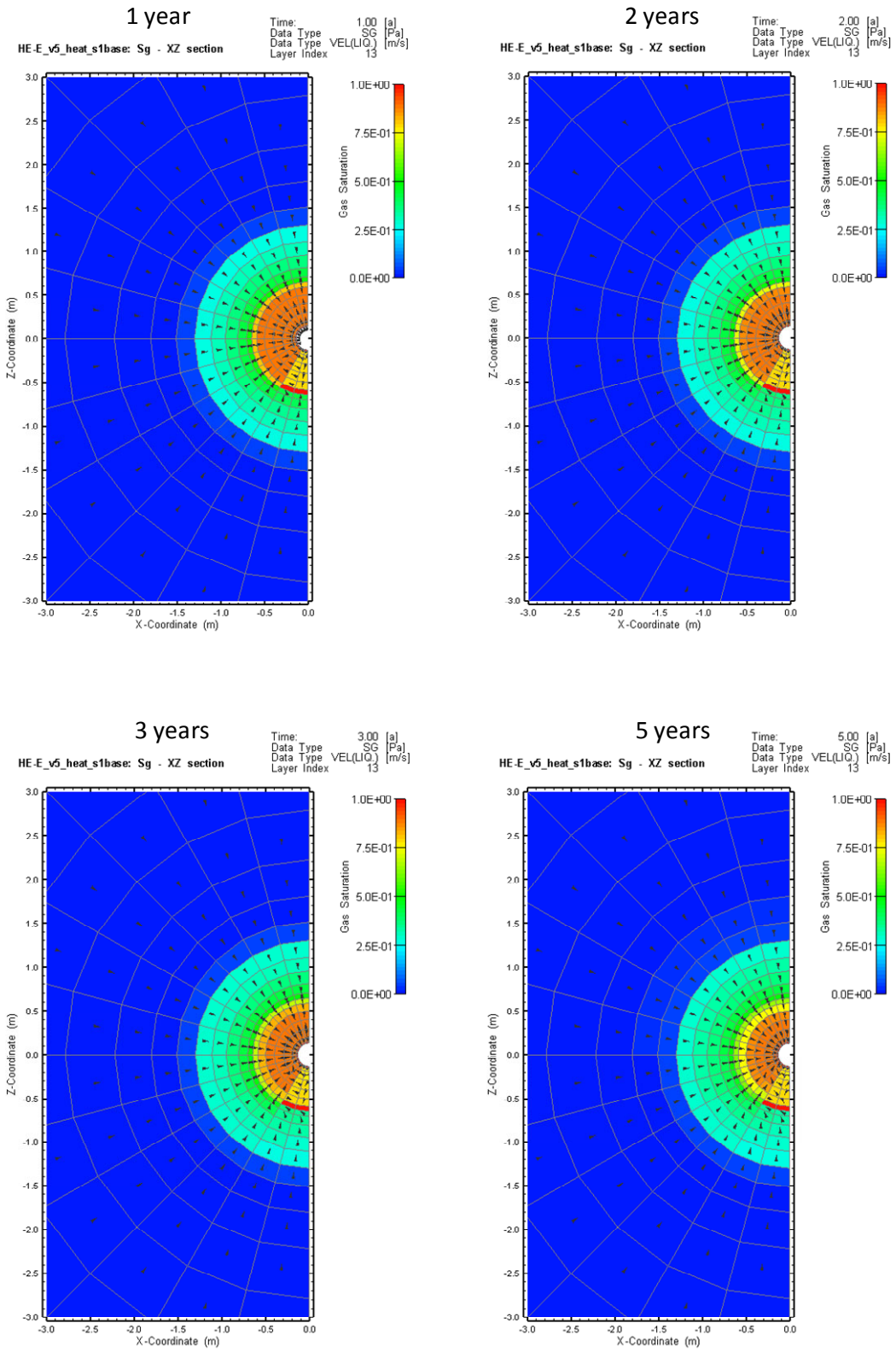

Figure 2.17 Case S1R0: Simulated distribution of gas saturations perpendicular to the tunnel axis in the bentonite pellet section at different times (arrows indicate the water fluxes)

Heating Strategy 2: The second heating strategies starts at an initial temperature of 10°C and linearly increases to temperatures of 135°C during a 1-year period, followed by constant temperatures.

The time histories of temperatures, pressures, and saturation are shown in Figure 2.18 and 2.19. The vertical profiles of temperature, pressure, and saturation at different times are given in Figures 2.20 and 2.21. The temperature histories for both the bentonite pellets and the sand/bentonite indicate temperature increases to 55 ºC after 1 year, corresponding to the maximum prescribed temperature of 135 ºC of the heater element. The pressures at the observation locations indicate an increase to near 150 kPa, whereby the increase is steeper than in the base case. Also, the pressures in the sand/bentonite show a gradual decline after about 2 years, whereas the pressures in the bentonite pellets continue to increase over 5 years. The simulated gas saturations indicate significantly different responses between the sand/bentonite and the pellets with the gas saturations at the upper and lateral edge of the bentonite pellets decreasing do about 65% after 5 years, whereas the gas saturations remain essentially the same in the sand/bentonite. At the bottom edge, which is in the EDZ next to the element representing the cable box, the gas saturations decrease to 34% for the pellet section and 30% for the sand/bentonite section.

The corresponding vertical temperature profiles are the same between sand/bentonite and pellets and are largely symmetric with only a slight difference around the cable box at the bottom of the bentonite blocks. The pressure profiles show distinct differences between the sand/bentonite and pellets in the upper part after two years. The pressure in the sand/bentonite actually decreased to a near constant profile above the heater element. The simulated pressure increase in the heater element is caused by thermal expansion for which a low porosity of 0.1% was assumed and negligible permeability ($k=1.E\text{-}50 m^2$). The corresponding saturation profiles indicate that the gas saturations in the pellets decrease above the heater element, whereas in the sand/bentonite the saturation remained near the initial emplacement saturation, but decreased noticeably in the adjacent EDZ. In the bentonite blocks beneath the heater element, the saturations are the same. The high saturation in the bottom element at the contact between the EDZ remained constant, due to the negligible permeability assigned to the cable box.

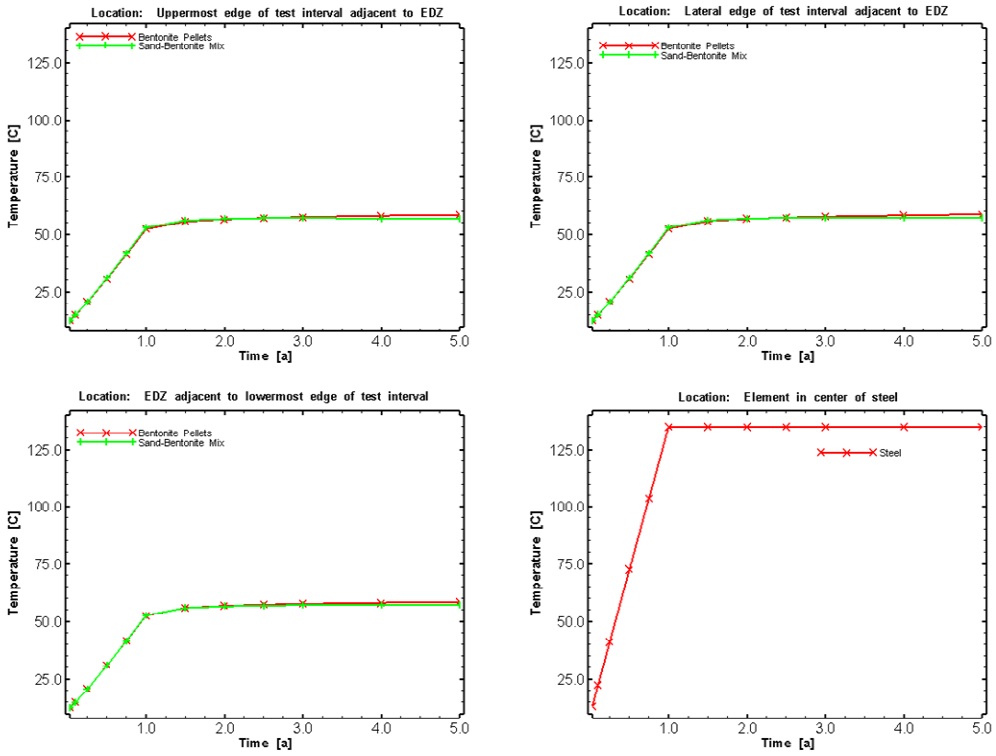

Figure 2.18 Case S2R0: Temperature histories at the different observation points, in addition to the prescribed temperature in the heater (lower right).

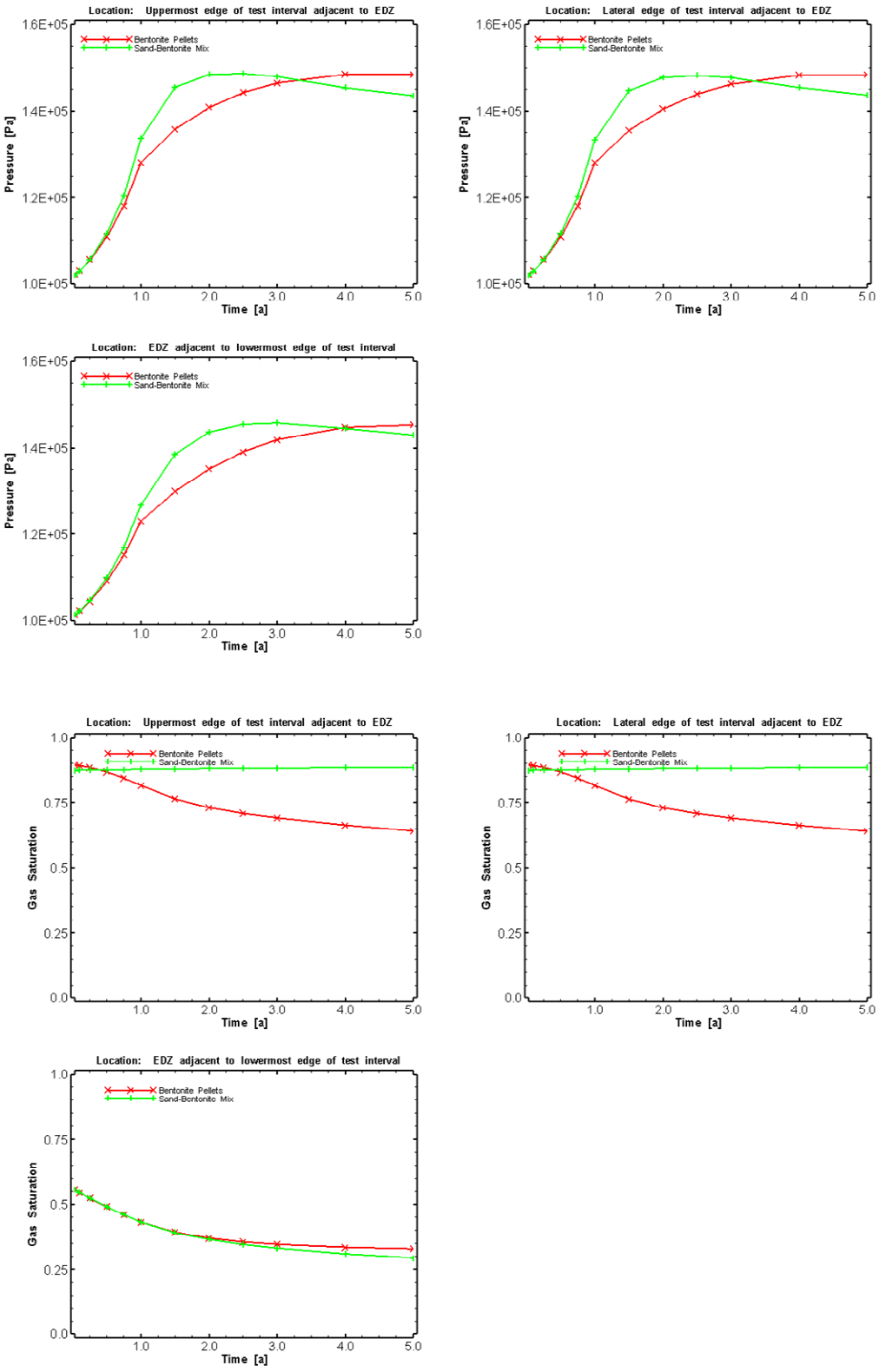

Figure 2.19 Case S2R0: Time histories of pressures (top) and saturation (bottom) at the different observation points.

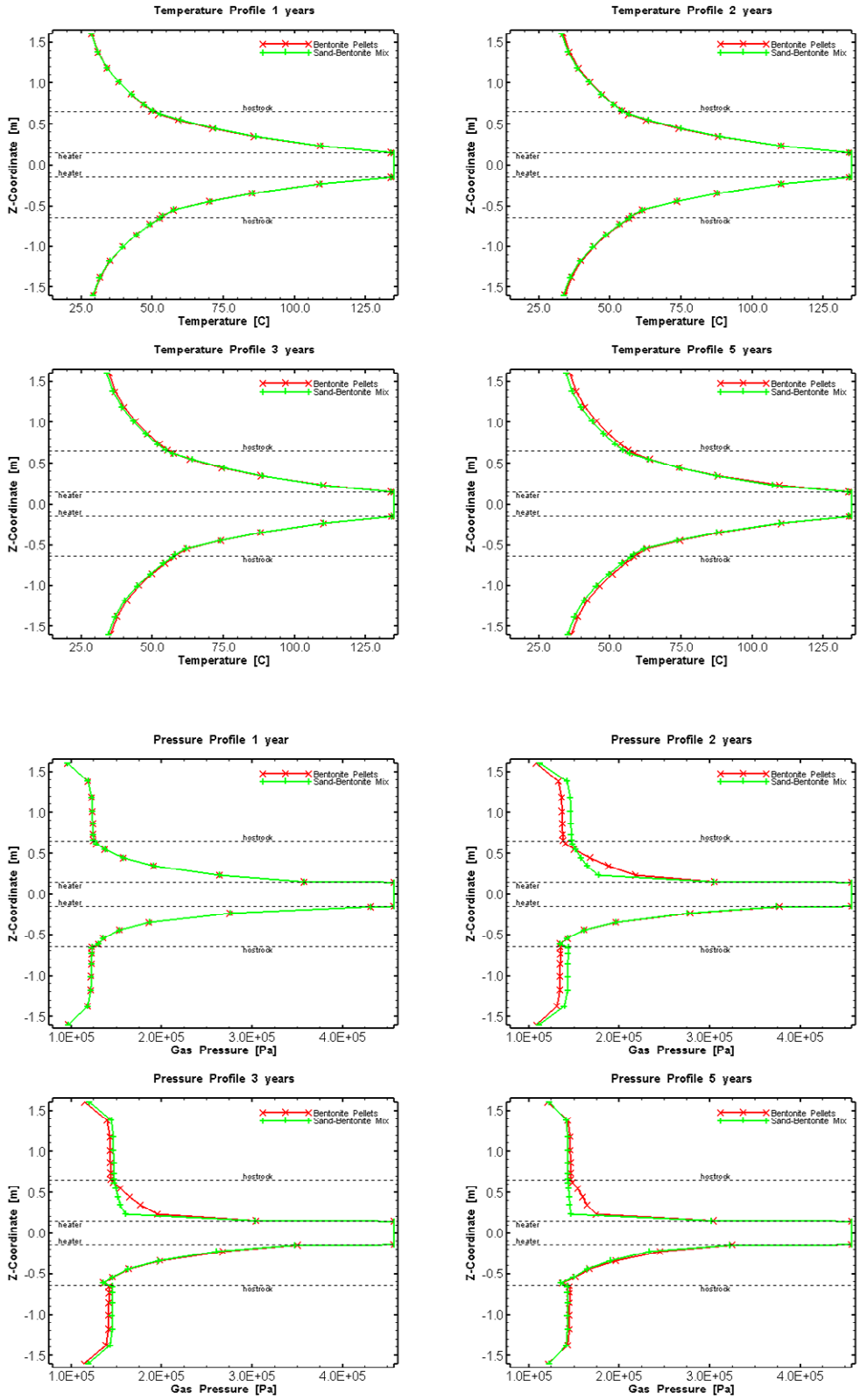

Figure 2.20 Case S2R0: Simulated vertical profiles of temperatures (top) and pressures (bottom) at different times.

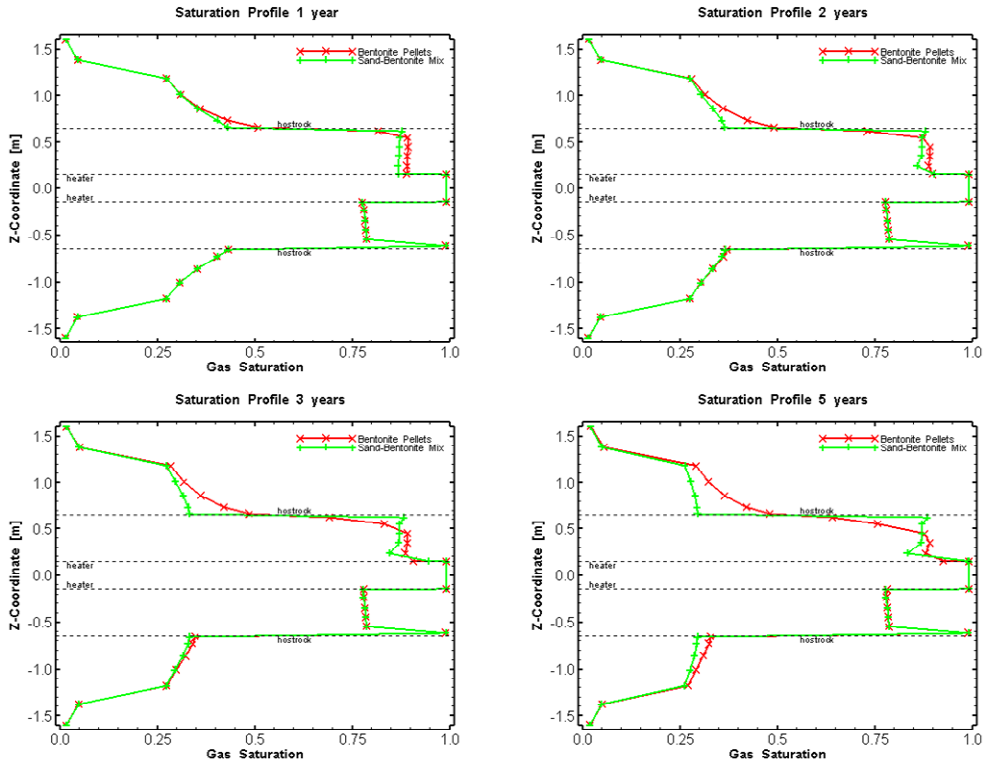

Figure 2.21 Case S2R0: Simulated vertical profiles of gas saturations (bottom) at different times

2.3.3 Sensitivity Simulations

2.3.3.1 S1R1: k (OPA) increase

Case S1R1 considers a one-order of magnitude increase in permeability of the Opalinus Clay and EDZ. For this case, the initial conditions from the corresponding simulation of the ventilation period, described in Section 2.3.1, was used. The time histories of temperatures, pressures, and saturation are shown in Figure 2.22 and 2.23. The vertical profiles of temperature, pressure, and saturation at different times are given in Figures 2.24 and 2.25.

The temperature histories for both the bentonite pellets and the sand/bentonite indicate temperature increases to near 60 ºC after 5 years, corresponding to the maximum prescribed temperature of 135 ºC of the heater element. The pressures at the observation locations indicate an increase to near 125 kPa in the sand/bentonite and 130 kPa in the pellets. This is less than in the base case due to the higher permeability of the Opalinus Clay/EDZ allowing more ready dissipation of the pressure buildup due to thermal expansion. The simulated gas saturations indicate significantly different responses between the sand/bentonite and the pellets with the gas saturations at the upper and lateral edge of the bentonite pellets decreasing do about 45% after 5 years, whereas the gas saturations remain essentially the same in the sand/bentonite. At the bottom edge, which is in the EDZ next to the element representing the cable box, the gas saturations decrease to 32% for the pellet section and 23% for the sand/bentonite section.

The corresponding vertical temperature profiles are the same between sand/bentonite and pellets and are largely symmetric with only a slight difference around the cable box at the bottom of the bentonite blocks. The pressure profiles show distinct differences between the sand/bentonite and pellets in the upper part after two years. The pressure in the sand/bentonite actually decreased to a near constant profile above the heater element. The simulated pressure increase in the heater element is caused by thermal expansion for which a low porosity of 0.1% was assumed and negligible permeability (k=1.E-50m^2). The corresponding saturation profiles indicate that the gas saturations in the pellets decrease above the heater element, whereas in the sand/bentonite the saturation remained near the initial emplacement saturation but decreased noticeably in the adjacent EDZ. In the bentonite blocks beneath the heater element, the saturations are the same. The high saturation in the bottom element at the contact between the EDZ remained constant, due to the negligible permeability assigned to the cable box.

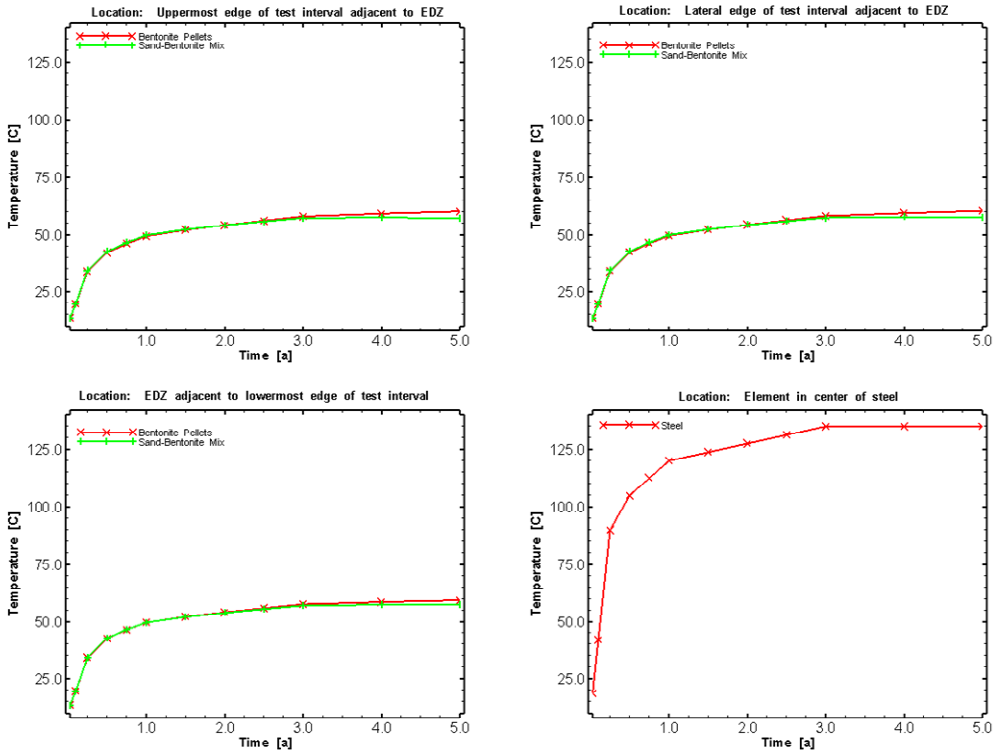

Figure 2.22 Case S1R1: Temperature histories at the different observation points, in addition to the prescribed temperature in the heater (lower right).

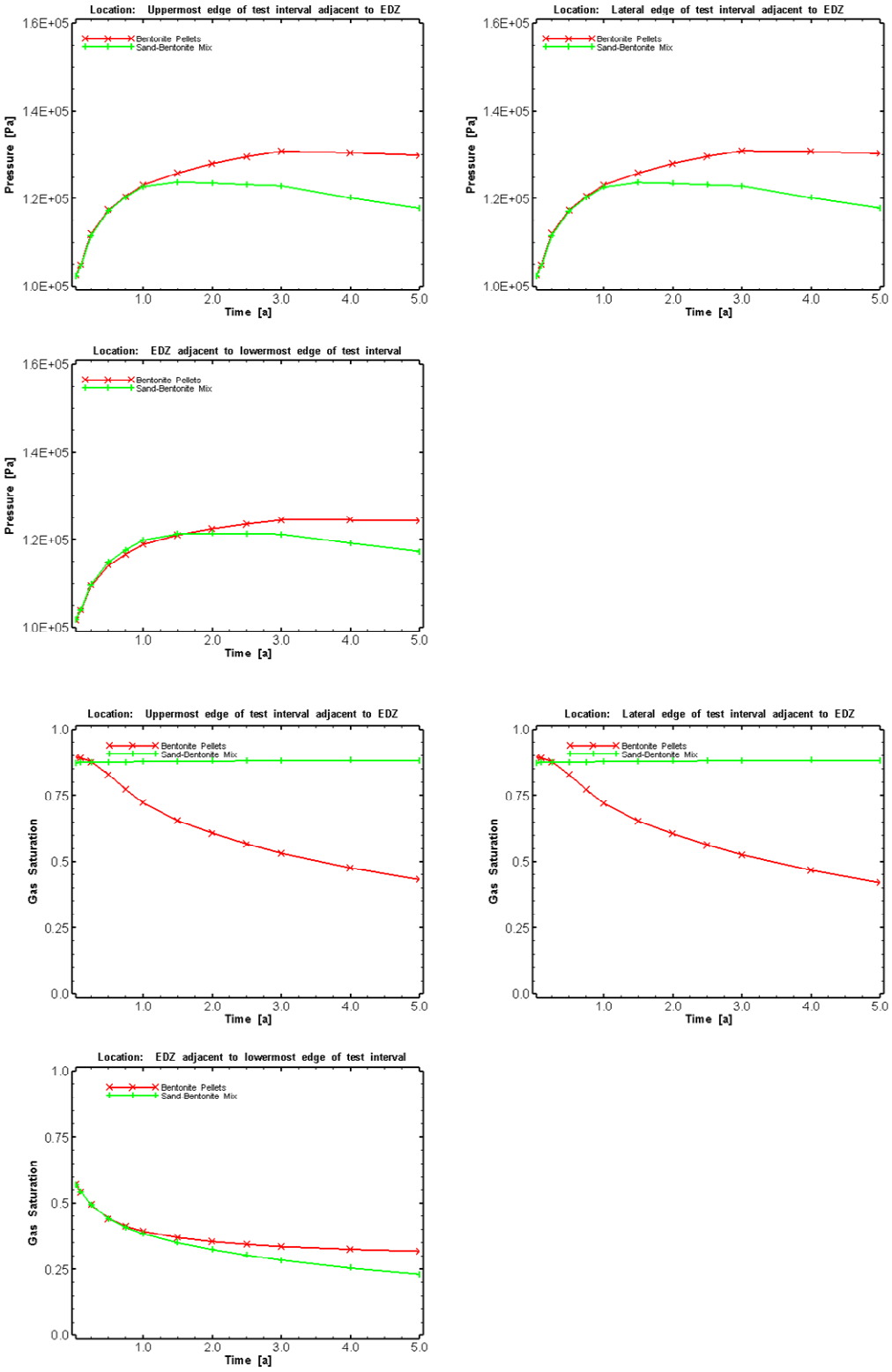

Figure 2.23 Case S1R1: Time histories of pressures (top) and saturation (bottom) at the different observation points.

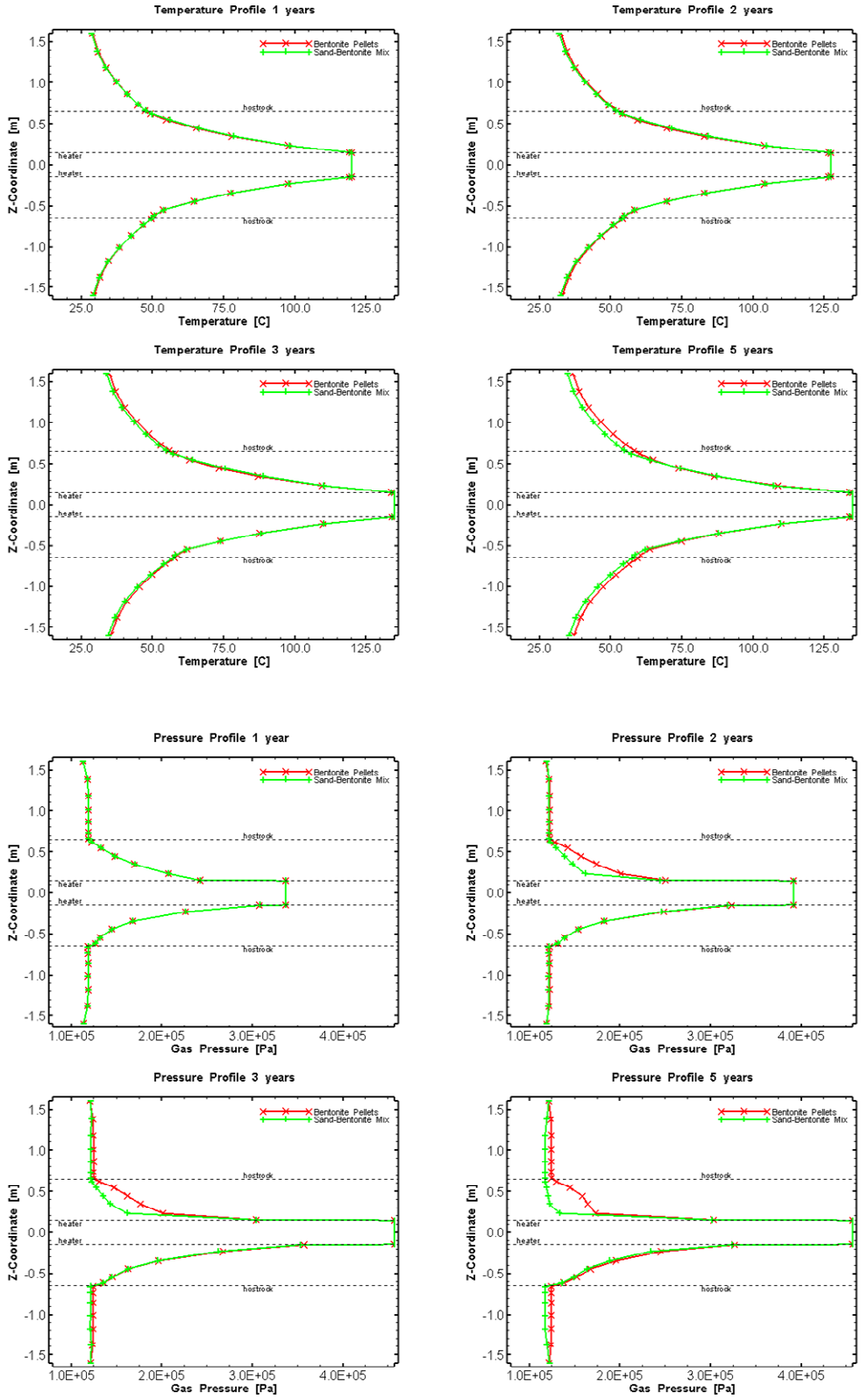

Figure 2.24 Case S1R1: Simulated vertical profiles of temperatures (top) and pressures (bottom) at different times.

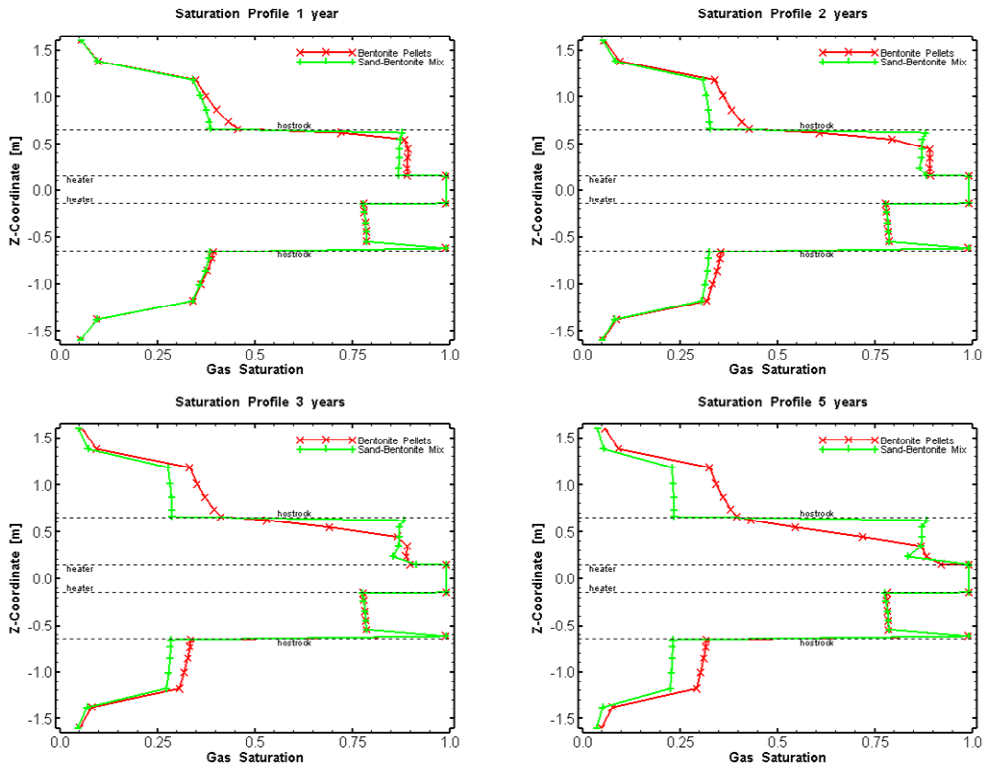

Figure 2.25 Case S1R1: Simulated vertical profiles of gas saturations at different times

2.3.3.2 S1R2: k(OPA) decrease

Case S1R2 considers a one-order of magnitude decrease in permeability of the Opalinus Clay and EDZ. . For this case, the initial conditions from the corresponding simulation of the ventilation period, described in Section 2.3.1, was used. The time histories of temperatures, pressures, and saturation are shown in Figure 2.26 and 2.27. The vertical profiles of temperature, pressure, and saturation at different times are given in Figures 2.28 and 2.29.

The temperature histories for both the bentonite pellets and the sand/bentonite indicate temperature increases to near 60 ºC after 5 years, which corresponds to the temperature increase in the base case. The pressures at the observation locations indicate an increase to near 165 kPa in the sand/bentonite and in the pellets. This pressure increase is greater than in the base case due to the lower permeability of the Opalinus Clay/EDZ allowing less dissipation of the pressure buildup associated with the thermal expansion. The simulated gas saturations indicate significantly different responses between the sand/bentonite and the pellets with the gas saturations at the upper and lateral edge of the bentonite pellets decreasing do about 70% after 5 years, whereas the gas saturations remain essentially the same in the sand/bentonite. At the bottom edge, which is in the EDZ next to the element representing the cable box, the gas saturations decrease to 25% for the pellet section and for the sand/bentonite section.

The corresponding vertical temperature profiles are the same between sand/bentonite and pellets and are largely symmetric with only a slight difference around the cable box at the bottom of the bentonite blocks. The pressure profiles show distinct differences between the sand/bentonite and

pellets in the upper part after two years. The pressure in the sand/bentonite actually decreased to a near constant profile above the heater element. The simulated pressure increase in the heater element is caused by thermal expansion for which a low porosity of 0.1% was assumed and negligible permeability (k=1.E-50m^2). The corresponding saturation profiles indicate that the gas saturations in the pellets decrease above the heater element, whereas in the sand/bentonite the saturation remained near the initial emplacement saturation but decreased somewhat in the adjacent EDZ. In the bentonite blocks beneath the heater element, the saturations are the same. The high saturation in the bottom element at the contact between the EDZ remained constant, due to the negligible permeability assigned to the cable box.

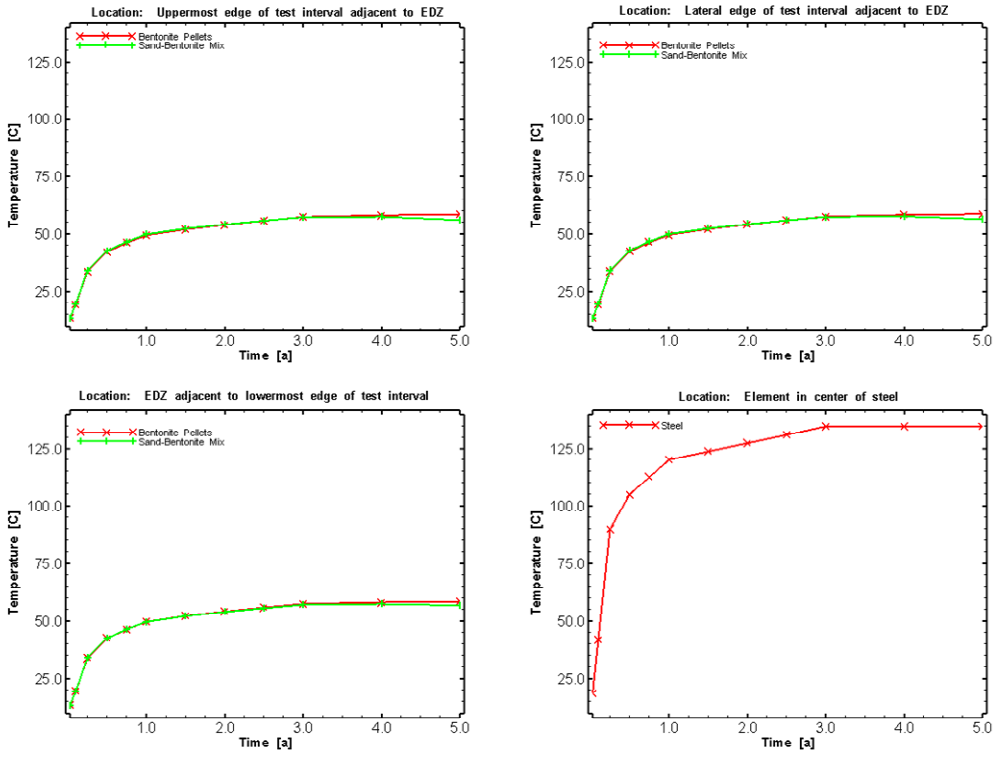

Figure 2.26 Case S1R2: Temperature histories at the different observation points, in addition to the prescribed temperature in the heater (lower right).

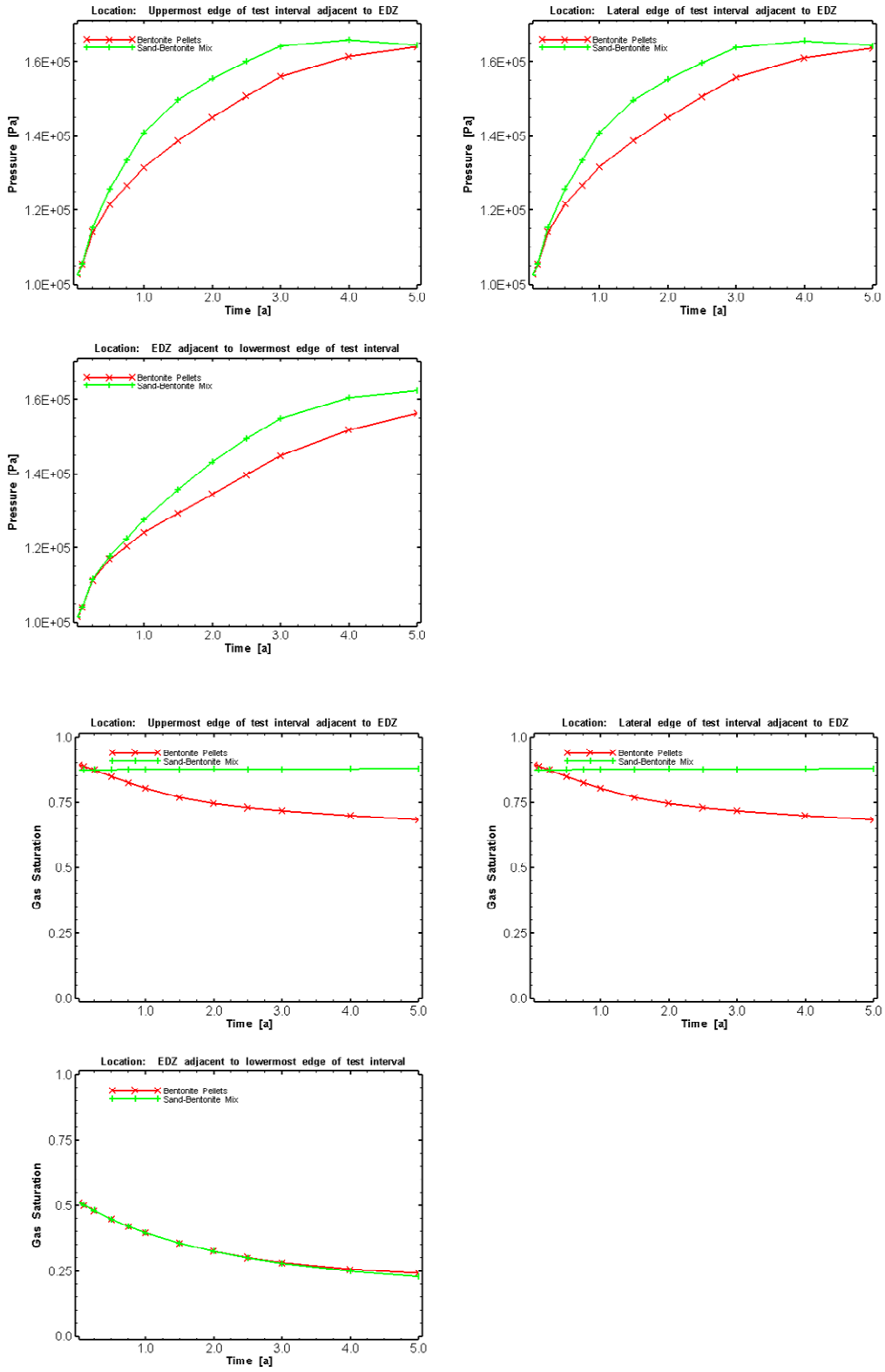

Figure 2.27 Case S1R2: Time histories of pressures (top) and saturation (bottom) at the different observation points.

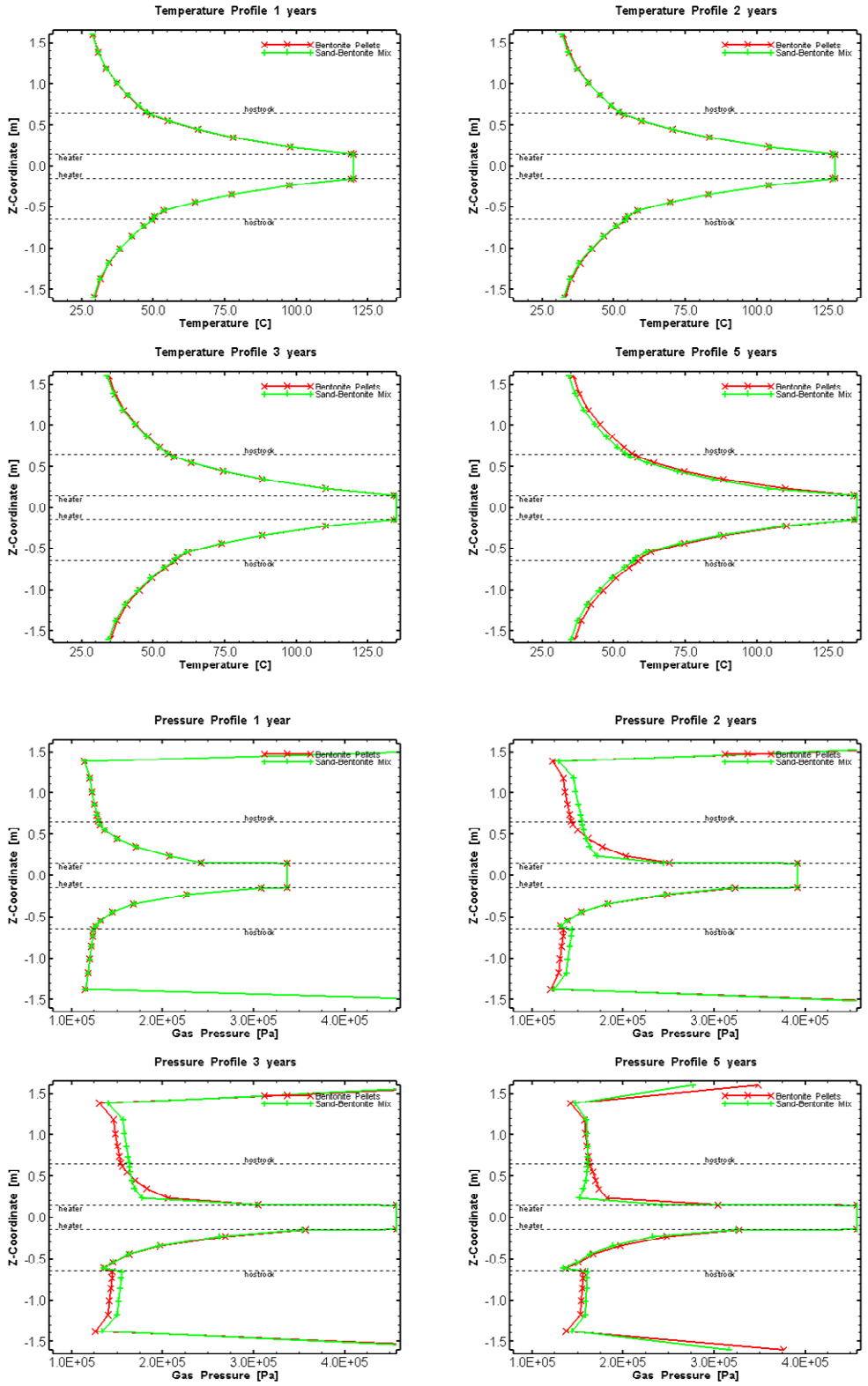

Figure 2.28 Case S1R2: Simulated vertical profiles of temperatures (top) and pressures (bottom) at different times.

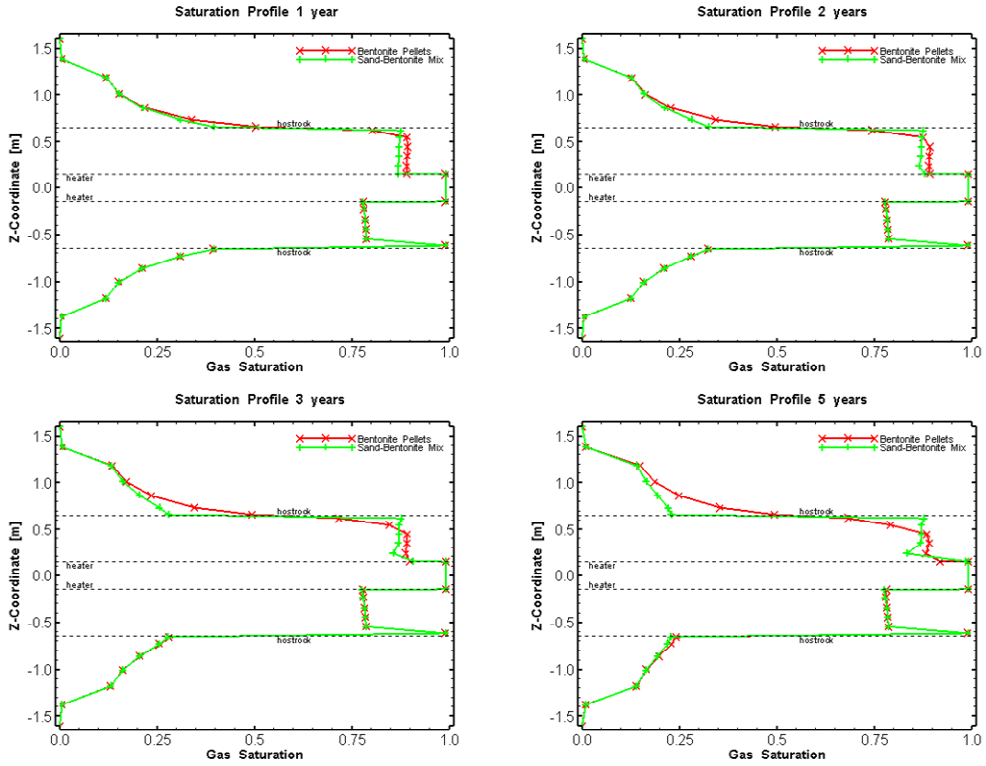

Figure 2.29 Case S1R2: Simulated vertical profiles of gas saturations at different times

2.3.3.3 S1R3: Linear Thermal Conduction

Case S1R3 considers a linear relationship between the wet and dry thermal conductivity of the bentonite. All other cases assumed a relationship that is scaled by the square root of the saturation. The time histories of temperatures, pressures, and saturation are shown in Figure 2.30 and 2.31. The vertical profiles of temperature, pressure, and saturation at different times are given in Figures 2.32 and 2.33.

The temperature histories for both the bentonite pellets and the sand/bentonite indicate temperature increases to 50ºC after 5 years, which is lower than the 60ºC in the base case. The pressures at the observation locations indicate an increase to only 140 kPa, with some difference between the sand/bentonite and the pellets. The simulated gas saturations indicate significant different responses between the sand/bentonite and the pellets with the gas saturations at the upper and lateral edge of the bentonite pellets decreasing do about 65% after 5 years. In the sand/bentonite, the gas saturation essentially remains the same. At the bottom edge, which is in the EDZ next to the element representing the cable box, the gas saturations decrease to 34% for the pellet section and 30% for the sand/bentonite section.

The corresponding vertical temperature profiles are the same between sand/bentonite and pellets and are largely symmetric with only a slight difference around the cable box at the bottom of the bentonite blocks. The pressure profiles show distinct differences between the sand/bentonite and pellets in the upper part after two years. The pressure in the sand/bentonite actually decreased to

a near constant profile above the heater element. The simulated pressure increase in the heater element is caused by thermal expansion for which a low porosity of 0.1% was assumed and negligible permeability (k=1.E-50m^2). The corresponding saturation profiles indicate that the gas saturations in the pellets decrease above the heater element, whereas in the sand/bentonite the saturation remained near the initial emplacement saturation, but decreased noticeably in the adjacent EDZ. In the bentonite blocks beneath the heater element, the saturations are the same.

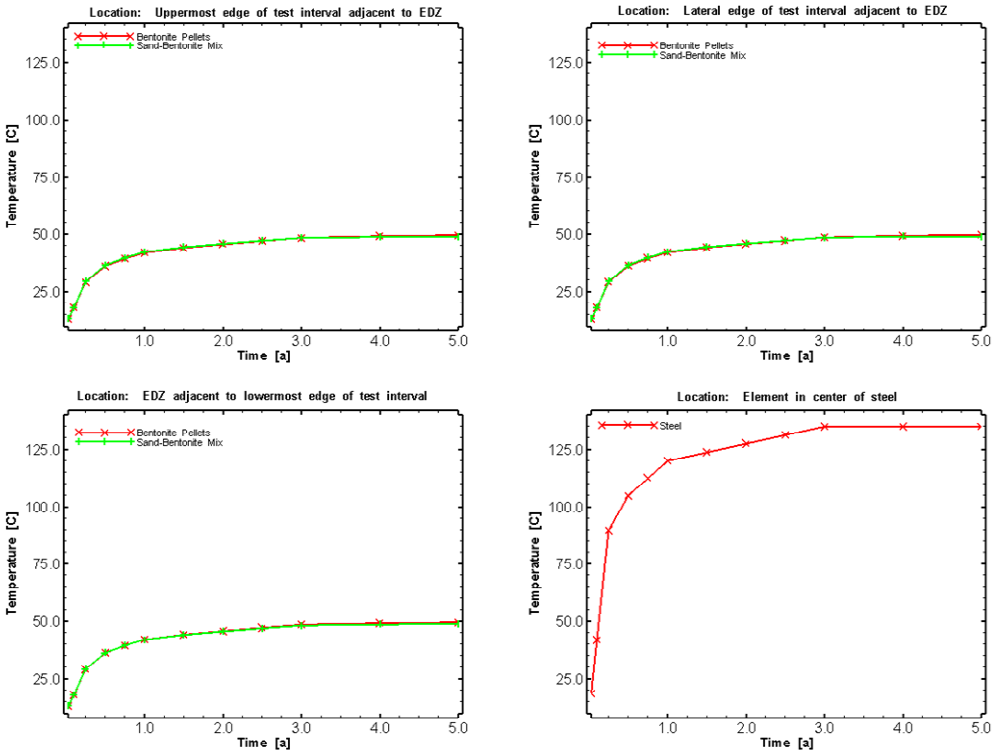

Figure 2.30 Case S1R3: Temperature histories at the different observation points, in addition to the prescribed temperature in the heater (lower right).

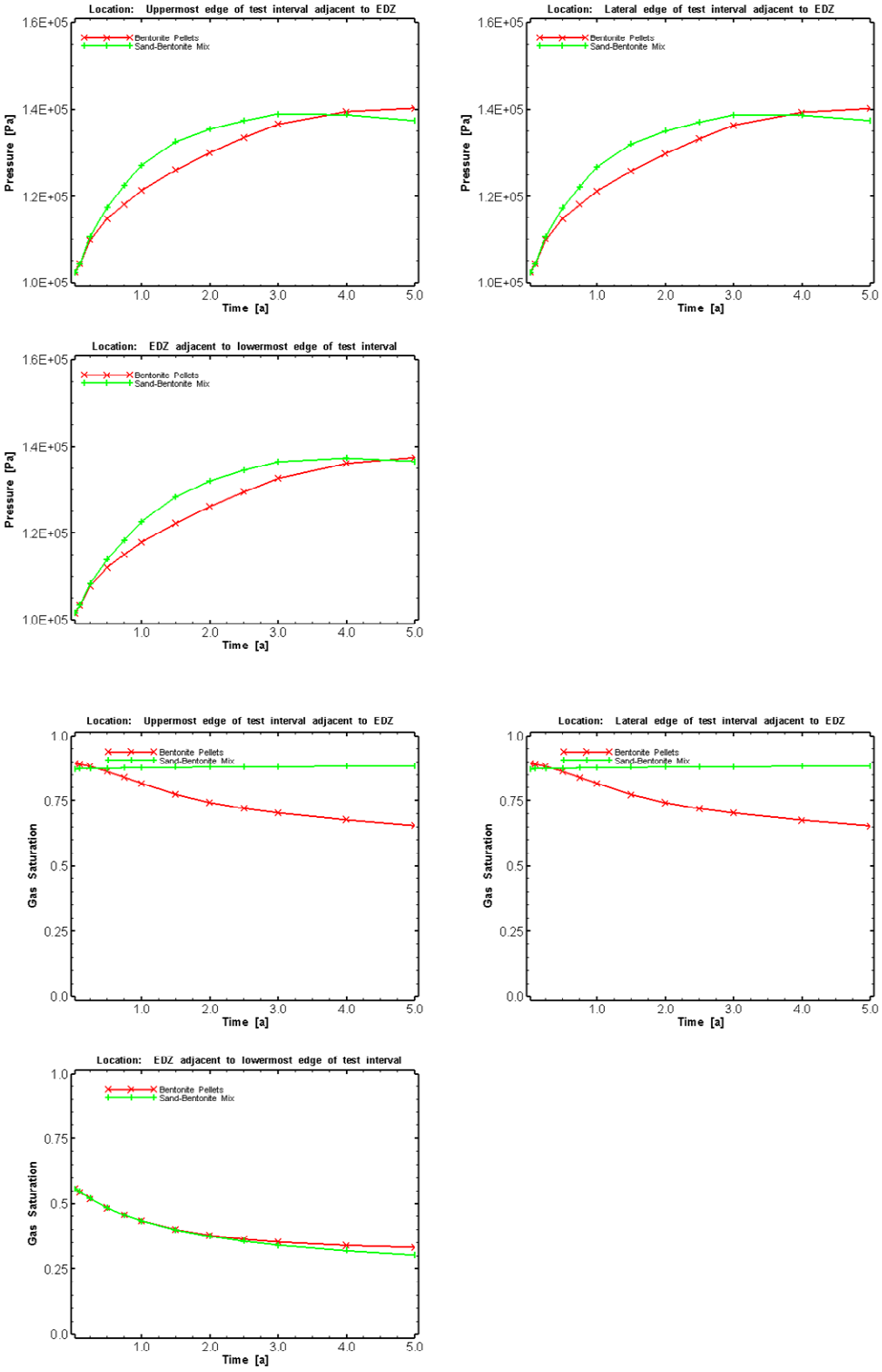

Figure 2.31 Case S1R3: Time histories of pressures (top) and saturation (bottom) at the different observation points.

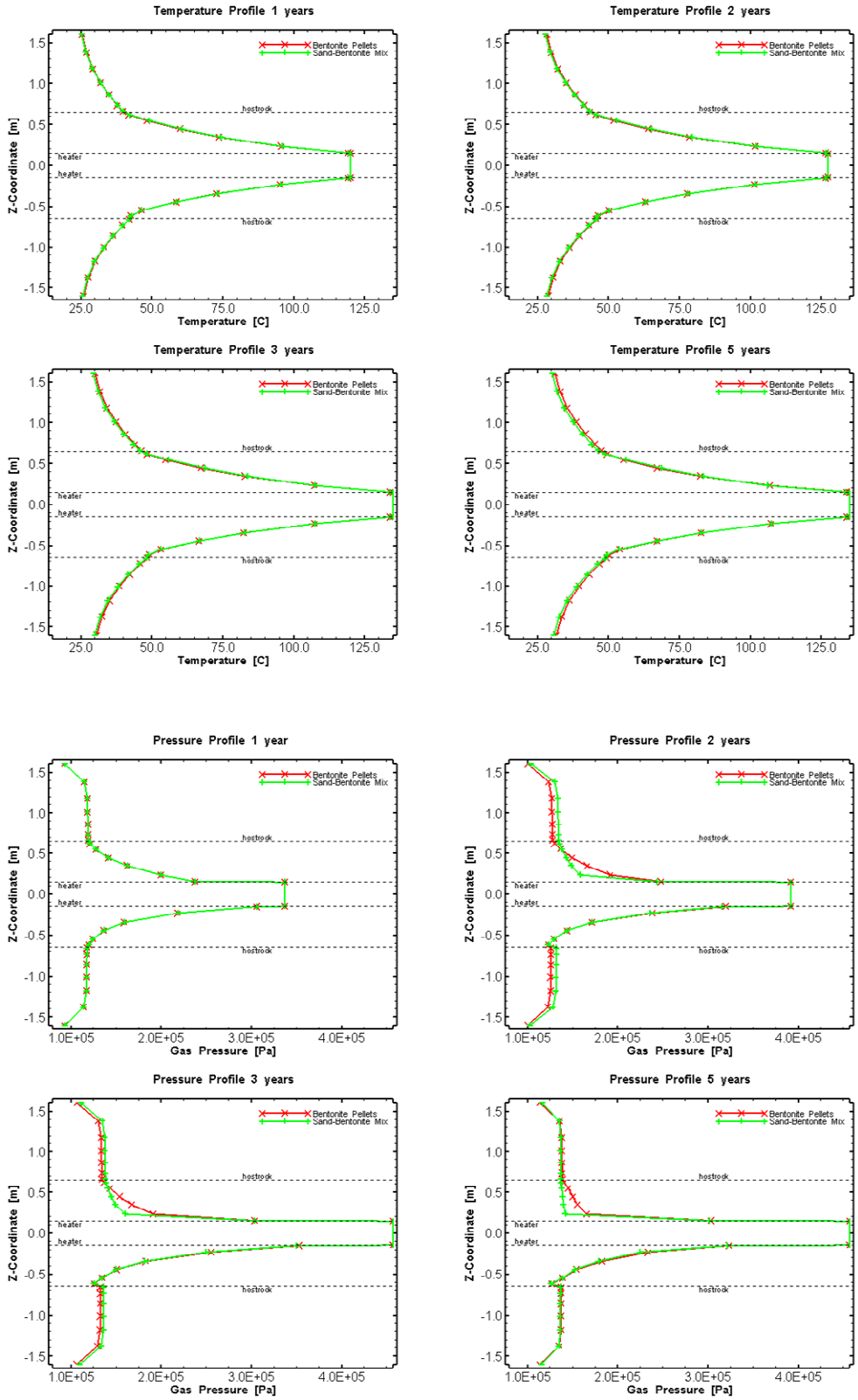

Figure 2.32 Case S1R3: Simulated vertical profiles of temperatures (top) and pressures (bottom) at different times.

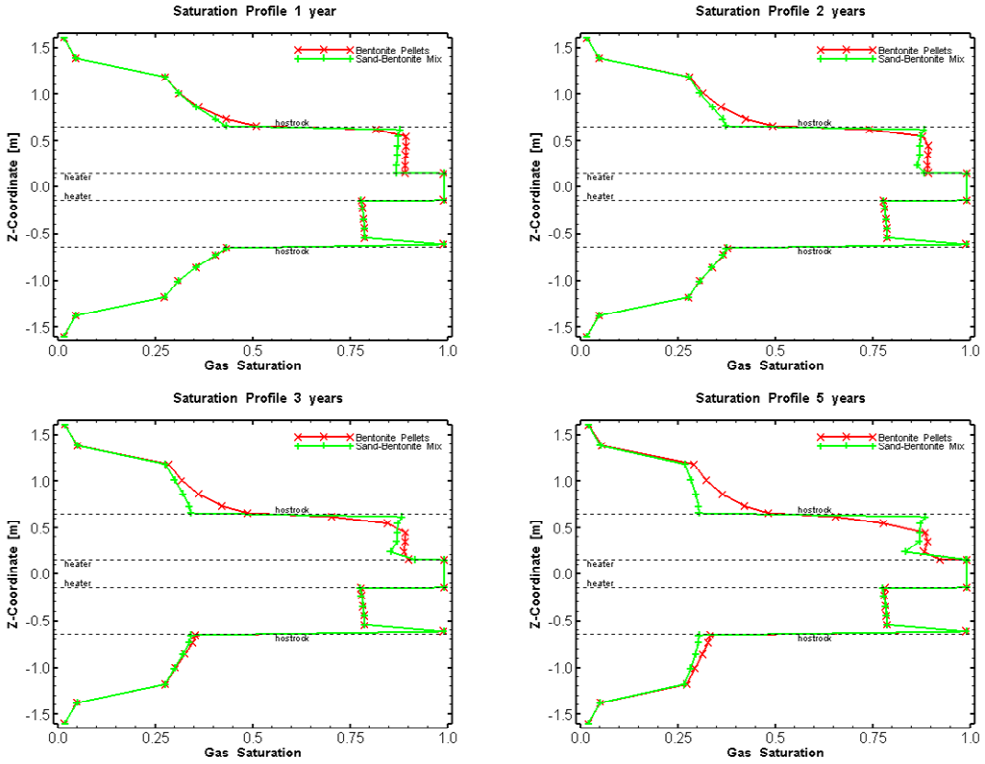

Figure 2.33 Case S1R3: Simulated vertical profiles of gas saturations at different times

2.3.3.4 S1R4: Initial Saturation

Case S1R4 considers higher initial water saturation in the bentonite blocks of (Sw = 0.5) and slightly lower saturations for the pellets and sand/bentonite (Sw =0.1). The time histories of temperatures, pressures, and gas saturation are shown in Figure 2.34 and 2.35. The vertical profiles of temperature, pressure, and gas saturation at different times are given in Figures 2.36 and 2.37.

The temperature histories for the bentonite pellets indicate temperature increases to near 60ºC after 5 years, with slightly lower temperatures for the sand/bentonite. The pressures at the observation locations indicate an increase to near 150 kPa, with some difference between the sand/bentonite and the pellets. The simulated gas saturations indicate significant different responses between the sand/bentonite and the pellets with the gas saturations at the upper and lateral edge of the bentonite pellets decreasing do about 65% after 5 years. In the sand/bentonite, the gas saturation essentially remains the same. At the bottom edge, which is in the EDZ next to the element representing the cable box, the gas saturations decrease to 34% for the pellet section and 30% for the sand/bentonite section.

The corresponding vertical temperature profiles are the same between sand/bentonite and pellets and are largely symmetric with only a slight difference around the cable box at the bottom of the bentonite blocks. The pressure profiles show distinct differences between the sand/bentonite and pellets in the upper part after two years. The pressure in the sand/bentonite actually decreased to

a near constant profile above the heater element. The simulated pressure increase in the heater element is caused by thermal expansion for which a low porosity of 0.1% was assumed and negligible permeability (k=1.E-50m^2). The corresponding saturation profiles indicate that the gas saturations in the pellets decrease above the heater element, whereas in the sand/bentonite the saturation remained near the initial emplacement saturation, but decreased somewhat in the adjacent EDZ. In the bentonite blocks beneath the heater element, the saturations in the sand/bentonite section remain the same, but increase in the pellet section. Overall, the effect of the higher initial water saturation in the bentonite blocks indicate negligible difference to the base case, which is due to the fact that the bentonite blocks are separated from the clay by the cable box and does not allow preferential water flow into the bentonite blocks.

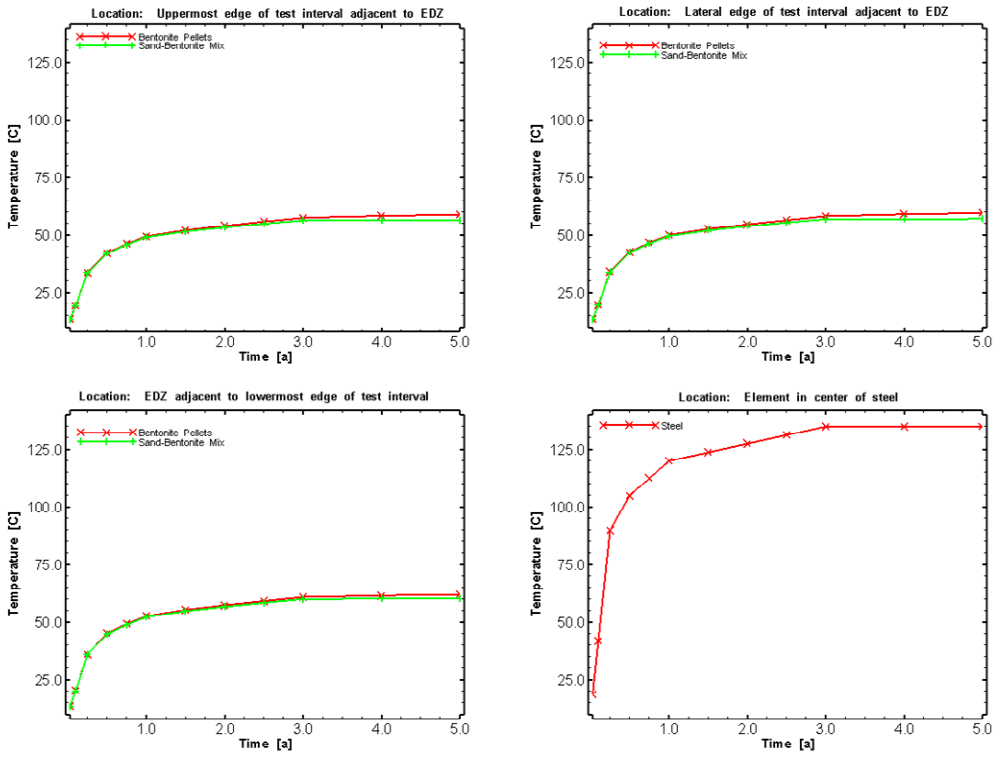

Figure 2.34 Case S1R4: Temperature histories at the different observation points, in addition to the prescribed temperature in the heater (lower right).

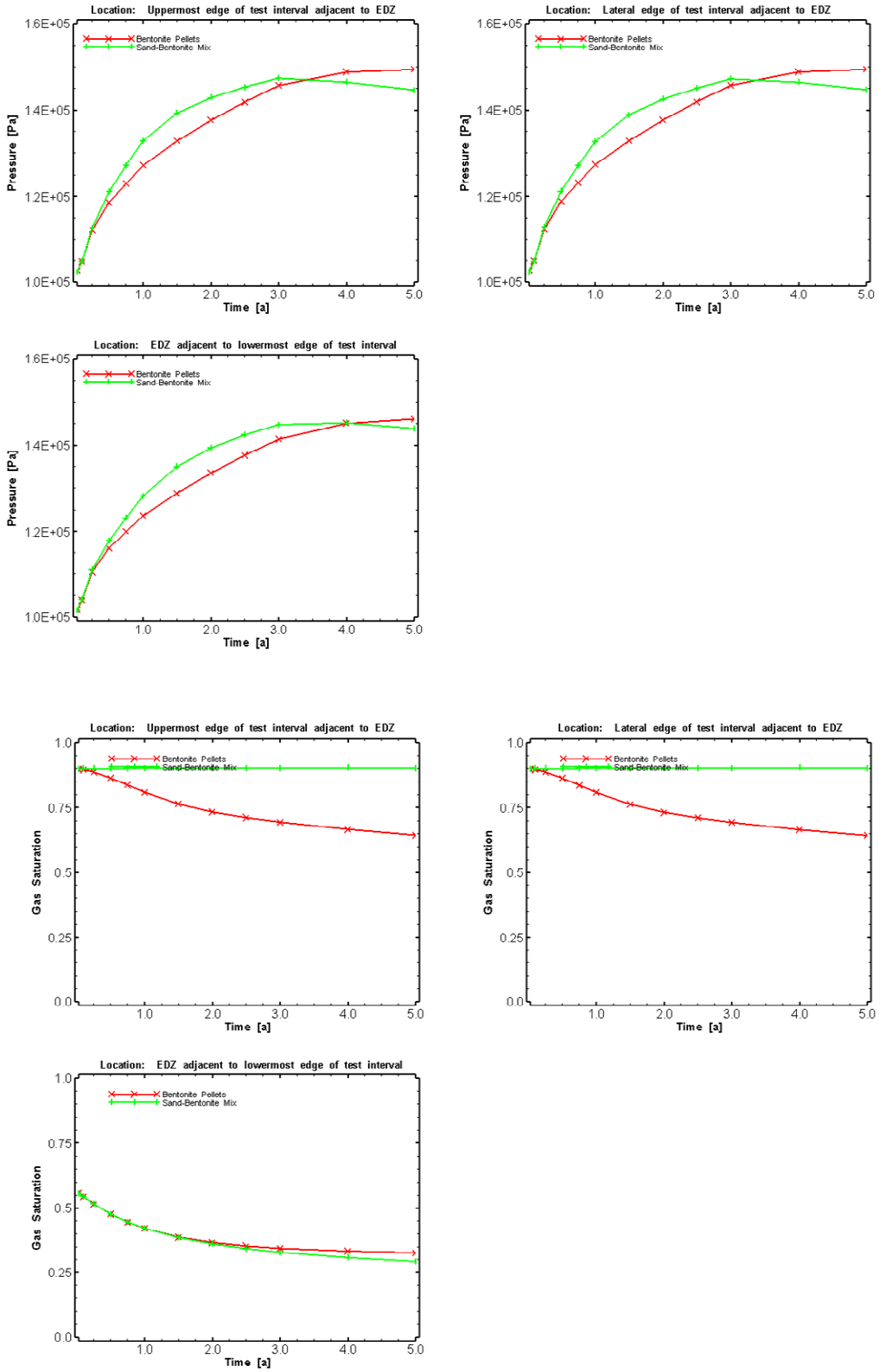

Figure 2.35 Case S1R4: Time histories of gas pressures (top) and saturation (bottom) at the different observation points.

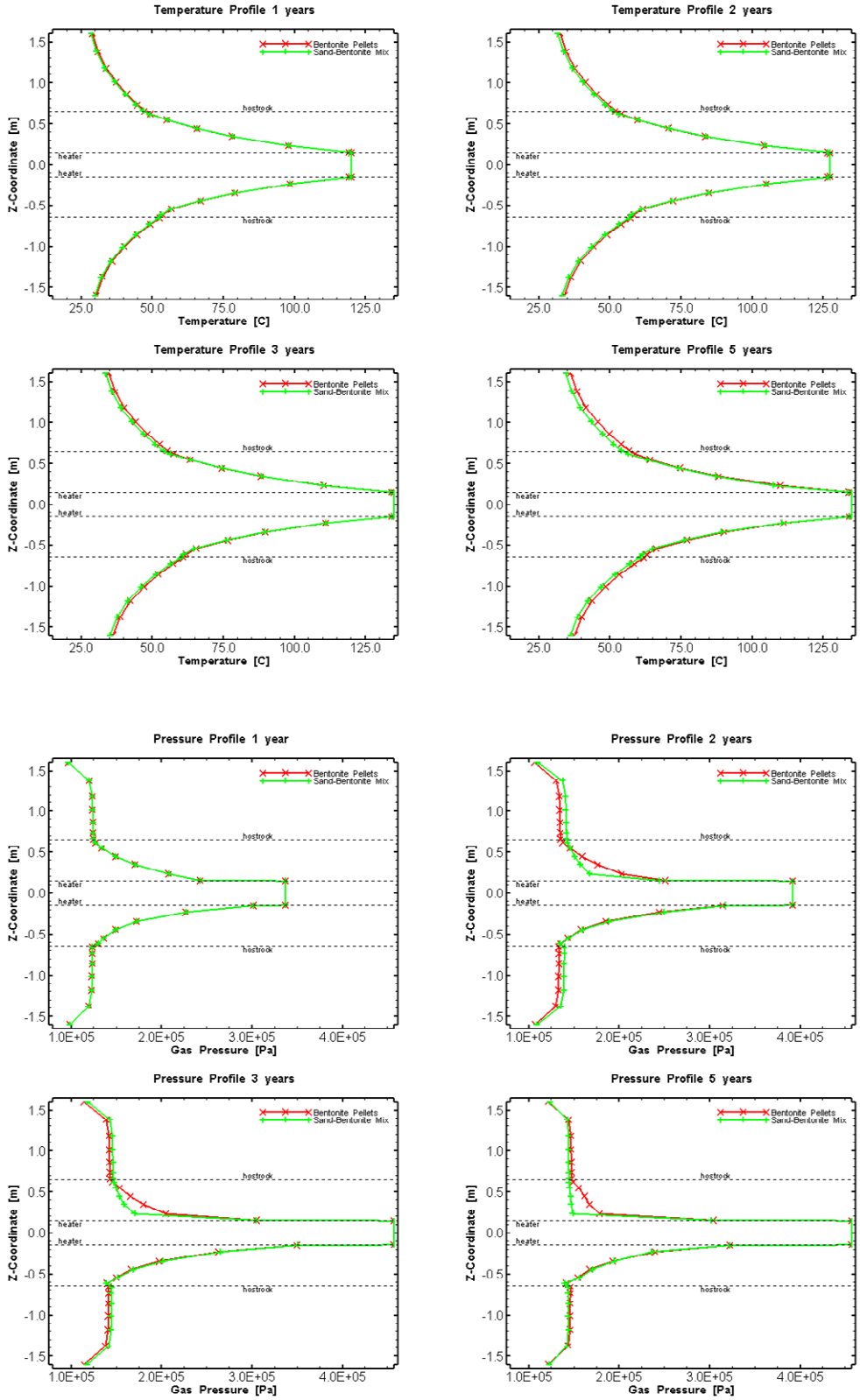

Figure 2.36 Case S1R4: Simulated vertical profiles of temperatures (top) and pressures (bottom) at different times.

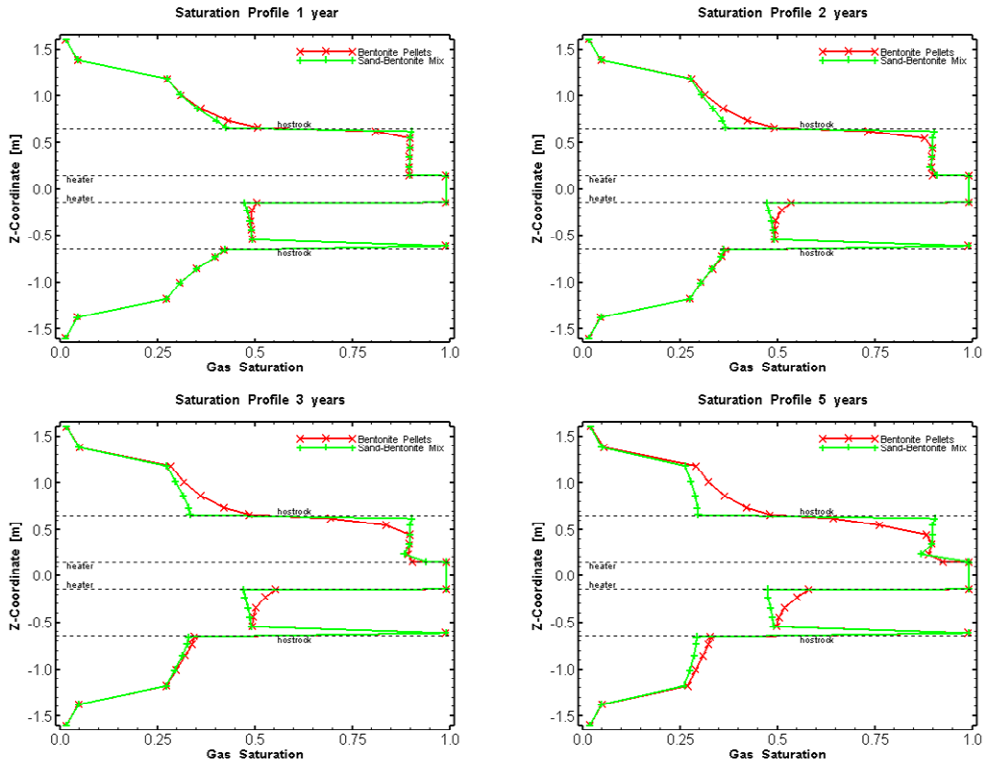

Figure 2.37 Case S1R4: Simulated vertical profiles of gas saturations at different times

2.3.3.5 S1R5: Anisotropy of Thermal Conductivity (OPA)

Case S1R5 examined the effect of anisotropy in the thermal conductivity of the Opalinus Clay (i.e. Tc(hor.)=2.5, Tc(vert.)=1.55). The time histories of temperatures, pressures, and saturation are shown in Figure 2.38 and 2.39. The vertical profiles of temperature, pressure, and saturation at different times are given in Figures 2.40 and 2.41.

The temperature histories for both the bentonite pellets and the sand/bentonite indicate temperature increases to slightly above 60ºC after 5 years. The pressures at the observation locations indicate an increase to near 150 kPa, with some difference between the sand/bentonite and the pellets. The simulated gas saturations indicate significant different responses between the sand/bentonite and the pellets with the gas saturations at the upper and lateral edge of the bentonite pellets decreasing to about 65% after 5 years. In the sand/bentonite, the gas saturation essentially remains the same. At the bottom edge, which is in the EDZ next to the element representing the cable box, the gas saturations decrease to 33% for the pellet section and 28% for the sand/bentonite section.

The corresponding vertical temperature profiles are the same between sand/bentonite and pellets and are largely symmetric with only a slight difference around the cable box at the bottom of the bentonite blocks. The pressure profiles show distinct differences between the sand/bentonite and pellets in the upper part after two years. The pressure in the sand/bentonite actually decreased to a near constant profile above the heater element. The simulated pressure increase in the heater element is caused by thermal expansion for which a low porosity of 0.1% was assumed and

negligible permeability (k=1.E-50m^2). The corresponding saturation profiles indicate that the gas saturations in the pellets decrease above the heater element, whereas in the sand/bentonite the saturation remained near the initial emplacement saturation, but decreased noticeably in the adjacent EDZ. In the bentonite blocks beneath the heater element, the saturations are the same. Overall, the results show little differences compared to the base case.

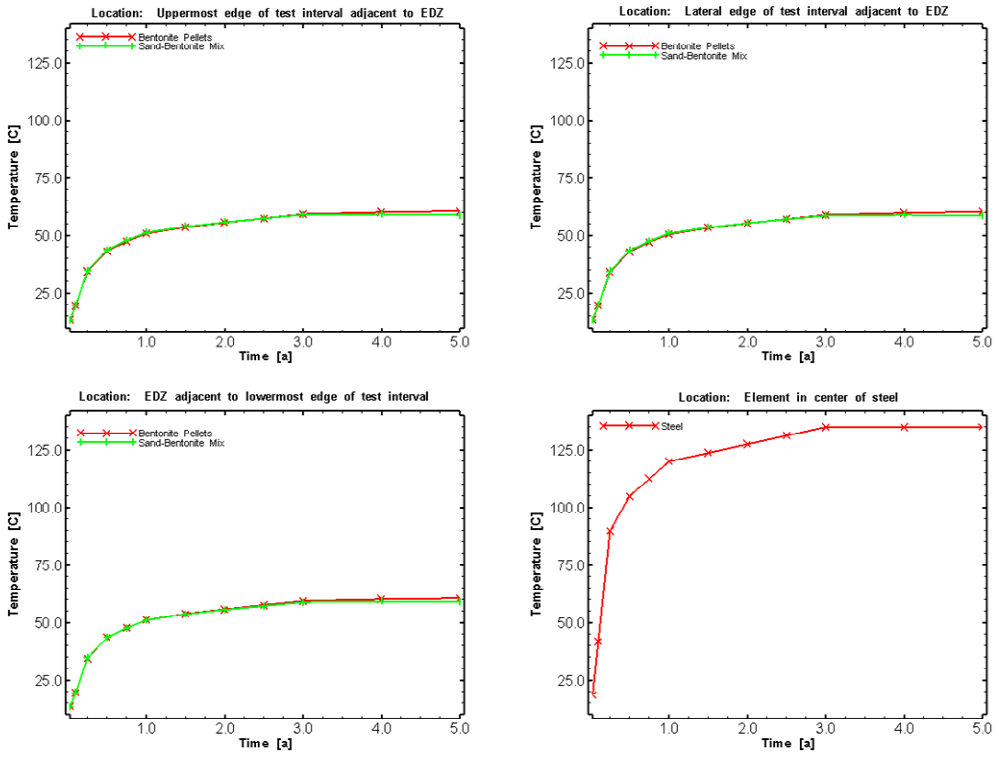

Figure 2.38 Case S1R5: Temperature histories at the different observation points, in addition to the prescribed temperature in the heater (lower right).

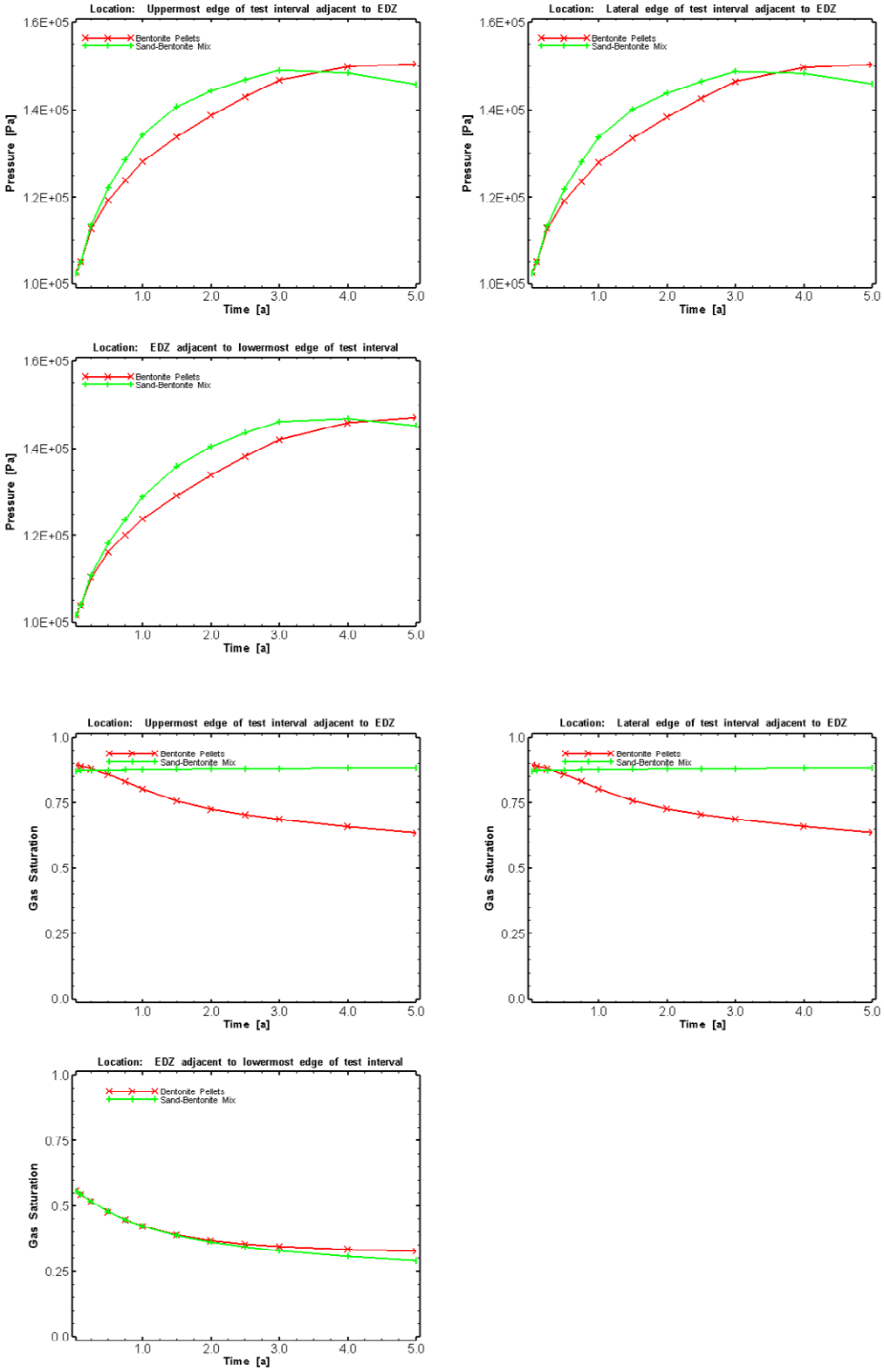

Figure 2.39 Case S1R5: Time histories of gas pressures (top) and saturation (bottom) at the different observation points.

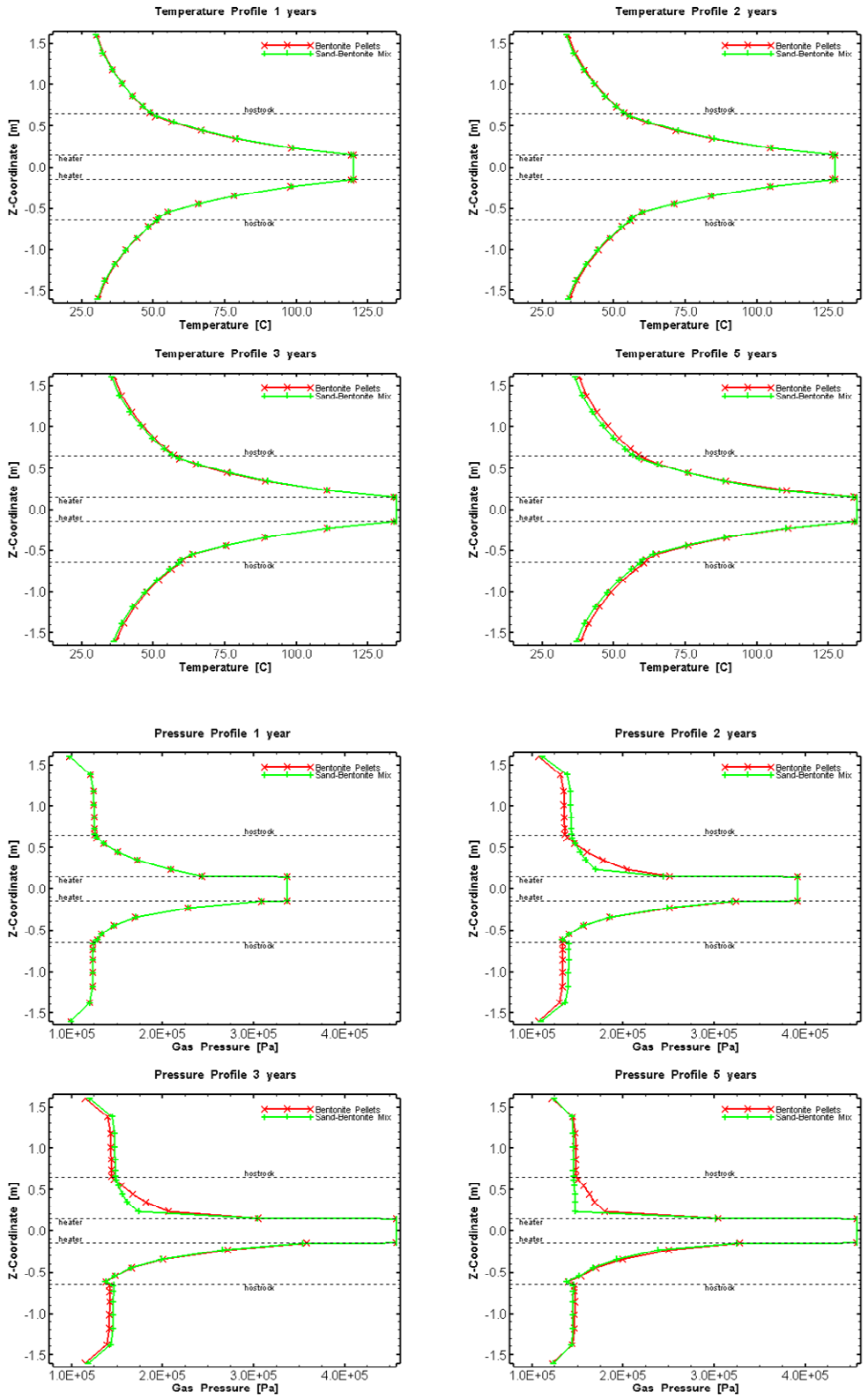

Figure 2.40 Case S1R5: Simulated vertical profiles of temperatures (top) and pressures (bottom) at different times.

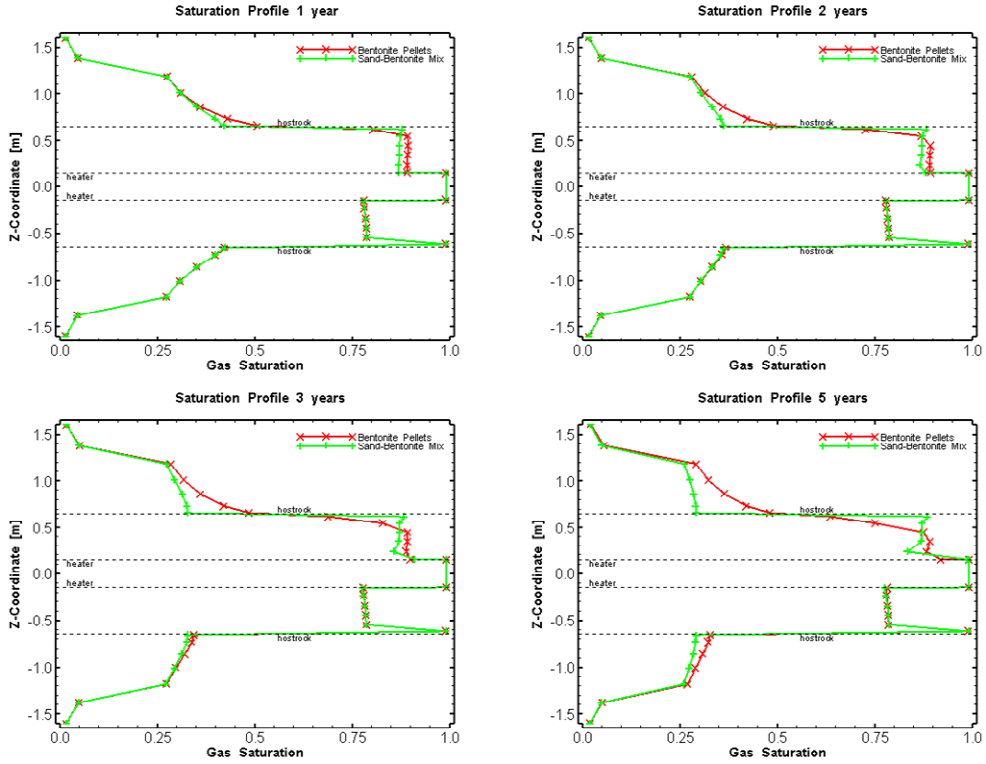

Figure 2.41 Case S1R5: Simulated vertical profiles of gas saturations at different times

2.3.3.6 S1R6: Increased Capillary Strength

Case S1R6 considers the effect of increased capillary strength in the Opalinus Clay (i.e. vG-P_0=2.5). The time histories of temperatures, pressures, and saturation are shown in Figure 2.42 and 2.43. The vertical profiles of temperature, pressure, and saturation at different times are given in Figures 2.44 and 2.45.

The temperature histories for both the bentonite pellets and the sand/bentonite indicate temperature increases to near 60ºC after 5 years. The pressures at the observation locations indicate an increase to near 150 kPa, with some difference between the sand/bentonite and the pellets. The simulated gas saturations indicate significant different responses between the sand/bentonite and the pellets with the gas saturations at the upper and lateral edge of the bentonite pellets decreasing do about 65% after 5 years. In the sand/bentonite, the gas saturation essentially remains the same. At the bottom edge, which is in the EDZ next to the element representing the cable box, the gas saturations decrease to 33% for the pellet section and 28% for the sand/bentonite section.

The corresponding vertical temperature profiles are the same between sand/bentonite and pellets and are largely symmetric with only a slight difference around the cable box at the bottom of the bentonite blocks. The pressure profiles show distinct differences between the sand/bentonite and pellets in the upper part after two years. The pressure in the sand/bentonite actually decreased to a near constant profile above the heater element. The simulated pressure increase in the heater

element is caused by thermal expansion for which a low porosity of 0.1% was assumed and negligible permeability (k=1.E-50m^2). The corresponding saturation profiles indicate that the gas saturations in the pellets decrease above the heater element, whereas in the sand/bentonite the saturation remained near the initial emplacement saturation, but decreased noticeably in the adjacent EDZ. In the bentonite blocks beneath the heater element, the saturations are the same. Overall the results indicate only small difference compared to the base case.

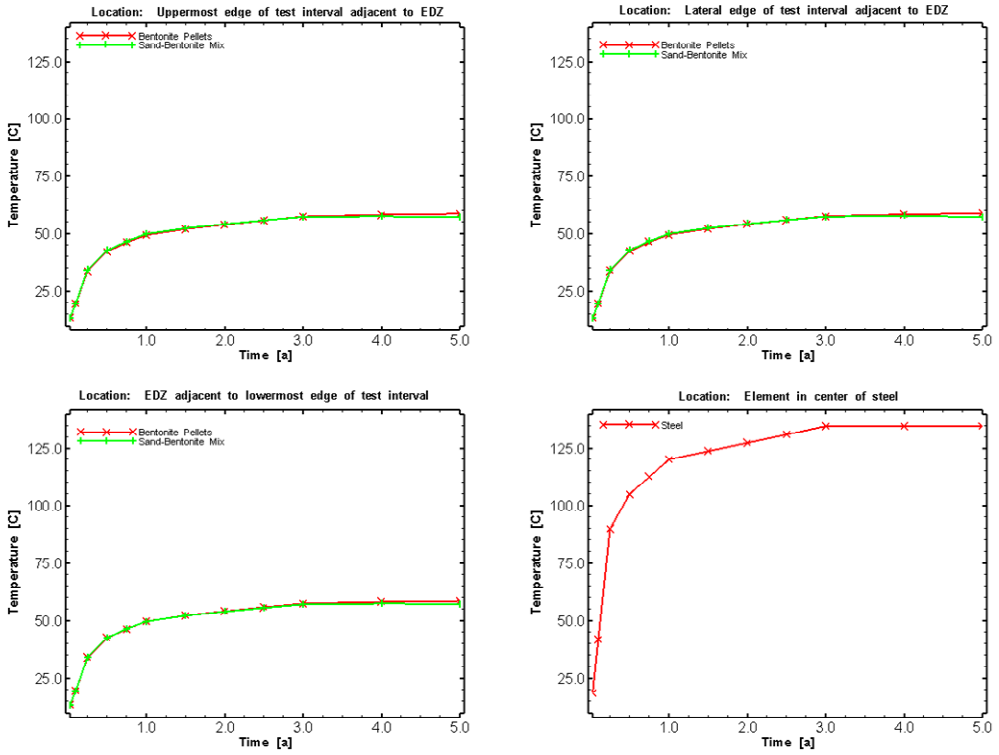

Figure 2.42 Case S1R6: Temperature histories at the different observation points, in addition to the prescribed temperature in the heater (lower right).

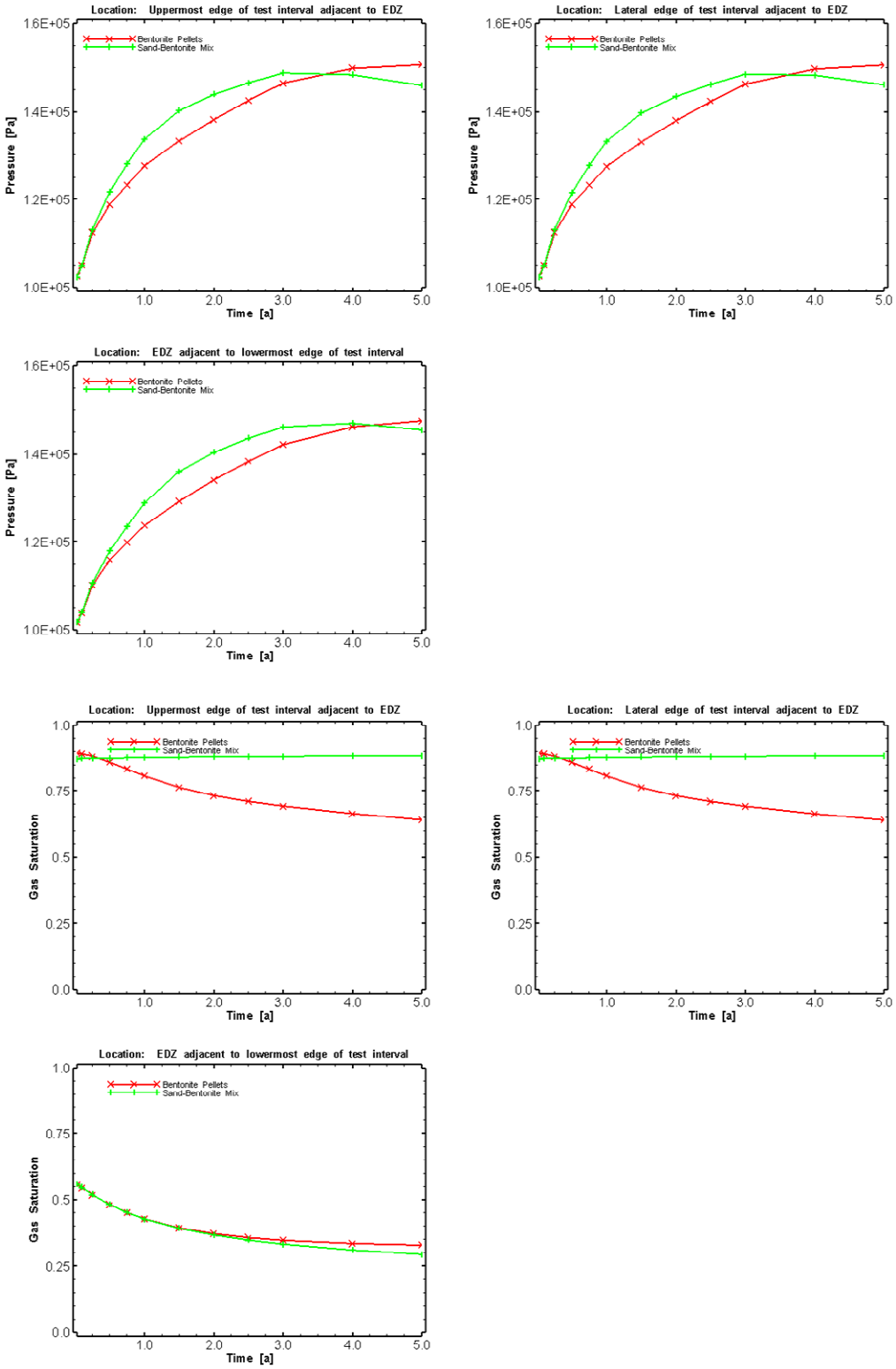

Figure 2.43 Case S1R6: Time histories of gas pressures (top) and saturation (bottom) at the different observation points.

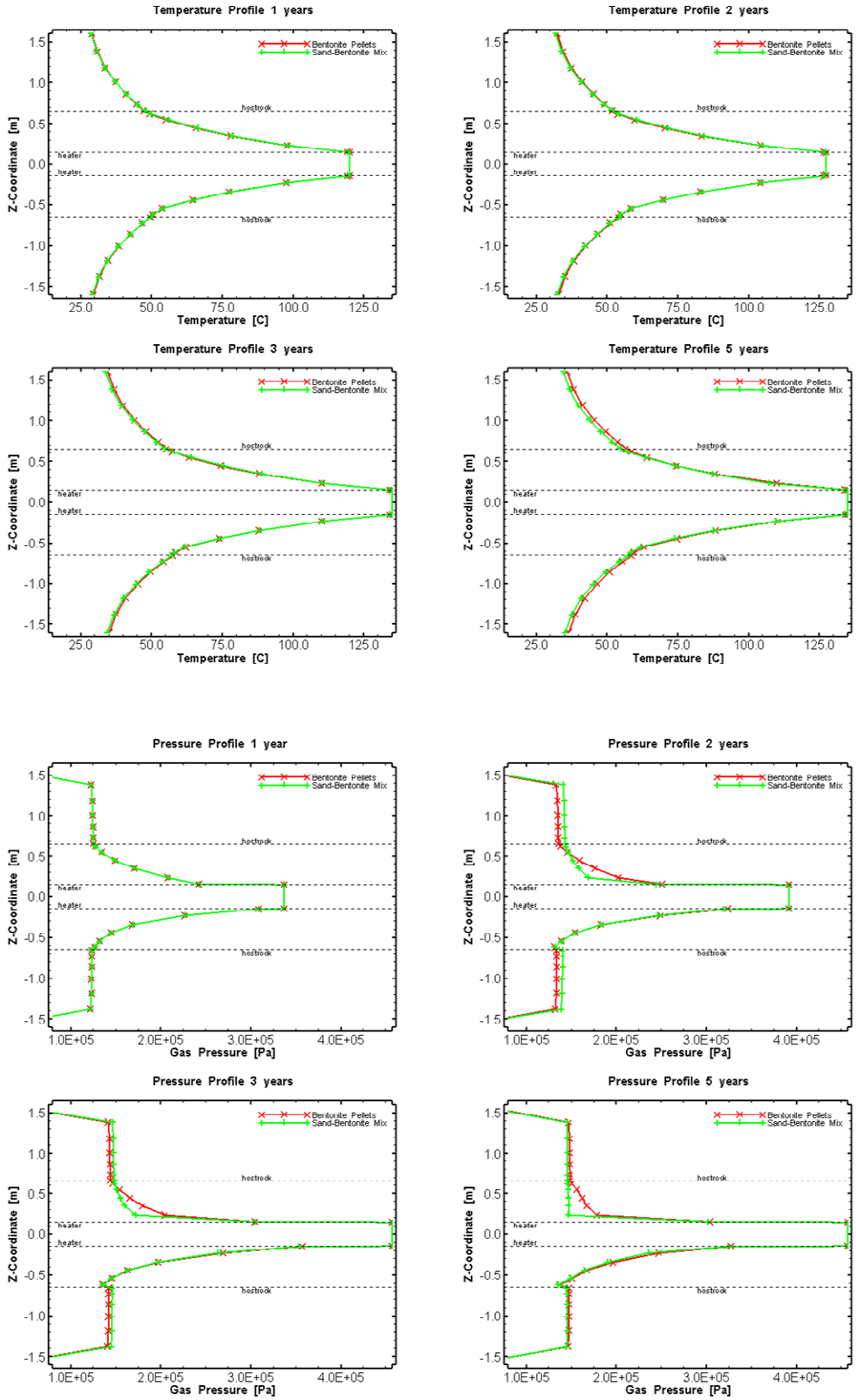

Figure 2.44 Case S1R6: Simulated vertical profiles of temperatures (top) and pressures (bottom) at different times.

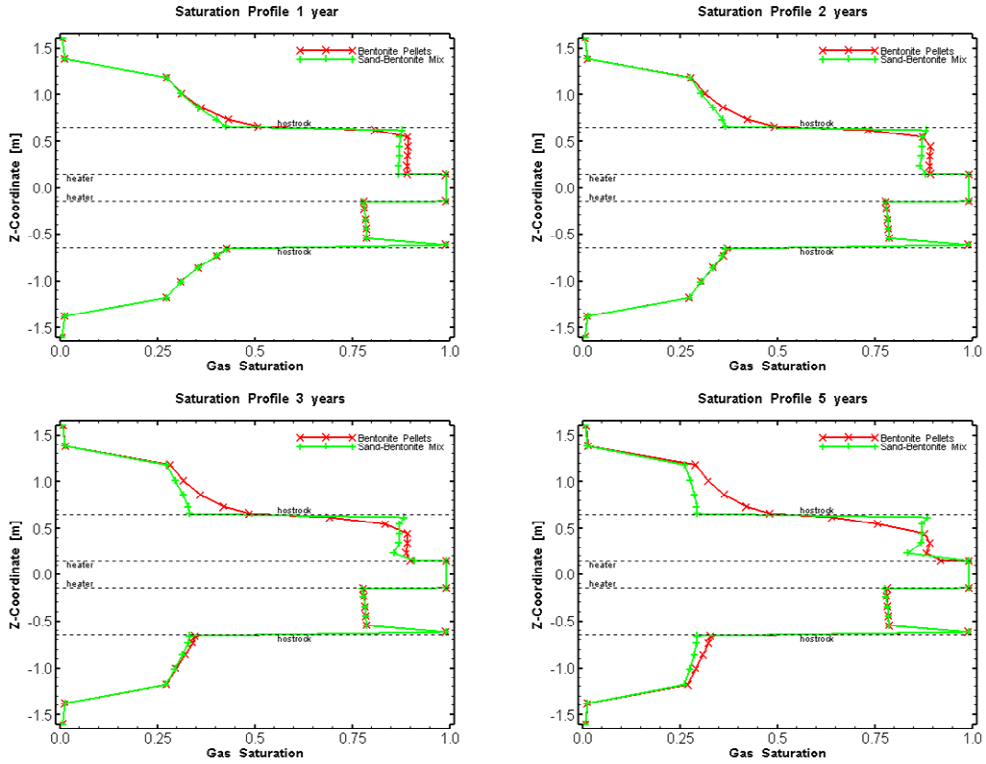

Figure 2.45 Case S1R6: Simulated vertical profiles of gas saturations at different times

2.3.3.7 S1R7: Corey krg-curve

Case S1R7 considers the Corey gas relative permeability curve for all materials (TOUGH2 input: IRP = 7). The time histories of temperatures, pressures, and saturation are shown in Figure 2.46 and 2.47. The vertical profiles of temperature, pressure, and saturation at different times are given in Figures 2.48 and 2.49.

The temperature histories for both the bentonite pellets and the sand/bentonite indicate temperature increases to near 60ºC after 5 years. The pressures at the observation locations indicate an increase to near 160 kPa, with some difference between the sand/bentonite and the pellets. This pressure increase is greater than that for the base case, due to the typically lower gas relative permeability of the Corey model compared to the van Genuchten model. The simulated gas saturations indicate significant different responses between the sand/bentonite and the pellets with the gas saturations at the upper and lateral edge of the bentonite pellets decreasing do about 65% after 5 years. In the sand/bentonite, the gas saturation essentially remains the same. At the bottom edge, which is in the EDZ next to the element representing the cable box, the gas saturations decrease to 33% for the pellet section and 30% for the sand/bentonite section.

The corresponding vertical temperature profiles are the same between sand/bentonite and pellets and are largely symmetric with only a slight difference around the cable box at the bottom of the bentonite blocks. The pressure profiles show distinct differences between the sand/bentonite and pellets in the upper part after two years. The pressure in the sand/bentonite actually decreased to

a near constant profile above the heater element. The simulated pressure increase in the heater element is caused by thermal expansion for which a low porosity of 0.1% was assumed and negligible permeability (k=1.E-50m^2). The corresponding saturation profiles indicate that the gas saturations in the pellets decrease above the heater element, whereas in the sand/bentonite the saturation remained near the initial emplacement saturation, but decreased noticeably in the adjacent EDZ. In the bentonite blocks beneath the heater element, the saturations are the same.

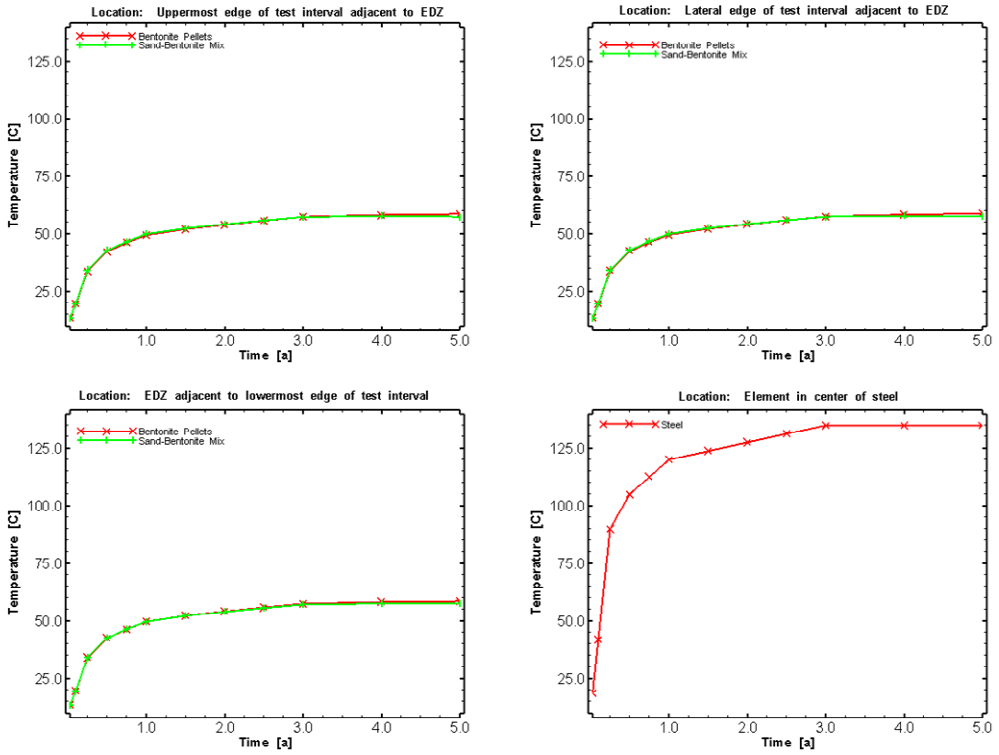

Figure 2.46 Case S1R7: Temperature histories at the different observation points, in addition to the prescribed temperature in the heater (lower right).

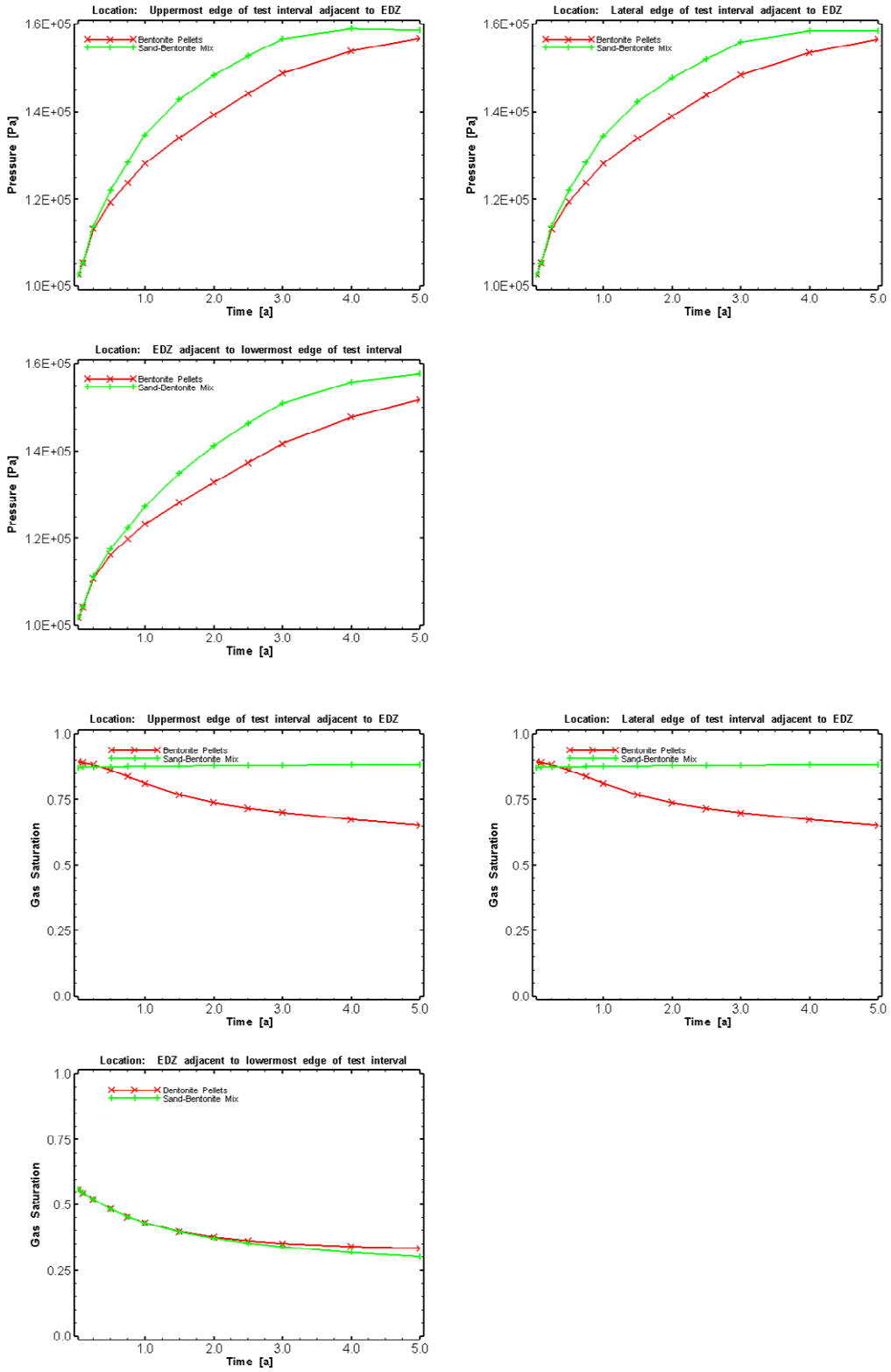

Figure 2.47 Case S1R7: Time histories of gas pressures (top) and saturation (bottom) at the different observation points.

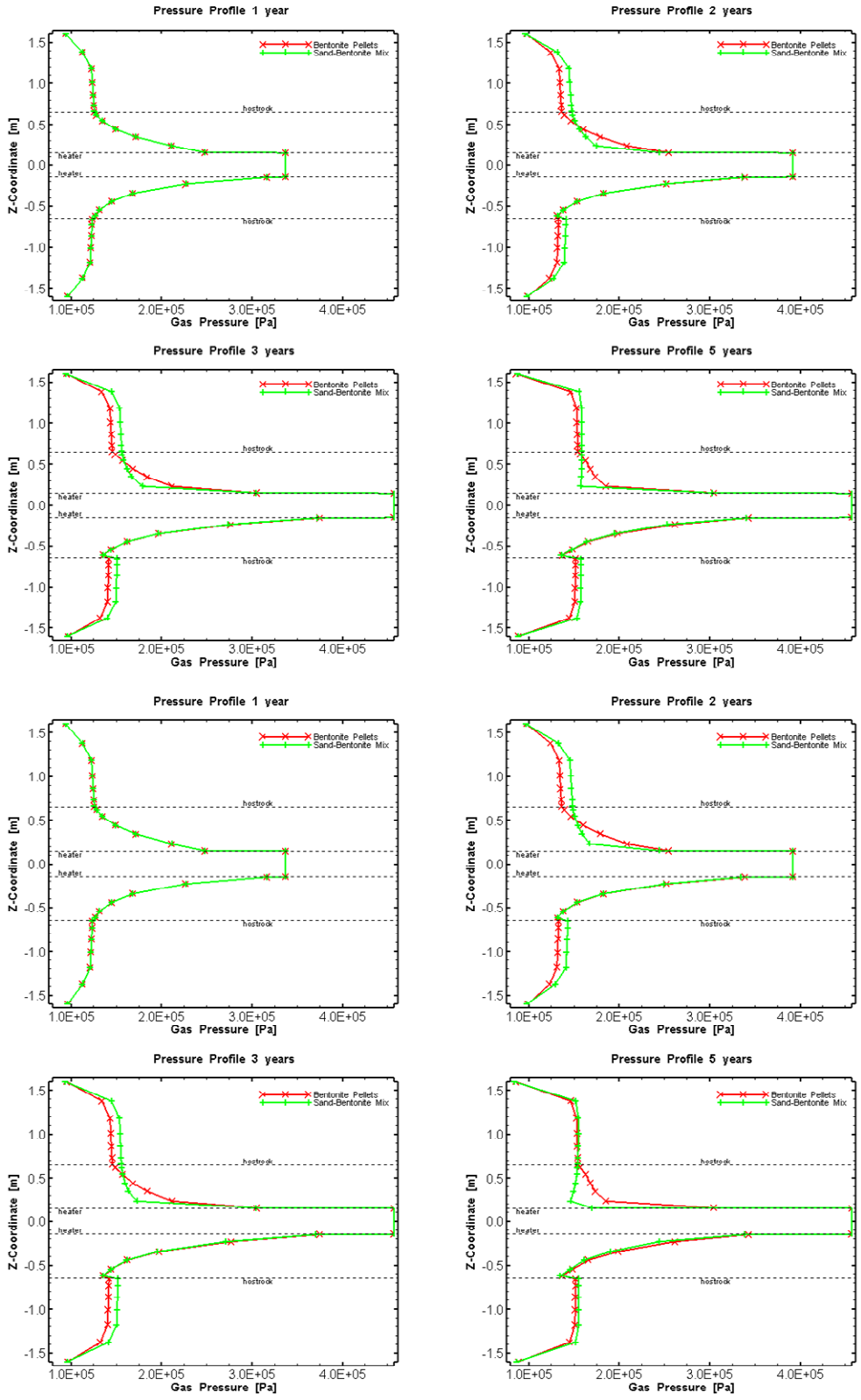

Figure 2.48 Case S1R7: Simulated vertical profiles of temperatures (top) and pressures (bottom) at different times.

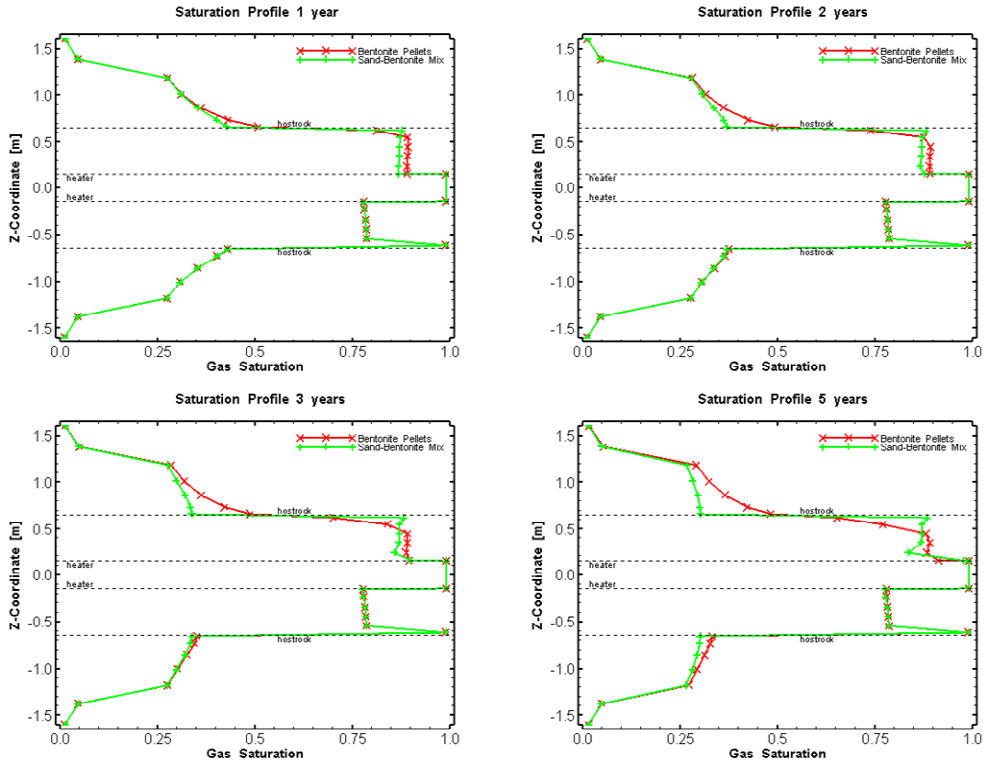

Figure 2.49 Case S1R7: Simulated vertical profiles of gas saturations at different times

2.3.3.8 S1R8: Increased Residual Water Saturation

Case S1R8 considers an increased residual water saturation of the sand/bentonite material (S_{lr}=0.3), which also shifts the capillary pressure curve higher at high gas saturations. The time histories of temperatures, pressures, and saturation are shown in Figure 2.50 and 2.51. The vertical profiles of temperature, pressure, and saturation at different times are given in Figures 2.52 and 2.53.

The temperature histories for the bentonite pellets indicate temperature increases to near 60ºC after 5 years, with slightly lower temperatures in the sand/bentonite. The pressures at the observation locations indicate an increase to near 150 kPa, with some difference between the sand/bentonite and the pellets. The simulated gas saturations indicate somewhat different responses between the sand/bentonite and the pellets with the gas saturations at the upper and lateral edge of the bentonite pellets decreasing do about 65% after 5 years. In the sand/bentonite, the gas saturation also decreased to about 67%. This is different compared to the base case which showed no noticeable change in saturation at the outer edge of the sand/bentonite. The decrease in gas saturation is due to the fact that the inflowing water from the EDZ can accumulate in the outer edge element of the sand/bentonite as the capillary pressure curve is shifted higher by the increased residual water saturation. However, the water cannot migrate farther until the residual water saturation of 30% is exceeded. With the relatively low permeability of the Opalinus Clay, there is not enough water flow to fill up the outer two layers of the sand/bentonite. At the bottom edge, which is in the EDZ next to the element

representing the cable box, the gas saturations decrease to 33% for the pellet section and 30% for the sand/bentonite section.

The corresponding vertical temperature profiles are the same between sand/bentonite and pellets and are largely symmetric with only a slight difference around the cable box at the bottom of the bentonite blocks. The pressure profiles show distinct differences between the sand/bentonite and pellets in the upper part after two years. The pressure in the sand/bentonite actually decreased to a near constant profile above the heater element. The simulated pressure increase in the heater element is caused by thermal expansion for which a low porosity of 0.1% was assumed and negligible permeability (k=1.E-50m^2). The corresponding saturation profiles indicate that the gas saturations in the pellets decrease above the heater element. In the sand/bentonite, only the gas saturation decreased only in the outer elements, whereas the main part of the sand/bentonite remained near the initial emplacement saturation.

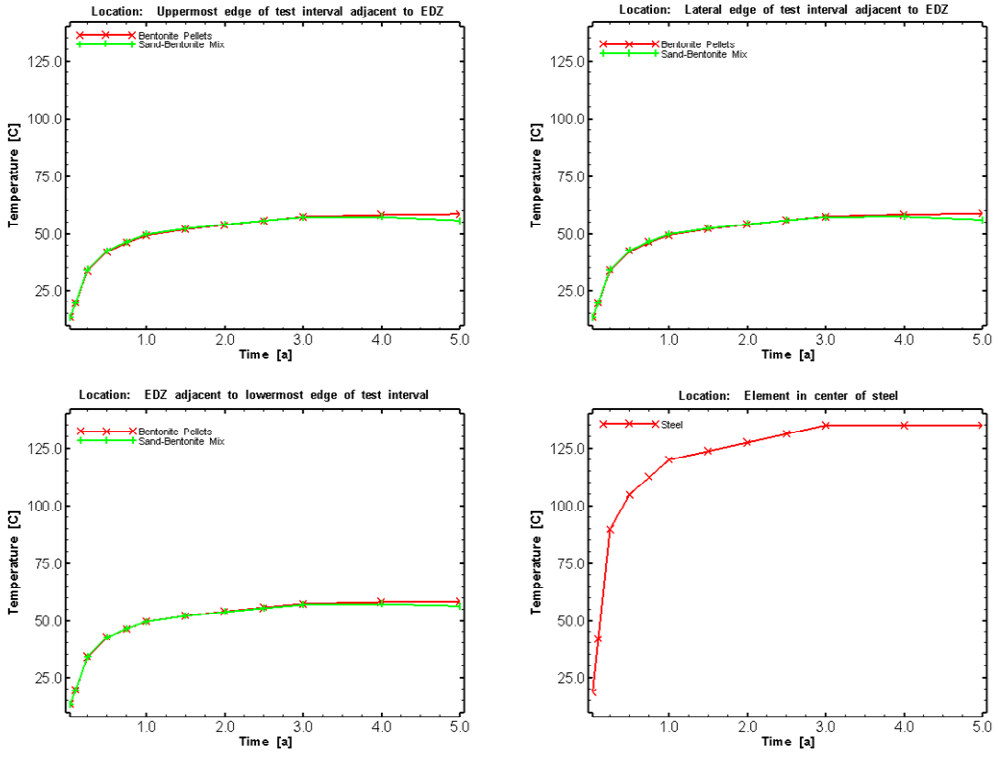

Figure 2.50 Case S1R8: Temperature histories at the different observation points, in addition to the prescribed temperature in the heater (lower right).

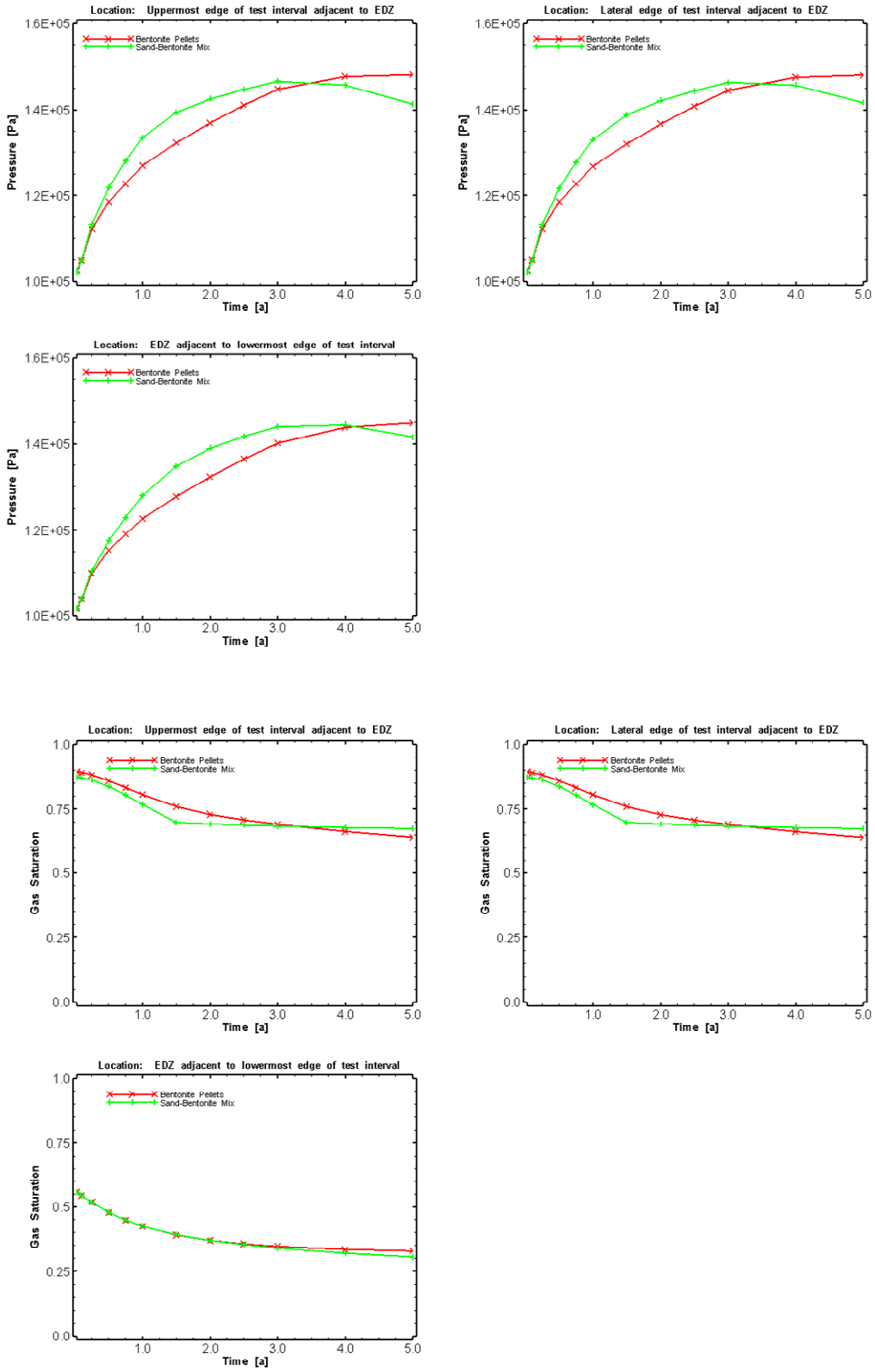

Figure 2.51 Case S1R8: Time histories of gas pressures (top) and saturation (bottom) at the different observation points.

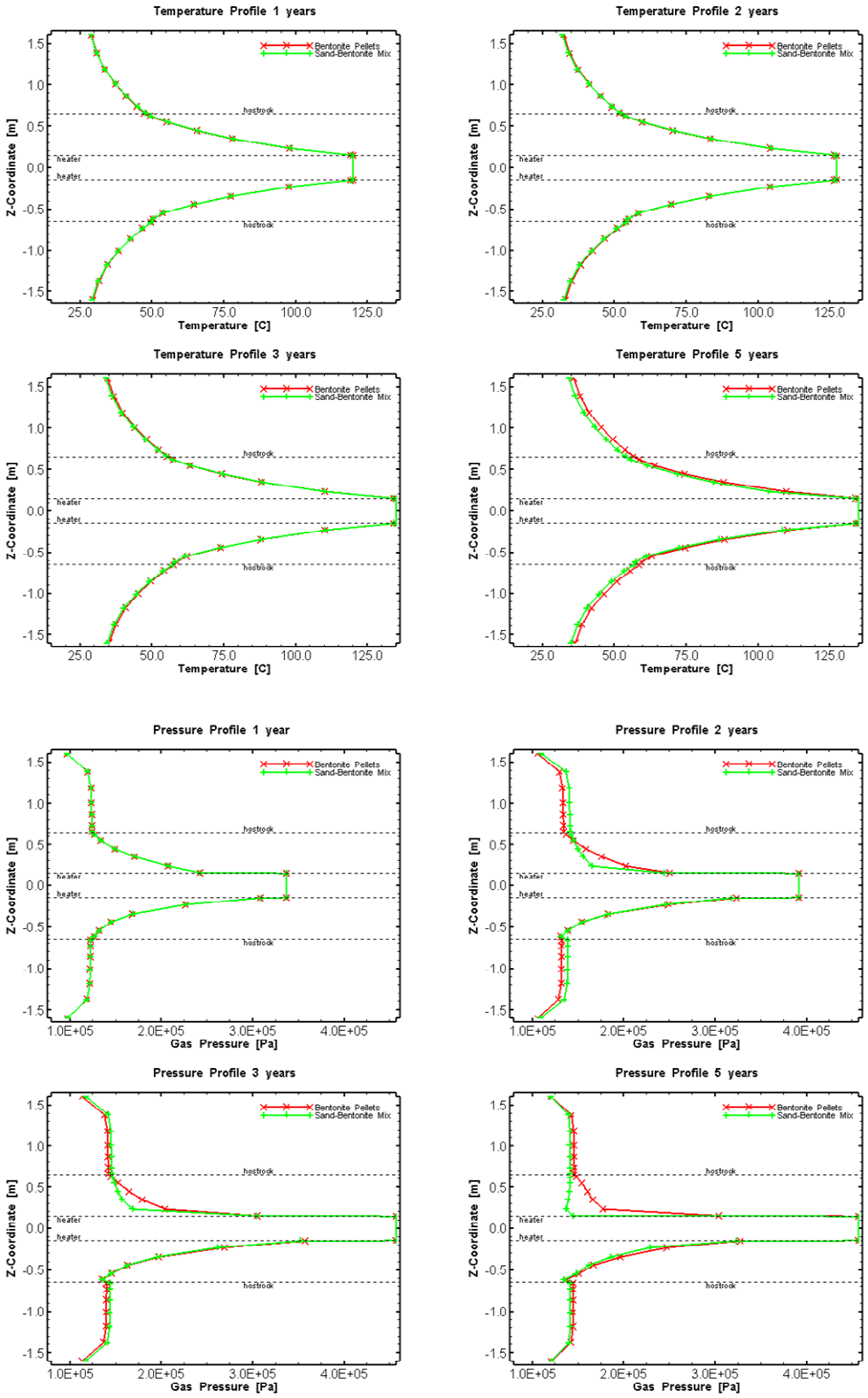

Figure 2.52 Case S1R8: Simulated vertical profiles of temperatures (top) and pressures (bottom) at different times.

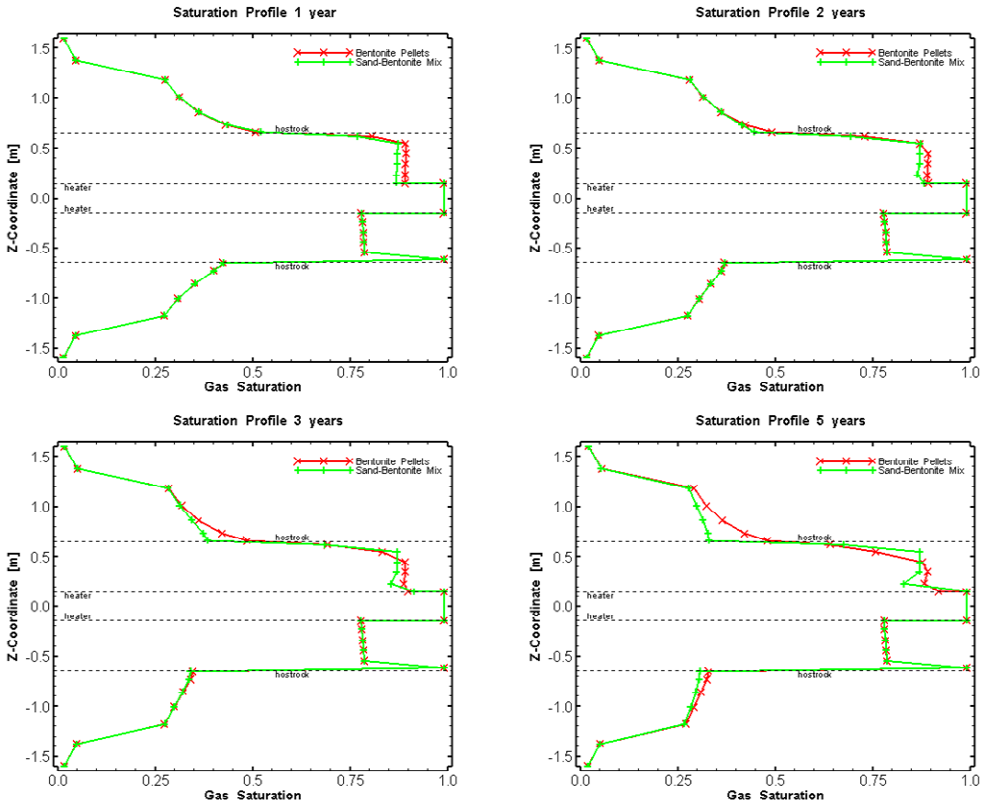

Figure 2.53 Case S1R8: Simulated vertical profiles of gas saturations at different times

2.3.3.9 S1R9: Const. Thermal Conduction for Bentonite

Case S1R9 considers a constant thermal conductivity of the bentonite corresponding to the maximum value at full saturation of 1.34 W/mK. All other cases assumed a saturation-dependent increasing thermal conductivity. The time histories of temperatures, pressures, and saturation are shown in Figure 2.54 and 2.55. The vertical profiles of temperature, pressure, and saturation at different times are given in Figures 2.56 and 2.57.

The temperature histories for both the bentonite pellets and the sand/bentonite indicate temperature increases to 75ºC after 5 years, which is 15ºC greater than in the base case. The pressures at the observation locations indicate an increase to near 170 kPa, with some difference between the sand/bentonite and the pellets. The simulated gas saturations indicate significant different responses between the sand/bentonite and the pellets with the gas saturations at the upper and lateral edge of the bentonite pellets decreasing do about 62% after 5 years. In the sand/bentonite, the gas saturation essentially remains the same. At the bottom edge, which is in the EDZ next to the element representing the cable box, the gas saturations decrease to 32% for the pellet section and27% for the sand/bentonite section.

The corresponding vertical temperature profiles are the same between sand/bentonite and pellets and are largely symmetric with only a slight difference around the cable box at the bottom of the bentonite blocks. The temperature gradienst across the bentonite is much lower than those in the base case, due to the higher thermal conductance. The pressure profiles show distinct

differences between the sand/bentonite and pellets in the upper part after two years. The pressure in the sand/bentonite actually decreased to a near constant profile above the heater element. The simulated pressure increase in the heater element is caused by thermal expansion for which a low porosity of 0.1% was assumed and negligible permeability (k=1.E-50m^2). The corresponding saturation profiles indicate that the gas saturations in the pellets decrease above the heater element, whereas in the sand/bentonite the saturation remained near the initial emplacement saturation, but decreased noticeably in the adjacent EDZ. In the bentonite blocks beneath the heater element, the saturations are the same.

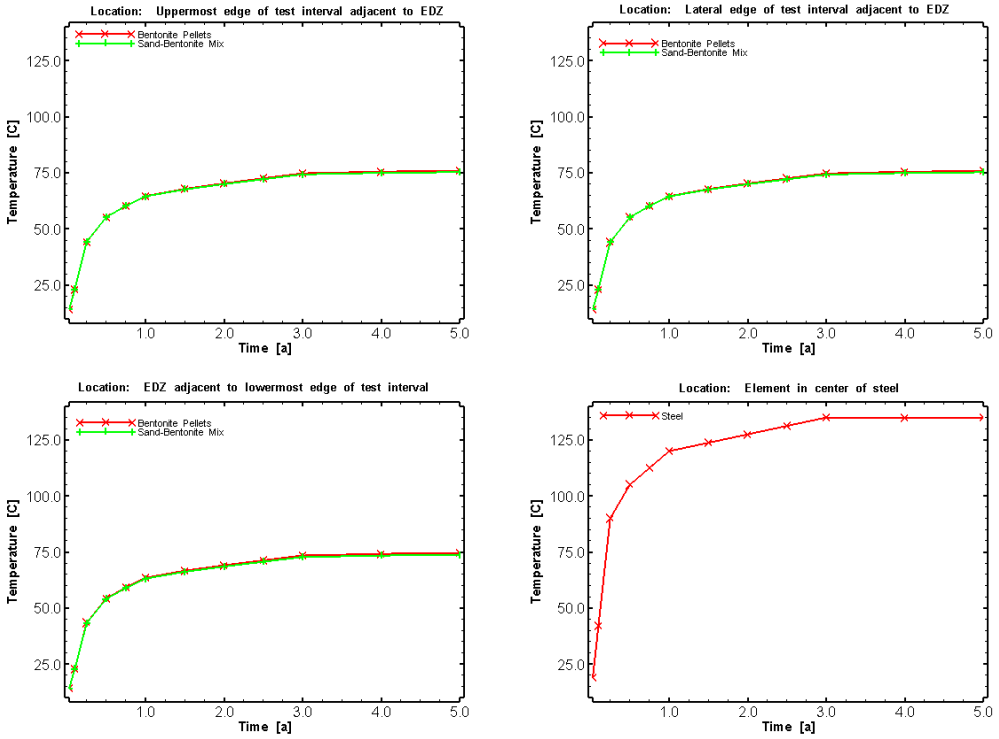

Figure 2.54 Case S1R9: Temperature histories at the different observation points, in addition to the prescribed temperature in the heater (lower right).

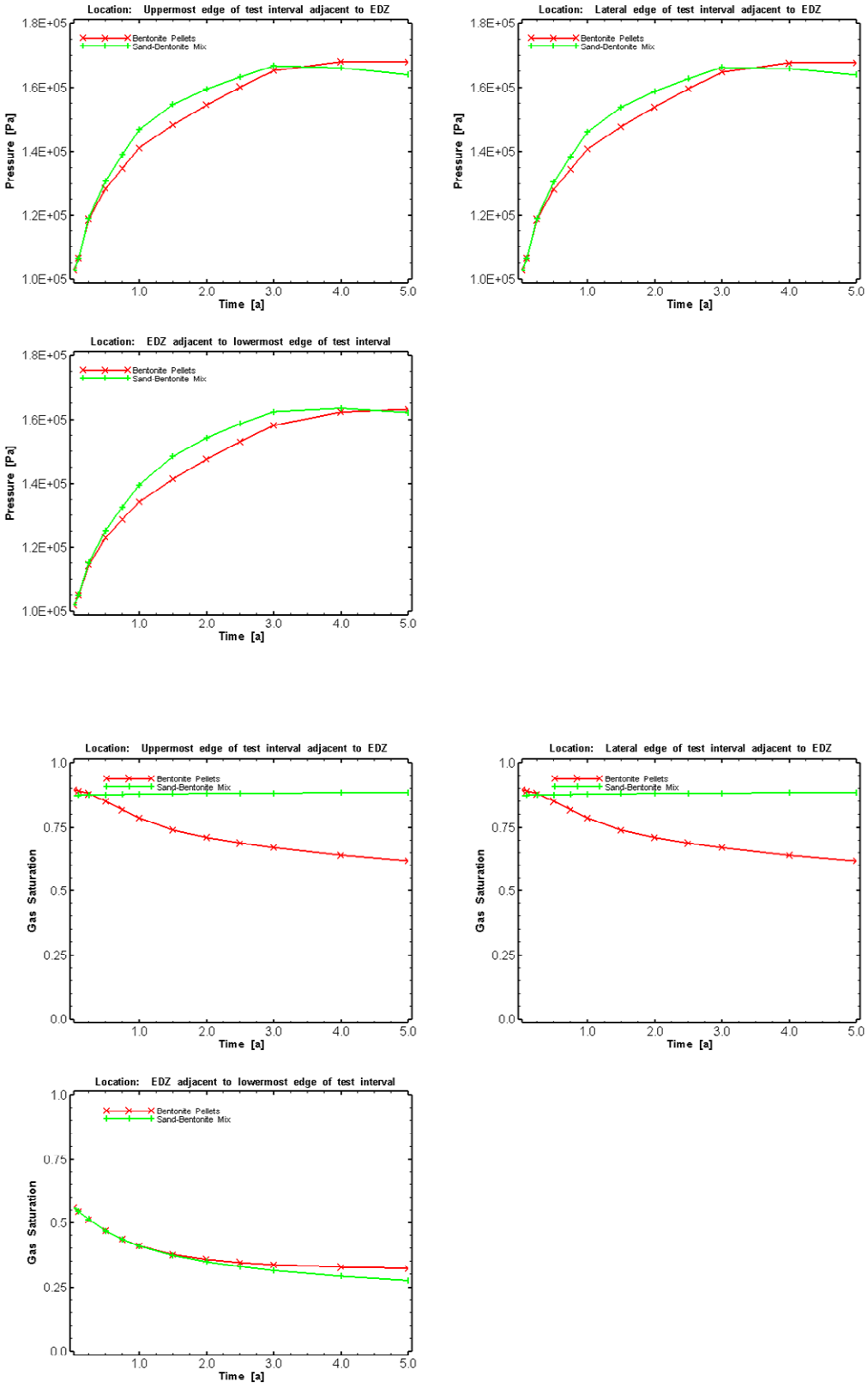

Figure 2.55 Case S1R9: Time histories of gas pressures (top) and gas saturation (bottom) at the different observation points.

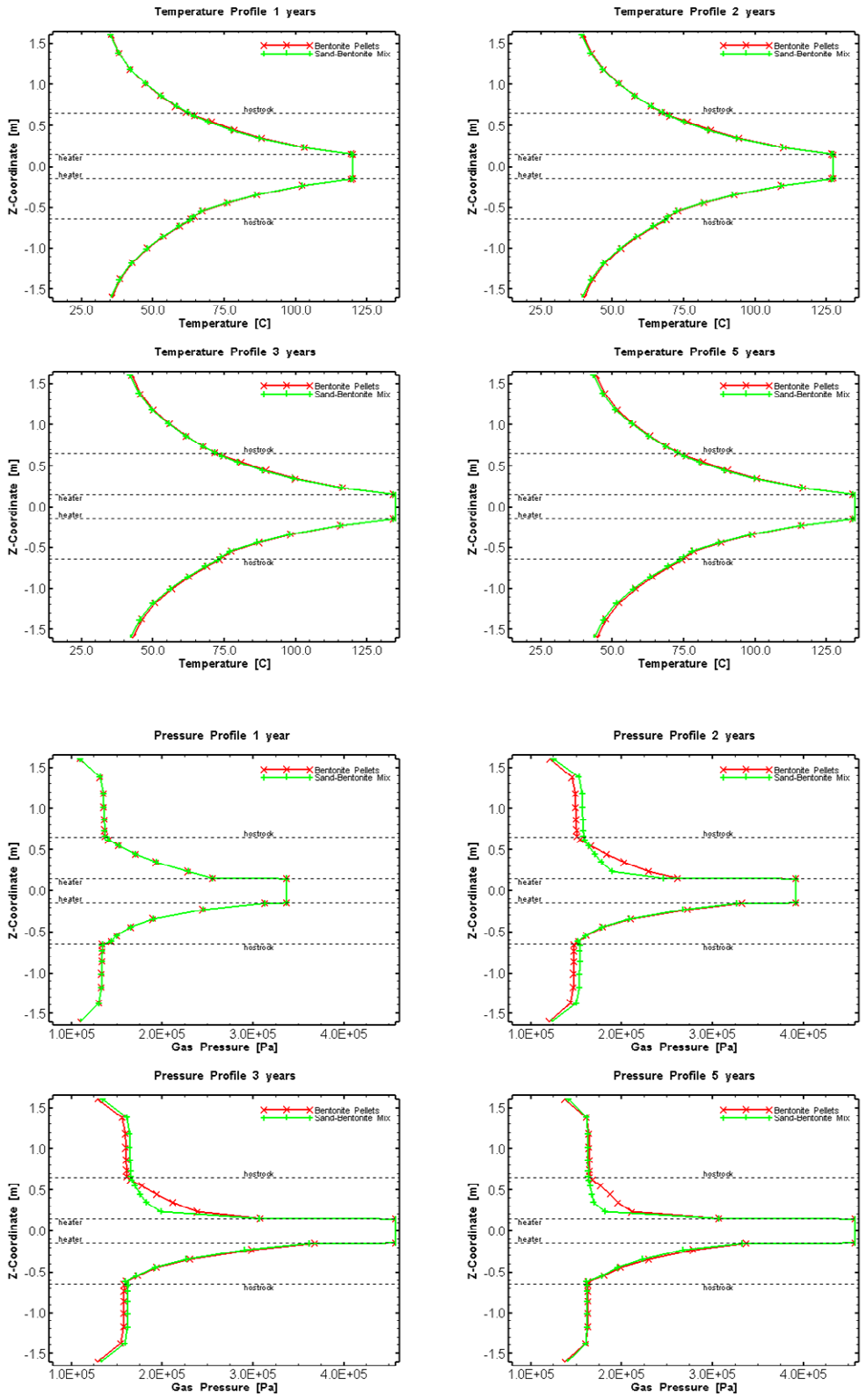

Figure 2.56 Case S1R9: Simulated vertical profiles of temperatures (top) and pressures (bottom) at different times.

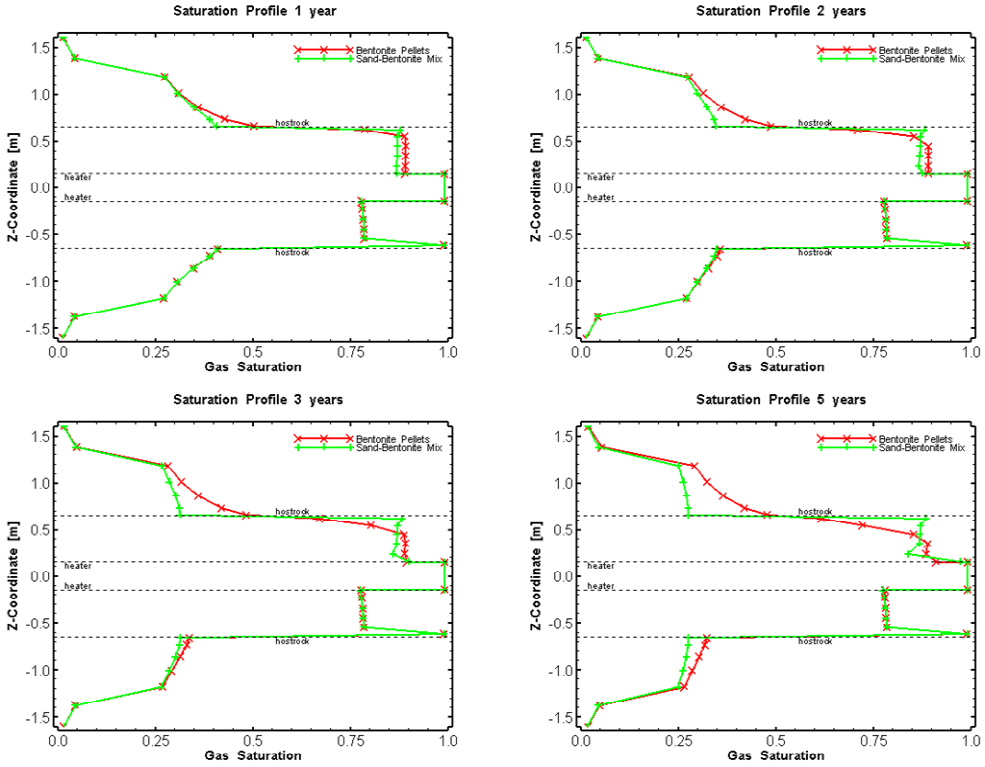

Figure 2.57 Case S1R9: Simulated vertical profiles of gas saturations at different times

2.4 Summary and Discussions

The results of the different simulations can be summarized as follows:

1. The resaturation of the sand/bentonite behaves differently from that in the bentonite pellets. Because of the lower capillary strength of the sand/bentonite material (vG-P_0=2.5E+5Pa), the liquid pressure gradient is relatively low for water flow into the sand/bentonite. In addition, the EDZ is at a relatively high gas saturation resulting in a relatively high capillary pressure and low liquid pressure. In comparison, the bentonite pellets have a much greater capillary strength parameter (vG-P_0=1.8E+7Pa) resulting in a steeper gradient for water flow into the bentonite, despite the lower permeability of the pellets compared to the sand/bentonite. Even the increased permeability of the Opalinus Clay did not provide sufficient water flow into the sand/bentonite to yield a noticeable change in saturation.
2. The temperature evolution shows relatively small differences between the sand/bentonite and the pellet sections, which is largely controlled by the thermal conductivity of the materials. A noticeable effect is indicated for different interpolation between wet and dry thermal conductivities of the bentonite materials, and to a lesser extend for the anisotropy in thermal conductivity of the Opalinus Clay.
3. The pressure increase in the bentonite largely depends on the thermal expansion of the material and pore water, which is controlled by the temperature development. The hydraulic properties of the bentonite and surrounding Opalinus clay do affect the pressure response owing to hydraulic dissipation of the pressure buildup.

4. The heating strategy 2 (increasing the temperature over 1 year to 135 degrees) produced somewhat steeper pressure increase followed by earlier dissipation of pressures in the sand/bentonite section than in the bentonite pellets.

The temperature distribution is mostly controlled by the thermal conductivity of the materials, whereby only for the bentonite a saturation-dependent thermal conductivity was assumed. At the contact between the bentonite and surrounding EDZ, the simulated temperatures varied over a relatively narrow range of between 55 and 60 ºC for most cases. Only for the Case S1R9 assuming constant thermal conductivity for the bentonite corresponding to the maximum value at full saturation did the temperatures significantly increase to 75 ºC. The relatively small temperature range is largely due to the relatively small changes in saturation, particularly near the heater, maintaining a steep temperature gradient across the relatively dry bentonite buffer.

The total heat flow from the heater element into the surrounding bentonite is shown in Figure 2.58 for the heating strategy 1 for the Base Case S1R0 and Case S1R9. The two curves show the total heat flux for the two bentonite sections, which differ slightly because of the different thermal conductivity of the sand/bentonite and pellets associated with the different saturations. For the case with the higher thermal conductivity of the bentonite, the heat flow rate significantly increased. Note that because of the symmetry of the heater-test configuration in the model, the actual heat generation rates required to reach the prescribed temperatures have to be doubled.

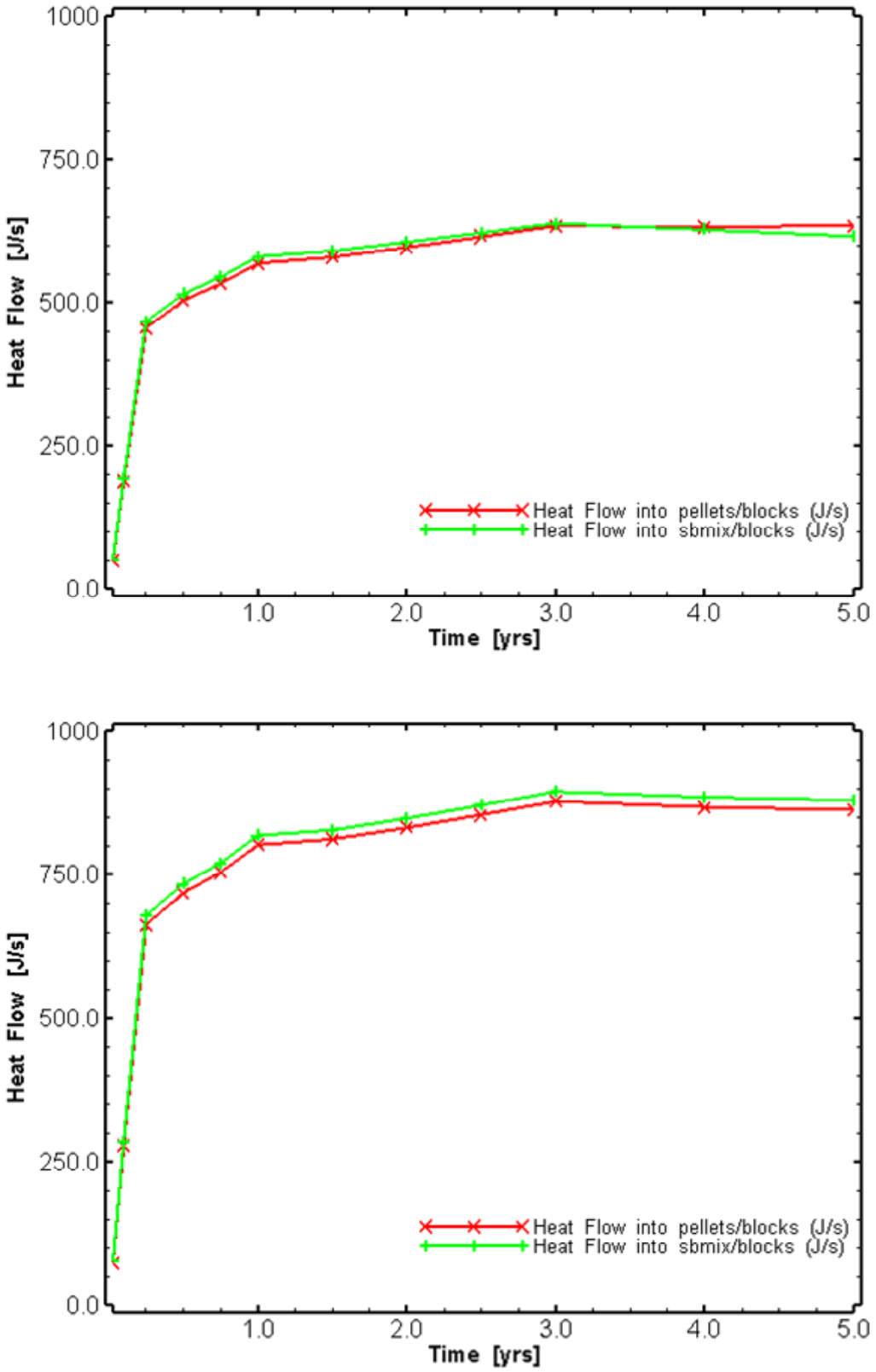

Figure 2.58 Computed total heat flow from heater element into the surrounding bentonite for BaseCase S1R0 (top) and Case S1R9 (bottom); based on half-geometry of the heater test configuration.

The water flow into the bentonite will resaturate the bentonite and causes swelling and potential swelling pressure buildup. The computed water flow rates from the surrounding host rock into the bentonite sections (i.e., sand/bentonite, pellets) are shown in Figure 2.59 for the Base Case S1R0 and the case with higher permeability of the Opalinus clay and the EDZ (Case S1R1). The results indicate water flow into the pellets. However, the actual water flow across the interface between the sand/bentonite and the EDZ is reversed. As mentioned above, the initially relatively dry EDZ creates a significant capillary pressure for water flow from the surrounding Opalinus clay. Moreover, there is also a small gradient between the sand/bentonite and the EDZ resulting in the some water flow from the sand/bentonite into the EDZ (Fig. 2.59). This relatively small rate decreases over time as the water saturation increases in the EDZ, thereby reducing the capillary pressure gradient.

The simulation Case S1R8 (S_{lr} = 0.3 for both the relative permeability and capillary pressure curve for the sand/bentonite) results in initially higher capillary pressures in the sand/ bentonite creating a capillary pressure gradient toward the sand/bentonite and corresponding water flow into the sand/bentonite (Fig. 2.60). However, the resaturation front does not extend far into the sand/bentonite (1. element), because the residual water saturation of 30% restrict water flow until the residual water saturation is exceeded. As the water saturation increases, the capillary pressure decreases and the water flow rate into the sand/bentonite rapidly decreases.

A potential concern is the pressure buildup in the Opalinus Clay at some distance from the tunnel outside of the cone of depression around the tunnel due thermal expansion of the pore water. For the base case (S1R0), the spatial distribution of both the pressure and temperature along a vertical cross section parallel to the tunnel axis is plotted in Figure 2.61. The results indicate pressures increasing from about 1.65 to a maximum of 1.80 MPa about 12 m above the tunnel. Below the tunnel, the pressures increase slightly less, but indicate a steeper gradient due to the initial hydrostatic pressures and the imposed cone of depression. The overall pressure increase is somewhat enhanced by the no-flow boundary conditions at the outer model boundaries, which indicate a maxuimum pressure increase of about 40 kPa at the top and bottom boundaries.

In general, the simulation results indicate relatively small variation in the temperature distribution in the different bentonite sections and surrounding host rock. This is largely due to the relatively small change in saturation over the entire thickness of the buffer materials (pellets and sand/bentonite). A major uncertainty concerns the EDZ in terms of the two-phase flow properties which affects the gradient for water flow to the bentonite sections, particularly the sand/bentonite. Lower capillary pressures in the EDZ (i.e., lower capillary strength parameter P_0) together with preferential flow paths in the EDZ could significantly change the saturation behaviour of the sand/bentonite. This could result in higher thermal conductivities of the sand/bentonite and affect the temperature gradient across the bentonite, yielding higher temperatures at the contact between the sand/bentonite and EDZ.

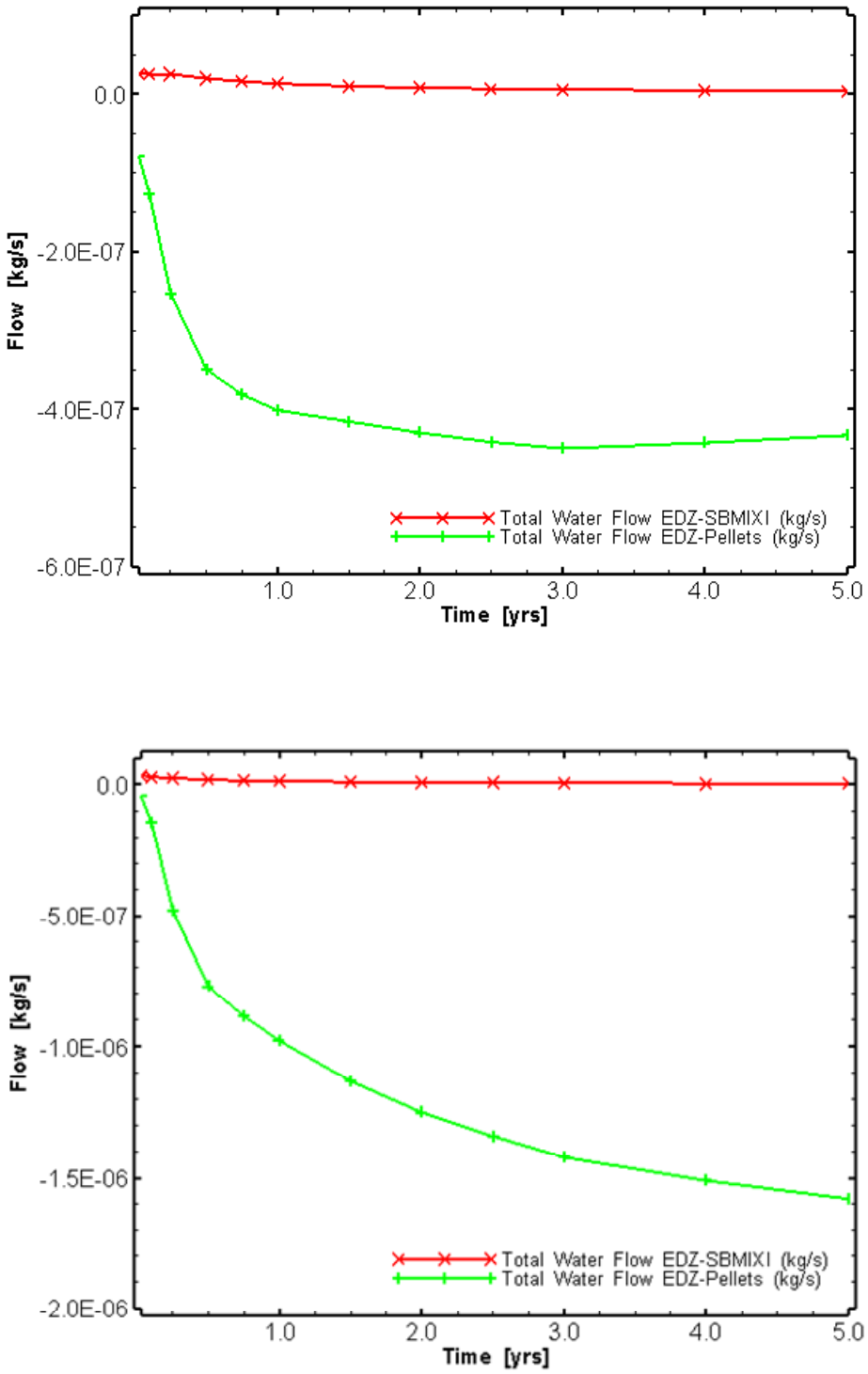

Figure 2.59 Computed total water flow from the EDZ into the different bentonite sections, based on the half-geometry of the heater test configuration: top for Base Case S1R0, and bottom for Case S1R1 (negative flow rates indicate water flow from the EDZ into the bentonite; positive flow rates indicate water flow from the bentonite to the EDZ).

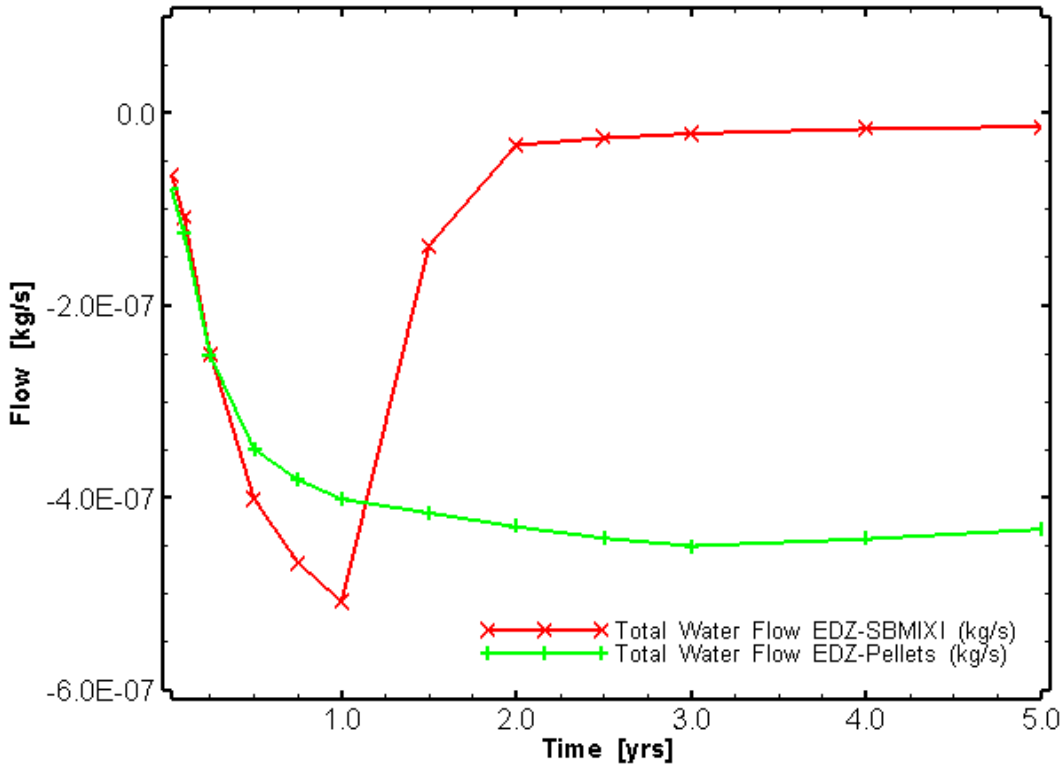

Figure 2.60 Case S1R8: Computed total water flow from the EDZ into the different bentonite sections, based on the half-geometry of the heater test configuration (negative flow rates indicate water flow from the EDZ into the bentonite; positive flow rates indicate water flow from the bentonite to the EDZ).

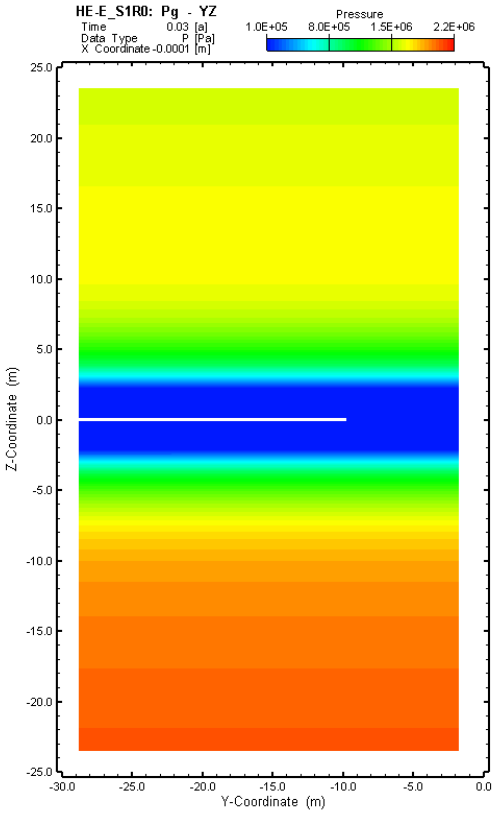
HE-E_S1R0: Pg - YZ
Time 0.03 [a]
Data Type P [Pa]
X Coordinate -0.0001 [m]
Pressure
1.0E+05 8.0E+05 1.5E+06 2.2E+06
Z-Coordinate (m)
Y-Coordinate (m)

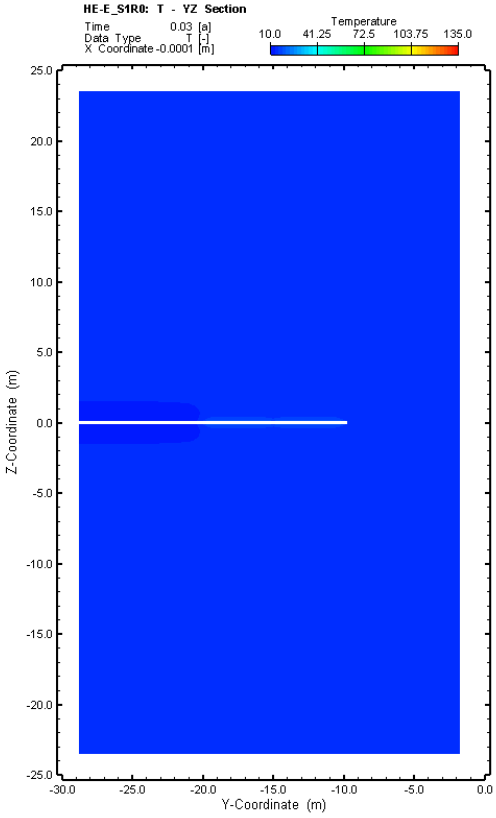
HE-E_S1R0: T - YZ Section
Time 0.03 [a]
Data Type T [-]
X Coordinate -0.0001 [m]
Temperature
10.0 41.25 72.5 103.75 135.0
Z-Coordinate (m)
Y-Coordinate (m)

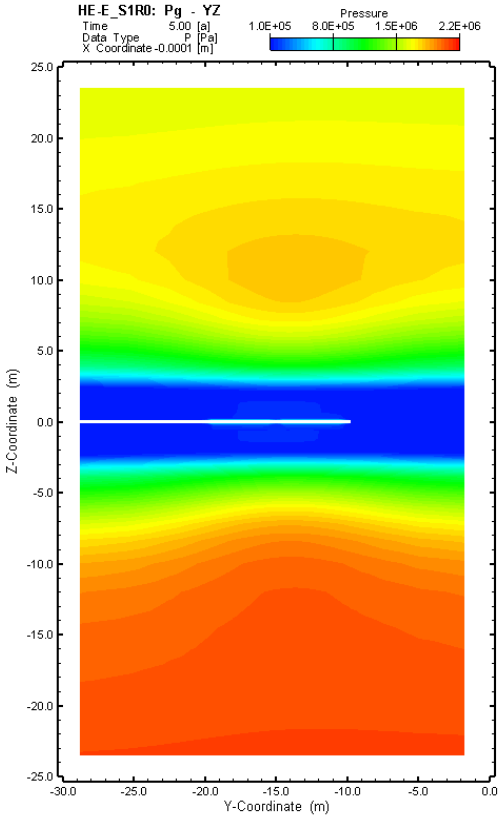
HE-E_S1R0: Pg - YZ
Time 5.00 [a]
Data Type P [Pa]
X Coordinate -0.0001 [m]
Pressure
1.0E+05 8.0E+05 1.5E+06 2.2E+06
Z-Coordinate (m)
Y-Coordinate (m)

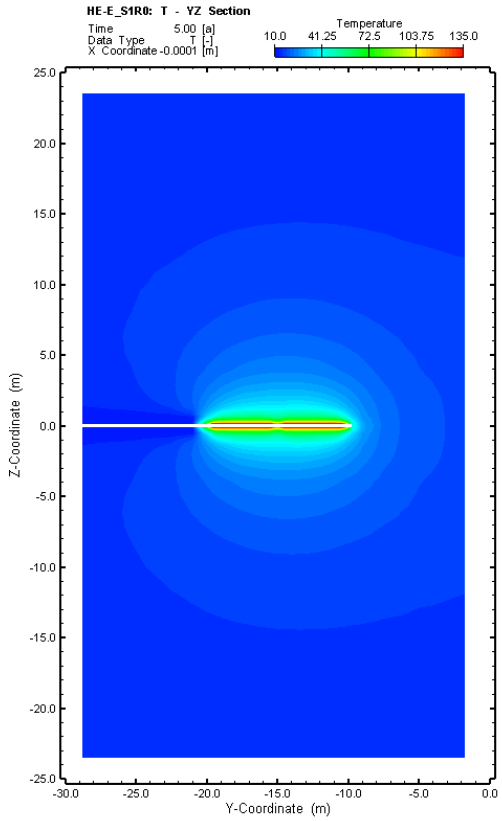

Figure 2.61 Case S1R0: Computed distributions of pressures and temperatures along the vertical cross section through the tunnel at the start (top) and after 5 years (bottom).

3 Scoping calculations using CODE_BRIGHT (CIMNE)

3.1 Introduction

The HE-E experiment is an in situ heating experiment in the Mont Terri underground rock laboratory (URL). It consists in the installation of two 4m long heaters with a diameter of 30cm in the microtunnel (past location of the Ventilation Experiment – VE) surrounded by a bentonite buffer. The microtunnel has a diameter of 1.3m. Heating was launched in July 2011. The temperature at heater-bentonite interface will increase linearly during one year to reach 135º in July 2012. After that, temperature will be kept constant during at least two years. The instrumentation system from the VE will be used and new sensors will be installed. Instrumentation from the VE was installed in the rock mass in the close field of the microtunnel and consists of:

- 20 hygrometers (measurement of relative humidity) coupled with temperature sensors,
- 24 pore water pressure sensors coupled with temperature measurement,
- 8 radial extensometers.

The bentonite buffer will be instrumented with hygrometers, temperature sensors, extensometers and absolute pressure cells. The rock mass instrumentation will be complemented with ten pore water pressure sensors (coupled with temperature measurements) in the far field. The aim of this work is to optimize the position of the new sensors and to provide a first approach of the system behaviour.

This work consists in 1) a review of the Thermo-Hydro-Mechanical (THM) formulation; 2) a description of the conceptual model and associated parameters developed to predict the temperature, saturation state and pore water pressure in the test area and 3) the modelling results. Some key issues that should be highlighted are:

- A section is dedicated to the history of the test site and how it can be tackled with in future modelling work. The history influences the initial conditions of the HE-E experiment.
- An effort is done to explain the mechanisms/processes behind the evolution of temperature, degree of saturation and pore water pressure.
- Parameters having an influence on the development of pore water pressure in the saturated zone were identified and their impact evaluated.

3.2 THM formulation

The formulation used is based on a general multi-phases/multi-species approach (Olivella et al., 1994). Three phases are considered, solid (s), liquid (l) and gas (g). Each phase is composed by one or two species:

- The solid phase contains the species “solid grain”
- The liquid phase contain the species “water” (in liquid form)
- The gas phase contains the species “air” and “water” (in vapour form)

The resolution of the coupled THM problem requires simultaneous solution of the mass balance of solid (mainly related to porosity), the mass balance of water (mainly related to pore water pressure and degree of saturation), the internal energy balance (mainly related to temperature)

and the momentum equilibrium (mainly related to the displacement field) (equations (1), (2), (3) and (4) respectively).

$$\frac{\partial}{\partial t}\left(\theta_s\left(1-\phi\right)\right)+\nabla\cdot\left(\mathbf{j}_s\right)=f^s=0 \qquad (1)$$

$$\frac{\partial}{\partial t}\left(\theta_l^w S_l\phi+\theta_g^w S_g\phi\right)+\nabla\cdot\left(\mathbf{j}_l^w+\mathbf{j}_g^w\right)=f^w \qquad (2)$$

$$\frac{\partial}{\partial t}\left(E_s\rho_s\left(1-\phi\right)+E_l\rho_l S_l\phi+E_g\rho_g S_g\phi\right)+\nabla\cdot\left(\mathbf{i}_c+\mathbf{j}_{Es}+\mathbf{j}_{El}+\mathbf{j}_{Eg}\right)=f^Q \qquad (3)$$

$$\nabla\cdot\boldsymbol{\sigma}+\mathbf{b}=\mathbf{0} \qquad (4)$$

Associated with this formulation there is a set of necessary constitutive and equilibrium laws. The constitutive equations establish the link between the independent variables (or unknowns) and the dependent ones. The governing equations for THM problems are written in terms of the unknowns when the constitutive equations are substituted in the balance equations. Herein, a finite element code CODE_BRIGHT (Olivella, 1995) is used to resolve these equations. The main equations implemented in CODE_BRIGHT and their corresponding dependent variables are shown in Table 3.1 and described in the next sections. The mass balance of solid and water are worked out into a more comprehensive form for the understanding of the present problem.

Table 3.1 Constitutive equations and equilibrium restrictions

EQUATION	VARIABLE NAME	VARIABLE
Constitutive equations		
Darcy's law	liquid and gas advective flux	$\mathbf{q_l}$, $\mathbf{q_g}$
Fick's law	vapour and air non-advective fluxes	$\mathbf{i_g^w}$, $\mathbf{i_l^a}$
Fourier's law	conductive heat flux	$\mathbf{i_c}$
Retention curve	Liquid phase degree of saturation	S_l, S_g
Mechanical constitutive model	Stress tensor	$\boldsymbol{\sigma}$
Phase density	liquid density	ρ_l
Gases law	gas density	ρ_g
Equilibrium restrictions		
Henry's law	Air dissolved mass fraction	ω_l^a
Psychrometric law	Vapour mass fraction	ω_g^w

3.2.1 Mass balance of solid

In the mass balance of solid, θ_s is the volumetric mass of solid (equivalent to the solid density: ρ_s), φ is the porosity. The first term is the variation of mass of solid in the medium in respect with the time and the second term is the divergence of the flux of solid. Using the concept of material derivative (derivative with respect to the solid):

$$\frac{D_s(\bullet)}{Dt} = \frac{\partial}{\partial t} + \frac{d\mathbf{u}}{dt} \cdot \nabla(\bullet) \tag{5}$$

We may find an expression for changes of porosity:

$$\frac{D_s\varphi}{Dt} = \frac{1}{\rho_s}\left[(1-\varphi)\frac{D_s\rho_s}{Dt}\right] + (1-\varphi)\nabla \cdot \frac{d\mathbf{u}}{dt} \tag{6}$$

This equation gives an expression for the variation of porosity that are induced by changes of solid density (expansion or compression of the solid grain) and by deformation of the skeleton (induced by changes of effective stress, suction and temperature). Changes in solid density are related to temperature changes by:

$$\rho_s = \rho_{s0} \exp\left[3b_s\left(T - T_{ref}\right)\right] \tag{7}$$

where b_s is the linear thermal expansion coefficient for the solid grain.

3.2.2 Water mass balance

In the water mass balance, we distinguish the changes of water mass in a certain volume due to property changes in respect with the time in the first term and the divergence of water fluxes in the second term. The third term is a sink/source term which is equal to 0 in the present problem. θ_l^w and θ_g^w are the volumetric masses of water in the liquid and the gas phase, respectively. $\theta^w{}_l = \omega^w{}_l.\rho_l$, where $\omega^w{}_l = m_w/m_l$ is the mass fraction of water in the liquid. S_l and S_g are the degrees of saturation of liquid and gas phases, respectively. j_l^w and j_g^w are the fluxes of water in the liquid and gas phases, respectively.

The advective flow of water in the liquid phase $j^w{}_l$ [$kg/m^2/s$] is:

$$\mathbf{j}_l^w = \theta_l^w \mathbf{q}_l \tag{8}$$

The first factor, $\theta^w{}_l = \omega^w{}_l.\rho_l$, where $\omega^w{}_l = m_w/m_l$ is the mass fraction of water in the liquid and ρ_l, the liquid density [kg/m^3] is dependent on water pressure and temperature:

$$\rho_l = \rho_{l0} \exp\left(\beta_l\left(p_l - p_{l0}\right) + \alpha T\right) \tag{9}$$

where β_l is the water compressibility and α is the volumetric thermal expansion coefficient of water.

The second factor, q_l [m/s], is the Darcy velocity, i.e. the volumetric flow/section, which is proportional, to the water pressure gradient (∇p_l [Pa/m]):

$$\mathbf{q}_l = -\frac{\mathbf{k}k_{rl}}{\mu_l}\nabla p_l \tag{10}$$

where $\mathbf{k}$ is the intrinsic permeability [m^2], μ_l is the dynamic viscosity [Pa.s] and k_{rl} is a coefficient depending on the degree of saturation.

The dependence of the permeability on the degree of saturation is introduced through:

$$k_{rl} = \sqrt{S_l}\left(1 - \left(1 - S_l^{1/\lambda'}\right)^{\lambda'}\right)^2 \tag{11}$$

known as Van Genuchten law, where λ' is a shape parameter.

The transport of water in the gas phase can be decomposed in:

$$\mathbf{j}_g^w = \left(\mathbf{i}_g^w\right)_{advection} + \left(\mathbf{i}_g^w\right)_{diffusion} + \left(\mathbf{i}_g^w\right)_{dispersion} \tag{12}$$

in which the first term represents the flux of water by motion of the gas phase and the second term the flux of water by diffusion of water vapour inside the gas phase (non-advective flow). Dispersion was neglected. Gas motion was found to be negligible. Vapour diffusion is expressed by Fick's law:

$$\left(\mathbf{i}_g^w\right)_{diffusion} = -\left(\phi \rho_g S_g D_g^w \mathbf{I}\right)\nabla \omega_g^w \tag{13}$$

where D^w_g [m^2/s] is the vapour diffusion coefficient and $\nabla \omega_g^w$ is the gradient of vapour concentration. Vapour diffusion was found to have a significant influence on the results. The molecular diffusion coefficient is given by:

$$D_g^w = D\left(\frac{\left(273.15+T\right)^n}{p_g}\right) \tag{14}$$

where D, n are material parameters, p_g [Pa] is the gas pressure and T [^oC] is the temperature.

The relationship between suction (p_g - p_l) and the liquid degree of saturation is idealised by the modified Van Genuchten retention curve:

$$S_e = \frac{S_l - S_{rl}}{S_{ls} - S_{rl}} = \left(1 + \left(\frac{p_g - p_l}{P}\right)^{\frac{1}{1-\lambda}}\right)^{-\lambda} \tag{15}$$

$$P = P_0 \frac{\sigma}{\sigma_0}$$

where λ is a shape parameter, S_{rl} is the residual saturation, S_{ls} is the maximum saturation. P is a material parameter.

Finally, Kelvin's law relates water content in gas to the suction:

$$\theta_g^w = \omega_g^w \rho_g = \left(\theta_g^w\right)_0 \exp\left[\frac{-\left(p_g - p_l\right)M_w}{R\left(273.15+T\right)\rho_l}\right] \tag{16}$$

M_w is the molecular mass of water and R the universal gas constant. The relative humidity (RH), defined as the ratio of the partial pressure of water vapour in the mixture to the saturated vapour pressure of water at a given temperature, can be related to θ^w_g through:

$$RH = \frac{p_v}{\left(p_v\right)_0} \cdot 100 = \frac{\theta_g^w}{\left(\theta_g^w\right)_0} \cdot 100 \tag{17}$$

where p_v is the vapour pressure and subscript $()_0$ stands for saturated state.

Combining the water mass balance (equation (2)), the mass balance of solid (equation (1)) and the concept of material derivative (equation (5)) and assuming saturated conditions (S_r=1), the water mass balance reduces to:

$$\phi \frac{D_s \rho_w}{Dt} + \frac{\rho_w}{\rho_s}(1-\phi)\frac{D_s \rho_s}{Dt} + \rho_w \nabla \cdot \frac{d\mathbf{u}}{dt} + \nabla \cdot (\rho_w \mathbf{q}_l) = 0 \quad (18)$$

in which the two first derivatives may be developed further accounting for the dependences of liquid (equation (9)) and solid (equation (7)) densities on temperature, solid and pore pressure:

$$\left[\phi b_w + (1-\phi)\cdot 3b_s\right]\frac{D_s T}{Dt} + \phi \alpha_w \frac{D_s p_w}{Dt} + \nabla \cdot \frac{d\mathbf{u}}{dt} + \frac{\nabla \cdot (\rho_w \mathbf{q}_l)}{\rho_w} = 0 \quad (19)$$

Equation (19) allows us for explaining variations of pore water pressure in the saturated part of the experiment. b_w and b_s stands for the volumetric and linear thermal expansion coefficients for water and the solid grain, respectively and α_w is the water compressibility. Pore water pressure variations measured throughout the experiments will be interpreted on the basis of this equation. Equation (19) is a balance of four terms each representing a change of the volume of water in function of some perturbation, e.g. a change of temperature, a change of pore water pressure, a change of pore volume, an in- or outcoming flux. Each perturbation has to be counterbalanced by a combination of the other ones in order to equilibrate equation (19). The first term expresses the volume change of the water and the solid grain associated to temperature variations and is negative when temperature increases, corresponding with an expansion of the water and the solid grain. The second term stands for the volume change associated to the compression of the water. This term is negative when the pressure decreases, corresponding with an expansion of the water. The third term expresses volume change of the solid skeleton, including contributions of effective stresses and temperature changes. An expansion of the solid skeleton corresponds with a positive value of this term. The balance of the first and the third term is known as the **differential expansion** of water and solid. The fourth term is the volume change associated to the flow of water in or out of the element considered and is positive for a net water outflow.

Note that in argillaceous rocks, changes in porosity are small. In the unsaturated part, the influence of a change of porosity on the degree of saturation may be neglected whereas in the saturated part, a change of porosity has a significant influence on the pore water pressure.

3.2.3 Internal energy balance

In the internal energy balance, E_s, E_l and E_g are specific internal energies per unit mass of each phase. S_l and S_g are the degrees of saturation of liquid and gas phases, respectively. ρ_s, ρ_l and ρ_g are the density of the solid, the liquid and the gas phase, respectively. i_c is the heat conduction, j_{El}, j_{Es} and j_{Eg} are energy fluxes due to phase motion and f^Q is an internal/external energy supply. Equation (3) takes into account the most important processes for energy transfer in a porous medium (conduction, advection and phase change). In a low permeability medium thermal equilibrium between the phases may be assumed and therefore only one equation of total energy is required. The internal energy for the medium is computed assuming additivity of the internal energy of each phase.

In low permeability media, convection (energy fluxes due to phase motion) may be neglected (Gens, 2007).

Conductive heat flux is governed by Fourier's law:

$$i_c = -\lambda \nabla T \quad (20)$$

where λ is the global thermal conductivity of the porous medium. λ generally depends on degree of saturation and porosity. In argillaceous rocks, the influence of changes of porosity on the

thermal conductivity may be neglected due to the relatively high stiffness. The dependence of thermal conductivity on degree of saturation (S_l) can be expressed as:

$$\lambda = \lambda_{sat}\sqrt{S_l} + \lambda_{dry}\left(1-\sqrt{S_l}\right) \tag{21}$$

where λ_{dry} and λ_{sat} are the thermal conductivity for the dry porous medium and for the water saturated porous medium, respectively. The law expressed by equation (21) was adopted for the thermal conductivity of FEBEX bentonite during the simulation works conducted by Sánchez & Gens (2006).

3.2.4 Momentum Equilibrium

In the momentum equilibrium, $\boldsymbol{\sigma}$ is the total stress tensor and **b** the body forces vector. In equation (4) inertial terms are neglected because it is assumed that both velocities and accelerations are very small (quasi-static conditions). The solid displacement vector (**u**) is the main variable associated with that equation. The assumption of small strain rate is also adopted. The average skeleton stress is described by Bishop's equation, introduced in the mechanical constitutive law:

$$\boldsymbol{\sigma}' = \boldsymbol{\sigma} - \left[S_l p_l + \left(1-S_l\right)p_g\right]\mathbf{I} \tag{22}$$

where Bishop's coefficient is the degree of saturation, p_l is the liquid pressure and p_g is the gas pressure (considered to be constant and equal to *0.1MPa*).

A linear elastic constitutive law is adopted to relate elastic strain increments ($d\varepsilon^{el}$) with effective stress increments $d(\sigma^{el})'$.

$$d\left(\sigma^{el}\right) = D^{el}\, d\varepsilon^{el} \tag{23}$$

where the elastic constitutive tensor D^{el} is defined by two parameters, e.g. Young's modulus (E [*MPa*]) and Poisson ratio (v). Changes in the volumetric part of the elastic deformation induced by temperature and matricial suction changes ($\Delta\varepsilon^{ve}{}_{T,s}$) can be evaluated from

$$\Delta\varepsilon^{ve}_{T,s} = 3\beta_s \Delta T + 3a_s \Delta s \tag{24}$$

where β_s and a_s are, respectively, the linear thermal expansion coefficient for the medium and the swelling coefficient for changes in suction.

3.3 Conceptual model

Different computations were run. The first one is called "Base Case" and is described in the first section of this chapter. The description consists in the modelling features: initial and boundary conditions, geometry, mesh and time schedule and in the parameters adopted for the analysis. A paragraph about the history of the test area meant as a discussion basis for future modelling was included. In each of the other computations, a slight change was applied to the Base Case to evaluate the influence of some key parameters and of uncertain initial conditions.

3.3.1 Base Case

Modelling features

The modelled domain, a detailed view of the heater and bentonite barrier and the flux (hydraulic and heat) boundary conditions are presented in Figure.

The mesh used is axisymmetric (around the microtunnel axis) and has a width of 40m and is 30m long. The dimensions used are in agreement with the indications given in Gaus 2010. The vertical symmetry plane between the two heaters was used. Therefore only one heater and half of the middle concrete plug are represented (in the upper left corner of the mesh). Null fluxes are imposed on the upper, the lower and left boundaries. Those boundaries act thus as symmetry entities (axisymmetric line for the left boundary and plane for the upper boundary), which implies a virtual second heater. The external mechanical boundary conditions are 0-displacement on all boundaries, excepted on the right side, where a compressive stress state of 4.5 MPa is applied. The initial conditions of the different materials are given in Figure 3.1. For numerical considerations, the insulator was modelled as a gap (empty space), rather than as a material.

Note: in Gaus 2010, the advised initial temperature in the VE test area is 10º. In reality, the rock temperature at Mont Terri is somewhat higher. In this work, we use 15º as initial temperature as what really matters is the amplitude of the temperature increase. A value of 2.0 MPa was taken for representing the initial pore water pressure in the host rock. Furthermore the initial stress state in the argillaceous rock was assumed to be isotropic with an average value of 4.5MPa. Before the excavation of the microtunnel, the rock mass is considered to be saturated.

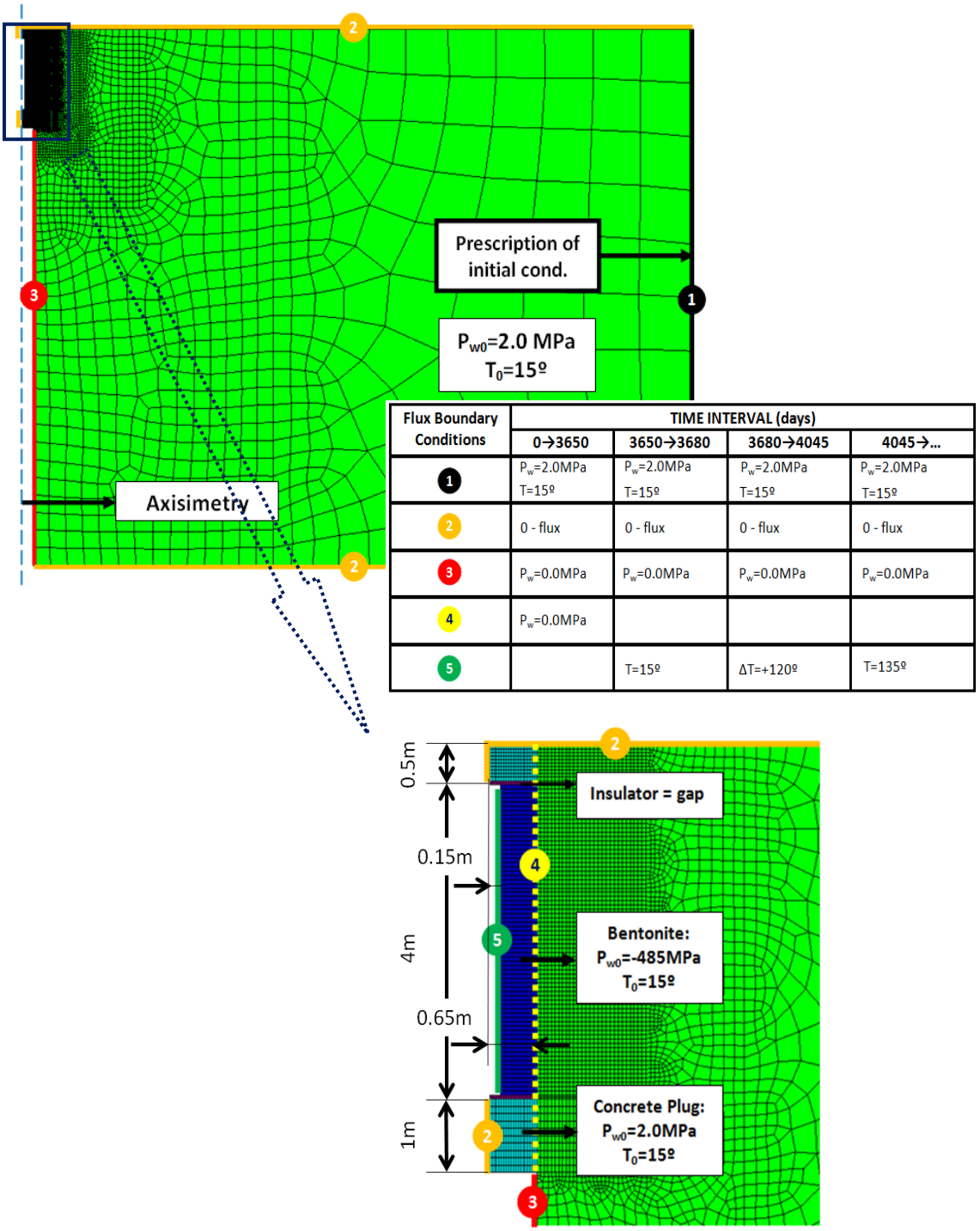

Flux Boundary Conditions	TIME INTERVAL (days)			
	0→3650	3650→3680	3680→4045	4045→...
1	P_w=2.0MPa T=15º	P_w=2.0MPa T=15º	P_w=2.0MPa T=15º	P_w=2.0MPa T=15º
2	0 - flux	0 - flux	0 - flux	0 - flux
3	P_w=0.0MPa	P_w=0.0MPa	P_w=0.0MPa	P_w=0.0MPa
4	P_w=0.0MPa			
5		T=15º	ΔT=+120º	T=135º

Figure 3.1 Modelled domain, finite element mesh, flux boundary conditions and detailed view of the heater and bentonite barrier

The modelling schedule is as follows:

- The microtunnel is excavated 3650 days (ten years) before the start of the test. At this stage of the project, the excavation is modelled by a relaxation of the total stresses (from initial value to 0) and by decreasing the pore water pressure from initial value to atmospheric

pressure. The EDZ is not considered. Correct modelling of the ten years history before the start of the HE-E experiment is important for the estimation of the initial conditions of the test area. Some considerations about the hypotheses made to model the history of the test area are given in the next section (Note on the history of the test area before the experiment).

- Buffer material and concrete are emplaced (instantaneously). A period of 30 days is left before heating start. The initial suction in the barrier material was set to 485MPa, which coincides with a water content value of 7.6% (Gaus et al., 2011). Note that at this stage, no difference was made between the pellets and the sand/bentonite section due to the model assumptions. Neither the bentonite blocks used to support the heaters are considered.
- Thirty days after buffer material emplacement, heating is switched on and the temperature is increased on the left bentonite boundary from 15ºC to 135ºC at a rate of 120ºC/year. The heating strategy corresponds with strategy nr. 2 (Figure 3.2) and corresponds with a smooth temperature increase. This is thought to be in closer agreement with real storage conditions. Moreover gradual heating instead of instantaneous heating may provide useful information about water evaporation and vapour diffusion in the buffer material.
- The temperature on the inner bentonite boundary is kept at 135ºC for the rest of the experiment.

In this work, the time reference used is the bentonite and concrete plug emplacement time:

- 0 days = bentonite emplacement
- 30 days = start of heating
- 395 days = end of temperature increase period
- Etc.

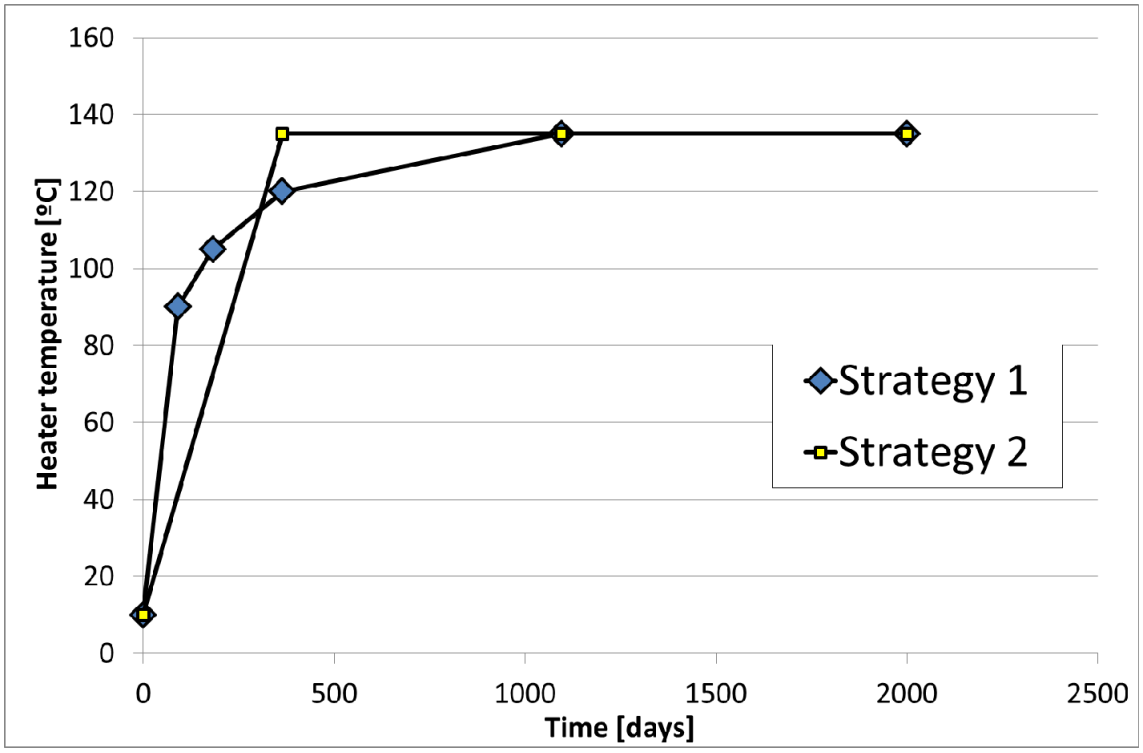

Figure 3.2 Heating strategies

Note on the history of the test area before the experiment

The area in which the HE-E experiment takes place has quite a long and complex history. It is illustrated in Figure 3.3, in which the relative humidity of the test section is plotted in function of the time in the 12 year interval (149 months) between the excavation of the microtunnel and the start of the HE-E. Three main periods may be distinguished:

- The period between the microtunnel excavation and the start of the controlled ventilation period, lasting for about 3.5 years (41months)
- The controlled ventilation period including two desaturation phases and lasting for 4.4 years (53 months)
- The period between the end of the second desaturation phase and the start of the HE-E, lasting 4.8 years (57 months).

This history has an influence on the initial conditions at the start of the HE-E experiment, mainly on the pore water pressure and possible desaturation, and hence it should be taken into account.

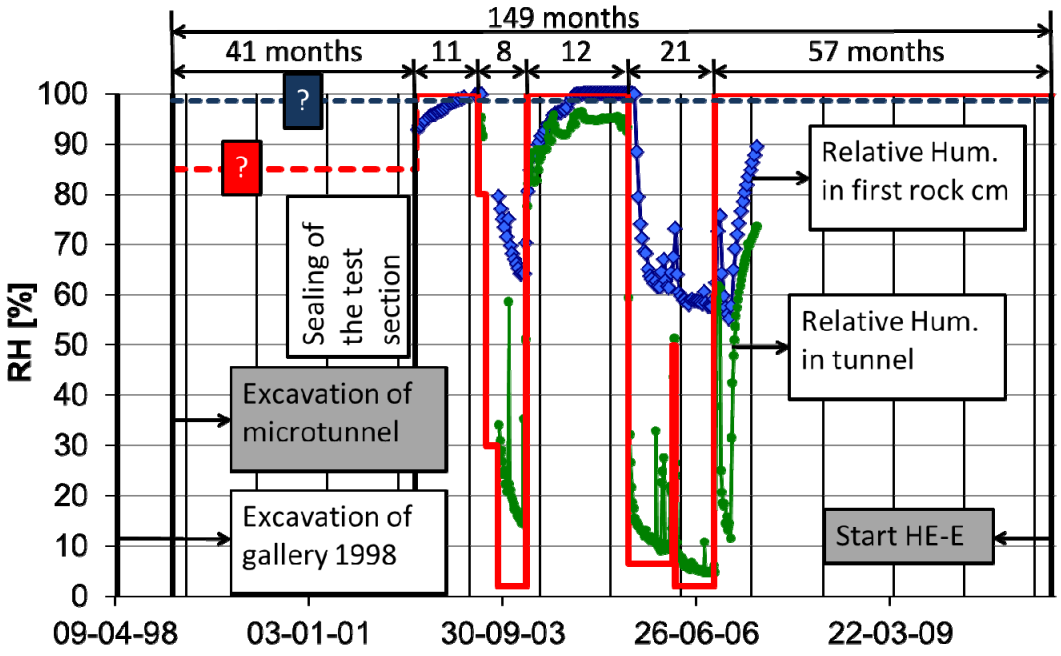

Figure 3.3 Relative humidity history of the test section

In the first period, representative of natural ventilation of a niche (tunnel is closed at one side), the relative humidity in the tunnel was not measured. Nevertheless some relative humidity measurements are available at several locations in the URL. Meier (1998) measured relative humidity in gallery 1998 and came up with values around 50%. Meier (2004) and Gisi (2007) measured the relative humidity in boreholes. They monitored values of 80-90% and 75-95%, respectively. As the microtunnel is closed at one side, its configuration is similar to that of a borehole. Moreover Garitte and Gens (2007) back calculated the value of the relative humidity in the tunnel (85%) in this period to reproduce correctly the pore water pressure and the water content gradient around the tunnel before the controlled ventilation period. The results from this back calculation are presented in Figure 3.4. The use of an anisotropic permeability seems to

explain the dispersion of the measurements. According to the measurements, natural ventilation seems to produce a zone in suction with an extent of about 1.75m from tunnel wall and a desaturated zone of about 20 cm. Saturation degree at tunnel wall before the controlled ventilation period reaches about 90% (equivalent to a water content of 6%).

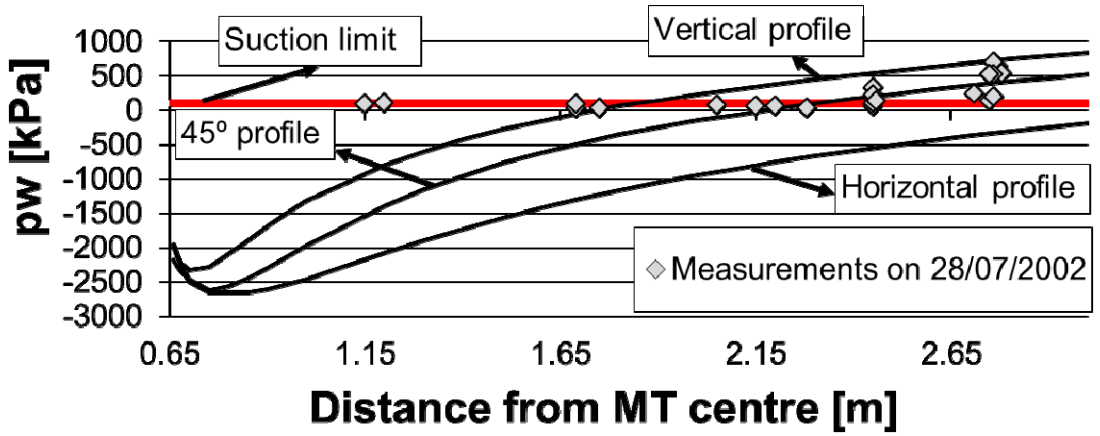

(a)

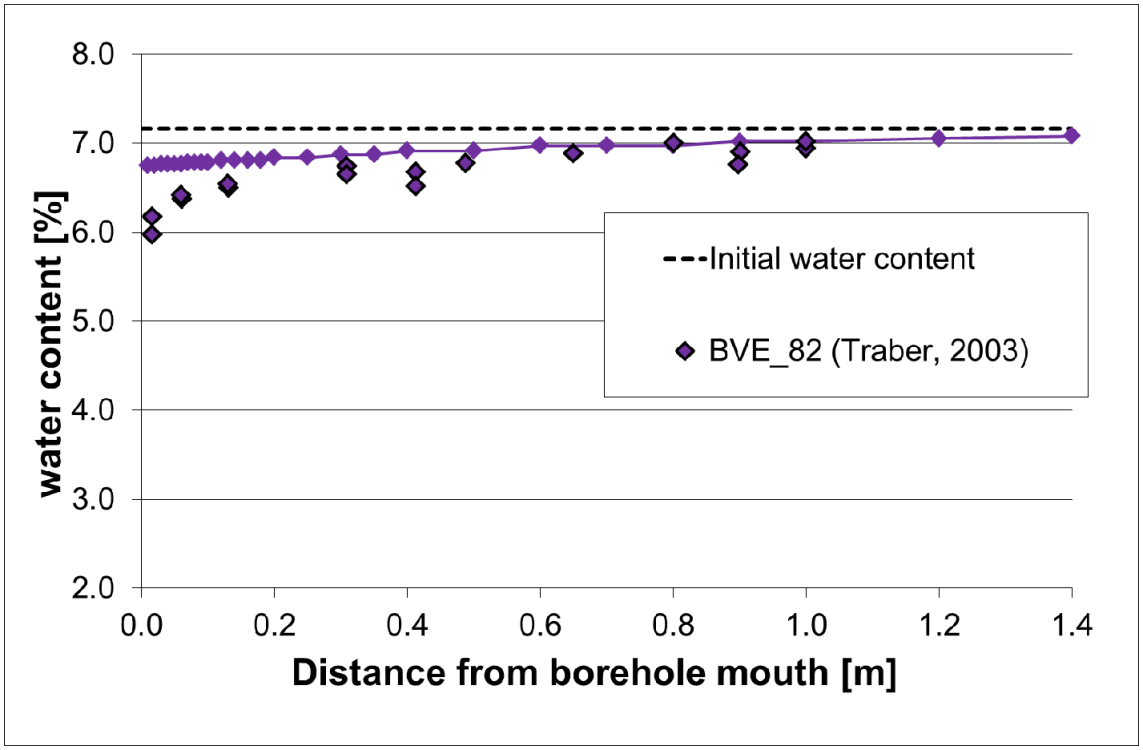

(b)

Figure 3.4 Pore water pressure (a) and water content (b) profiles before the controlled ventilation period (measurements and simulation)

The second period corresponds with the Ventilation Experiment itself and starts with the sealing of the test section with two double doors. Only by isolating the section, the measured relative humidity in the tunnel approaches 100% (red line). The relative humidity in the first rock cm

(blue dots) increases progressively. After 11 months, the rock mass is believed to be saturated and the first drying phase starts. Relative humidity of blown air is as low as 2% and the relative humidity in the tunnel decreases down to 15%. In the first rock cm, relative humidity decreases to 65%. The re- and desaturation process is then repeated. Some aspects of the Ventilation Experiment are recalled:

- Different geophysical methods (seismic refraction, interval velocity and cross-hole measurements) were applied to evaluate the extent and the development of the EDZ around the microtunnel (Schuster, 2007). The main conclusions are that the extent of the EDZ was estimated to be about 5-25cm in the bedding planes and 10 cm in the perpendicular direction. No significant changes induced by ventilation were identified and the EDZ was thus related to stress redistribution during the excavation exclusively. Moreover, observation of the tunnel wall showed that the state of the rock surface in the test section before and after the two drying phases was fairly good: neither relevant rock failures nor far-reaching cracking were observed on the walls (Mayor and Velasco, 2008). The small displacements registered in the extensometers during the different cycles tend to confirm the fact that the EDZ is not developing during drying and wetting. Garitte and Gens (2007) predicted an extent of the EDZ (by modelling) of about 30cm. The EDZ was intensified during the ventilation cycles but not extended significantly.
- The Ventilation Experiment may be regarded as a huge pump test (Mayor and Velasco, 2008) and may thus be used to determine the hydraulic conductivity of Opalinus Clay. In the modelling presented by Garitte and Gens (2007), the intrinsic permeability value used to reproduce the water mass balance of the experiment, the relative humidity in the rock mass and degree of saturation is only dependent on the degree of saturation (about 4E-20m^2 for saturated rock). In other words, no increase of permeability in the EDZ was necessary to reproduce the measurements satisfactorily. The measurements compared to the simulation results are presented in Figure 3.5, Figure 3.6, and Figure 3.7.
- After the two resaturation periods (11 and 12 months), the rock was estimated to be saturated: the hygrometers in the rock mass registered relative humidity close to 100%, the water content measured in radial boreholes showed full saturation and resistivity measurements also indicated full saturation. Pore water pressure measurements shows that throughout the experiment, the extent of the zone in suction is about 2m, even after the resaturation (Mayor and Velasco, 2008).

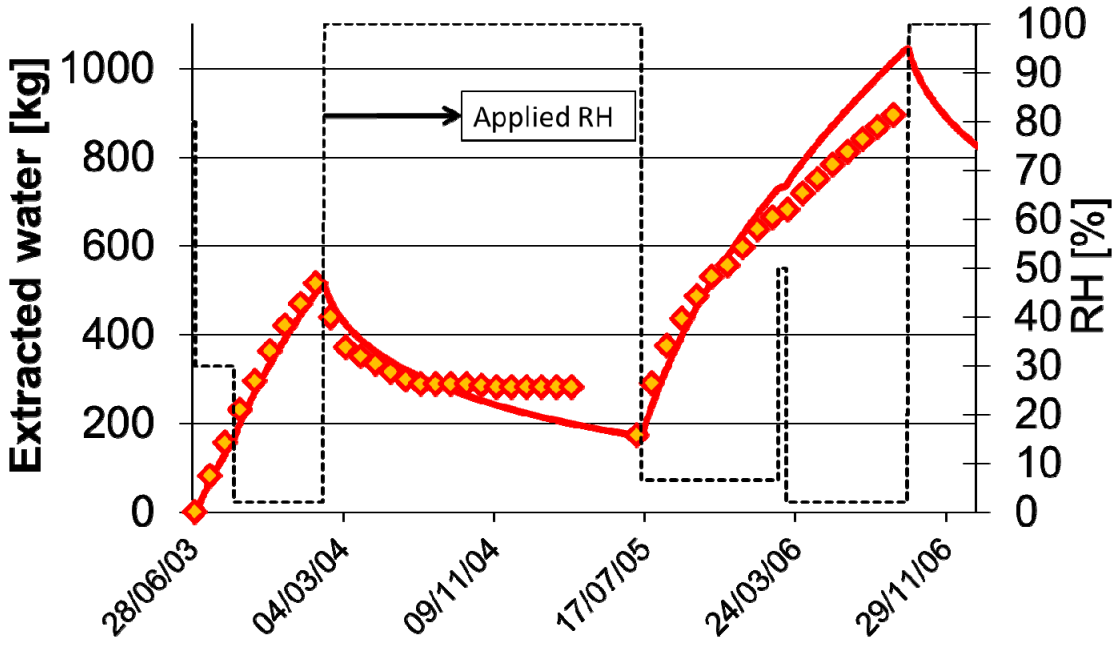

Figure 3.5 Water mass balance of the of the test section during the Ventilation Experiment: measurements and simulation (using a permeability value depending only on the degree of saturation)

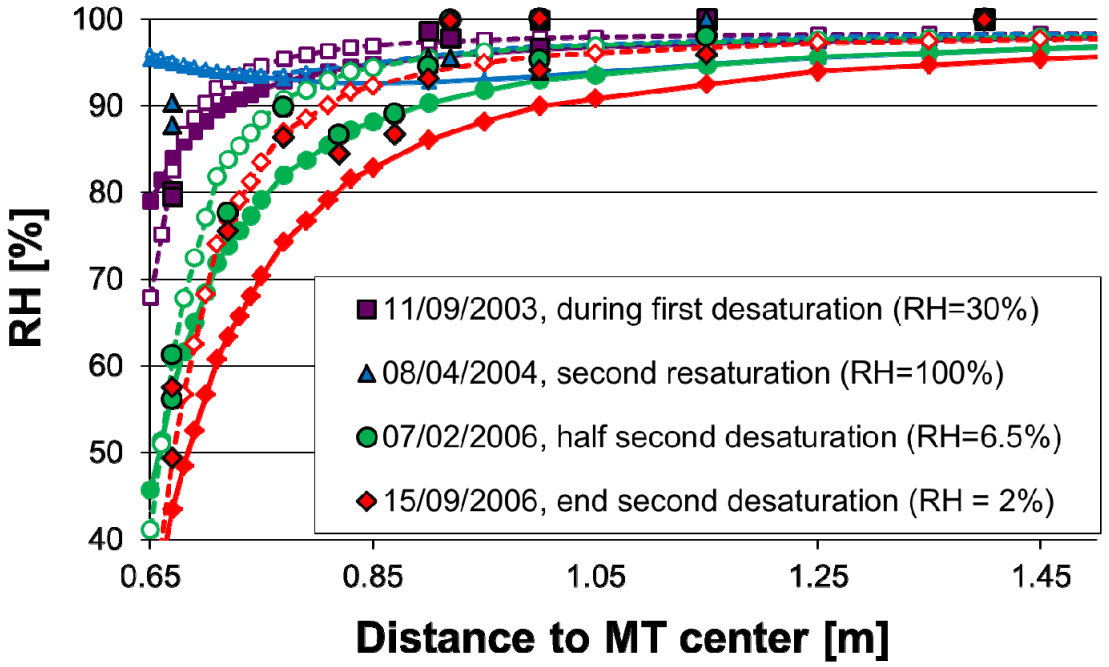

Figure 3.6 Relative humidity profiles at several moments during the Ventilation Experiment: measurements and simulations.

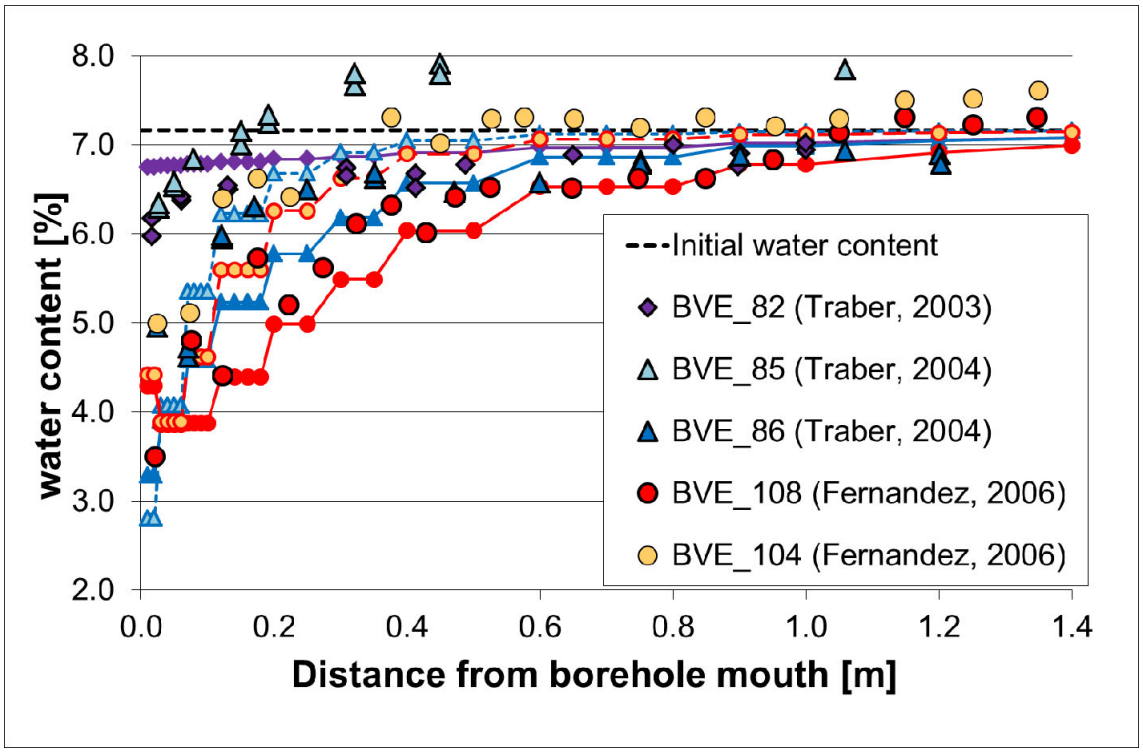

Figure 3.7 Water content profiles at several moments during the Ventilation Experiment: measurements and simulations

In the third period, the test section is left closed as in the two previous resaturation periods for 57 months. That is five times more than in the previous resaturation period. It is thus reasonable to state that the rock mass in the test area is saturated at the start of the HE-E experiment. The pore water pressure state instead has to be further investigated. It should be noted that considering the large time interval between the excavation of gallery 1998 and the start of the HE-E (13 years) and the relative small distance between gallery 1998 and the test area, the presence of gallery 1998 may have an influence on the pore water pressure state at the start of the HE-E experiment.

The measured pore water pressure gradient before the start of the HE-E experiment (Rösli, 2010) is compared to the results from different simulations Figure 3.8. The position of the wall of the microtunnel and of the extent of the EDZ is indicated by a vertical black and red line, respectively. In each of the simulations the entire history of the test section has been idealized by applying a constant pore water pressure value to the wall of the microtunnel:

- In C0, the atmospheric pressure was applied.
- In C1, a suction of 1MPa was applied.
- In C2, a suction of 2MPa was applied.
- In C3, a suction of 25MPa was applied.

Using Kelvin's law, we can calculate that a suction of 2MPa corresponds with a relative humidity of about 98.5% and a suction of 25MPa with a relative humidity of 85%. A relative humidity of 98.5% is likely to be close to the ambient condition in the closed tunnel section and a relative humidity of 85% to the ambient condition in a half-open tunnel. Note that a suction of

2MPa will not produce any desaturation whereas a suction of 25MPa will cause desaturation as the air entry value of Opalinus Clay is about 10MPa.

Out of computations C0, C1, C2 and C3, C2 is the computation that shows the best agreement with the measured extent of the suction zone before the start of the HE-E experiment. C3 highly overestimates the extent of the suction limit. Deeper into the rock mass the measured pore water pressure decrease is underestimated by simulation C2. The larger pore water pressure dissipation indicated by the measurements may be due to two reasons: an increase of permeability in the EDZ or a significant influence of the drainage induced by gallery 1998 that is not taken into account in the simulation. The influence of an increase of the permeability in the EDZ is evaluated to be negligible as a consequence of the limited extent of the EDZ. To illustrate this the C3 computation was repeated using an EDZ similar as that found around normal sized galleries (extent of several metres) and that results in a pore water pressure gradient that approaches that of the measurement (although it is displaced into the rock mass). Using the mirror method, assuming that dissipation is additive, we may evaluate the influence of dissipation induced by gallery 1998. The results of the mirror method are presented in curve C2bis, which shows a somewhat better agreement with the measurements.

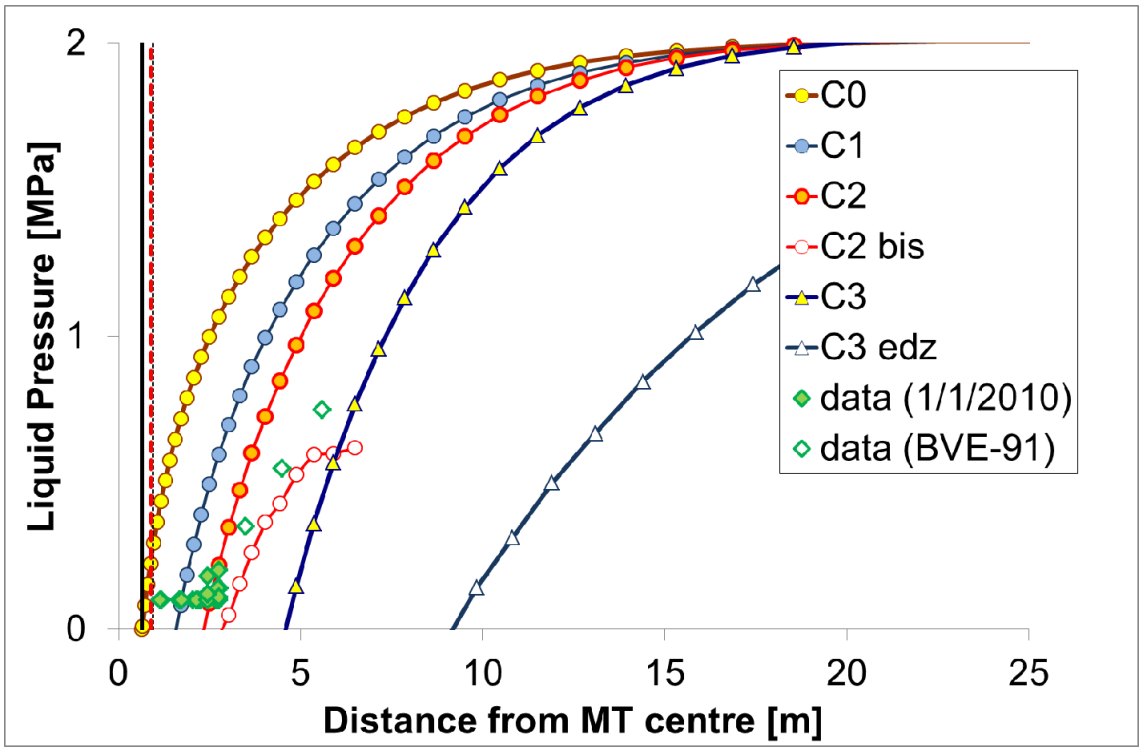

Figure 3.8 Pore water pressure profile before the start of the HE-E experiment

As a conclusion some recommendations may be made for the next modelling round. The complex 13 years history of the HE-E test area may be simplified applying a low constant suction value (about 2MPa) on the microtunnel wall. This allows for reproducing quite well the pore water pressure state before the start of the HE-E experiment. A suction value of 2MPa is quite a realistic condition for a closed tunnel as it corresponds to a relative humidity value of about 98.5%. The initial state of the rock would be better reproduced if the influence of gallery 1998 is also taken into account. In a first approach, the influence of the EDZ may be neglected because:

- Its extension is quite small.
- The measurements from the Ventilation Experiment that is similar to a large scale pump test were reproduced satisfactorily using an intrinsic permeability value depending only on the degree of saturation and not on the damage state of the rock.
- After bentonite emplacement the EDZ will desaturate, bringing together a reduction of the permeability far more important than the increase induced by damage.
- The swelling of the saturated bentonite will probably restore initial permeability values.

Model parameters

The material parameters used in this work are summarized in 3.2 (for Opalinus Clay) and in Table 3.3 (for bentonite). Parameter values were taken according to modelling experience (Gens et al., 2007), experimental investigations (Floria et al., 2002, Muñoz et al., 2003, Zhang and Rothfuchs, 2005, Villar, 2007) and/or to the reference work by Bock (2001).

Table 3.2 Opalinus Clay parameters

Properties	Parameters	Symbol	Value
Physical	Solid grain density	ρ_{s0}	2.70e03 kg.m^{-3}
	Solid phase specific heat	C_s	800 J kg^{-1} K^{-1}
	Porosity	ϕ	0.15
	Linear thermal expansion for grains	b_s	1.50e-05 ºC^{-1}
	Linear thermal expansion for the medium	β_s	1.50e-05 ºC^{-1}
Hydraulic	Intrinsic permeability	$k_{//}$	3.16e-20 m^2
	Liquid relative permeability	λ	0.52
	Diffusive Flux of vapour	D	5.90e-06
	Diffusive Flux of vapour	n	2.30
	Retention curve	P_0	11MPa
	Retention curve	σ_0	7.20e-02 N/m
	Retention curve	λ	0.20
	Retention curve	$S_{rl} - S_{rs}$	7e-3 – 1
Thermal	Saturated thermal conductivity	λ_{sat}	1.70 W/m/K
	Unsaturated thermal conductivity	λ_{dry}	1.06 W/m/K
Mechanical	Young modulus	E	4.00e03 MPa
	Poisson's ratio	ν	0.24

Table 3.3 Bentonite parameters

Properties	Parameters	Symbol	Value
Physical	Solid grain density	ρ_{s0}	2.82e03 kg.m^{-3}
	Solid phase specific heat	C_s	950 J kg^{-1} K^{-1}
	Porosity	ϕ	0.475
	Linear thermal expansion for grains	b_s	1.50e-05 ºC^{-1}
Hydraulic	Intrinsic permeability	$k_{//}$	3.50e-20 m^2
	Liquid relative permeability	λ	3.00
	Liquid relative permeability	A	1.00
	Gas relative permeability	λ	4.17
	Gas relative permeability	A	2.20e08
	Diffusive flux of vapour	D	5.90e-06
	Diffusive flux of vapour	n	2.30
	Retention curve	P_0	20MPa
	Retention curve	σ_0	7.20e-02 N/m
	Retention curve	λ	0.31
	Retention curve	$S_{rl} - S_{rs}$	0 – 1
Thermal	Saturated thermal conductivity	λ_{sat}	1.30 W/m/K
	Unsaturated thermal conductivity	λ_{dry}	0.30 W/m/K

The porosity was chosen such that the water content of the saturated material is equal to *7.14%*, the average undisturbed water content of saturated Opalinus clay in the vicinity of the microtunnel (calculated from project data):

where w is the water content, S_l is the degree of saturation (=1), φ is the porosity and ρ_w and ρ_s are the water and solid grain density, respectively.

$$w = S_l \frac{\phi}{1-\phi} \frac{\rho_w}{\rho_s} \qquad (25)$$

The liquid relative permeability was determined by back-analysis of the drying test (Floria et al., 2002): the liquid relative permeability was decreased until a good agreement was reached between outcoming flux and water content profiles (Figure 3.9). Figure 3.10 and Figure 3.11 show the dependency of the permeability and the thermal conductivity on the degree of saturation for the Opalinus Clay and the buffer material.

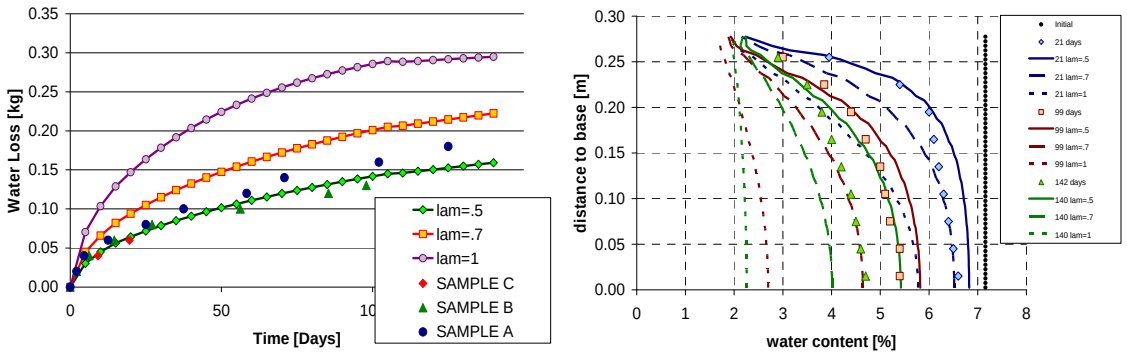

(a) **(b)**

Figure 3.9 Comparison between lost water and water content profiles measured during the the drying test (Floria et al., 2002) and simulations using several values of liquid relative permeability.

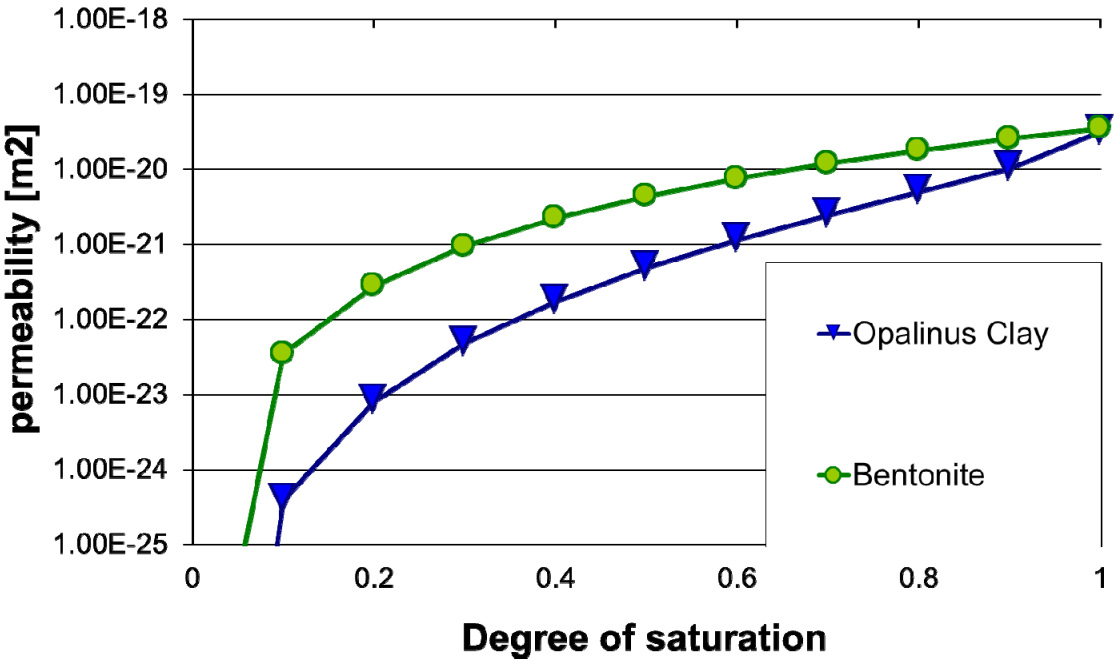

Figure 3.10 Dependency of the permeability on the degree of saturation for the Opalinus Clay and the bentonite.

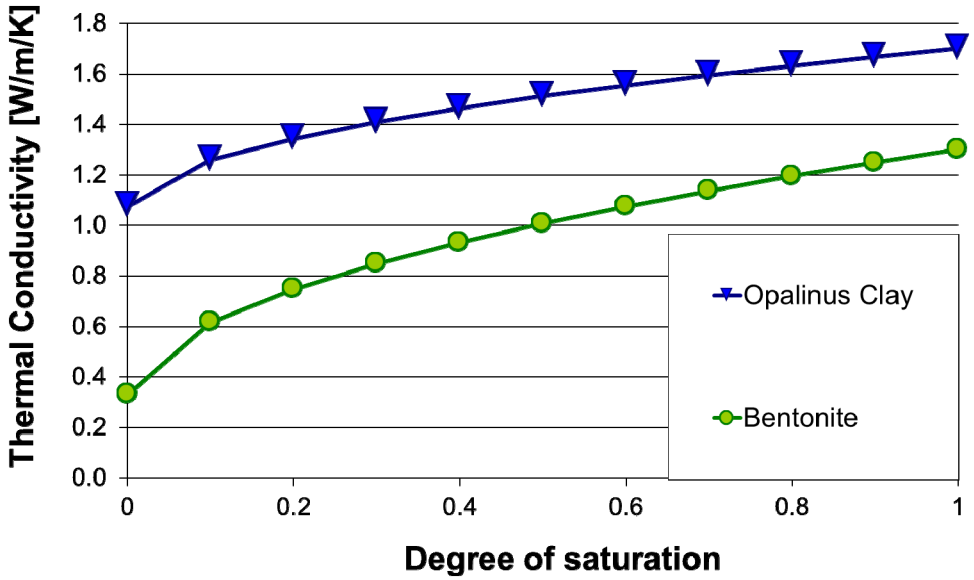

Figure 3.11 Dependency of the thermal conductivity on the degree of saturation for the Opalinus Clay and the bentonite

The retention curve parameters were determined based on several experimental investigations (Gens, 2000; Muñoz et al., 2003; Zhang & Rothfuchs, 2005; Villar, 2007). The comparison of the Van Genuchten model and the experimental data given by the different authors is given in Figure 3.12 and Figrue 3.13. The samples used by Muñoz et al. (2003) and Villar (2007) came from the immediate vicinity of the microtunnel.

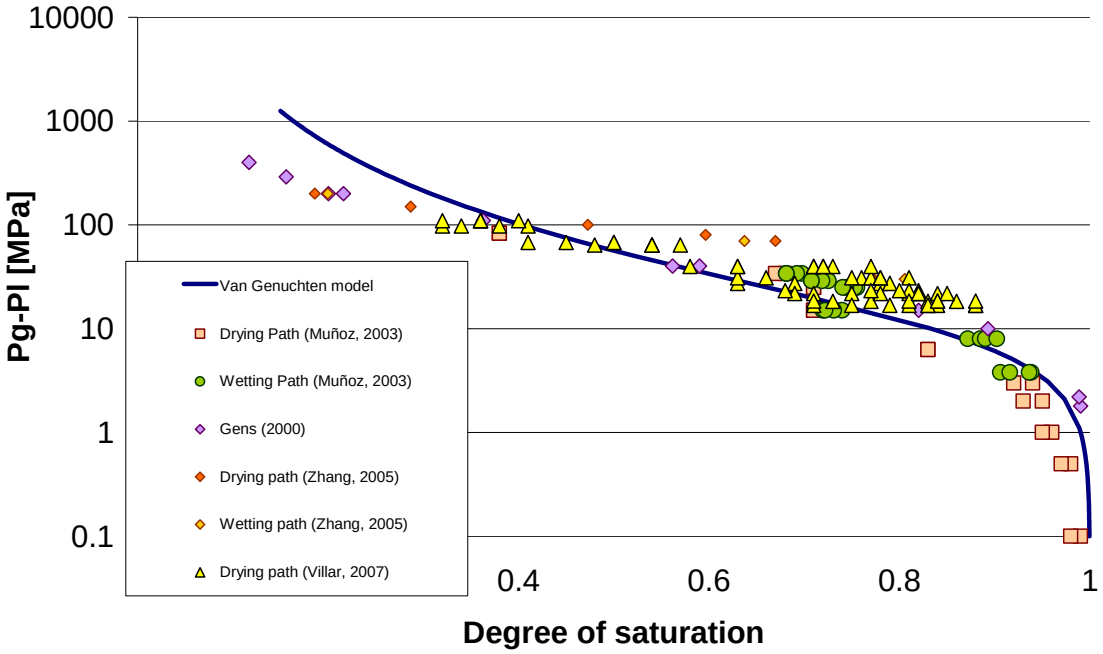

Figure 3.12 Comparison of the retention curve used for the analysis of the VE and experimental results obtained by several authors.

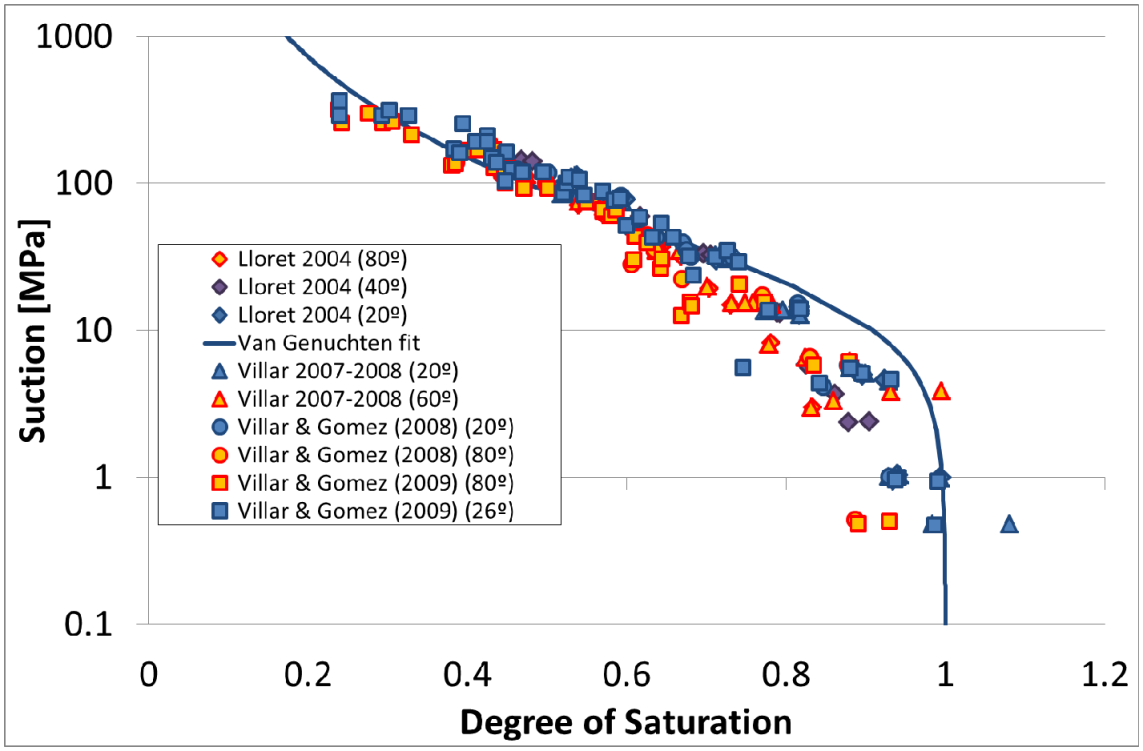

Figure 3.13 Comparison of the retention curve used for the bentonite and experimental results obtained by several authors

Some key features of the theoretical formulation are: the water thermal expansion is considered constant (3.40e-04 K^{-1}), both, solid grain and skeleton thermal expansion are considered, the rigidity of the rock skeleton is taken into account, the thermal conductivity and the water permeability are computed as a function of water saturation, water phase exchange (evaporation and condensation) and vapour diffusion are considered.

3.3.2 Variants of the Base Case

Six variant computations were run to estimate the influence of key parameters controlling the pore water pressure response in the saturated part and the influence of the initial degree of saturation of the host rock. The mechanisms triggering pore water pressure changes by temperature load were shown to be the differential thermal expansion of water and solid and the drainage capacity of the excess pore water pressure (Gens et al., 2007). The magnitude of the pore water pressure peak was found to be very much dependent on (Garitte and Gens, 2010):

1. The thermal expansion coefficient of water
2. The thermal expansion of the skeleton
3. The thermal expansion of the solid grain
4. The water compressibility
5. The skeleton compressibility
6. The water permeability

The thermal expansion coefficient of water is a physical parameter depending on temperature. In this work it was taken constant and its value is typical of a temperature of 40ºC (Figure 3.14). The dependency of the pore water pressure peak on the thermal expansion of the skeleton and of the solid grain is illustrated in Figure 3.15, for an infinitely stiff medium. Generally, a lower thermal expansion of the skeleton (equivalent to lower thermal expansion of the pores) induces a higher pore water pressure peak, but a lower thermal expansion coefficient of the grains induces a lower pore water pressure peak. Fundamental studies (Booker and Savvidou, 1985) showed that if no irreversible deformations are induced by temperature changes, both thermal expansion coefficients should be taken equal. For Opalinus Clay, the range of temperature changes in the experiment is believed to generate only reversible (and small) deformations. This situation is thus considered in the base case and the other combinations have been tested in additional runs (Var/01, Var/02 & Var/03). The influence of an increase of the thermal expansion coefficient for the skeleton and the grain by a factor of 2 has been tested in Var/04. The water compressibility is a physical constant and hence, it has not been modified. The influence of the skeleton compressibility (equivalent to the rigidity) has been evaluated in Var/05. The influence of the water permeability was the main subject of several previous works (Gens et al., 2007 or Garitte et al., 2010). On the one hand, water permeability was found to be the most influent parameter by far. On the other hand, the possible range for this parameter in Opalinus Clay was determined quite precisely in the same works.

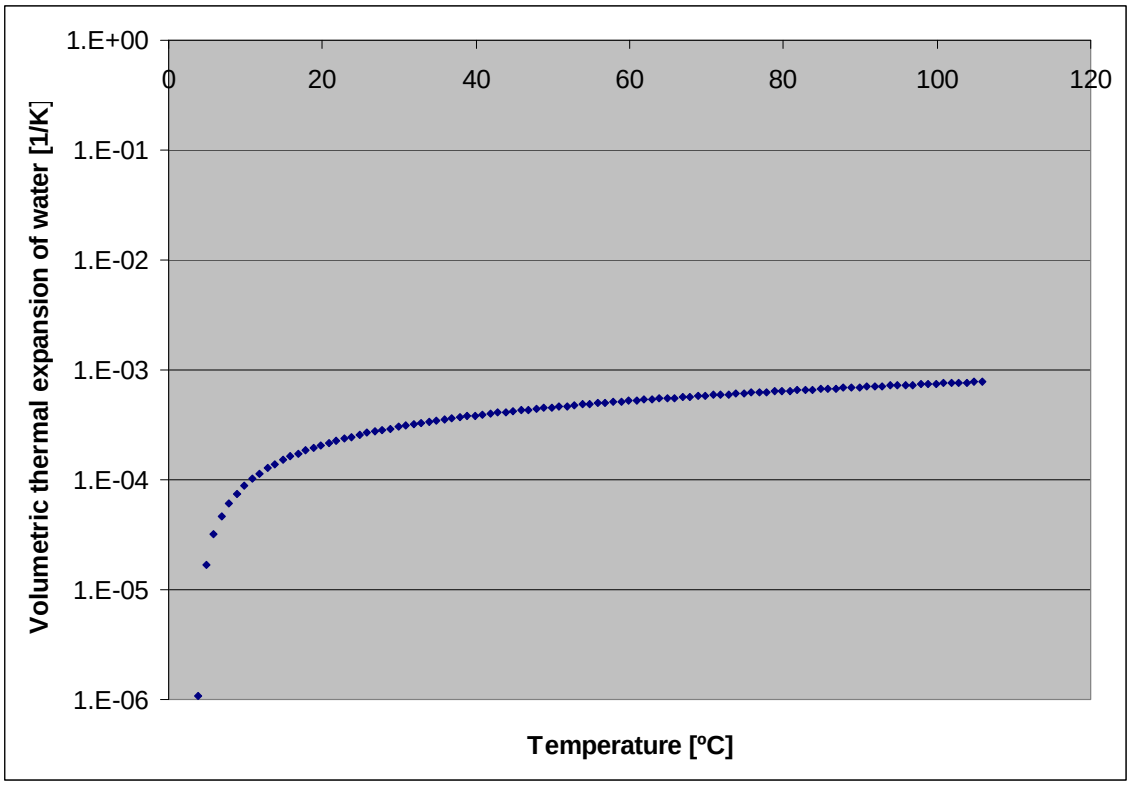

Figure 3.14 Volumetric thermal expansion of water

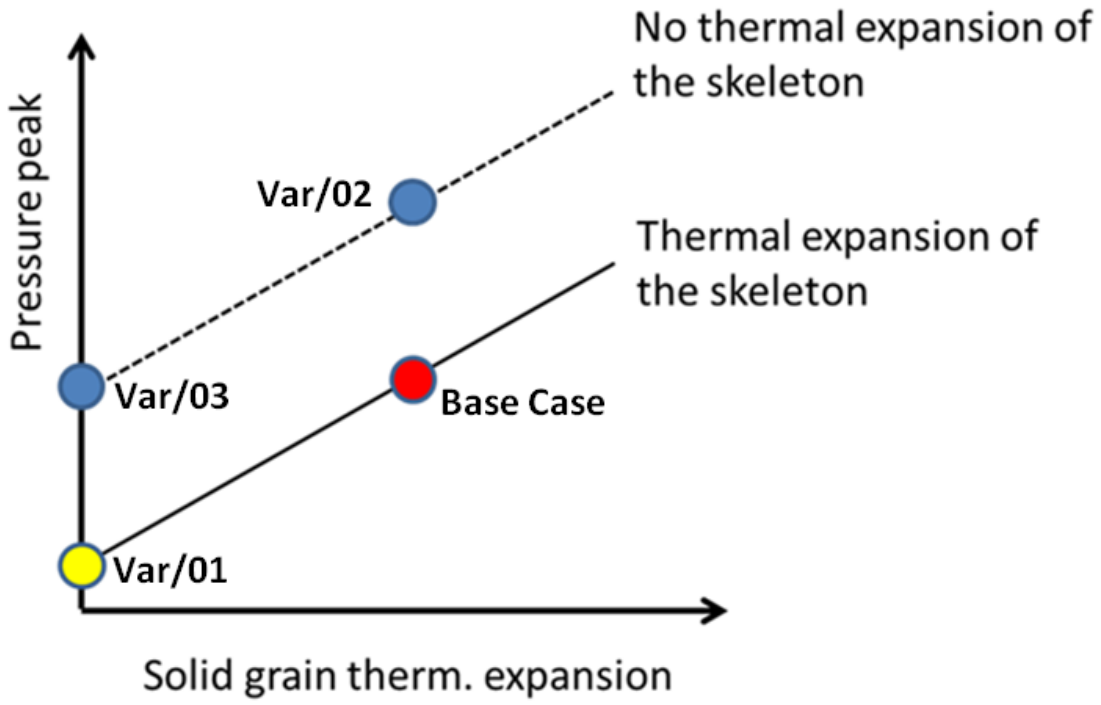

Figure 3.15 Schematic representation of the dependency of the pore water pressure peak magnitude in function of the solid grain and the skeleton thermal expansion

Although it is believed that the rock mass around the microtunnel is saturated before the start of the HE-E experiment, the influence of a desaturated rock mass before the start of the heating experiment was evaluated in Var/06. In this variant, a suction of 25MPa was imposed on the microtunnel wall during the 10 years prior to the heating experiment. The different parameters sets used in the sensitivity analysis are summarized in Table 6.

Table 6 Parameters for sensitivity analyses

Case	Parameters			
	Thermal expansion for solid grain ($^oC^{-1}$)	Thermal expansion for medium ($^oC^{-1}$)	Young's Modulus (Opalinus Clay) (MPa)	Suction on the microtunnel walls (MPa)
Base Case	1.50e-05	1.50e-05	4000	0
Var/01	0	1.50e-05	4000	0
Var/02	1.50e-05	0	4000	0
Var/03	0	0	4000	0
Var/04	3.00e-05	3.00e-05	4000	0
Var/05	3.00e-05	3.00e-05	40000	0
Var/06	1.50e-05	1.50e-05	4000	25

3.4 Modelling results

In this section, the modelling results obtained for the Base Case are discussed and a tentative explanation is given for the system behaviour. In order to avoid an overload of the main text, only the most relevant results are presented in the text. For the sake of completeness (important for scoping computations), all output results are given in annexes. In those annexes, the reader will find the modelling results (temperature, degree of saturation, RH and pore pressure) along six profiles described in Figure 3.16:

- Three profiles parallel to the microtunnel wall (B-profiles).
- Three radial profiles (A-profiles).

Time evolution curves of the same variables at several distances from the heater on "A" and "B" profiles and isocurves at significant times are also presented in the annexes.

In section 3.4.4, comparisons of the more relevant results obtained for the Base Case and for the variants are made in order to provide a better understanding of the role played by some parameters/boundary conditions on the global response of the system.

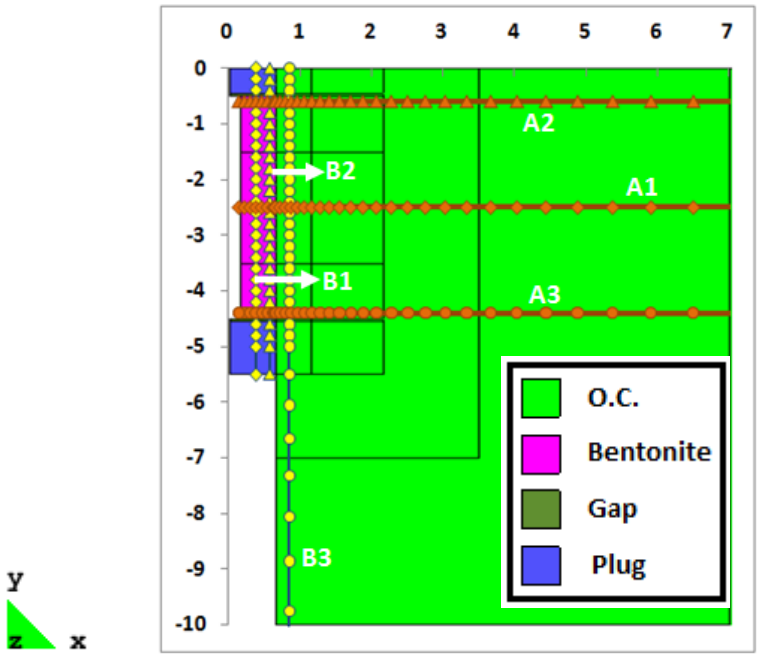

Figure 3.16 Location of the output profiles

3.4.1 Temperature evolution

The predicted evolution of temperature in the buffer and in the host rock around the buffer is presented in Figure 3.17 and Figrue 3.18, respectively. In the near field of the experiment, most of the temperature increase occurs during the temperature build-up at heater-bentonite interface. The buffer-rock interface reaches about 63ºC after the temperature increase period. It keeps increasing in a slower way up to 72ºC in the two following years. In the farther field, the temperature rises in a continuous way, even after heater temperature has reached 135ºC.

Note: in all time evolution figures, vertical lines indicate the time at which profiles are available

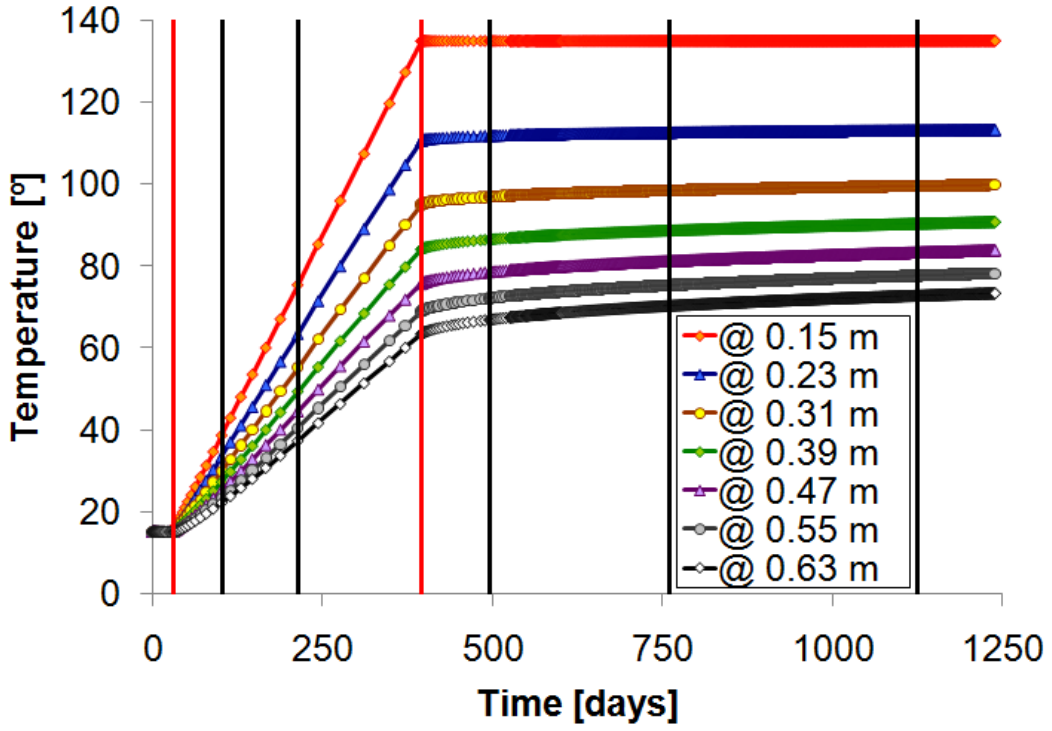

Figure 3.17 Predicted temperature evolution in the bentonite buffer.

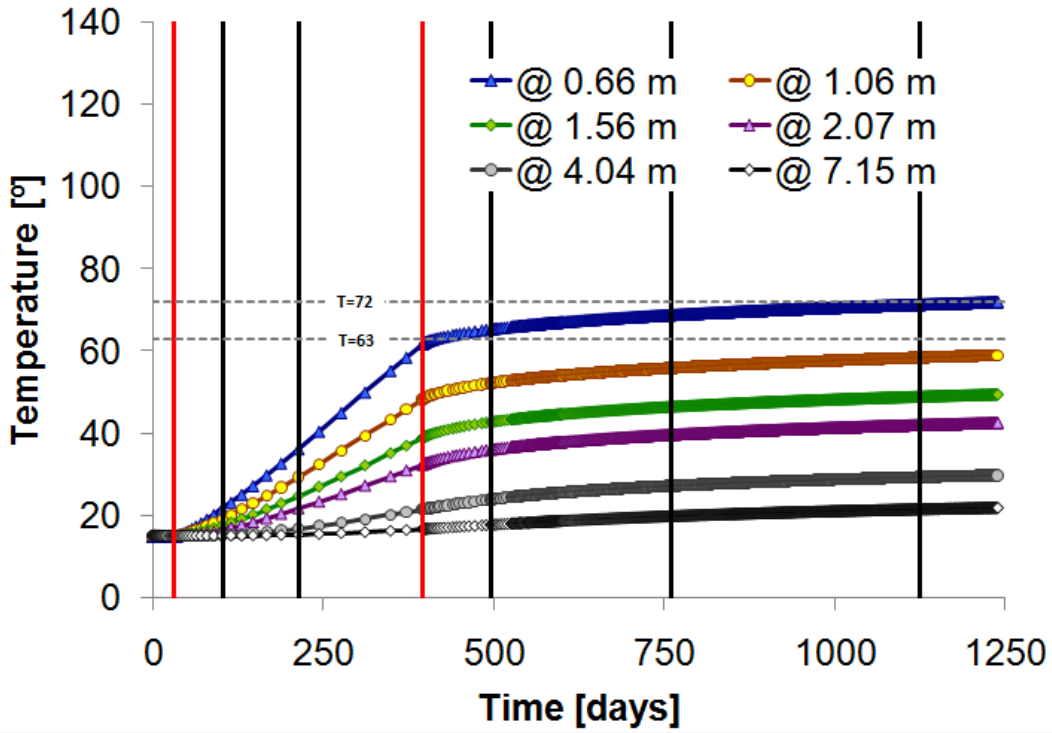

Figure 3.18 Predicted temperature evolution in the host rock

The required power applied to one heater to reach the target temperature at heater-bentonite interface is given in Figure 3.19 and is estimated to be about 1200W/ heater (300W/heater metre).

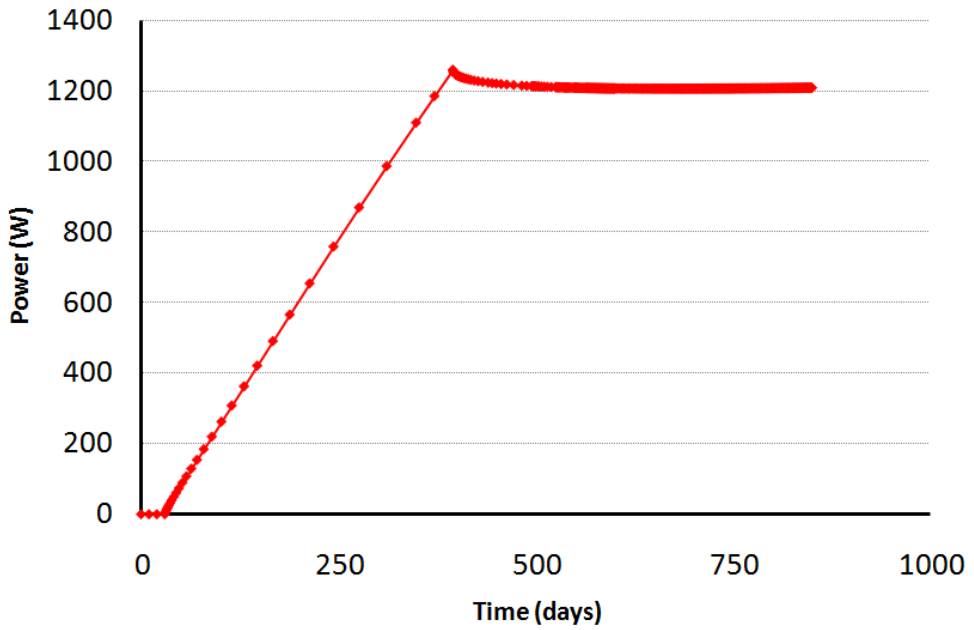

Figure 3.19 Predicted heating power required to apply the temperature path of the selected heating strategy

In Figure 3.20 a profile of temperature along A1 is depicted at different times after the start of heating. Approximately three years (1125 days) after the start of the experiment, the rock volume with a temperature increase larger than 15° is estimated to reach about four metres from the tunnel axis.

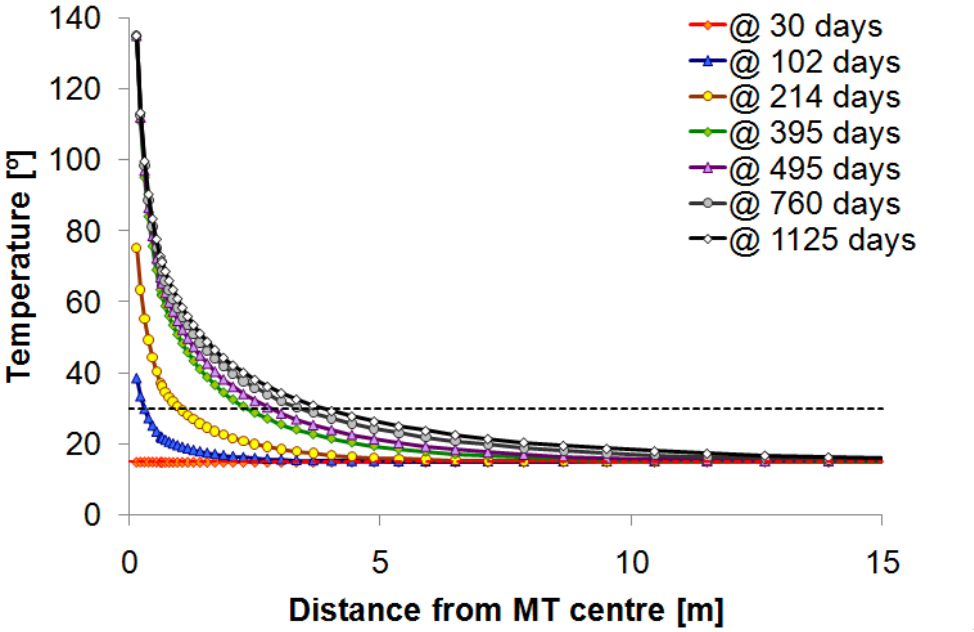

Figure 3.20 Predicted profiles of temperature at different times along A1.

A set of iso-temperature lines for points in vicinity of the heater is shown at different times in Figure 3.21 and Figure 3.22. The coloured zone represents the rock mass in which an increment of more than 15ºC in temperature is predicted one year (Figure 3.21) and three years (Figure 3.22) after heating start. From these figures we can deduce the optimal zone in which temperature sensors should be installed.

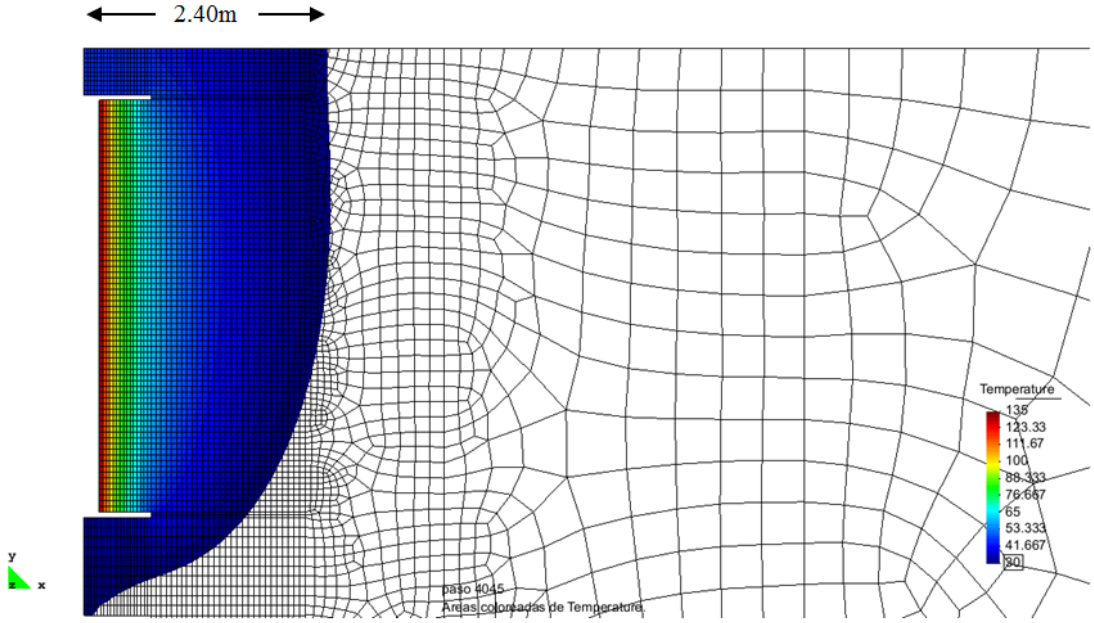

Figure 3.21 Equivalue lines of temperature at day 395 (end of temperature increase period)

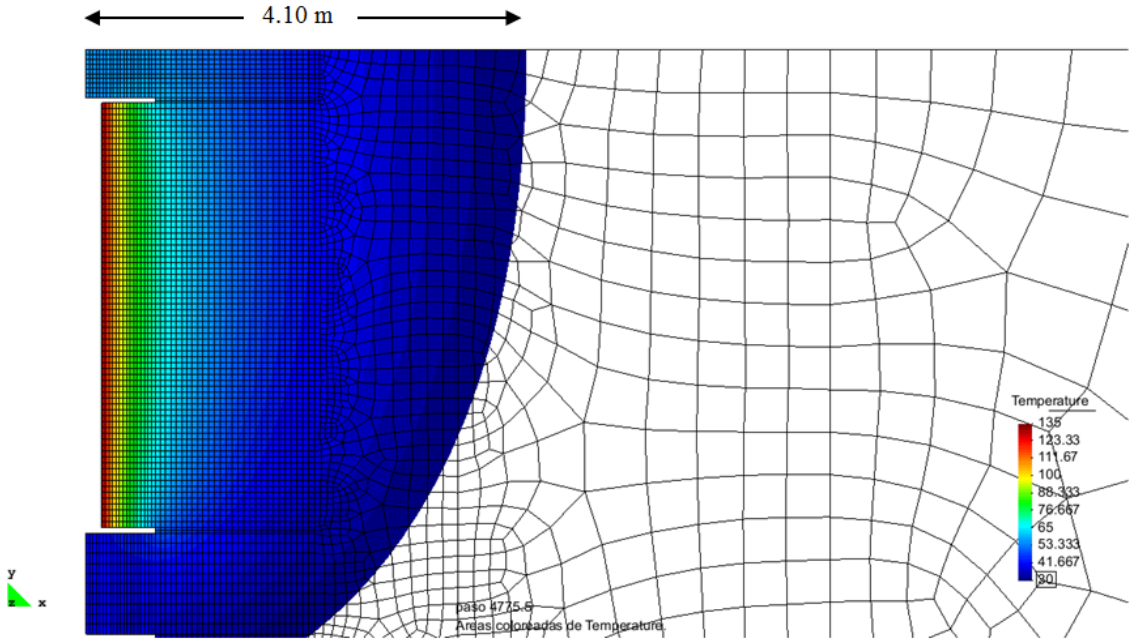

Figure 3.22 Equivalue lines of temperature at day 1125 (three years after starting the heating phase)

In Figure 3.23 some profiles of temperature along B3 are given at different times. As shown in Figure 3.16 these profiles are parallel to the tunnel axis in Opalinus Clay and close to the bentonite-rock interface. The vertical red dashed line represents a plane perpendicular to the microtunnel axis and passing through the heater centre. Line y=0 represents the upper boundary of the modelled geometry. As mentioned in section 3.1, this boundary is a symmetry plane for the problem considered in this work. We can observe that the maximum temperature increase at a selected time does not occur at the centre of the heater as we would expect in a single heater experiment. The maximum is slightly displaced towards the middle plane between the two heater. As a result, temperature differences between symmetrically opposited points with respect to the heater centre line can be significant. At the end of the temperature increase period (day 395) and for points at 2.5 m from the heater centre line this difference is about 13ºC.

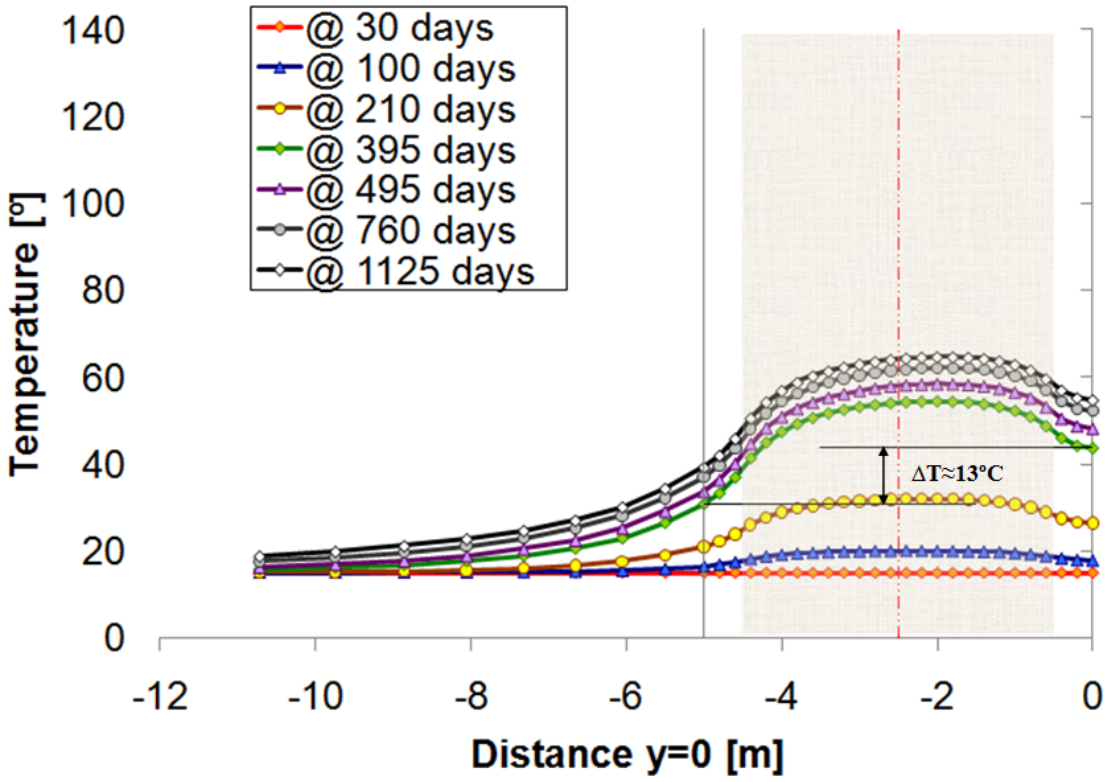

Figure 3.23 Predicted profiles of temperature at different times along B3

3.4.2 Evolution of the degree of saturation

The evolution of the degree of saturation in the bentonite and in the rock is depicted in Figure 3.24 and Figure 3.25, respectively. Initially, the degree of saturation is approximately 25% in the buffer material and 100% in the host rock. After buffer emplacement, the bentonite takes water up from the host rock. As a consequence, buffer material is wetted (increase of the degree of saturation) and host rock near the buffer is dried (decrease of the degree of saturation). In the first 100 days after heating start, the evolution of the degree of saturation seems not to be influenced by temperature changes. However, two temperature related processes do influence water uptake: thermal expansion of the liquid phase and of the pores and water phase changes (evaporation and condensation).

Aproximately 160 days after heating start, the temperature near the heater is high enough to produce significant evaporation. Evaporation is the conversion of water in the liquid phase into vapour (water in the gas phase) and as a consequence the degree of saturation (measure of the liquid water content in the pores) starts to decrease near the heater. As vapour production occurs in hot zones, a vapour gradient is settled between hot and relatively colder zones resulting in vapour transport by diffusion. Vapour condensates in the relatively colder zones and enhances saturation increase.

The constant and slow temperature increase at heater surface provided by heating strategy nr 2 allows for a better identification of these processes. The conjugated observation of temperature and degree of saturation in the buffer will allow us for determining the moment at which evaporation occurs. Once the target temperature is reached at the heater (second vertical red line), temperature at this location stops increasing. As a consequnce, the degree of saturation stops decreasing (no power supply for further water evaporation) and restarts increasing, because of advective water transport from Opalinus Clay.

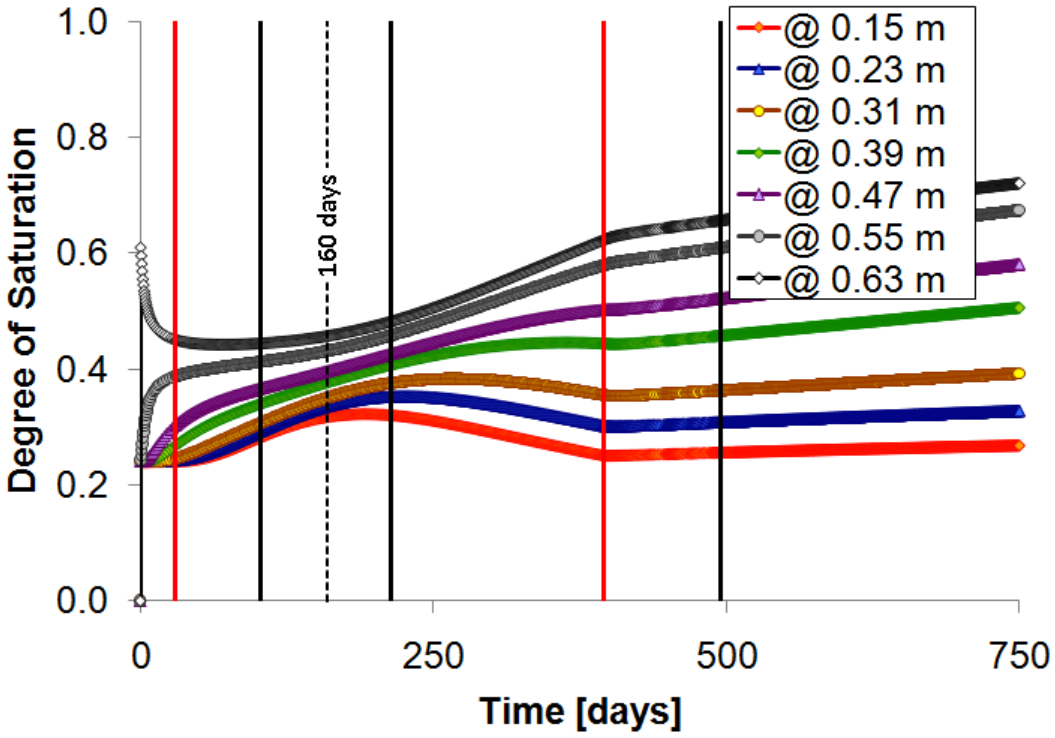

Figure 3.24 Predicted evolution of the degree of saturation in the bentonite barrier

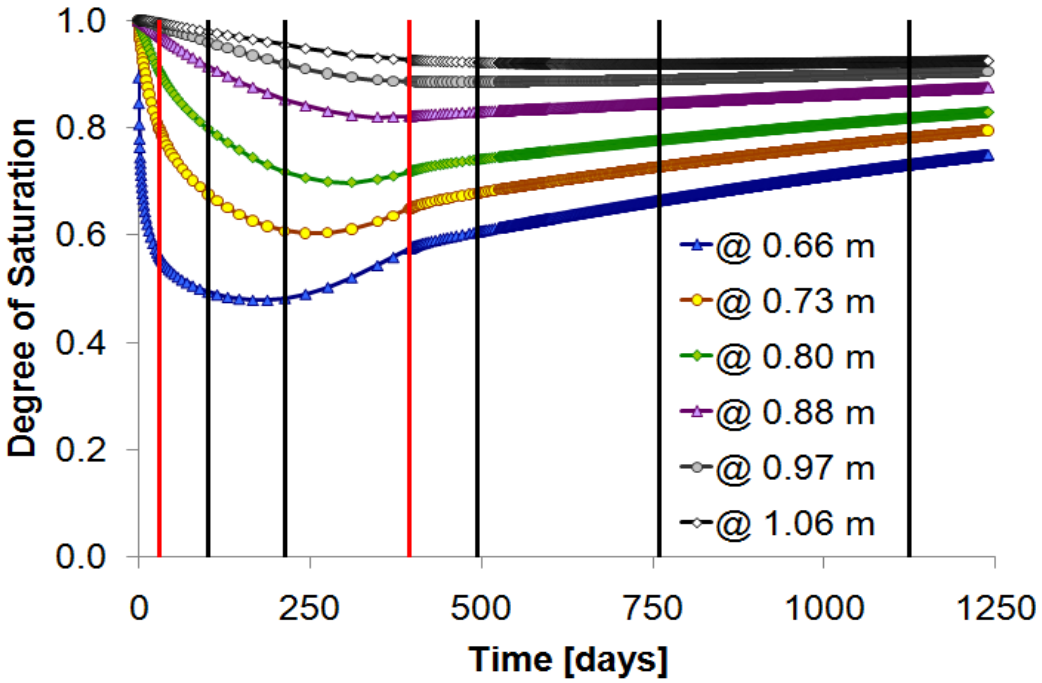

Figure 3.25 Predicted evolution of the degree of saturation in the first 40 cm of OC

Thermal expansion of the liquid phase induces a somewhat faster saturation of the buffer than in an isothermal case (Garitte and Gens, 2010), but its influence is rather limited. Effects of water phase changes instead are significant. In fact, evaporation and condensation are generating most of the saturation gradient in the buffer. This is illustrated in Figure 3.26, where the evolution of the degree of saturation close to the heater (at a distance of 0.15m from the axis of microtunnel) and near the buffer-rock interface (at 0.63m) are shown for two different simulations. In the base case (lines with symbols), water phase changes are allowed whereas in the second computation this process is neglected. When water phase change is not considered, the degree of saturation increases monotonely in the entire buffer. The only driving force is advective water transport from Opalinus Clay. Furthermore water saturation increase occurs faster in relatively colder zones when phase exchanges are allowed.

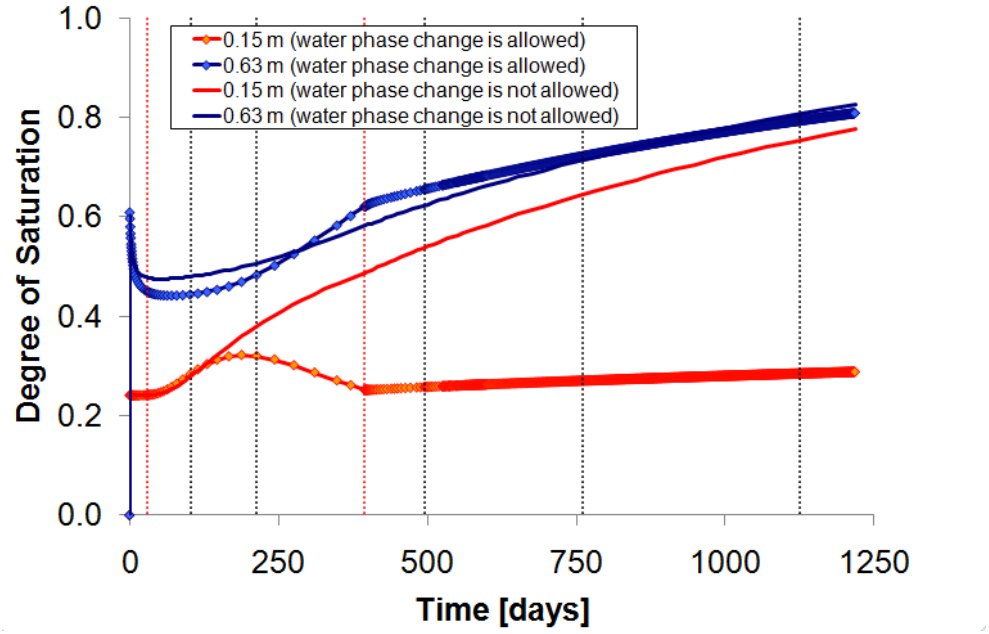

Figure 3.26 Predict evolution of the degree of saturation for the Base Case and for a case in which water phase change is not allowed (in the buffer material)

In Figure 3.27 profiles of degree of saturation are plotted at several times. A very high gradient in degree of saturated is observed in the first 10-20 cm inside Opalinus Clay (indicated by a grey background in this figure). Approximately three years after the heater is switched on, the desaturated zone around the heater extends up to 1.5 m from the microtunnel centre.

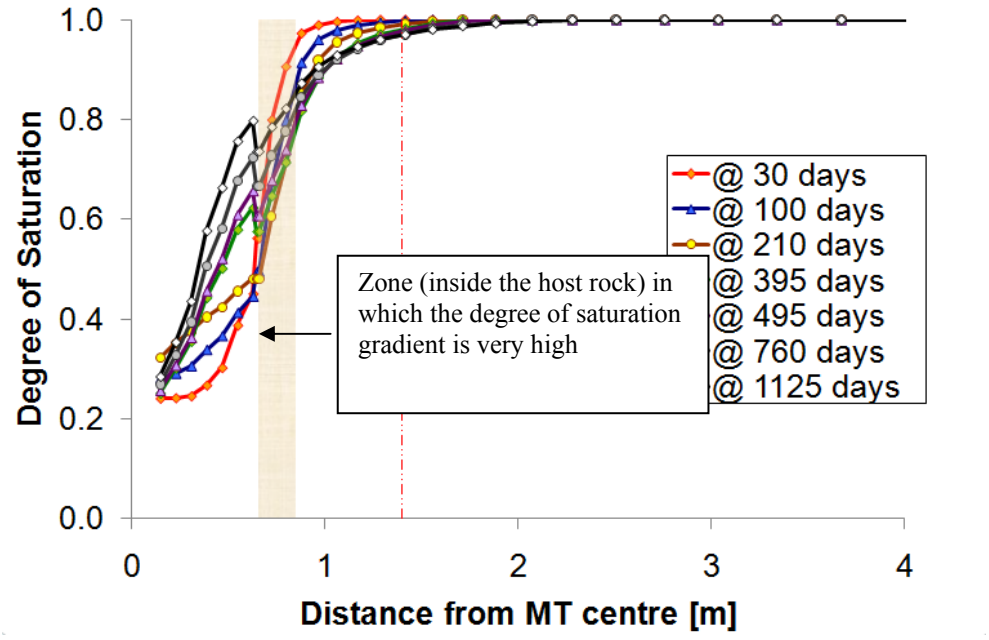

Figure 3.27 Predicted profiles of degree of saturation at different times along A1

In situ sensors measure the relative humidity which is an indirect measurement of the degree of saturation. Relative humidity is a measurement of the vapour concentration in the unsaturated part of the pores which may be related to the suction state of the liquid phase in the pores through Kelvin's law if equilibrium between water in liquid and gas phase is assumed. Suction and degree of saturation are correlated by mean of the so-called water retention curves calibrated in the laboratory.

The evolution of the relative humidity for several points in the bentonite barrier and in the host rock is depicted in Figure 3.28 and Figure 3.29, respectively. An estimation of relative humidity at different times along a radial profile (A1) is also given (Figure 3.30). Significant changes in relative humidity of Opalinus Clay extent up to a distance of about 20 cm inside the rock mass. Some recommendations are made on the basis of these figures and of the previous remarks:

- Relative humidity measurements should be concentrated in the unsaturated zones of the experiment- 1) in the buffer and 2) in the 10-20 first cm of Opalinus Clay (RH measurements in the VE showed that these sensors were reliable only for values smaller than 90-95%). For distances (from the microtunnel wall) greater than 50 cm relative humidity measurements may monitor constant RH values of 100%.
- The retention curve for Opalinus Clay is relatively well known but it should be characterized as well as possible for the buffer materials as it is the main unknown in the relationship degree of saturation – relative humidity. The importance of a correct reproduction of the degree of saturation is tremendous as all constitutive laws are built on the basis of this variable.

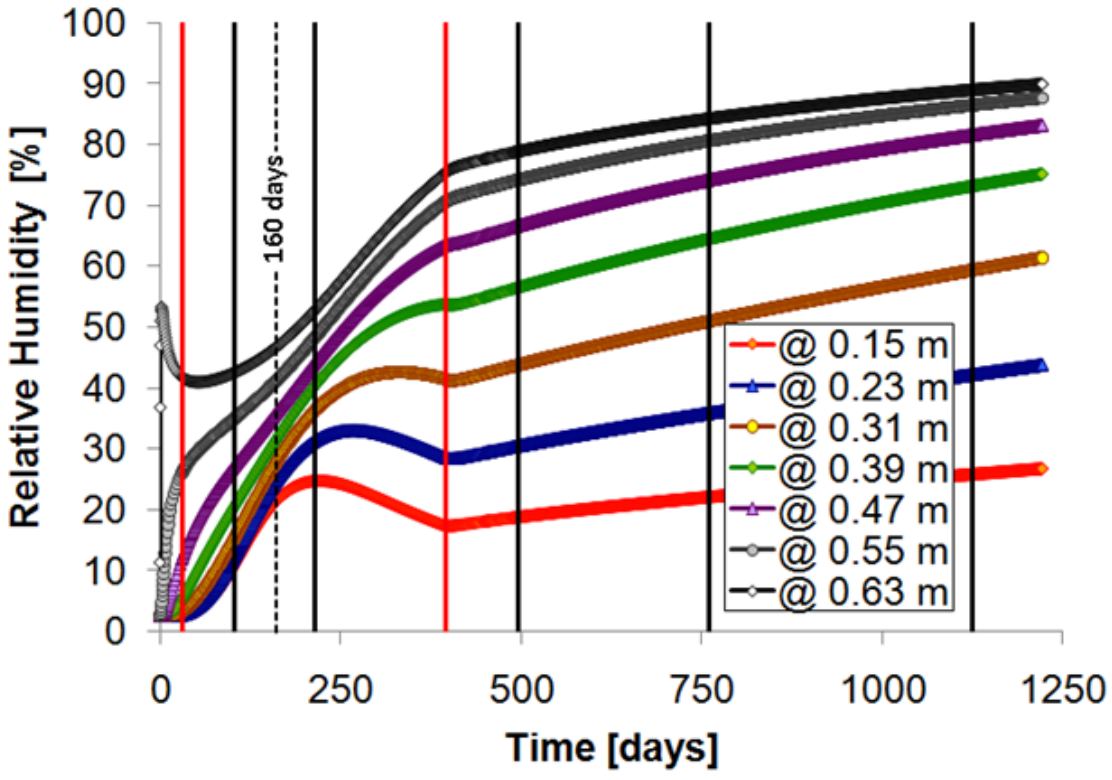

Figure 3.28 Predicted evolution of the Relative Humidity in the bentonite barrier.

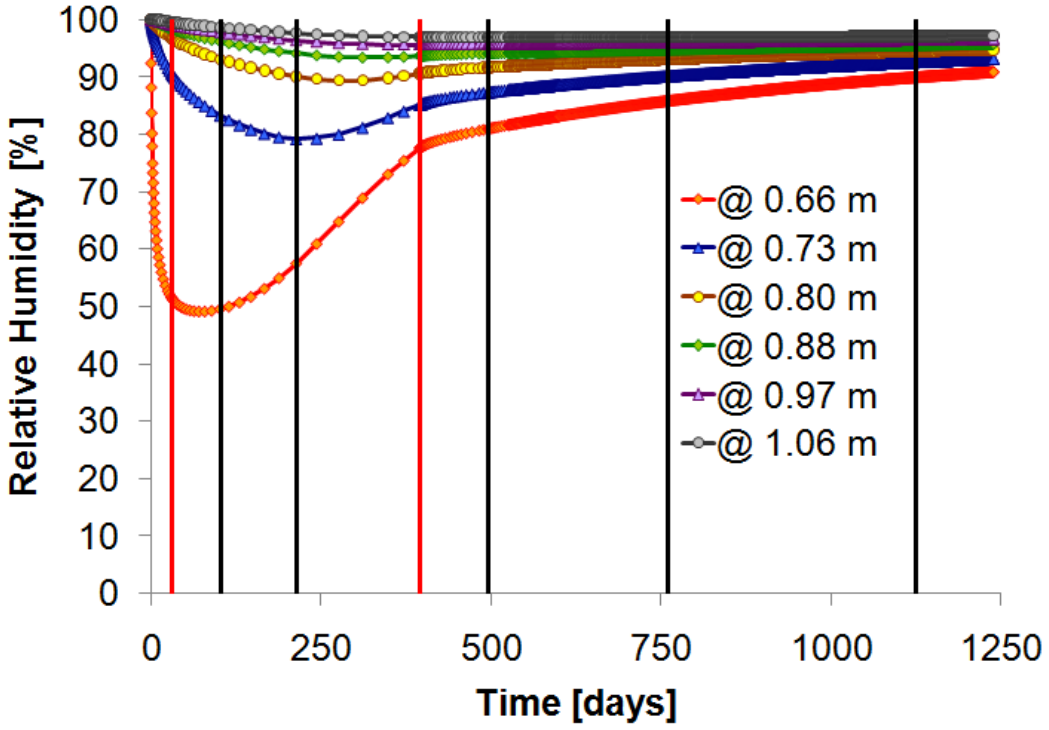

Figure 3.29 Predicted evolution of the Relative Humidity in the first 40 cm of OC

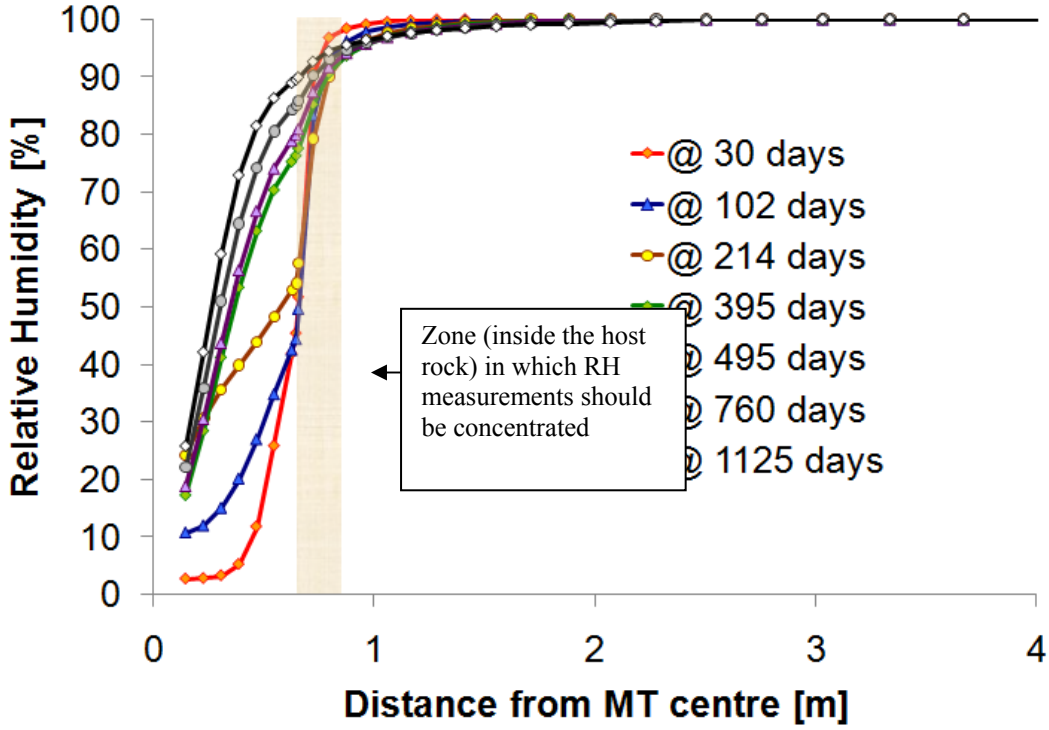

Figure 3.30 Predicted profiles of Relative Humidity at different times along A1.

3.4.3 Pore water pressure evolution

The predicted liquid pressure evolution until a distance of about 7.15 m from the microtunnel axis is given in Figure 3.31 and Figure 3.32. Three zones may be distinguished in the rock mass around the experiment:

1. From the previous section, we know that the predicted extent of the unsaturated zone reaches 1m to 1.5m from the tunnel centre depending on the time since bentonite emplacement. In the unsaturated zone, pore water pressure can not be measured as the liquid phase is in suction and installation of pore water pressure sensors here makes thus no sense.
2. Beyond the unsaturated zone, we will find a zone in suction but with values lower than the air entry value. According to the prediction, this zone is situated between 1 and 2m from the tunnel centre for experiment times smaller than 2 years and may grow to 2-3m after 4 years. In this zone, it makes sense to install pore water pressure sensors as it will allows us for detecting the suction limit (even if some pore water pressure sensors will not register any response).
3. Beyond the suction zone, we have zone in which the temperature increase will give rise to a pore water pressure increase that may be as large as 1MPa according to the prediction. Maximum absolute pore water pressure values of 3.1MPa are predicted. The extension of this zone was found to be between 2 and 10-15m. The maximum absolute pore pressure peak is located at about 7m from the axis centre.

Pore water pressure sensors should be concentrated in zone 2 and 3.

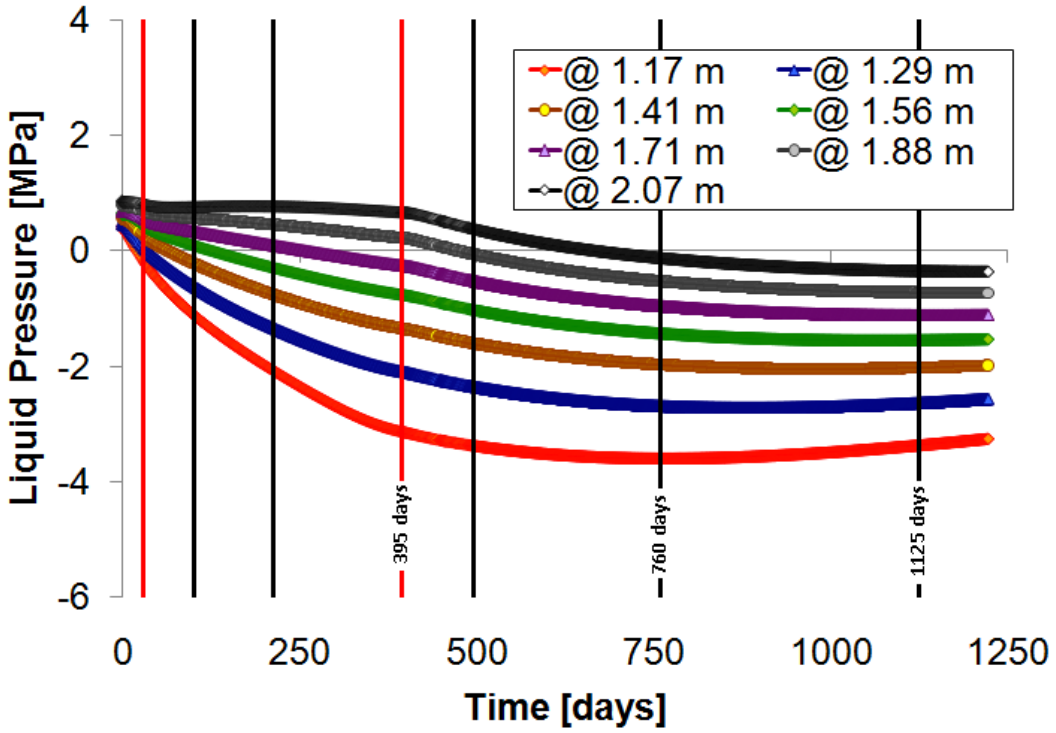

Figure 3.31 Predicted evolution of the liquid pressure between 50 and 150cm from the microtunnel wall.

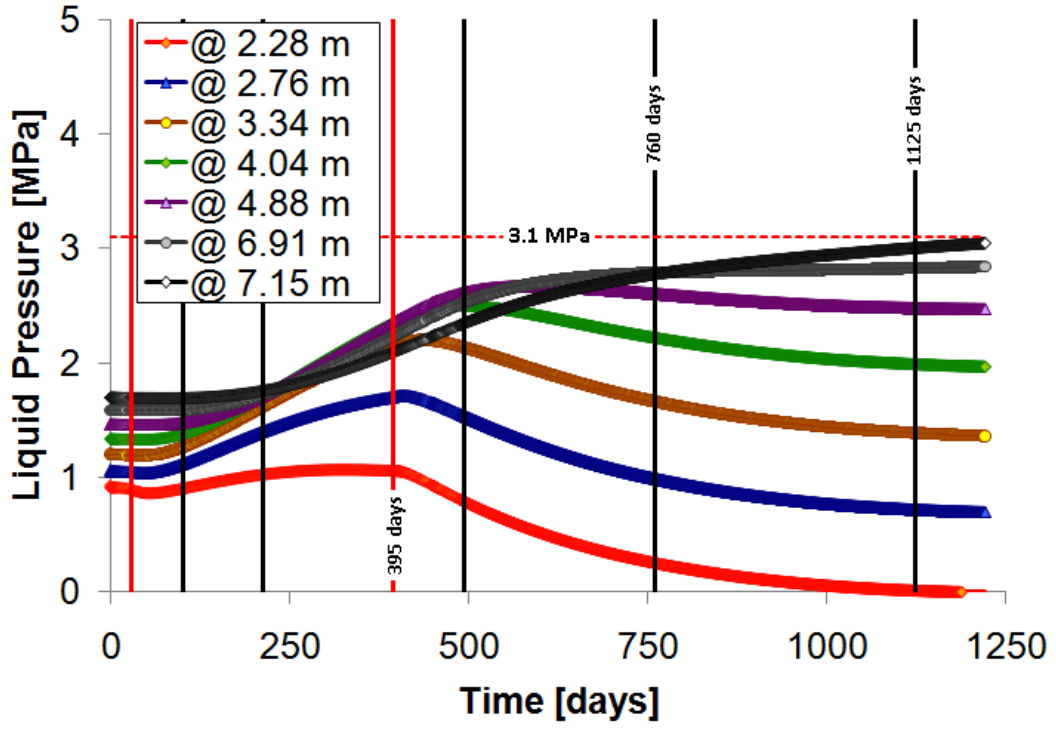

Figure 3.32 Predicted evolution of the liquid pressure between 150 and 750cm from the microtunnel wall.

These three zones can also be identified through some radial profiles of pore water pressure at selected times as indicated in Figure 3.33 (along A1) and Figure 3.34 (along A2). In these figures, "Zone 2" represents the rock volume between 1.40 m and 3.00 m (from microtunnel centre). Profile A2 corresponds to the upper boundary of the modelled geometry. We can see that pore water pressure peak is somewhat higher throughout A2 (Figure 3.34) when compared to the peak value obtained for A1 (Figure 3.33). At day 1125 the maximum absolute pore pressure peak is located at about 7-8 m from the axis centre. Maximum absolute pore water pressure values of 3.1MPa are predicted. Furthermore the water pressure peak moves toward the right side of the figures for increasing times.

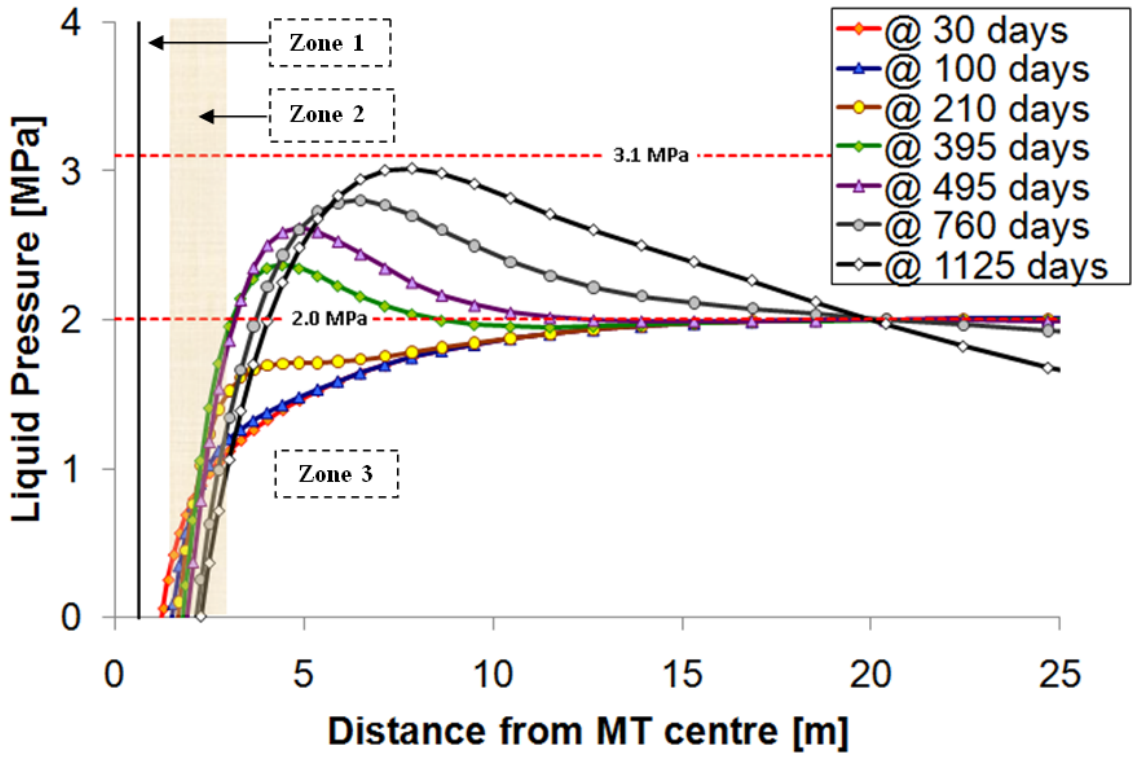

Figure 3.33 Predicted profiles of liquid pressure at different times along A1.

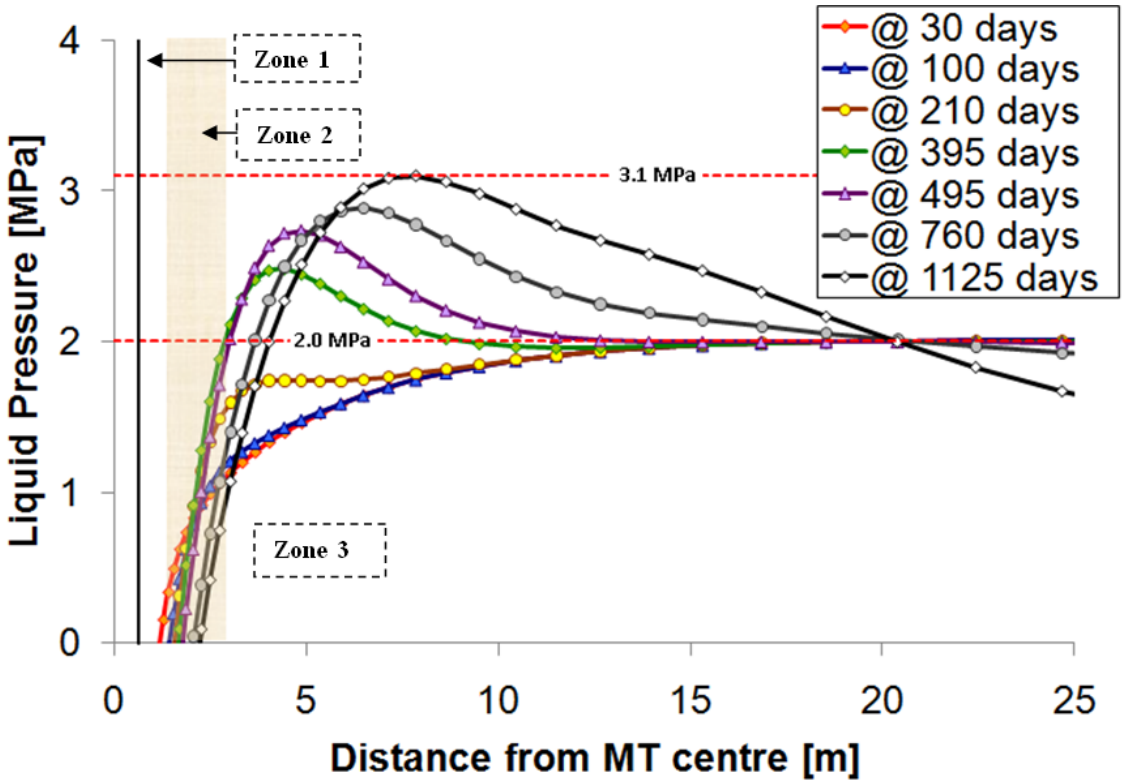

Figure 3.34 Predicted profiles of liquid pressure at different times along A2

Iso-pressure lines representing the liquid pressure distribution in Opalinus Clay at different times are shown in Figure 3.35 and Figure 3.36. Uncoloured zones stand for zones in suction. The remarks made previously about the displacement of the pore water pressure peak inside the rock can be noted clearly by these figures. Furthermore we can note that the rock volume in which liquid pressure increase is around or higher than 0.5 MPa (zone in dark red) grows over time.

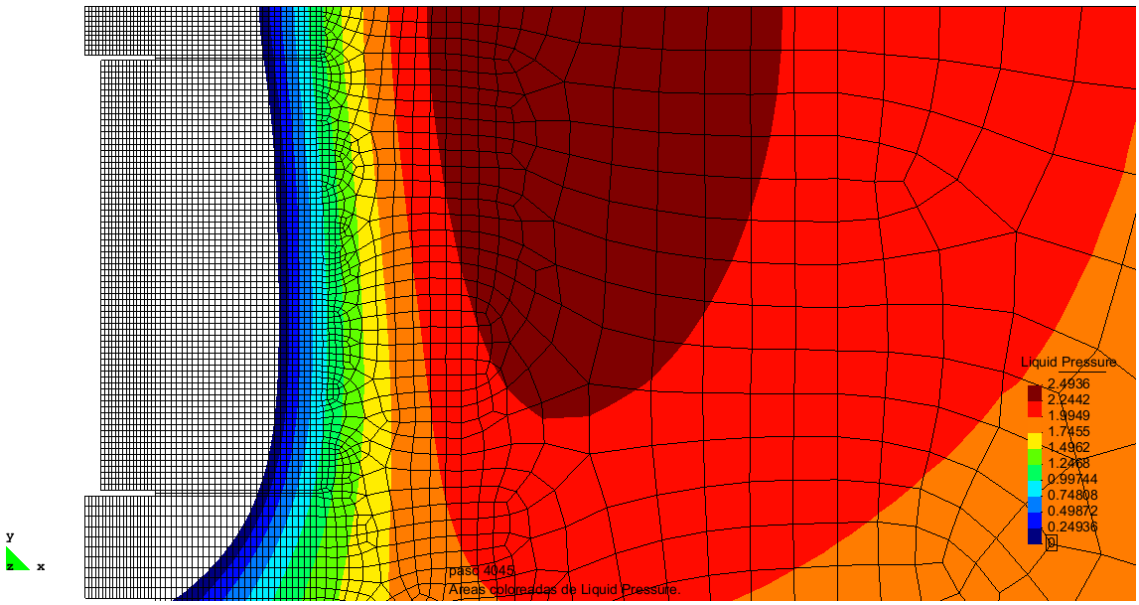

Figure 3.35 Equivalue lines of liquid pressure at day 395

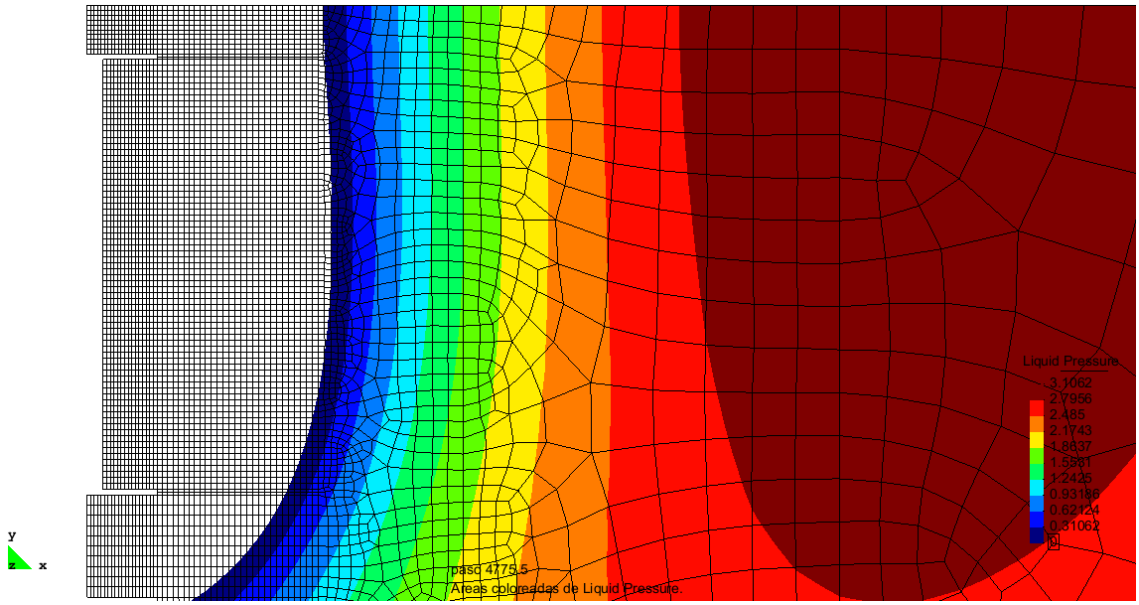

Figure 3.36 Equivalue lines of liquid pressure at day 1125

3.4.4 Results from the sensitivity analysis

The evolution of liquid pressure increment estimated from the additional runs (variants of the Base Case) is given in Figure 3.37. These results were obtained for a point located on the upper boundary of the modelled geometry at a distance of 5.0 m from the microtunnel axis. As mentioned previously this point belongs to a zone where maximum pore water pressure is expected (between the heaters). When compared to the Base Case,

- the pore water pressure increment is reduced by 70% if the solid grain thermal expansion, b_s, is not considered (Var/01);
- the increment is multiplied by 1.5 if the skeleton thermal expansion, β_s, is not considered (Var/02);
- the increment differs slightly for Var/03 in which both thermal expansion coefficients are not considered;
- the increment difference is also small for Var/04. Note that in Var/04, the thermal expansion of the skeleton and the solid grain thermal expansion are doubled when compared to the corresponding values of the Base Case.
- A multiplication of the rigidity of the solid skeleton by 10 (Var/05) has an important effect on the pore water pressure increase. Var/05 in which we consider a negligible skeleton compressibility is the equivalent of what would be obtained in a TH computation.

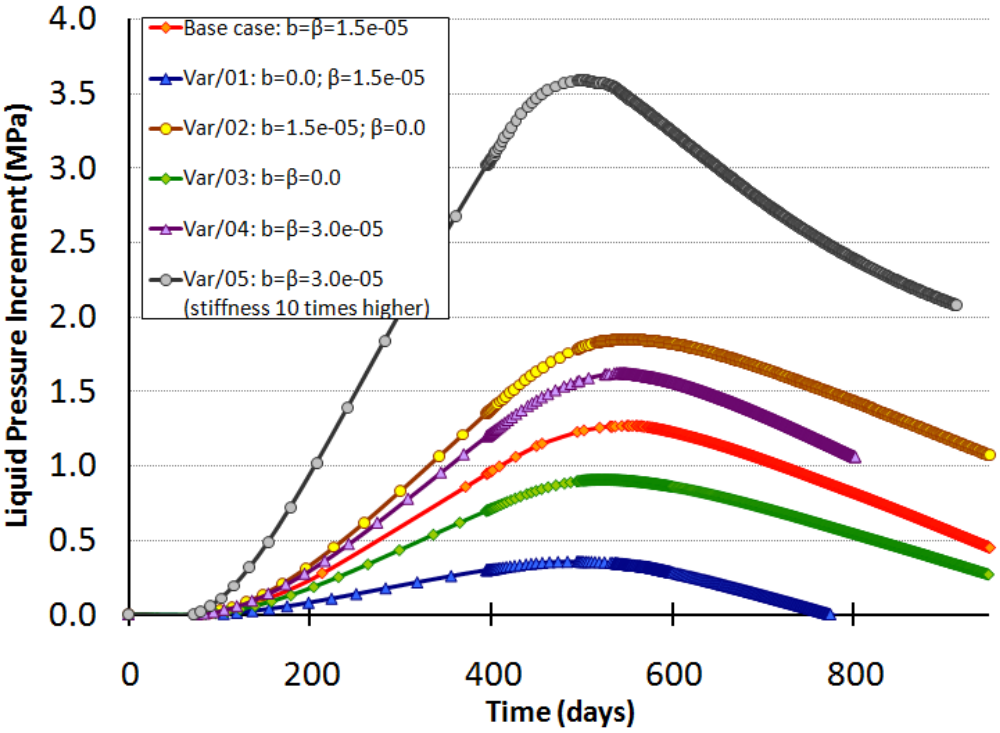

Figure 3.37 Influence of thermal expansion parameters on the pore water pressure increment at 5m (on the upper boundary) from the heater axis (in the legend, b stands for thermal expansion of the grain and β for thermal expansion of the skeleton)

The influence of the thermal expansion of the solid grain, of the solid skeleton and the skeleton compressibility is further illustrated in Figure 3.38 in which the pore water pressure increment generated by heating was plotted for the different computations. To explain the differences between the computations we should keep in mind that when temperature increases:

- thermal expansion of the solid grain is equivalent to a structure rearrangement in which the solid grains are not moving relative to each other but they expand
- thermal expansion of the skeleton is equivalent to a structure rearrangement in which the solid grains are moving relative to each other to increase the pore space

- in the range of the experiment, thermal expansion of the solid grain and of the skeleton should be taken equal for Opalinus Clay because no irreversible deformations are thought to take place (Booker and Savvidou, 1985)

The red dot representing the base case is thus the most likely prediction. If the thermal expansion of the skeleton is set to 0 (blue dot), the pore water pressure peak increases as temperature increases do not induce pore volume increase directly. If the thermal expansion of the solid grain is set to 0, the pore water pressure peak is much lower (red open dot). In this case, the maximum pore water pressure increase is 0.4MPa. If both, the thermal expansion of the solid grain and of the skeleton are set to 0 (blue open dot) the pore water pressure increment is lower than in the base case. Note that this case is equivalent to a porous medium that does not have any structure rearrangement induced by temperature changes. For constant thermal expansion of the skeleton, we observe a linear relationship between pore water pressure increment and linear thermal expansion of the grain. The slope of this linear relationship is the same for different values of the thermal expansion of the skeleton.

Changes of equal thermal expansion coefficients (black line through the open blue dot, the red dot and the yellow diamond dot) also provide a linear relationship with the pressure increment. It should be stressed that the influence of a change of equal thermal expansion coefficients, is much less than taking not equal thermal expansion coefficients. Note that for a thermal expansion coefficient value of the skeleton of $3E\text{-}5K^{-1}$ in combination with a null thermal expansion coefficient for the solid grain, no pore water pressure would be generated at 5m during heating (red dotted line). The pore water pressure increment increases drastically when a high rigidity is considered.

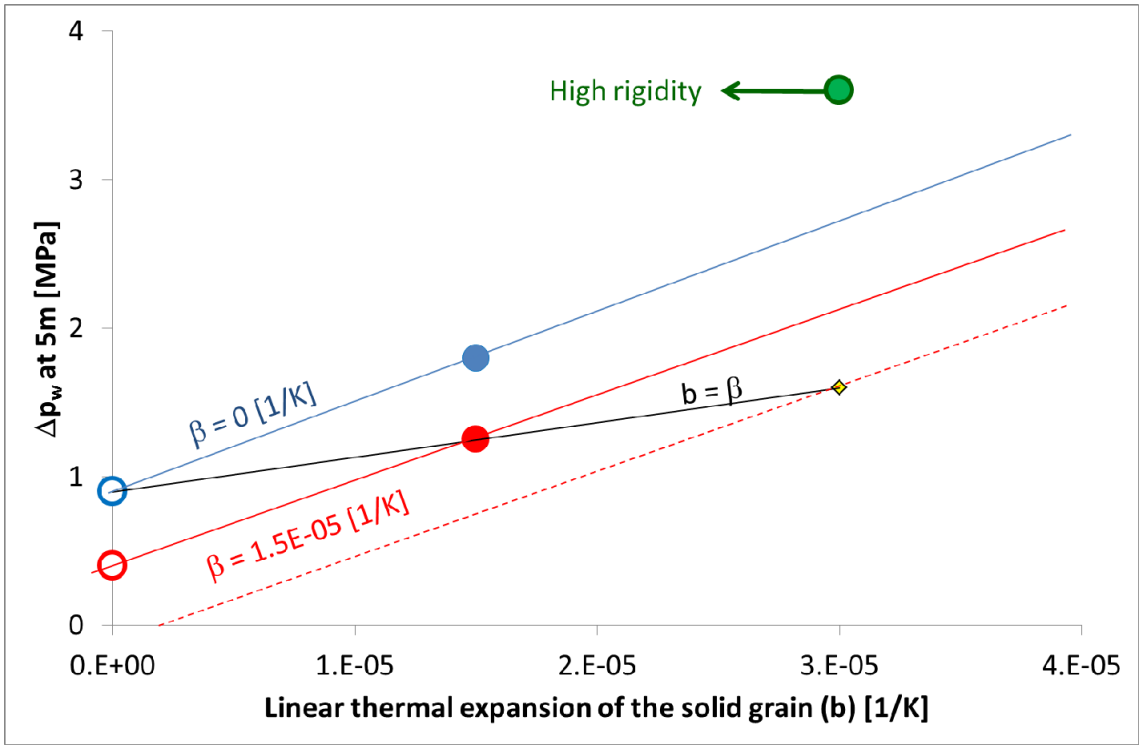

Figure 3.38 Predicted pore water pressure increase in function of the linear thermal expansion coefficient of the solid grain

The results from Var/06 in which a suction of 25 MPa is applied at tunnel wall are compared to the base case in Figure 3.39 and Figure 3.40. Radial profiles of pore water pressure and degree of saturation are presented. The empty symbols correspond to the results from the Base Case. In Var/06, the extension of the suction zone at the start of the HE-E experiment is much larger. During heating, pore water pressure increases but not as high as to generate a peak higher than the initial pore water pressure (2MPa). The important difference between the two cases is mainly due to the fact that in Var/06, pores are unsaturated (up to three metres) and have to be saturated (mostly by the volume expansion of water induced by temperature increase), before water pressure starts to increase.

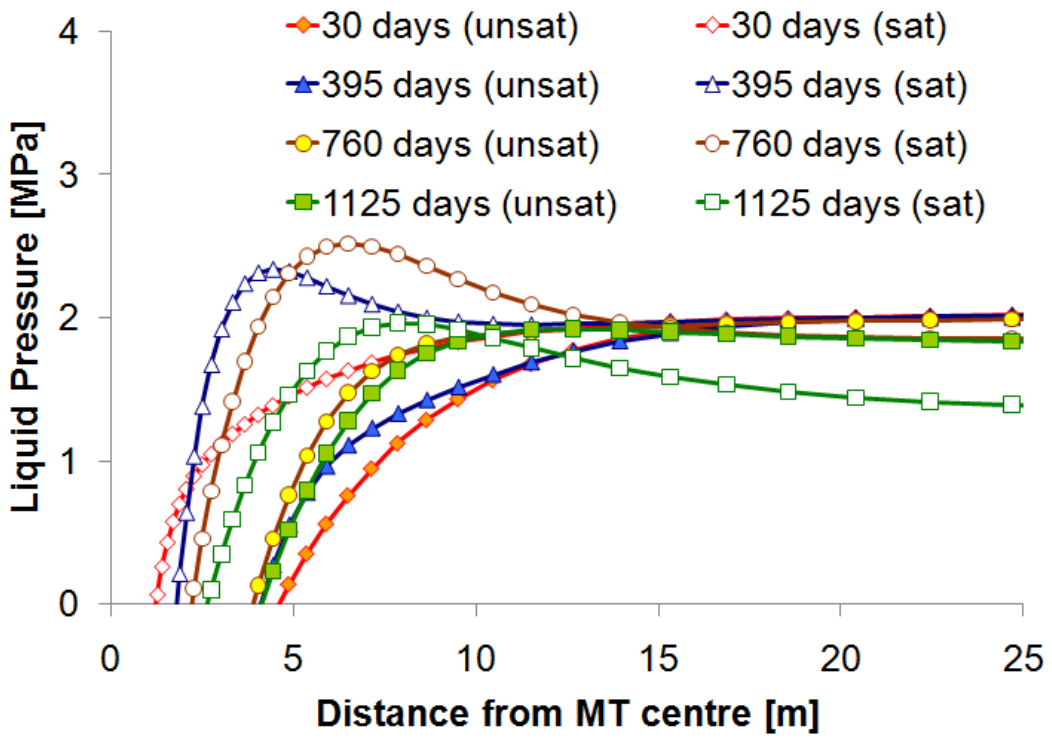

Figure 3.39 Predicted profiles (along A1) of liquid pressure for the Base Case (sat) and for Var/06 (unsat).

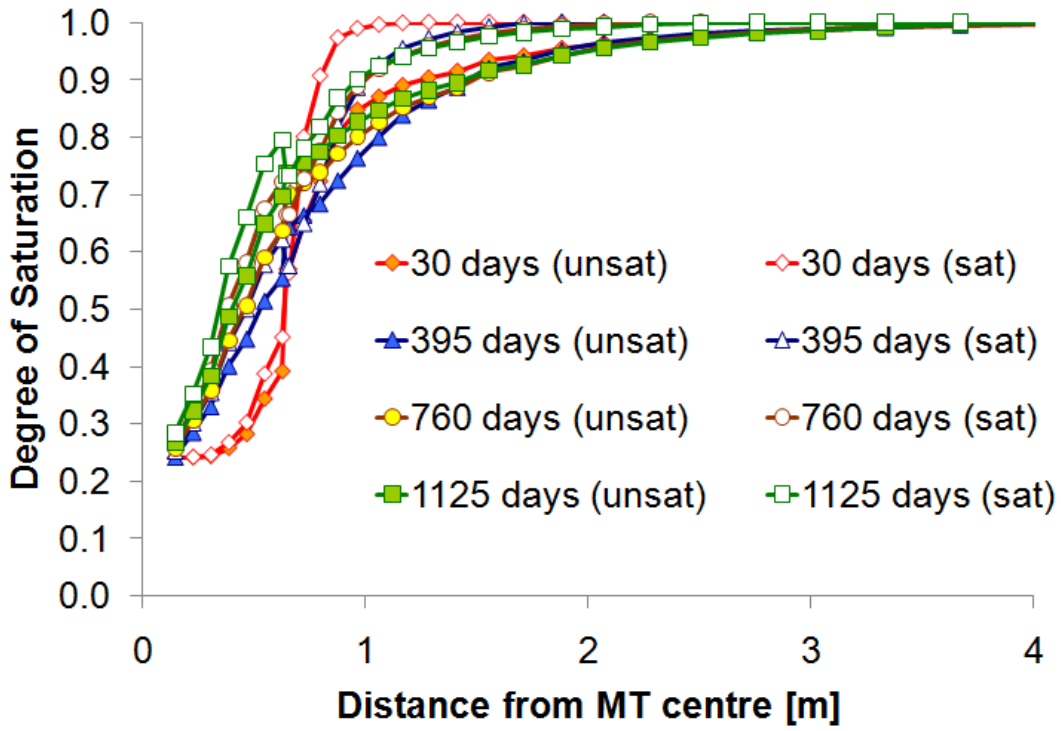

Figure 3.40 Predicted profiles (along A1) of degree of saturation for the Base Case (sat) and for Var/06 (unsat)

Conclusions and discussion

In this report, the results and experience gained from the THM scoping calculations run for the design of the HE-E experiment are summarized. According to the simulations and the adopted parameters, we found that:

- After three years, the rock volume undergoing a temperature increment larger than 15ºC reaches about 4m from the tunnel axis.
- Each of the heaters should provide a power of about 1200W in order to maintain a constant temperature of 135ºC at heater-bentonite interface.
- After three years, the saturation degree in the buffer is expected to vary between 25% (near the heater) and 70% (near the rock). The key process generating this high saturation gradient was shown to be the evaporation of liquid water near the heater and transport of vapour through diffusion from the heater towards colder zones.
- The desaturation front advances in the rock mass up to 1.5m from the tunnel centre after three years.
- The suction front lies at about 2m before the start of the HE-E experiment and advances up to 3m during the first three heating years.
- In the positive water pressure zone, increase of pore water pressure induced by heating is expected. After three years, the predicted pore water pressure increase reaches over 1MPa above the initial pressure state (2MPa) at about 7m from the tunnel axis.

- The water pressure state prior to the HE-E experiment is not well reproduced by the current simulations. Taking gallery 1998 into account would probably provide a better match between measured and simulated pore water pressure.
- An increase of water permeability in the EDZ was evaluated to be unnecessary due to the small extension of the EDZ.

All advices are given on the basis of numerical models which are in essence an imperfect way to reproduce reality. Quantities given (as time and distances) are thus merely indicative. In general, common sense and experience are as important (or even more) than the modelling results. Some important general features of an in situ instrumentation system are:

- Redundancy of the system, geometrically as well as conjugated variables, as power and temperature for instance (allows for checking the behaviour of the sensors).
- Implementation of the system to track anisotropic features (presence of bedding plane) and the difference between the experiment side at which gallery 1998 is located.

Before conducting the experiment, it is may be of interest to determine:

- The in situ permeability as a function of the distance to the microtunnel wall to confirm its negligible influence on the results;
- The saturation state of rock as function of distance to microtunnel wall as this has a non-negligible influence on results.

It is recommended to use power control instead of temperature control in a first step of the heating phase because:

- (from experience in previous projects) In this case, we then know exactly what is injected. In case, we apply and control temperature, the experimental setup is much more difficult and errors are to be expected.
- The temperature sensors readings in the bentonite and the rock mass may improve our understanding of the condensation and evaporation processes.
- The pattern of temperature variation in the bentonite buffer would allow for better characterizing the thermal conductivity of the buffer. In case the temperature is prescribed, the temperature field dependency on the thermal conductivity is much less than in a power controlled configuration.

A long period of temperature increase at the start of the experiment as implemented in the HE-E experiment (longer than in the case of the FEBEX experiment for instance) is interesting to obtain a better determination of the moment at which the peak in degree of saturation near the heater is reached. A linear increase in heating (Heating Strategy 2) rather than a stepwise increase is also preferred from a modelling point of view.

4 Scoping calculations using CODE_BRIGHT (GRS)

The main objectives of the GRS calculations were to get a feeling about pore water pressure changes to be expected in the rock mass near the microtunnel, because the installation of additional micro piezometers is planned.

Regarding the tight coupling between fluid flow processes and mechanical deformation in argillaceous rock mass a simplified approach of the argillite model was used (plane strain hypothesis), taking into account anisotropic hydraulic response as well as the anisotropic primary stress field without any damaging process.

4.1 Recommendations regarding the location of the temperature sensors

The heating period will be started in April 2011 from the initial rock temperature of 14°C following the proposed second heating strategy with a gradual temperature increase to reach 135°C after 1 year and then having a constant temperature of 135°C at the heater surface for the following 4 years.

Figure 4.1 shows calculation results on temperature evolution as a result of thermo-hydro-mechanical coupled numerical simulation. The temperature value marked in red presents the heater surface and the adherence of the boundary conditions. The calculated temperature values at the HE-E contour zone and in 20 cm distance to the gallery contour inside the clay rock mass (marked in green and yellow colour) are around T = 40 – 45°C after 1 year.

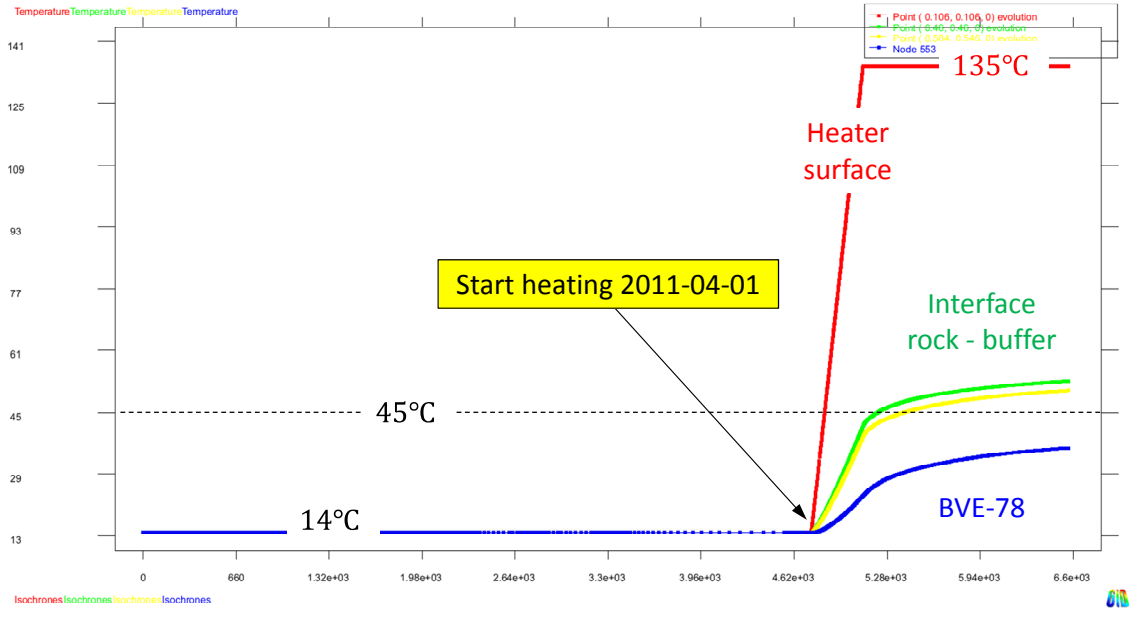

Figure 4.1 Calculation results on temperature evolution with time as a result of THM-coupled numerical simulation (green = HE-E contour zone, yellow = 20 cm from contour, red = heater surface)

On April 1st, 2016 the temperature evolution in the clay rock mass near the BVE micro piezometers is predicted to have reached values of 35°C, whereas the temperature at the HE-E

gallery contour will be about 54°C, Figure 4.2. The calculation results on temperature distribution in the host rock as well as in the buffer material as a result of THM-coupled numerical simulation after different times (0a/1a/5a) of heating in a horizontal intersection are shown in Figure 4.3.

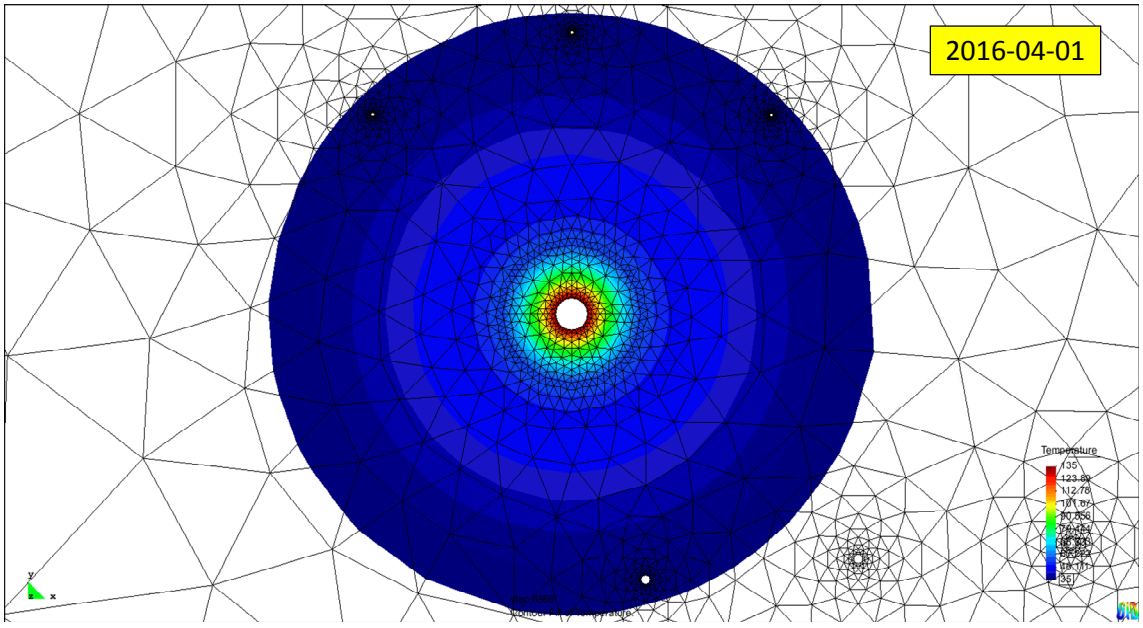

Figure 4.2 Calculation results on temperature evolution after 5 years of heating as a result of THM-coupled numerical simulation (T > 35°C), temperature at HE-E contour zone is about 54°C

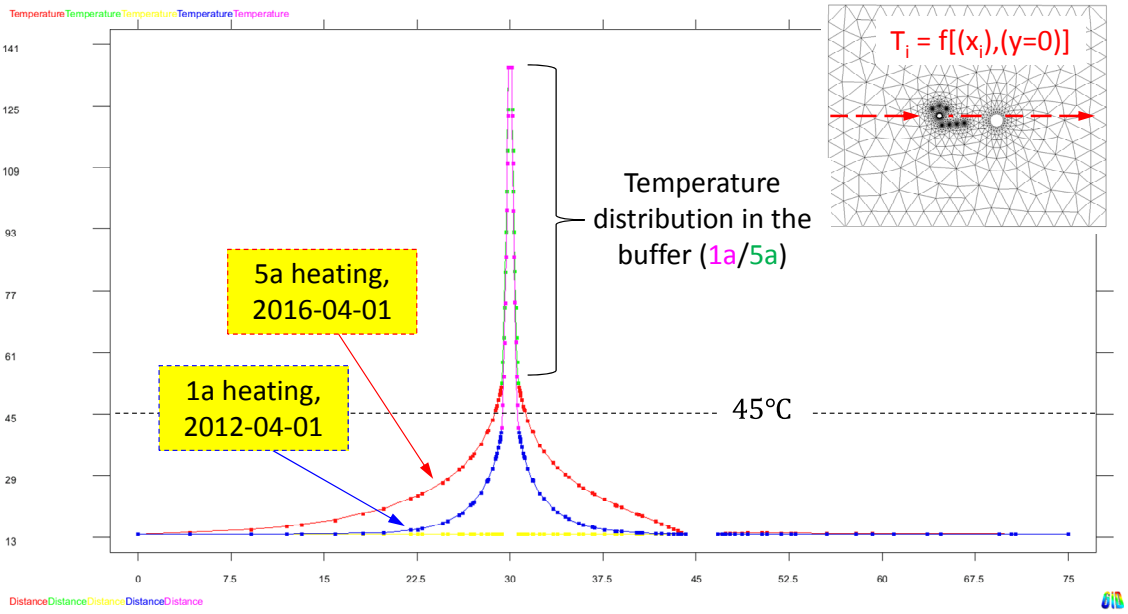

Figure 4.3 Calculation results on temperature evolution in a horizontal intersection as a result of THM-coupled numerical simulation

The usage of a 2-dimensional plane strain model for a coupled THM simulation implies that the temperature evolution is overestimated in the rock mass. However, the calculation results show values of about 42°C at the HE-E gallery contour after linear increase of heating within the first year. After 4 years of constant heating the temperature evolution in the clay rock mass near the BVE micro piezometers will have reached values of 35°C, whereas the temperature at the HE-E gallery contour will be about 54°C.

4.2 Recommendations regarding the location of the pore pressure sensors

On April 1st, 2011 all the installation work is assumed to be finished and the microtunnel will have been prepared to start heating. Figure 4.4 gives an impression on the calculated pore pressure values for the selected mini piezometers BVE-55/ -62/ -78 (marked in red, green and yellow).

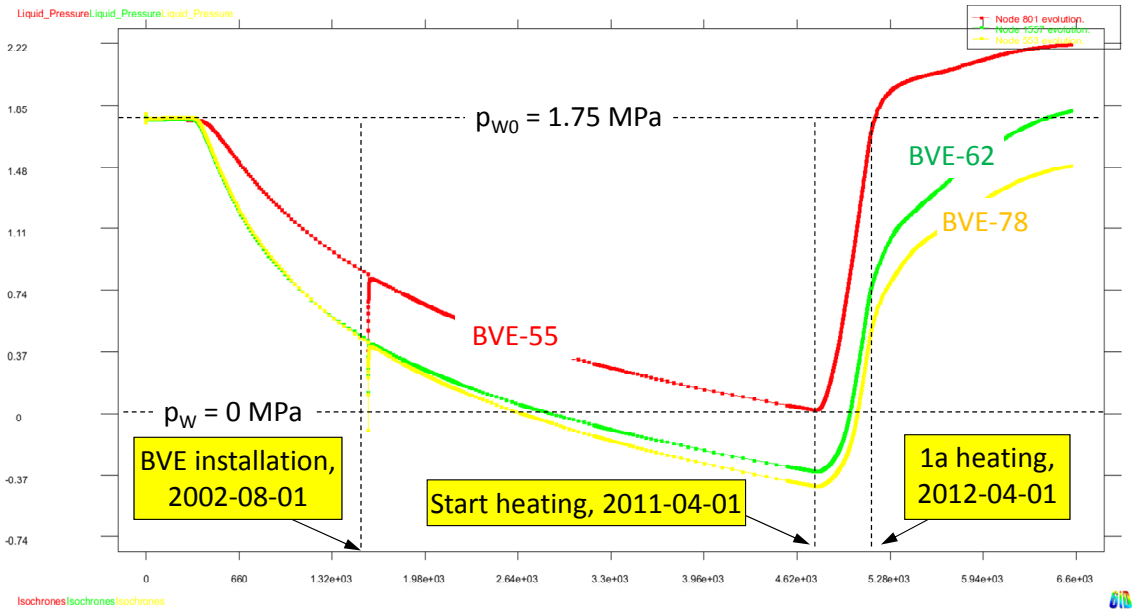

Figure 4.4 Calculation results on pore water pressure evolution with time as a result of THM-coupled numerical simulation for the selected BVE micro piezometers

It can be taken from the figure that the pore pressure recovery process around the BVE mini piezometer is still active and the recording values of pore water pressure are around atmospheric pressure before heating.

As a result the increase in temperature within the first year leads to a pronounced increase of pore water pressure in the range of $p_W = 0.5 – 0.8$ MP for the mini piezometer BVE-62 and BVE-78. The pore water pressure sensor of BVE-55 shows even higher values up to the initial pore water pressure value of $p_{W0} = 1.75$ MPa. During the second heating period of 4 years when the temperature at heater surface is kept constant the pore water pressure values show an on-going increasing tendency but with reduced pressure rates.

Figure 4.5 and Figure 4.6 show calculation results on pore water pressure distribution as a result of thermo-hydro-mechanical coupled numerical simulation at different heating periods: (a) Initial p_W conditions before heating, (b) p_W distribution after increasing temperature up to 135°C during the first year and (c) p_W distribution after 4 years of constant temperature.

In order to investigate the influence of the Gallery'98 on pore water pressure distribution, the gallery excavation is neglected in a second simulation case and the results on pore pressure distribution are shown and compared to the original case.

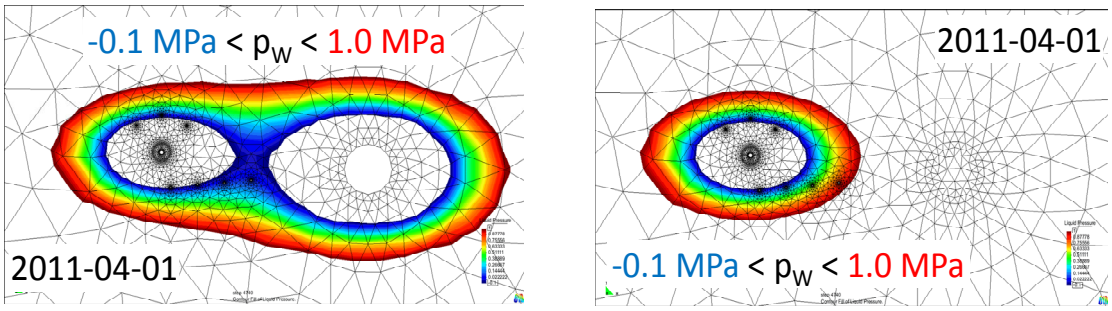

(a) Initial p_W conditions before heating (*right*: Ga98 neglected)

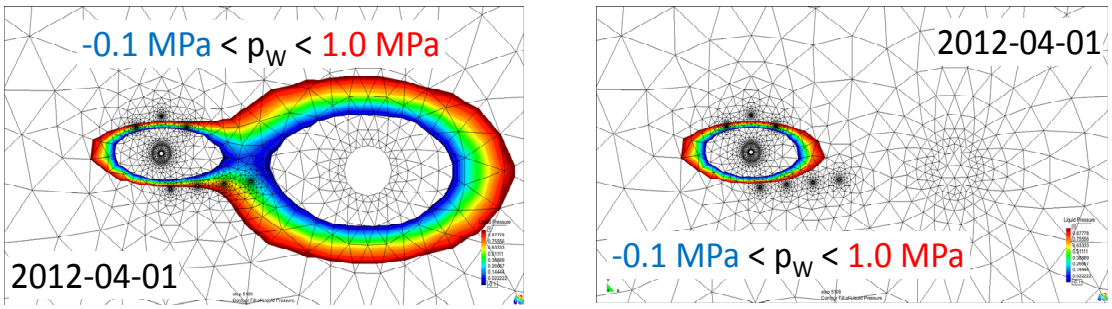

(b) p_W distribution after increasing temperature up to 135°C during 1a (*right*: Ga98 neglected)

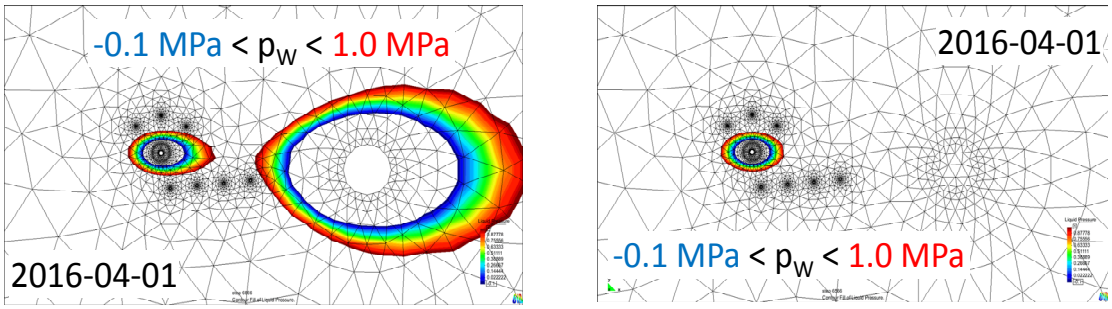

(c) p_W distribution after 4a of constant temperature (*right*: Ga98 neglected)

Figure 4.5 Calculation results on pore pressure distribution as a result of THM-coupled numerical simulation (P_{atmos} < P_W < 1.0 MPa)

While the presence of the Gallery'98 does not influence the simulated pore pressure evolution in the BVE mini piezometers before the first heating period (Fig. 4.5-a), the consideration of the drift excavated in 1998 plays an important role on the pore water pressure evolution during increasing temperature both below (Fig. 4.5-b,c) and above (Fig. 4.6-b,c) the primary pore pressure. No overpressure is simulated before heating hence case (a) has been removed from Fig. 4.6.

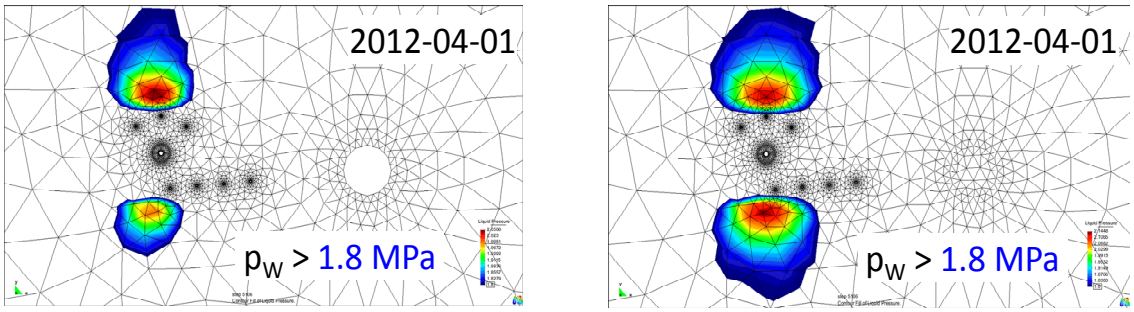

(b) p_W distribution after increasing temperature up to 135°C during 1a (*right*: Ga98 neglected)

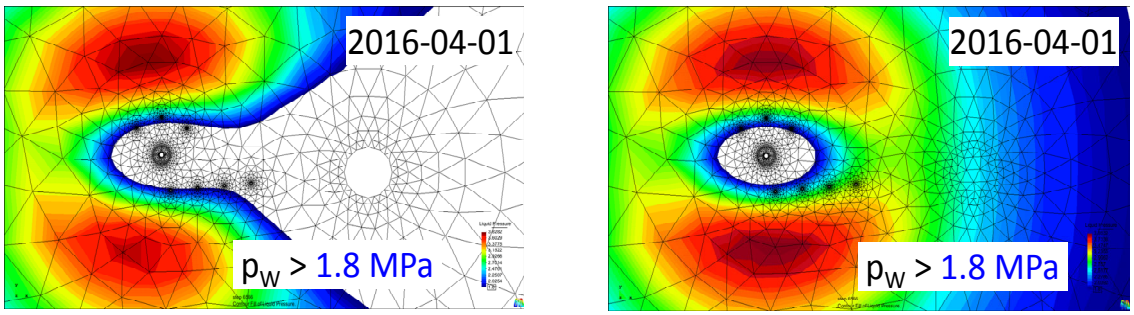

(c) p_W distribution after 4a of constant temperature (*right*: Ga98 neglected)

Figure 4.6 Calculation results on pore pressure distribution as a result of THM-coupled numerical simulation (P_W > 1.8 MPa)

It can be taken from the figures, that the temperature evolution around the HE-E test gallery caused re-saturation in the rock mass that reduces the de-saturated rock zone to a radial extent around the gallery of 1 m in maximum, with an ellipsoid shape due to the anisotropic hydraulic conductivity. The consideration of Gallery'98 influences the distribution of the pore water overpressures and therefore the final layout of the additional sensors, but not the calculated maximum value, which is supposed to be around 4.0 MPa.

4.3 Recommendations regarding the location of the relative humidity sensors

The following figures will be targeted to show the difference in state of saturation for the buffer material and the surrounding rock mass though they are subjected to identical boundary conditions. Figure 4.7 shows calculation results on pore water pressure evolution with time as a result of THM-coupled numerical simulation for the buffer-rock interface marked in red colour and for a zone 20 cm from contour inside the rock. It can be taken from the figure that the rock zone is influenced by the hydraulic boundary condition for the non-heating pre-experimental phase, that is set to a negative pore water pressure of p_W = -5.0 MPa at the interface.

Due to numerical stability the buffer material is emplaced together with the excavation of the micro tunnel and the hydro-mechanical interaction to the rock contour zone is superposed by the given boundary condition.

The hydraulic boundary condition is highlighted in the water retention curves of the Opalinus clay and the buffer material in Figure 4.8. It can be taken from the figure that the application of different retention curves together with an identical hydraulic boundary condition leads to a different state in saturation in the order of $S_r = 60$ % at the buffer interface and about $S_r = 95$ % inside the contour near rock zone, Figure 4.9.

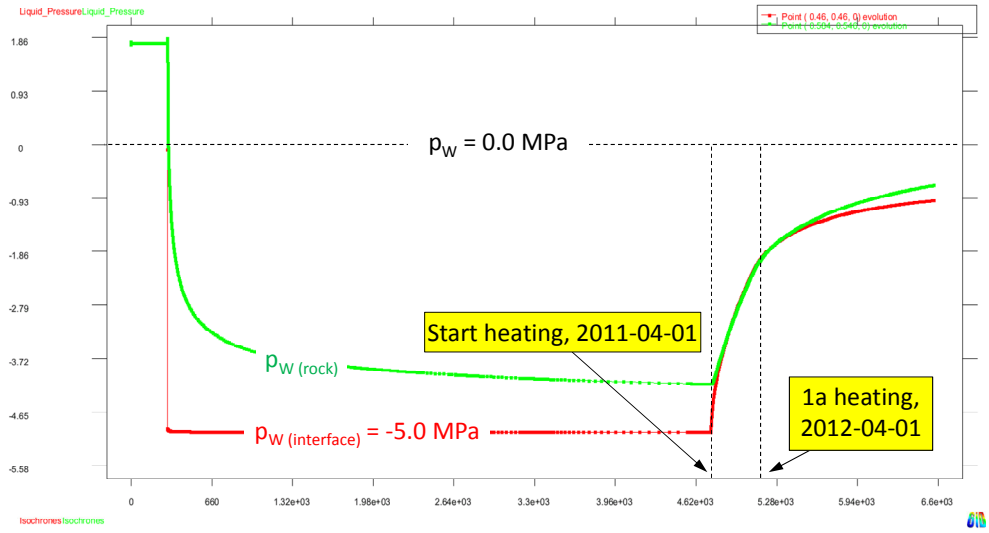

Figure 4.7 Calculation results on pore water pressure evolution with time as a result of THM-coupled numerical simulation (red = interface, green = 20 cm from contour inside rock)

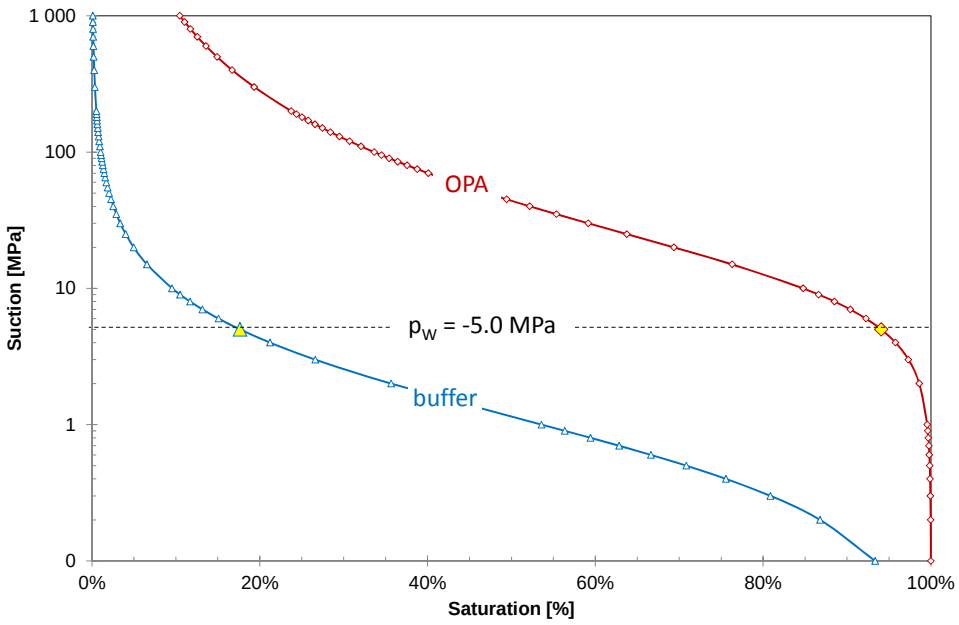

Figure 4.8 Water retention curve of the Opalinus clay and the buffer material, highlighting the boundary condition at the interface between rock and buffer material during the non heating pre-experimental phase

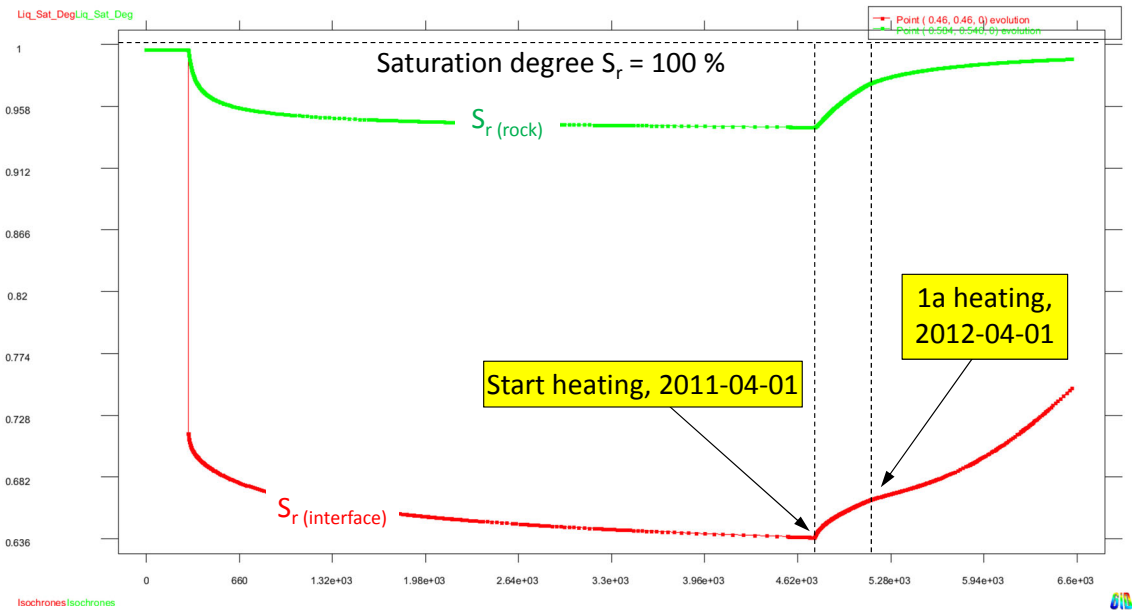

Figure 4.9 Calculation results on the evolution of saturation with time as a result of THM-coupled numerical simulation (red = interface, green = 20 cm from contour inside rock)

Due to the reduced range of desaturation in the rock mass with a radial extent around the gallery of not more than 1 m and the expected pore pressure increase it is recommended to arrange the relative humidity sensors in the bentonite buffer as well as in the first few centimetres of the rock mass up to a maximum distance of about 1 m.

4.4 Overall recommendations

In a first approach, a 2-dimensional plane strain model was used for a coupled THM simulation. It is understood that the temperature evolution is overestimated in the rock mass. This simplification, however, enabled us to consider a rather realistic initial pore water pressure distribution in the scoping calculations, which incorporates also the available measurement results of the recording VE piezometers.

However, the calculation results show values of about 42°C at the HE-E gallery contour after linear increase of heating within the first year. After 4 years of constant heating the temperature evolution in the clay rock mass near the BVE micro piezometers will have reached values of 35°C, whereas the temperature at the HE-E gallery contour will be about 54°C.

It is expected that the temperature evolution around the HE-E test gallery will cause re-saturation in the rock mass that reduces the de-saturated rock zone to a radial extend around the gallery of 1 m in maximum with an ellipsoid shape due to the anisotropic hydraulic conductivity. The consideration of Gallery'98 influences the distribution of the pore water over pressures and therefore the final layout of the additional sensors, but not the calculated maximum value, which is supposed to be around 4.0 MPa.

Due to the expected range of desaturation in the rock mass it is recommended to arrange the relative humidity sensors in the bentonite buffer as well as in the first few centimetres of the rock mass up to a maximum distance of about 1 m.

With respect to the different modelling outcomes of the project partners it is concluded that it is of large interest to have measurement sensors located at a certain extent around the drift contour that is of interest for all partners.

5 Conclusions from the design calculations

As the modellers have selected different concepts for representing the experiment in this design phase of the HE-E modeling exercise, the modelled outcomes are also slightly different. Examples of differences between the modelling approaches are:

- CIMNE decided to model the two sections as one section in an axisymmetric configuration a radial symmetry. In that case no differences between the bentonite and the sand-bentonite sections can be represented.
- TK Consult modeled the two sections separately but did not include a dependency of the thermal conductivity on the saturation in the OPA.
- GRS selected a 2D plane strain model, including also the impact of the presence of the Gallery 98

The three models however indicate a similar overall behaviour of the experiment and are not contradicting with respect to major processes or impacts.

The definition of the relationship between the thermal conductivity and the saturation of both the OPA and the bentonite and sand/bentonite introduces uncertainty and results in slight differences in modelled maximum temperatures at the host rock/engineered barrier interface but a maximum temperature around 60-70°C seems to be most likely.

A potential concern is the pressure built up in the Opalinus Clay at some distance from the tunnel, due the thermal expansion of the pore water and the porous medium. Results indicate water pressures increasing from about 1.6 MPa up to 4 MPa approximately 10 m away from the tunnel. The consideration of Gallery98 influences the distribution of the pore water over-pressures but not the calculated maximum value.

It is expected that the HE-E test section will cause de-saturation in the rock mass to a radial extend around the gallery of 1 m maximum with an ellipsoid shape due to the anisotropic hydraulic conductivity. The modeling confirmed that no significant swelling pressure develops in the engineered barriers within the duration of the experiment.

One can conclude that the behaviour between the two sections in the experiment is not expected to be very different in terms of temperature, while the modelled resaturation and humidities are in essence linked to the initial saturation at emplacement and the differences in retention behavior of the materials.

The initial saturation state of the OPA and the influence of the EDZ on the experimental outcomes are further identified as affecting significantly the modelled temperatures and pressures. Both should be assessed as accurately as possible in the next predictive modeling step which will be based on the as-built data.

6 References

Baechler S. (2010). Tests hydrauliques dans les forages de l'unité de programme TER en galerie GEX Forages TER1401 à TER1405. ANDRA report D.RP.0CPE.09-0025.

Bock, H., 2001. RA Experiment. Rock Mechanics analyses and synthesis: Data Report on Rock Mechanics. *Technical Report 2000-02. Mont Terri Project.*

Booker, J.R. & Savviddou, C. 1985. Consoldation around a point heat source. Int. J. Num. Anal. Meth. In Geomech. Vol. 9, 173-184.

CODE_BRIGHT User's Manual, 2009. *UPC Geomechanical Group.*

Fernández, A.M., Melón, A., Turrero, M.J., Villar, M.V. 2006. Geochemical characterisation of the rock samples for the VE-Test before a second cycle of drying. Ventilation Test Phase II Deliverable D4.3.5

Floria, E., Sanz, F.J. and García-Siñeriz, J.L., 2002. Drying test: evaporation rate from core samples of "Opalinus Clay" under controlled environmental conditions. *Deliverable D6, FIKW-CT2001-00126.*

Garitte, B. and Gens, A., 2010. TH Scoping computations for the definition of an optimal instrumentation layout in the Full scale Emplacement experiment. *NAGRA report NIB 10-34.*

Garitte, B. and Gens, A., (2007). Modelling and Interpretation of the Ventilation Experiment: HM-C mechanisms in Opalinus Clay. NF-PRO Deliverable D4.3.23. Final Activity Report. CIMNE/DETCG 04/07., Barcelona, Spain.

Gaus I., 2010. Modellers dataset for the scoping calculations of the HEE experiment. Unpublished document.

Gaus I. (Ed), 2011. Mont Terri HE-E experiment: detailed design report. NAB 11-01.

Gens, A., 2000. HE Experiment: complementary rock laboratory tests. *Technical Note 2000-47. Mont Terri Project.*

Gens, A., Vaunat, J., Garitte, B. & Wileveau, Y. (2007). In situ behaviour of a stiff layered clay subject to thermal loading: observations and interpretation. Géotechnique 57, No. 2, 207-228.

Gisi M. 2007. Evaporation logging FM-D experiment: Modification of the equipment. Mont Terri Project: Technical Note 2007-27.

Mayor, J.C., García-Siñeriz, J.L., Velasco, M., Gómez-Hernández, J., Lloret, A., Matray, J.M., Coste, F., Giraud, A., Rothfuchs, T., Marschall, P., Rösli, U. and Mayer, G., 2005. Ventilation Experiment in Opalinus Clay for the management of radioactive waste. *Enresa Technical Report 07/2005, Madrid, Spain.*

Mayor, J.C., Velasco M. (2008). The Ventilation Experiment Phase II (Synthesis Report). DELIVERABLE (D-N°:4.3.18) NF-PRO Poject Work Package: WP 4.3.

Meier E., 1998. FM-D experiment: Evaporation logging in the new Gallery. Mont Terri Project: Technical Note 98-51

Meier E., 2004. Evaporation logging (FM-D) Experiment, Phase 9: documentation of raw and processed data. Mont Terri Project: Technical Note 2004-50.

Muñoz, J.J., Lloret, A. and Alonso, E., 2003. Laboratory Report: Characterization of hydraulic properties under saturated and non saturated conditions. *Project Deliverable 4 EC contract FIKW-CT2001-00126.*

Olivella, S., 1995. Nonisothermal multiphase flow of brine and gas through saline media. *Doctoral Thesis, Technical University of Catalonia (UPC), Barcelona, Spain.*

Rösli U. (2010). VE Experiment: Long Term Monitoring Data Report - Phase 15. 1 July 2009 – 30 June 2010. Mont Terri Project Technical Report TN 2010-12.

Sánchez, M. and Gens, A., 2006. FEBEX Project: Final report on thermo-hydro-mechanical modelling. *ENRESA Technical Report 05-2/2006, Madrid, Spain.*

Schuster K. 2007. Ventilation Test (VE) Experiment: Final activity report on high resolution seismic investigations within the VE-Experiment. Mont Terri project: Technical Report 2007-06

Traber, 2003. Geochemical characterisation of samples from drill core BVE82. Project Deliverable D5b EC contract FIKW-CT2001-00126

Traber, 2004. Geochemical characterisation of samples from drill core BVE85 and BVE86. Project Deliverable D5c&d/D22 EC contract FIKW-CT2001-00126

Villar, M.V., 2007. Retention curves determined on samples taken before the second drying phase. *Technical Report M2144/5/07.*

Wileveau Y., Cornet F.H., Desroches J., Blumling P. (2007). Complete in situ stress determination in an argillite sedimentary formation. Physics and Chemistry of the Earth 32 (2007) 866–878.

Zhang, C. L. and Rothfuchs, T., 2005. Report on instrument layout and pre-testing of large lab VE-tests. *Deliverable 4.3.11.*

App. A Modellers dataset for the scoping calculations

HE-E experiment

Modellers dataset for the scoping calculations. Version 8 June 2010 – I. Gaus

1. Introduction

This document describes the dataset for the scoping calculations of the HE-E experiment.

The dataset will be revised and completed (also including results from the excavation of the EB experiment) later in the PEBS project to allow for the modelling prediction and the validation part of the experiment.

The following was agreed at the HE-E kick-off meeting in Hannover regarding the scoping calculations:

- For the scoping calculations to be relevant for the design the results need to be available by 15 September at the latest
- Intermediate results will be reported by 31 August (draft report).

If modellers are in favour of this we could organise a meeting to discuss the final results (GRS, CIMNE, Nagra, TK Consult) and assess the impact of the scoping calculations on the planning of the experiment.

It is up to the modellers to define the appropriate conceptual models (T, TH, THM) and grids, the strategy for the sensitivity analysis, appropriate parameter ranges etc.

2. Dimensions of the experiment

A technical description of the experiment is included in Appendix 1 which also includes the dimensions which are shown in the Figure below.

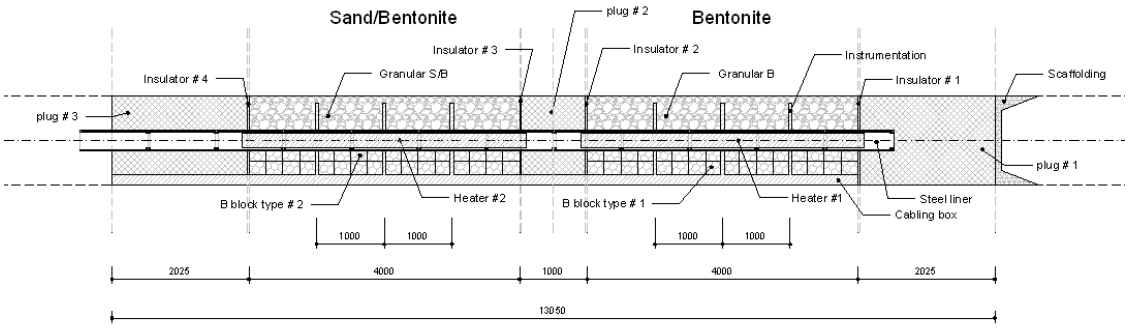

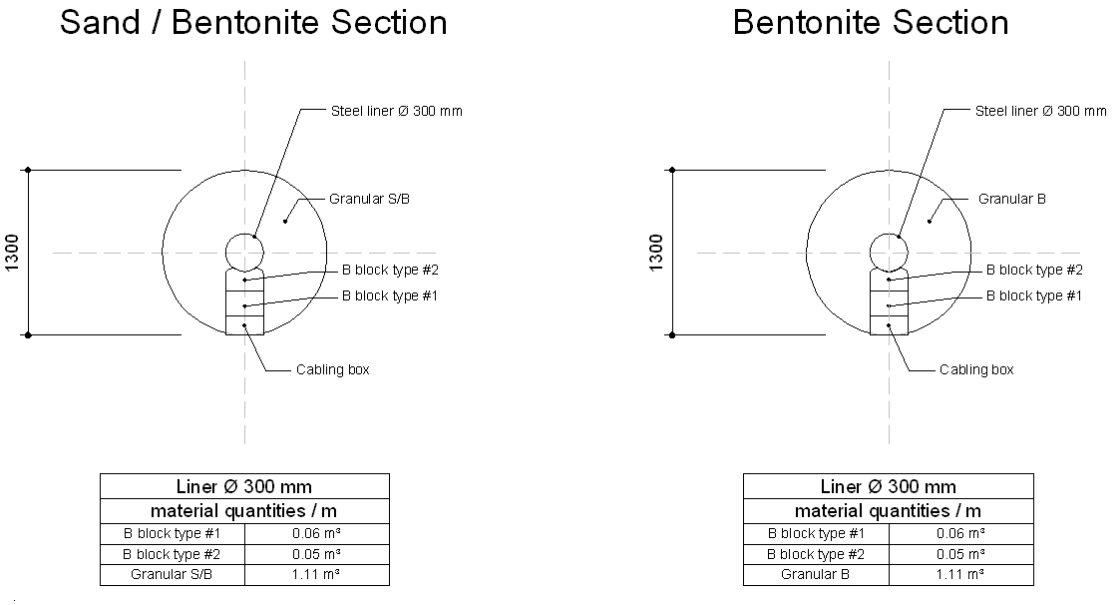

Figure 1. Current dimensions of the planned HE-E experiment.

3. Proposed two phase flow and thermal properties for the materials

The parameters below are proposed values only. While in Table 1 a compilation is given, the background on the selected values is given in Appendix 2. If there are arguments to use other values then feel free to do so. However, in that case please list the parameters that have been chosen differently and indicate why a different choice was made.

Table 1. Proposed parameter values for the scoping calculations of the HE-E experiment.

	OPA	**EDZ**	**Bentonite blocks**	**Bentonite pellets**	**Sand/bentonite mix**	**Concrete (plugs)**	**Insulator**	**Steel**
Permeability [m^2]	1e-20	1e-18	2.5e-21	3.5e-20	1e-19	1e-20	1e-20	1e-50
Porosity	0.12	0.14	0.475	0.475	0.41	0.15	0.002	0.001
Residual Water Saturation S_{wr}	0.3	0.3	0.01	0.01	0.3	0.01	0.01	0.01
Residual Gas Saturation S_{gr}	0.01	0.01	0.001	0.001	0.01	0.0	0.0	0.0
Van Genuchten n	1.67	1.67	1.82	1.82	2.5	1.49	1.49	2
Van Genuchten 1/a [Pa]	3e6	1e6	3e7	1.8e7	2.5e5	1.5e7	1.5e7	1e8
Pore compressibility [1/Pa]	1.7e-9	1.7e-9	2e-9	2e-9	2e-9	6.7e-10	6.93e-10	0

Thermal expansion [1/K]	3.47e-5	3.47e-5	1.5e-5	1.5e-5	1.5e-5	1.5e-5	1.5e-5	1.5e-5
Wet Thermal conductivity~ [W/m K]	2.5	1.5	1.35	1.35	1.35	1.35	0.035	52
Dry Thermal conductivity~ [W/m K]	2.5	1.5	0.4	0.4	0.4	0.4	0.035	52
Specific Heat [J/kg C]	946.5	1068	964	964	920	964	1400	1e20*

* Specific Heat of Steel set to high value to maintain constant temperatures
~ Linear relation between wet and dry thermal cond. values

The parameters provided are those needed to complete the TH modelling. In case parameters for the mechanical modelling are needed, these can be provided on request.

4. Target heating profiles

Two heating strategies are proposed. Both strategies could be tested in the modelling.Depending on the modelled outcomes one of the two or a combination of both will be selected. The indicated temperatures are the temperatures at the liner surface.

Strategy 1	Initial temperature of 10°C , reaching 90°C after 3 months, 105°C after 6 months, 120°C after 1 years and 135°C after 3 years .
Strategy 2	Initial temperature of 10°C, then gradual temperature increase to reach 135°C after 1 year, then constant temperature of 135°C for the two following years.

5. Initial conditions

5.1 Saturation in the VE-tunnel

The initial saturation conditions in the VE tunnel are somewhat unclear. The tunnel has been actively ventilated during the VE test and also afterwards ventilation took place. Certain pore pressure sensors at a depth of up to 2 m in the OPA are no longer providing reliable results suggesting that a certain degree of desaturation occurs.

Two types of initial conditions are proposed.

Initial VE tunnel 1	Simulation of the initial conditions through ventilation such that the saturation is 100% at a depth of 0.5 m at the start of the heating
Initial VE tunnel 2	Simulation of the initial conditions through ventilation such that the saturation is 100% at a depth of 1.5 m at the start of the heating

Based on the selected OPA parameters a saturation gradient toward the tunnel (0% water saturation) will develop during the calculation. This modelled saturation and pressure pattern can be used as the initial condition for the scoping modelling.

5.2 Initial saturation in the bentonite

Initial emplacement water content of the pellets: 7%
Initial emplacement water content of the bentonite blocks: 32%

5.3 Initial pressures.

The initial pressure in the OPA is hydrostatic, the top of the experiment corresponds to a column of 175 m, the tunnel itself is at atmospheric pressure.

6. Sensitivity analysis

The selection of the runs for sensitivity is left to the modellers. The following aspects could be targeted in the sensitivity analysis:

- impact of the thermal properties
- the heating strategy
- initial saturation condition of the VE tunnel
- two phase flow properties
- permeability of the OPA
- conceptualisation of the bentonite.

7. Performance measures for comparison between the models

The following parameters will be targeted for comparison between the models:

- pressures versus time, pressure profile at given times (1, 2 , 3, 5 years)
- temperatures versus time, temperature profile at given times (1, 2 , 3, 5 years)
- saturation versus time, saturation profile at given times (1, 2 , 3, 5 years)

The points for the time series suggested are:

- Top OPA/bentonite interface of the experiment/middle of each section (bentonite and sand/bentonite)
- Bottom OPA/bentonite interface of the experiment/middle of each section (bentonite and sand/bentonite)
- Horizontal OPA/bentonite interface of the experiment/middle of each section (bentonite and sand/bentonite)

Further illustration could include 3D views at certain times (1, 2 , 3, 5 years) to characterise the symmetry of the developing parameter patterns.

PEBS: design of HE – E experiment at Mont Terri

1. Experiment overview

A new long term experiment elucidating the early non-isothermal resaturation period and its impact on the thermo-hydro-mechanical behaviour is planned. Its objectives are: 1) to provide the experimental data base required for the validation of existing thermo-hydraulic models of the early resaturation phase; 2) to provide experimental data bases for model calibration; 3) to upscale thermal conductivity of the partially saturated buffer from laboratory to field scale (pure bentonite and bentonite-sand mixtures). The experiment HE-E will be performed in the VE microtunnel (Fig.1) (Mont Terri Rock Laboratory) and is aimed at improving the understanding of the thermal evolution of the near field around a SF/HLW waste container, during the very early phase after emplacement in a 1:2 scale in-situ configuration. Special interest is on the temperature evolution in the buffer and the thermal impact on the clay rock close to the tunnel.

2. Current site conditions

VE microtunnel access is from niche MI, width and minimum height are 4.2m (Fig.2). Mouth of the microtunnel is ca. 1.5m higher respect to MI niche floor level, access is therefore granted by a metallic ladder. Microtunnel total length is ca. 50m and can be split-up into the following zones: Zone #1 (0m - 30m): from the mouth (Fig.3a) till the second forward door (Fig. 3b). Rock mass, very fractured, is secured with steel nets, steel rings and occasional bolts; Zone #2 (30m-40m): VE Experiment Test Section (Figs.3c and 3d). Rock mass seems to be less fractured respect to previous section and it self-supported (possibility of having a laser scan to characterise the surface exists). Relatively high air humidity; Zone #3 (40m-50m): from first rear door (Fig.3e) till end of the tunnel (Fig.3f). Even though the rock mass seems to be as fractured as the previous section, it has been secured with steel nets and rings. Very high air humidity (very sticky).
Emplacement should consider minimum tunnel diameter of 1.1m (Zone #1).

3. Experiment layout

Two buffer materials will be used in the experiment: bentonite pellets (granular B) and bentonite blocks will be used in one section of the test as reference material of the Swiss disposal concept in order to gain representative data on buffer evolution; sand/bentonite pellets (granular S/B) mixture and bentonite blocks, having a higher thermal conductivity will be used in the other section to reach the maximum design temperature in the rock (Fig.4a).

4. Emplacement technology

In terms of backfilling the tunnel, two different emplacement methods are so far considered and have to be substantiated in order to find the most appropriate one: pneumatically (good flexibility, but high dust formation), starting from MI-niche or from gallery 98; a combination of conveyor and auger technique, starting from MI-niche (more preliminary construction effort, less flexibility, less dust formation). Testing on a different site will be performed for verifying the chosen emplacement technique feasibility and material quality.

5. Materials

The following main materials will be used: bentonite blocks (shape to be defined); granular bentonite (identical to the EB experiment, maybe adding a coarser fraction to reduce porosity); granular sand/bentonite; reinforced concrete (for constructing the plugs); insulator,

high temperature (150°C) and flexible continuous sheets (for example 25mm thick HT/Armaflex®); - steel, for constructing the cabling boxes and the liner; - wood, for constructing the dying end scaffolding.

6. Heating system

A heater system, capable of representing the temperature curve of the anticipated heat production in the canisters (up to a maximum of 140°C), will, over a period of 3 years gradually lead to and increase in the temperature in the EBS and the surrounding host rock while natural saturation is ongoing. Two heaters, capable of functioning independently will be emplaced in a modular liner system (steel tunnel). Heater's length will be less than 4.2m.

7. Instrumentation

During the experiment the temperature and the water saturation will be monitored through a system of sensors (i) on the heater surface within the liner (Aitemin), (ii) in the bentonite (Solexperts) and (iii) in the surrounding host rock based on the existing sensors and additional pressure transducers (GRS). A total of 200 sensors in 6 vertical planes will provide the required data density. Seismic transmission measurements to capture expected changes in the near field of the rock due to the temperature and/or resaturation impact will be installed.. The existing three 1m long boreholes in the microtunnel which were used for seismic measurements during the Ventilation Experiment will be used for the installation of eight receivers (for example six in the boreholes and two in the GBM) and four source transducers. A daily automated seismic transmission measurement will be performed for one year. Current instrumentation sections layout respect to the construction layout are shown if Fig.4b. Before construction starts, instrumentation within the rock mass must be emplaced.

8. Installation logistics and procedures

MI niche is a good stocking area and usage needs to be coordinated with other Mont Terri activities. Mouth of the microtunnel is ca. 1.5m higher respect to MI niche floor level; therefore it will be necessary to use a platform truck for material emplacement. To facilitate and accelerate working operations, material transportation and emplacement within the limited dimensions a simple railway system (single loading capacity of 200-300kg) for zones #1 and #2 seems to be most appropriate.

An appropriate ventilation system is necessary due to production of high dust quantities (depending on the chosen emplacement technique).

Construction procedures sequence will be as follows (see Fig.4a): - emplacement of dying end scaffolding; - construction of r.c. plug #1 (length depends on resisting capacity against bentonite swelling pressures); - first steel liner segment imbedded into plug #1; - emplacement of insulator #1; - modular approach emplacement of bentonite blocks, liner and instrumentation; - emplacement of granular bentonite (emplacement length according to chosen emplacement technique); - emplacement of insulator #2; -construction of plug #2 with imbedded steel liner segment (plug material depending on the unbalanced longitudinal forces developed in the two buffers and construction feasibility); - emplacement of insulator #3; - modular approach emplacement of bentonite blocks, liner and instrumentation; - emplacement of granular sand/bentonite (emplacement length according to chosen emplacement technique); - emplacement of insulator #4; - construction of r.c. plug #3 (length depends on resisting capacity of sand/bentonite swelling pressures).

Instrumentation cables passage is permitted thanks to the cabling box (Fig.5).

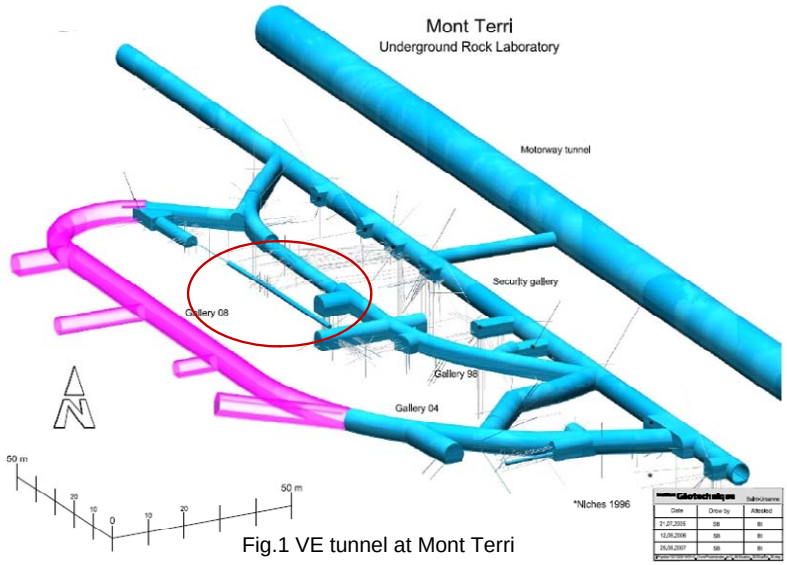

Fig.1 VE tunnel at Mont Terri

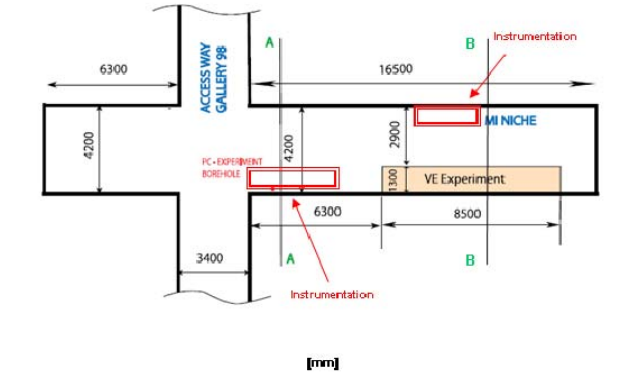

Fig.2 MI niche layout

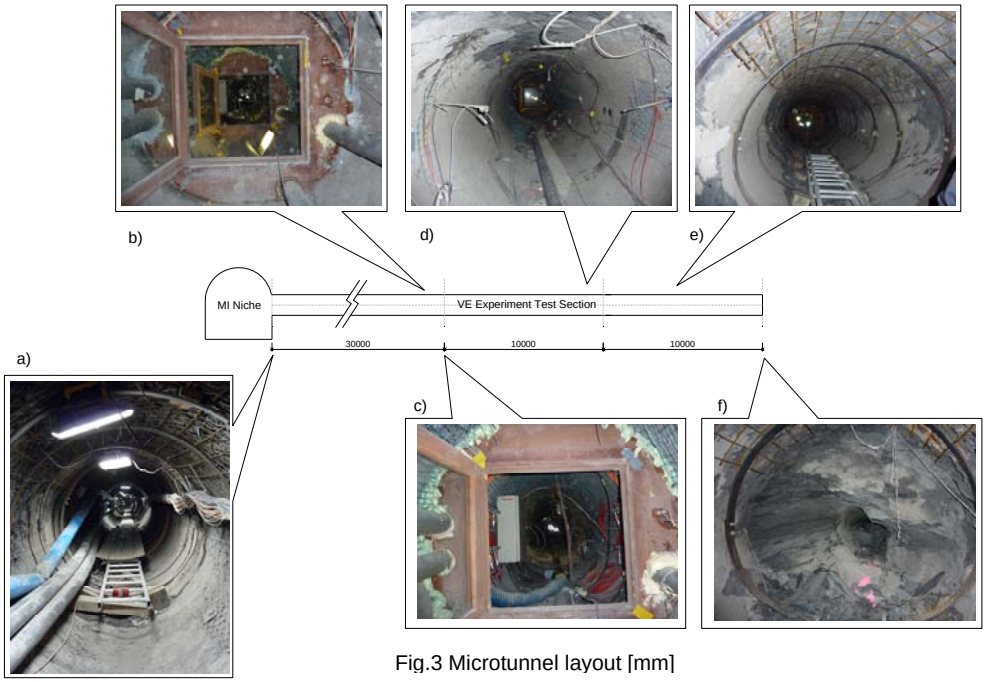

Fig.3 Microtunnel layout [mm]

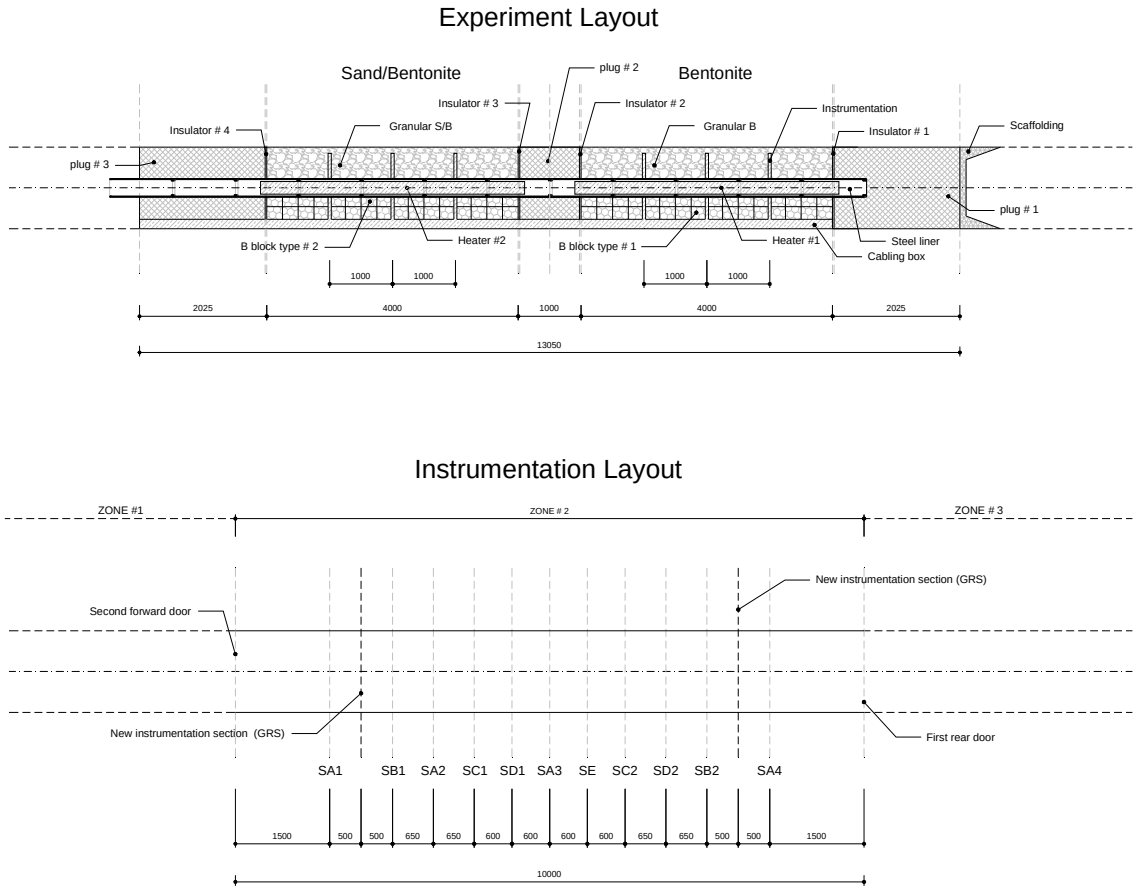

Fig.4 Experiment and instrumentation layout [mm]

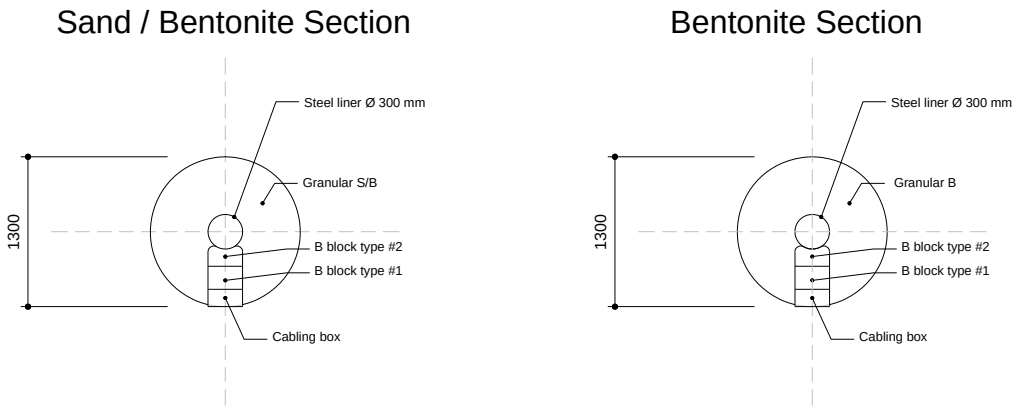

Liner Ø 300 mm	
material quantities / m	
B block type #1	0.06 m³
B block type #2	0.05 m³
Granular S/B	1.11 m³

Liner Ø 300 mm	
material quantities / m	
B block type #1	0.06 m³
B block type #2	0.05 m³
Granular B	1.11 m³

Fig.5 Experiment section's layout [mm]

Appendix 2 to the HE-E modelers dataset

1. Thermal properties

(Tables 1 below taken from NAB 08-32)

Table. 1: Thermal properties of different materials (Johnson et al. 2002, Nagra 2002a and Poppei et al. 2002).

Material	Thermal conductivity ($W\ m^{-1}\ K^{-1}$)	Specific Heat ($J\ kg^{-1}\ C^{-1}$)	Initial temperature (°C)
Steel canister	52	*388.5*[1]	60
Bentonite (2% moisture)	0.4	964	38
Bentonite (saturated)	1.35	1928[4]	38
Opalinus Clay: average value	2.5	*946.5*[2]	38[3]
Opalinus Clay (OPA)EDZ*)*	1.5	*1068*	38
OPA: : Horizontal*: Vertical*:	 2.5 1.55	*946.5*[2]	38[3]
Johnson et al. 2002: upper OPA and the upper confining units	3.2 (horizontal) 1.8 (vertical)		
Alternative value: OPA	1.65		
Johnson et al. 2002: lower OPA and the lower confining units	2.0 (horizontal) 1.3 (vertical)		

* anisotropy of thermal conductivity was implemented in TOUGH2 code (not part of standard code)

[1]*Poppei et al. (2002); increased by a factor of 20 to account for heat-generating waste*

[2]*Nagra(2002a);* [3] *Johnson et al. (2002): defined by thermal gradient*

[4]*a constant value for the dry bentonite of 964 J* $kg^{-1}C^{-1}$ *was used in the model*

2. Two –phase flow parameters (OPA at Benken)

(Tables 2 below taken from NAB 08-32)

Tab. 2: Input parameters for the TOUGH2 simulations (SF/HLW) - reference case

Parameter	**Value**	**Remarks**
Material properties – Container		
Thermal expansion (1/K)	1.2E-5	Gerthsen et al. 1989
Porosity (-)	0.01	Canister hull (assumption): fictive porosity value needed as input
Permeability (m^2)	1E-50	Canister hull (assumption): steel is impermeable to water an gas
Res. Liquid saturation (-)	0.0	
Res. Liquid saturation (-)	0.0	
Initial liquid saturation (-)	0.0	
Van Genuchten Parameter n (-)	2	
Van Genuchten parameter 1/a (MPa)	100	Canister hull (assumption): no gas entry
Material properties – Bentonite		
Pore compressibility: C_p (1/Pa) $C_p=\alpha/\phi$; $\alpha= S_s/\rho g - \phi\beta$;	2.E-9	Assumption α=1E-9 (1/Pa); cf. AN 05-128 β=4.4E-10 Pa^{-1} ; ρ = 1000 kg/m^3
Thermal expansion (1/K)	1.5E-5	Assumption
Initial porosity (-)	0.475	According to Johnson et al 2002
Permeability (m^2) - uniform - Bentonite pellets - Bentonite blocks	1E-19 3.5E-20 2.5E-21	According to Nagra 2002a Reduced Reduced
Resid. water saturation S_{wr}	0.0	
Resid. Gas saturation S_{gr}	0.0	
Van Genuchten parameter n	1.82	
Van Genuchten parameter 1/a (Pa) - Bentonite pellets - Bentonite blocks	 1.8E7 3.0E7	

Material properties – Opalinus Clay		
Pore compressibility C_p (1/Pa) $S_s=\rho g(\alpha+\phi\beta) \rightarrow \alpha= S_s/\rho g - \phi\beta$; $C_p=\alpha/\phi$	1.7E-9	AN 05-128 (S_s=2.6E-6 1/m) β = 4.4E-10 Pa^{-1}, ρ=1000kg/m^3, ϕ=0.12
Thermal expansion (1/K)	3.47E-5	First heating path (cooling path 2.65E-5), NTB 02-03
Porosity (-)	0.12	Reference value OPA / Benken
Permeability (m^2)	1E-20	Referenzwert OPA / Benken (Kh)
Resid. water saturation S_{wr} (-)	0.0	Nagra 2004 (p. 44): lower bound OPA
Resid. gas saturation S_{gr} (-)	0.003	Nagra 2004 (p. 44): best guess OPA
Van Genuchten parameter n (-)	1.67	Nagra 2004 (p. 44): range OPA
Van Genuchten parameter 1/a (Pa)	1.8E7	Nagra 2004 (p. 44): range OPA
Geometry & material properties – EDZ		
EDZ radial thickness (m)	0.7	Reference value OPA / Benken
Pore compressibility (1/Pa)	1.7E-9	As intact OPA
Thermal expansion (1/K)	3.47E-5	As intact OPA
Porosity (-)	0.14	Nagra 2002a (short term phase, p. 475)
Permeability (m^2)	1E-20 1.E-19	As intact OPA Nagra 2002a (short term phase)
Resid. water saturation S_{wr} (-)	0.0	As intact OPA
Resid. gas saturation S_{gr} (-)	0.003	As intact OPA
Van Genuchten parameter n (-)	1.67	As intact OPA
Van Genuchten parameter 1/a (Pa)	1.8E7	As intact OPA
Two-phase Parameter Model (used for all materials)	– van Genuchten Pc; $P_c=P_o\cdot\left(S_{ec}^{\,n/(1-n)}-1\right)^{1/n}$ $S_{ec}=\frac{S_l-S_{lr}}{1-S_{lr}}$ $m=1-1/n$	– van Genuchten kr; $k_{r,l}=S_e^{\,0.5}\cdot\left[1-\left(1-S_e^{\,1/m}\right)^m\right]^2$ $k_{r,g}=1-k_{r,l}\rightarrow S_{gr}=0$ $k_{r,g}=(1-S_e)^2(1-S_e^2)\rightarrow S_{gr}>0$ $S_e=\frac{S_l-S_{lr}}{1-S_{gr}-S_{lr}}$

Further parameters describing vapor transport in the unsaturated bentonite, such as the vapor diffusion coefficient and tortuosity, parameter values were chosen according to the TOUGH standard input:

- vapour diffusion coefficient: d_0 = 2.13E-5 m^2/s
- tortuosity: τ_0 = 1. (τ = f(k_{rg})).

3. Additional parameter input for OPA data at Mont Terri

Table 3. Specific input for Mt Terri (from HG-A) (Lanyon et al., ?)

Parameter	**Value**	**Comments**
Hydraulic Diffusivity (m2/s):	1.00E-07	
Hydraulic Conductivity (m/s)	1.00E-13	k = 2.E-19 to 2.E-20m2
Specific Storage(1/m)	1.00E-06	Ss = 4.E-7 to 3.E-5 1/m
Compressibility α(1/Pa)	4.91E-11	Ss=rho*g(alpha+n*beta)
Pore Compressibility Cp(1/Pa)	4.09E-10	beta(1/Pa)= 4.40E-10 alpha=Ss/(rho*g)-n*beta Cp=alpha/n

App. B Temperature

All simulation results in terms of temperature are given in this annexe. All distances are given in relation to the centre of the microtunnel. Time runs from bentonite emplacement.

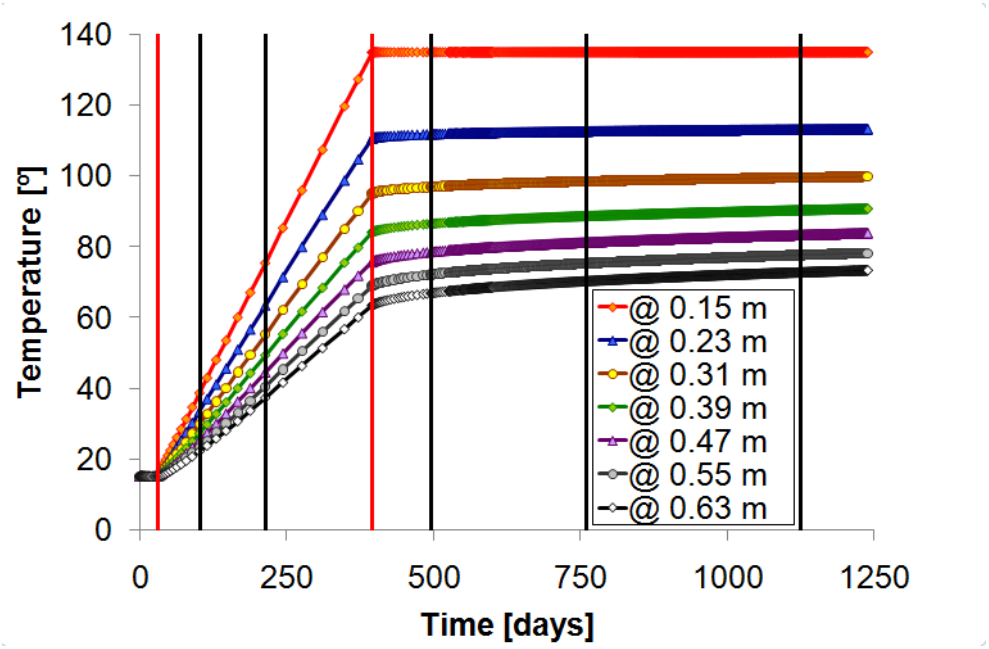

Figure B-1 Predicted evolution of the temperature in the bentonite barrier.

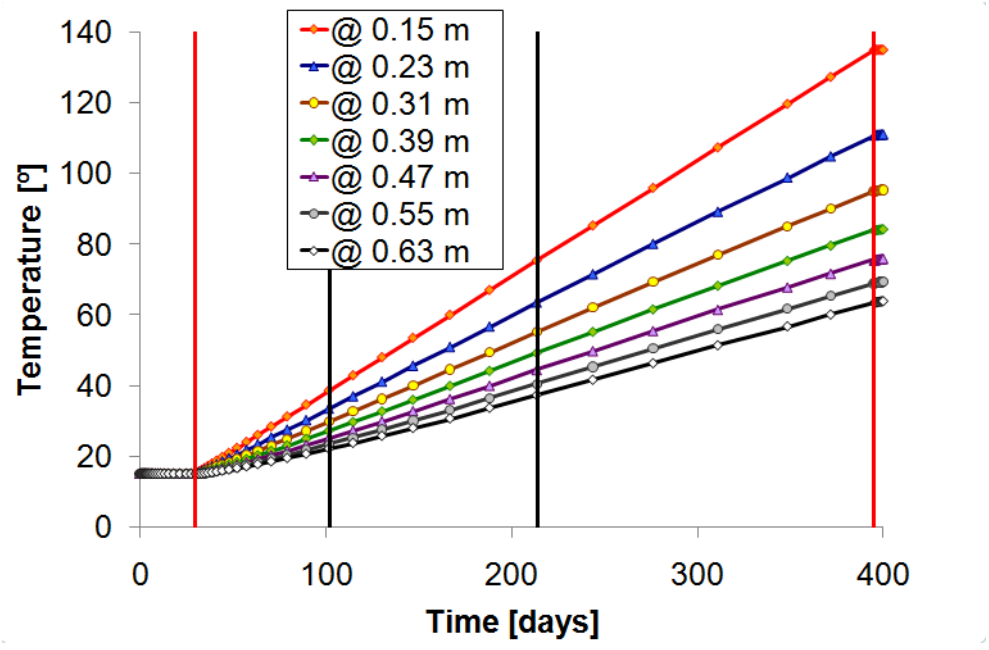

Figure B-2 Predicted evolution of the temperature in the bentonite barrier during the temperature increase period.

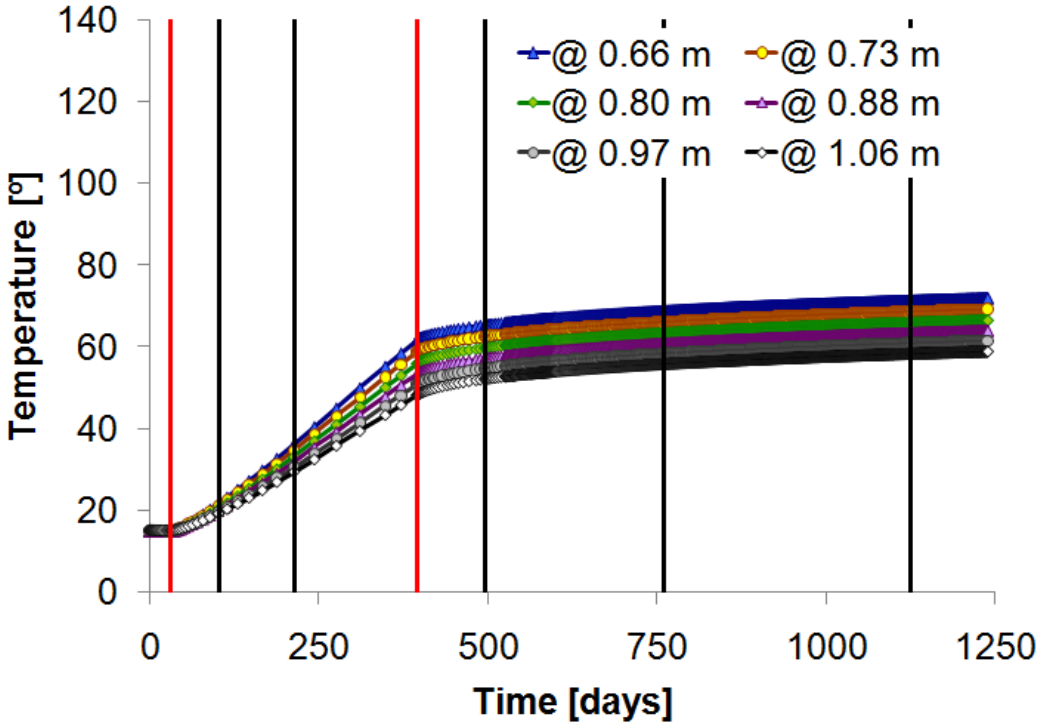

Figure B-3 Predicted evolution of the temperature in the first 40 cm of OC.

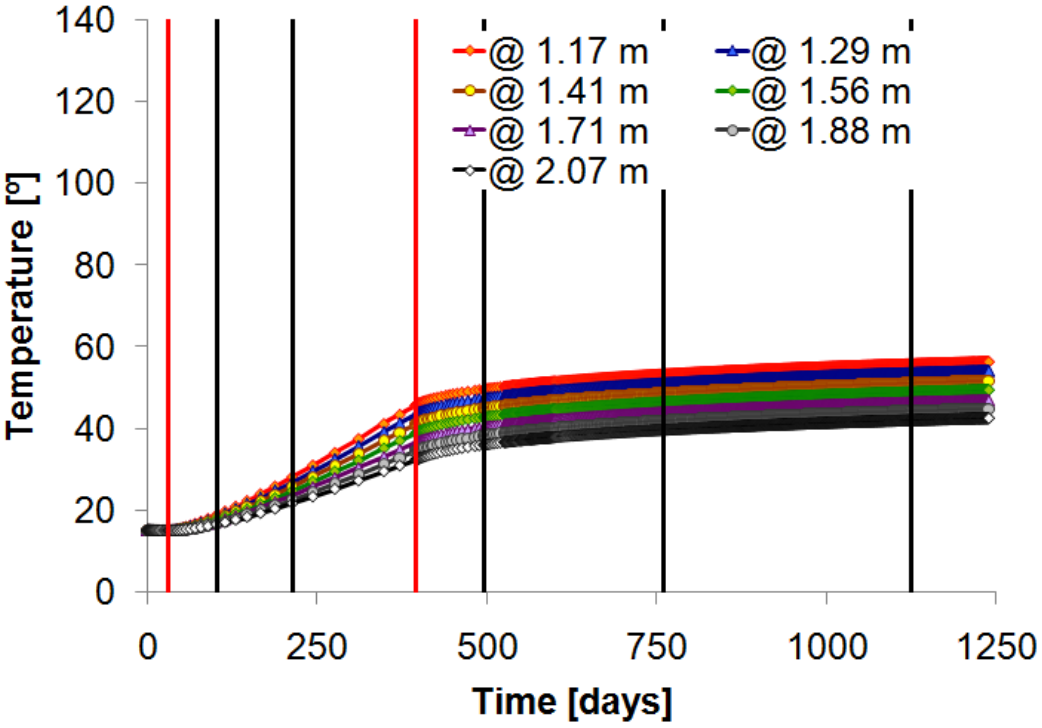

Figure B-4 Predicted evolution of the temperature between 50 and 150cm from the microtunnel wall.

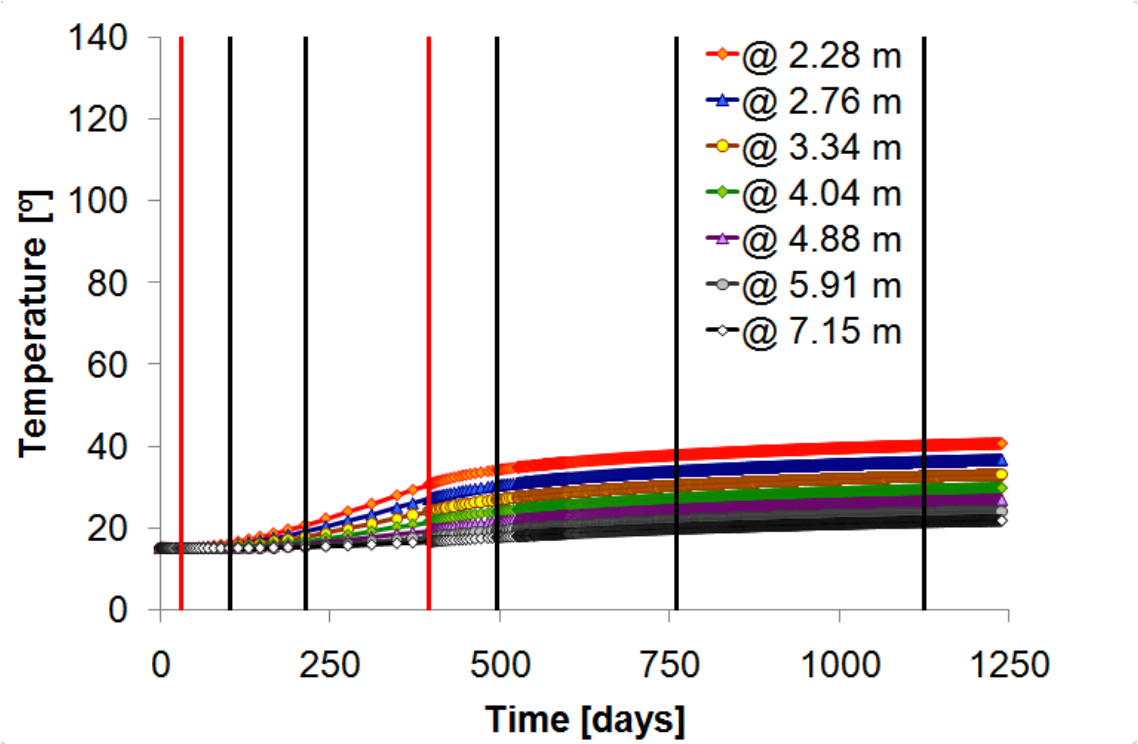

Figure B-5 Predicted evolution of the temperature between 150 and 750cm from the microtunnel wall.

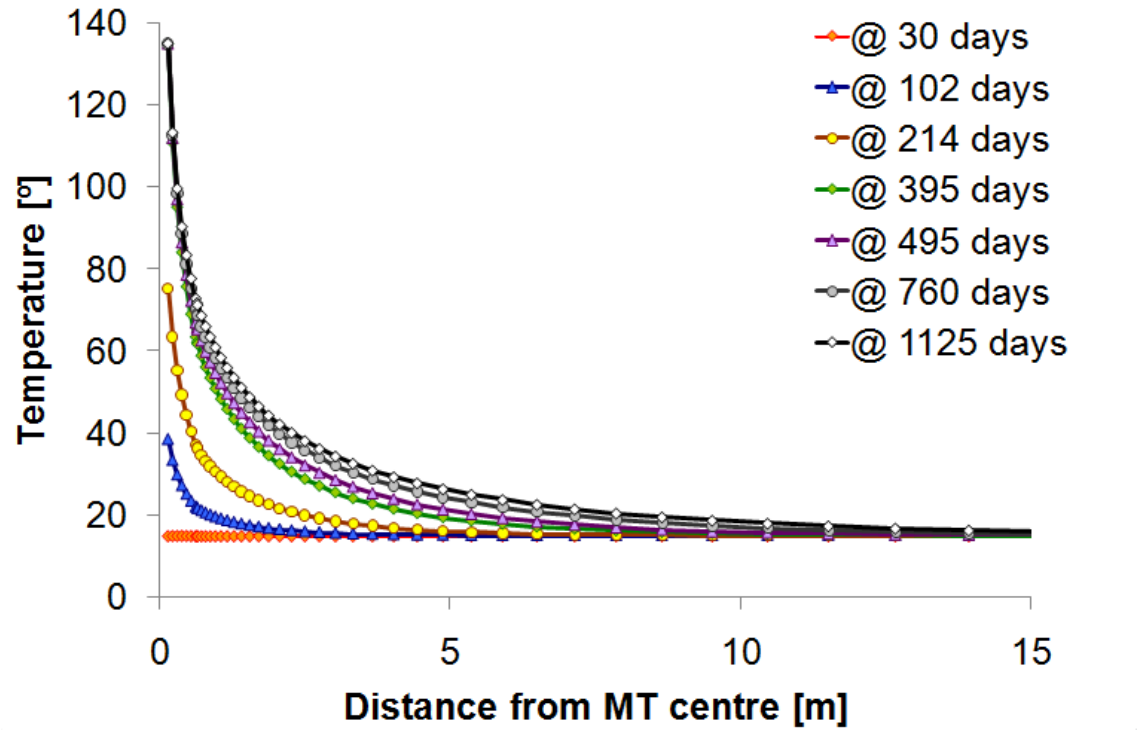

Figure B-6 Predicted profiles of temperature at different times along A1.

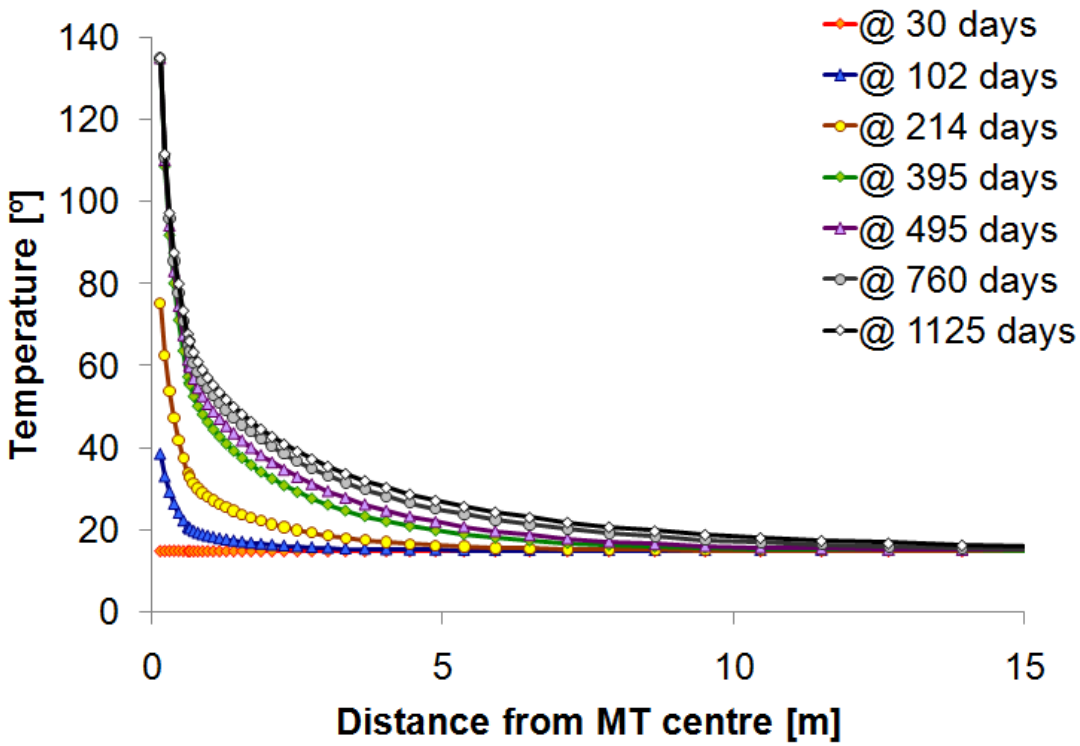

Figure B-7 Predicted profiles of temperature at different times along A2.

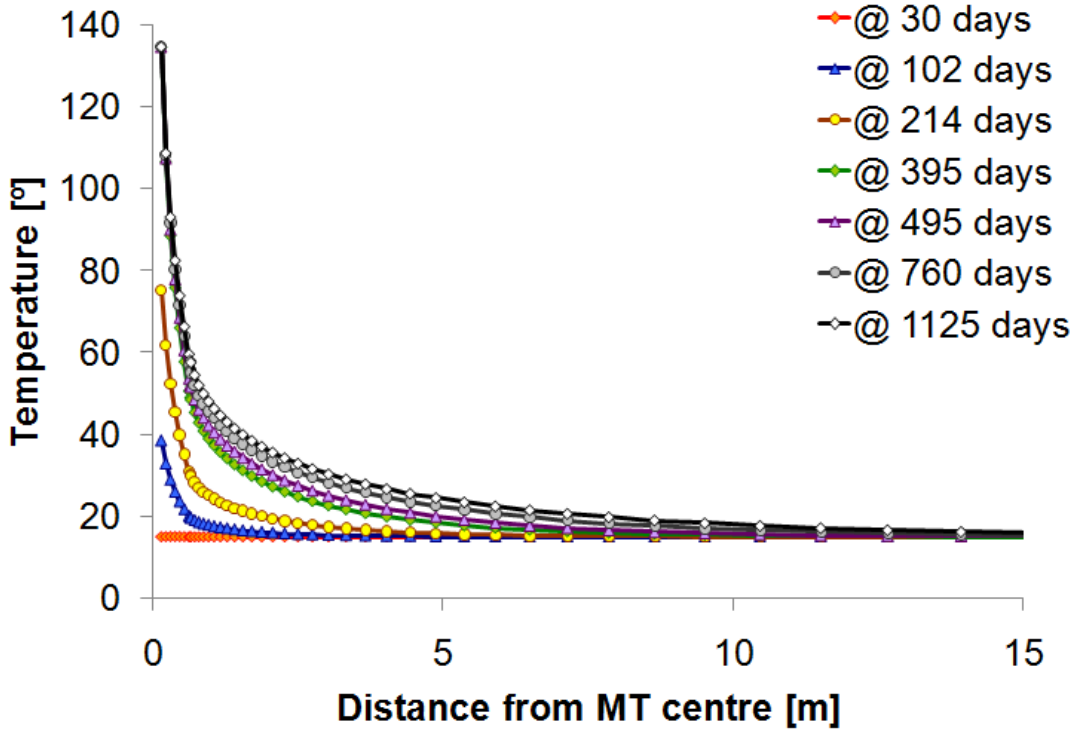

Figure B-8 Predicted profiles of temperature at different times along A3.

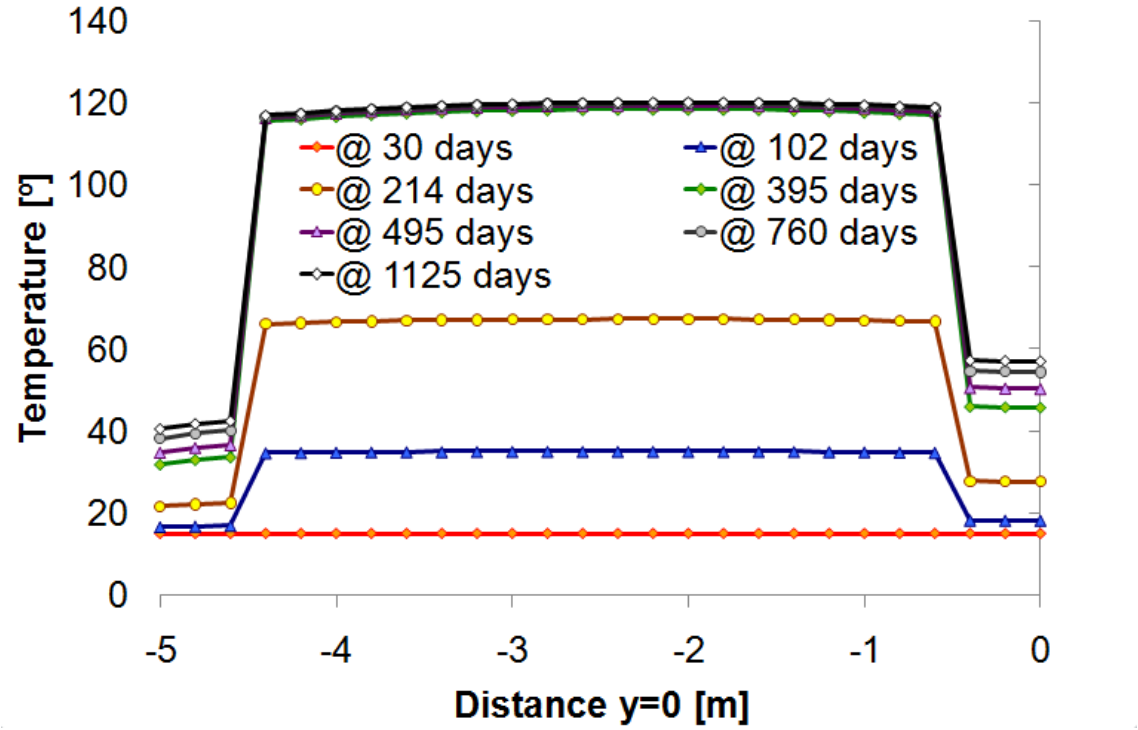

Figure B-9 Predicted profiles of temperature at different times along B1.

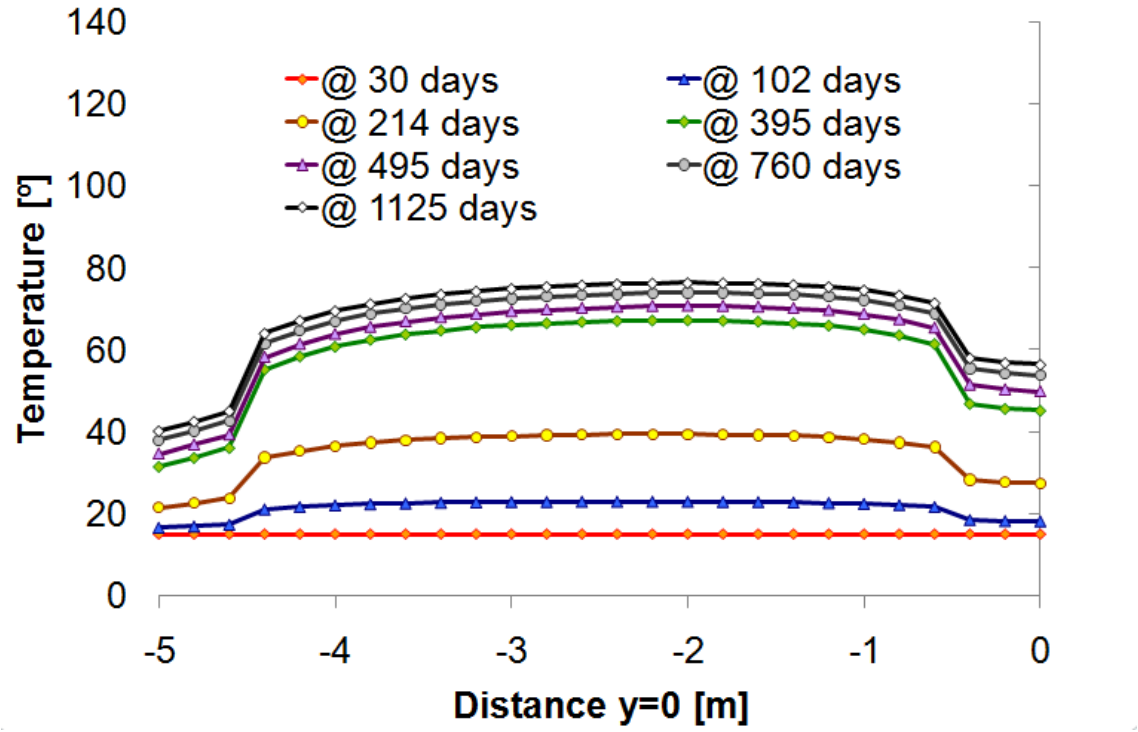

Figure B-10 Predicted profiles of temperature at different times along B2.

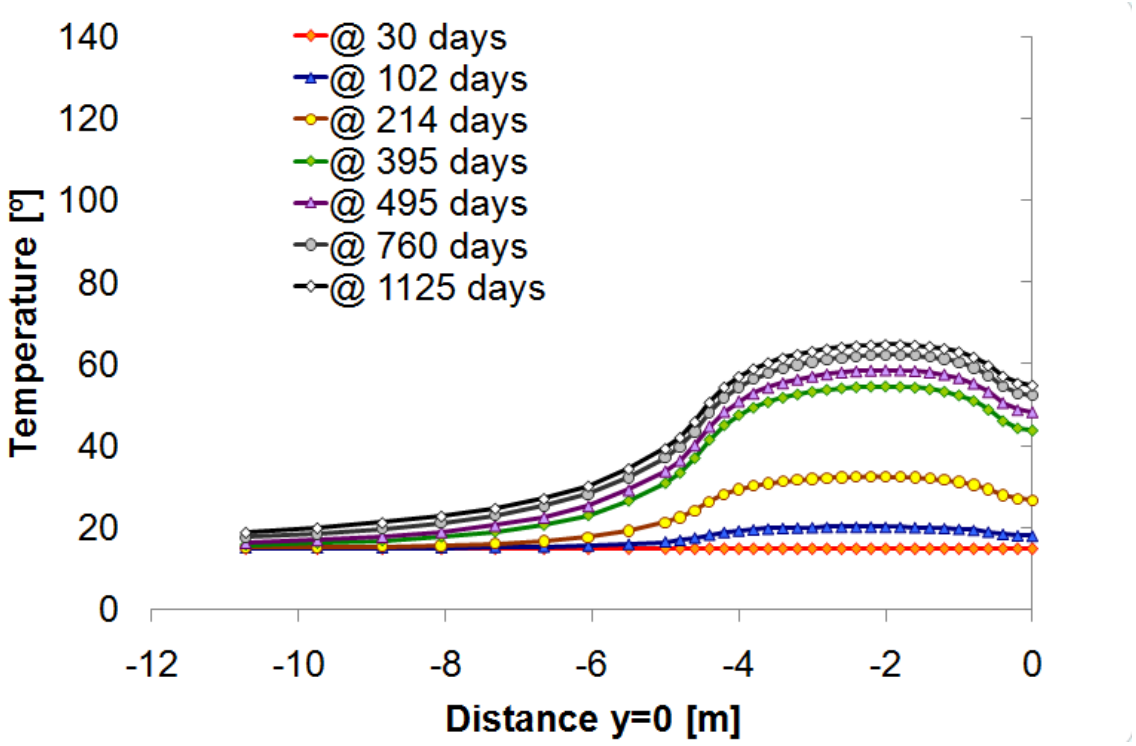

Figure B-11 Predicted profiles of temperature at different times along B3.

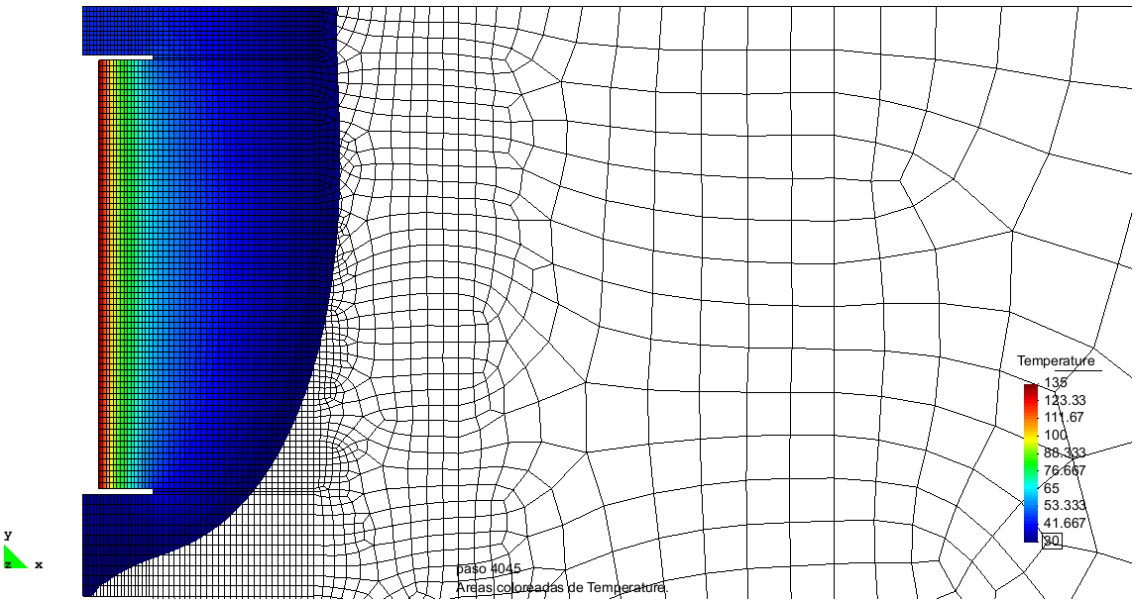

Figure B-12 Equivalue lines of temperature at day 395.

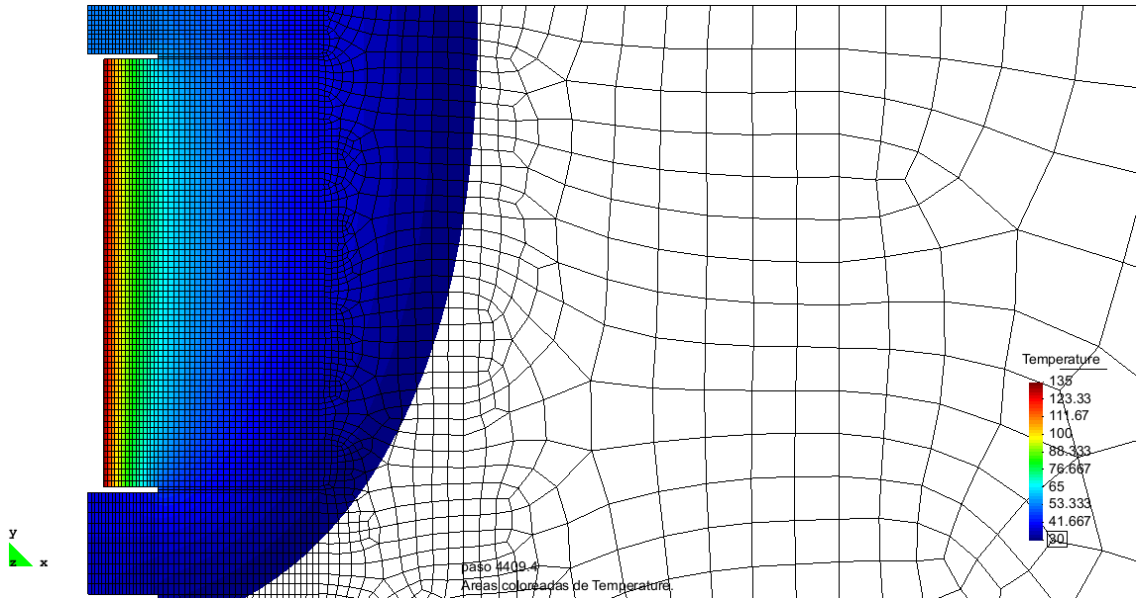

Figure B-13 Equivalue lines of temperature at about day 760.

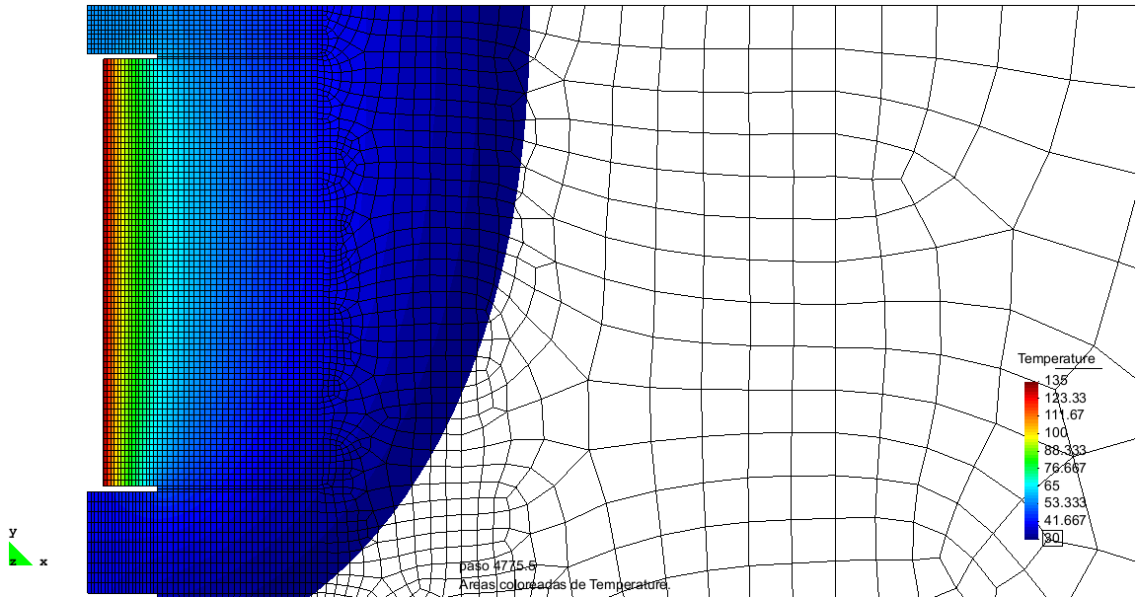

Figure B-14 Equivalue lines of temperature at day 1125.

App. C Degree of Saturation

All simulation results in terms of degree of saturation are given in this annexe. All distances are given in relation to the centre of the microtunnel. Time runs from bentonite emplacement.

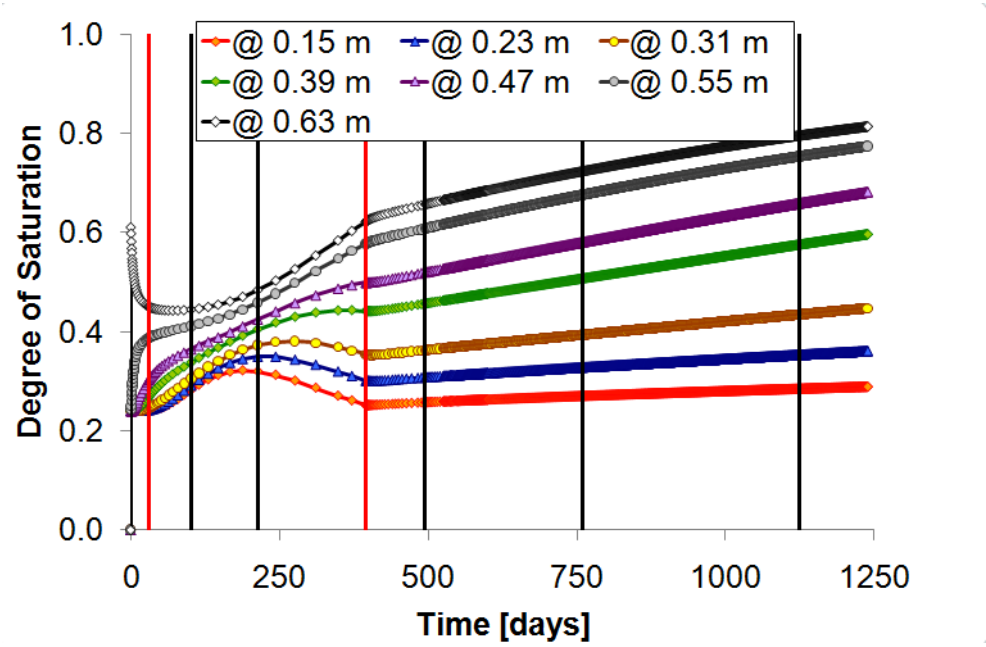

Figure C-1 Predicted evolution of the degree of saturation in the bentonite barrier.

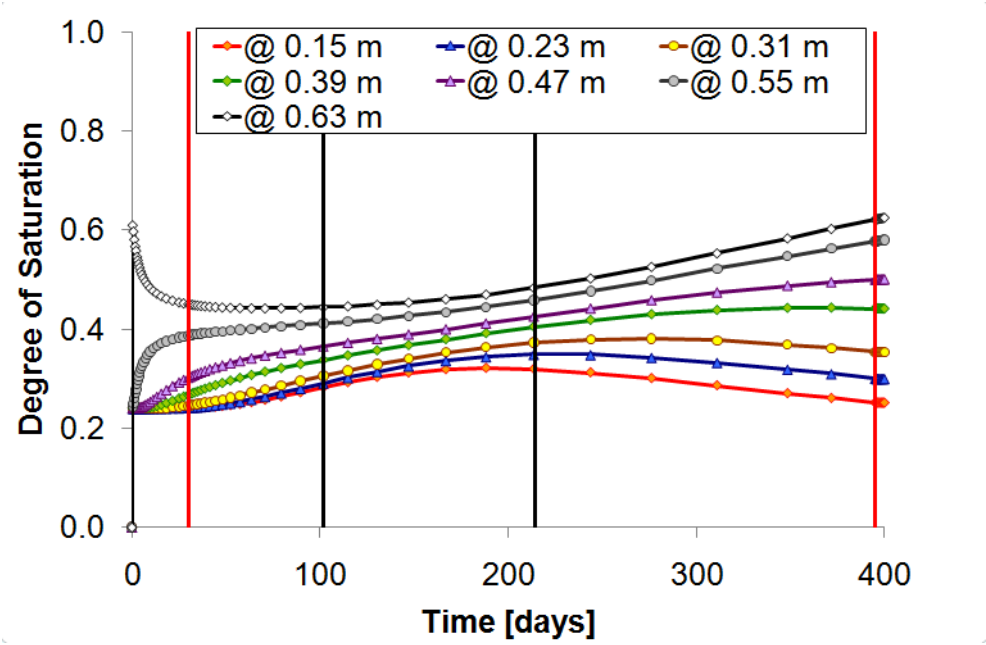

Figure C-2 Predicted evolution of the degree of saturation in the bentonite barrier during the temperature increase period.

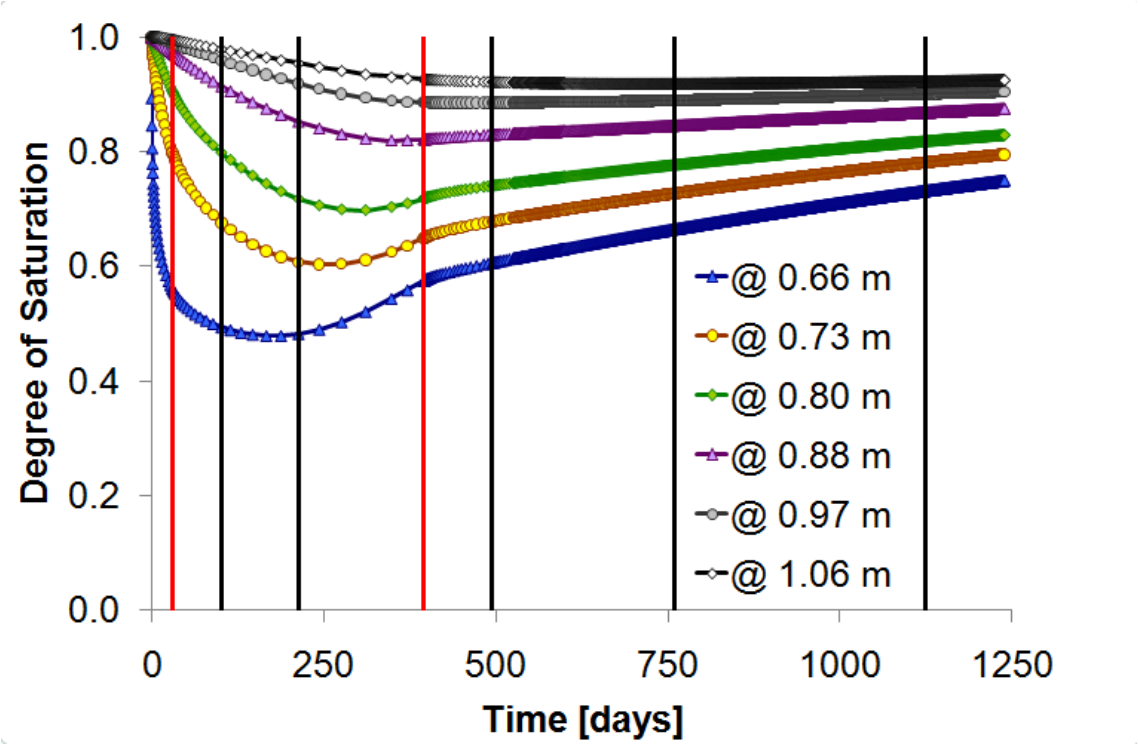

Figure C-3 Predicted evolution of the degree of saturation in the first 40 cm of OC.

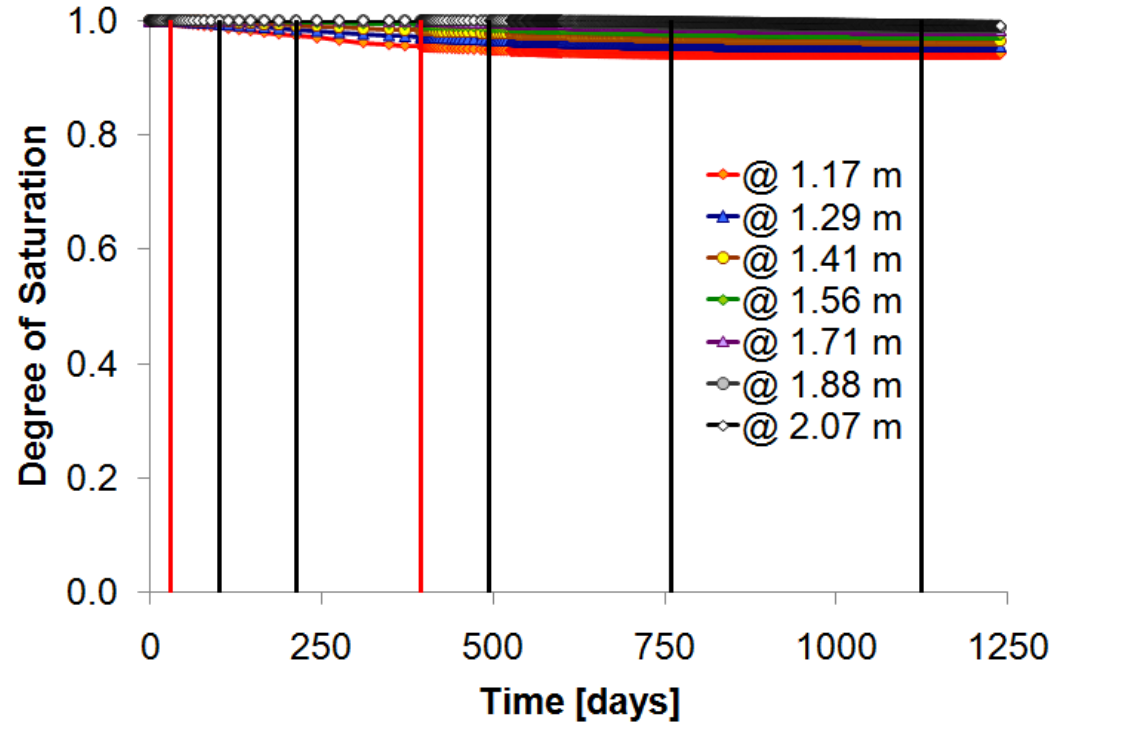

Figure C-4 Predicted evolution of the degree of saturation between 50 and 150cm from the microtunnel wall.

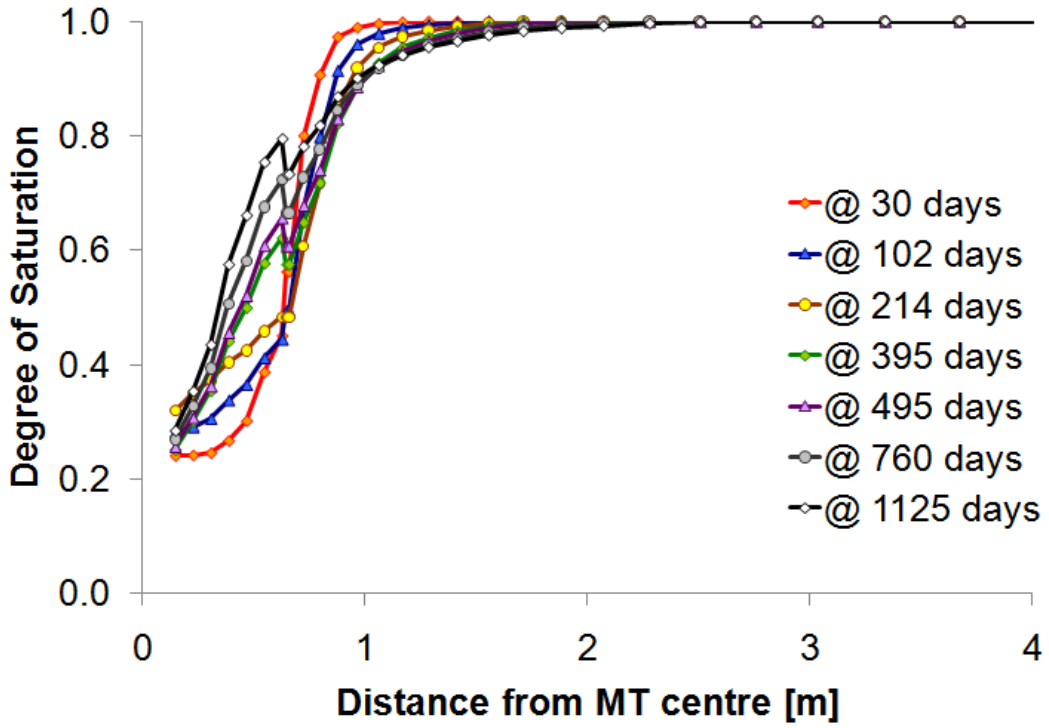

Figure C-5 Predicted profiles of degree of saturation at different times along A1.

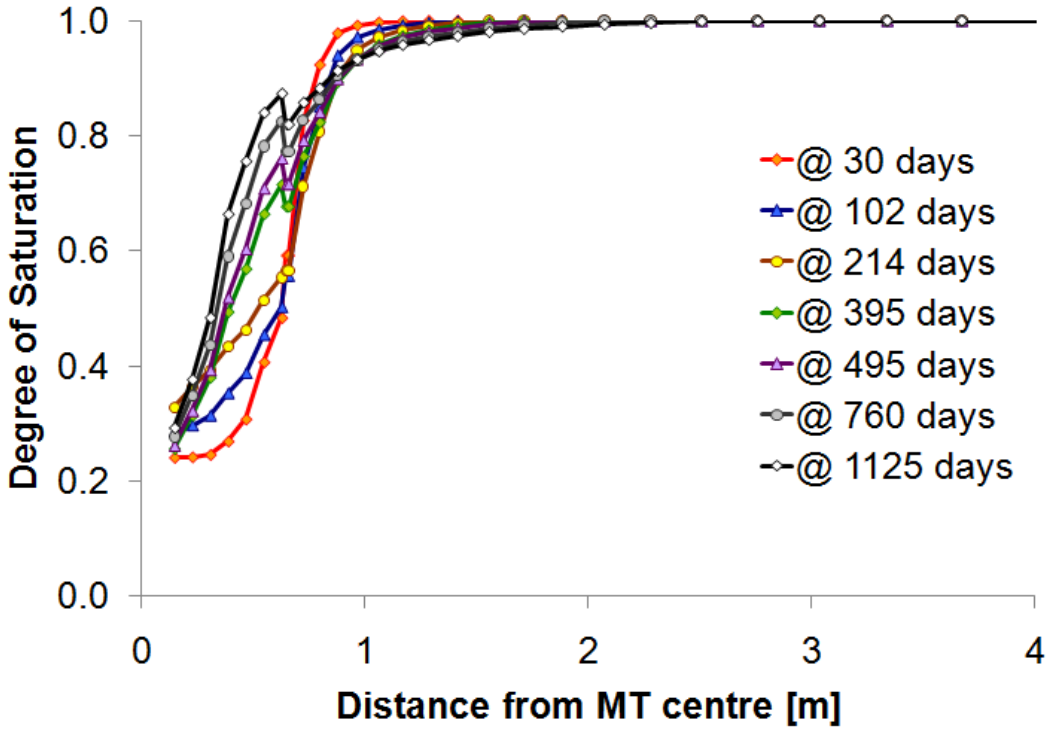

Figure C-6 Predicted profiles of degree of saturation at different times along A2.

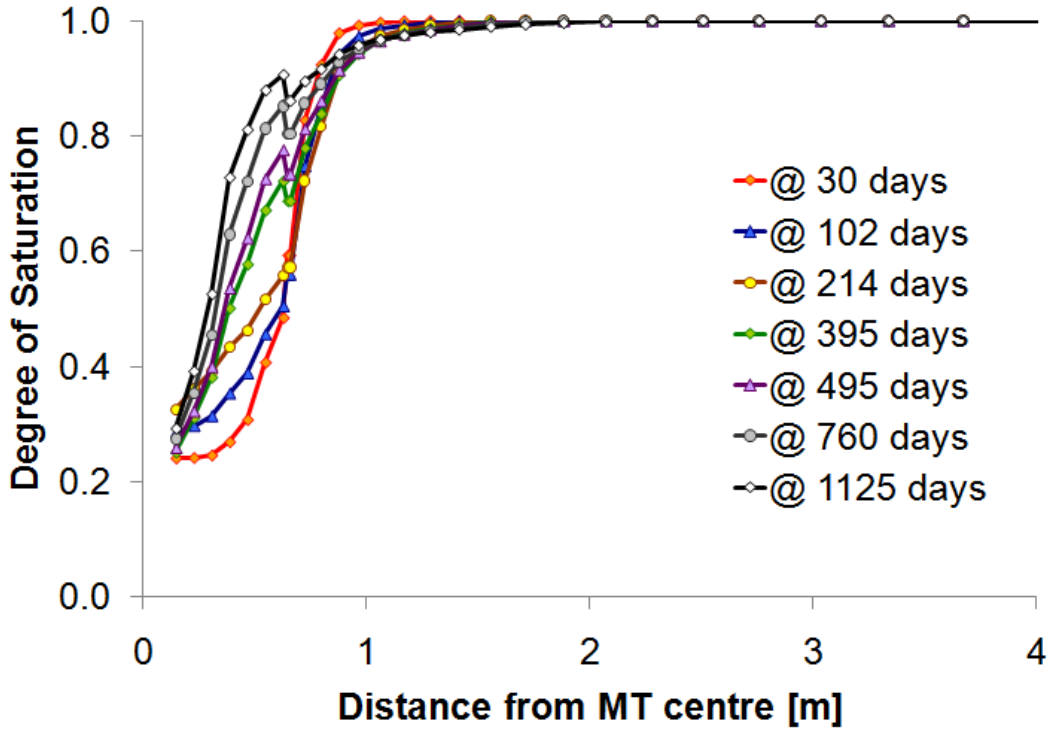

Figure C-7 Predicted profiles of degree of saturation at different times along A3.

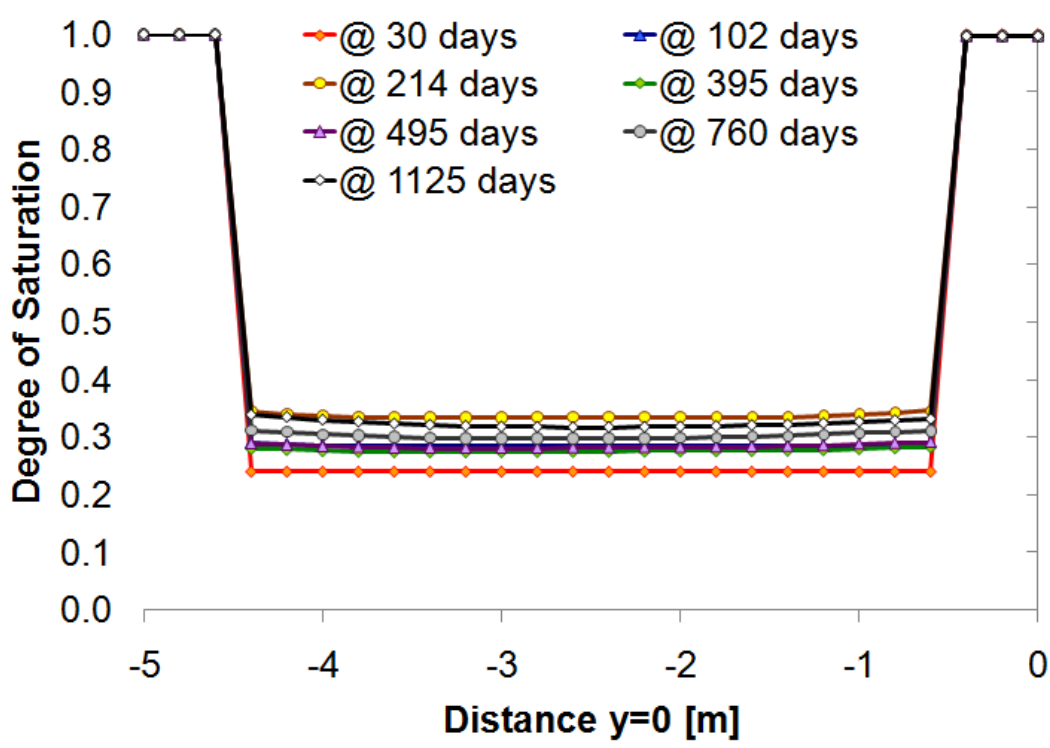

Figure C-8 Predicted profiles of degree of saturation at different times along B1.

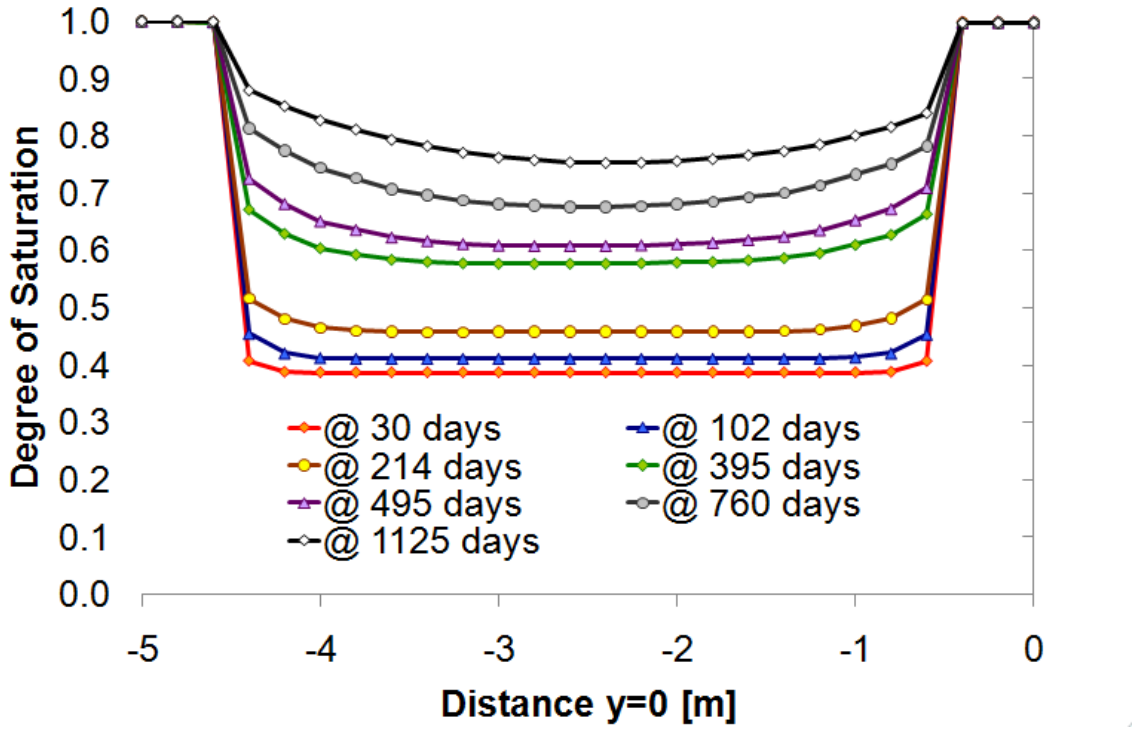

Figure C-9 Predicted profiles of degree of saturation at different times along B2.

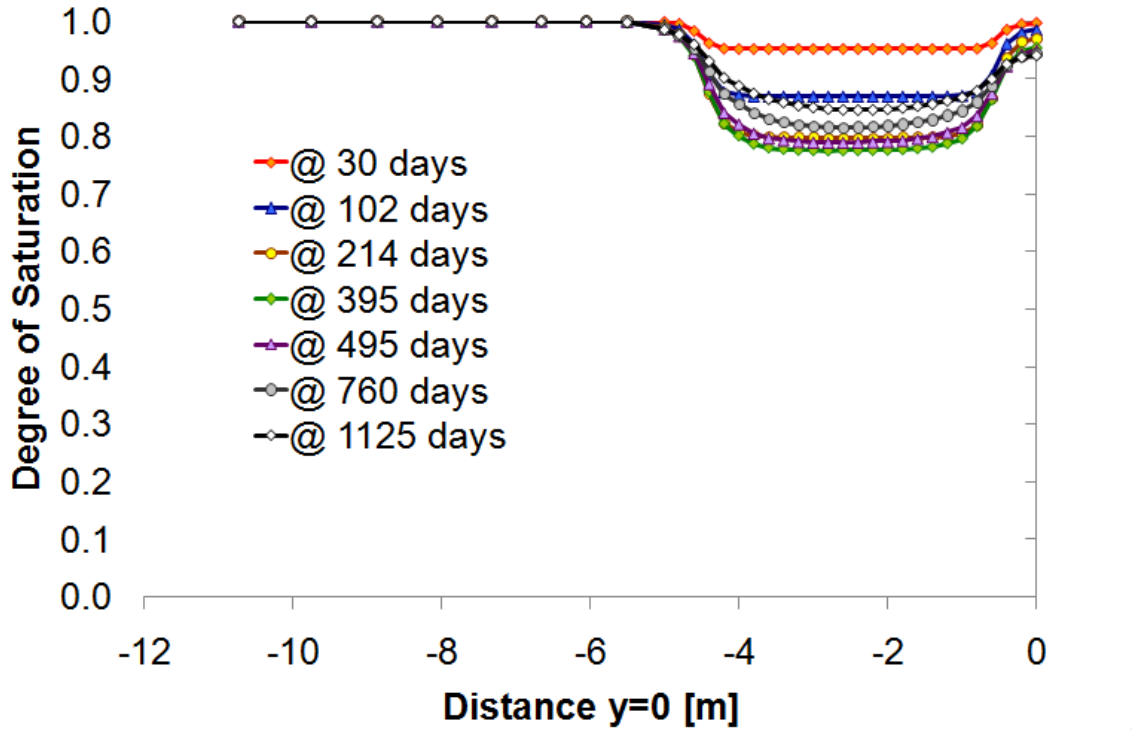

Figure C-10 Predicted profiles of degree of saturation at different times along B3

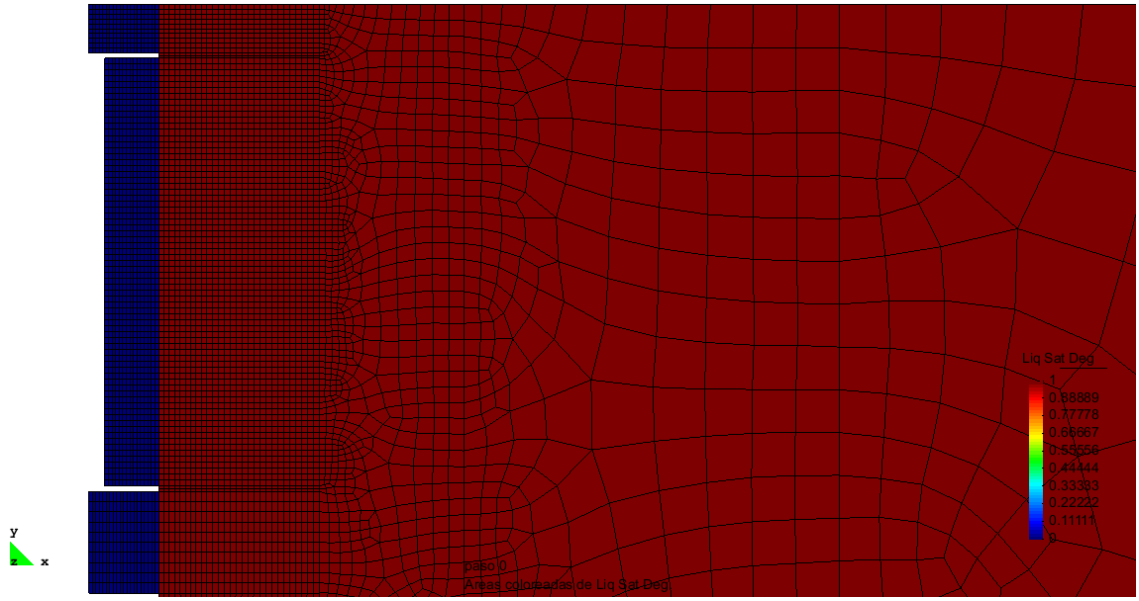

Figure C-11 Equivalue lines of degree of saturation at day 0.

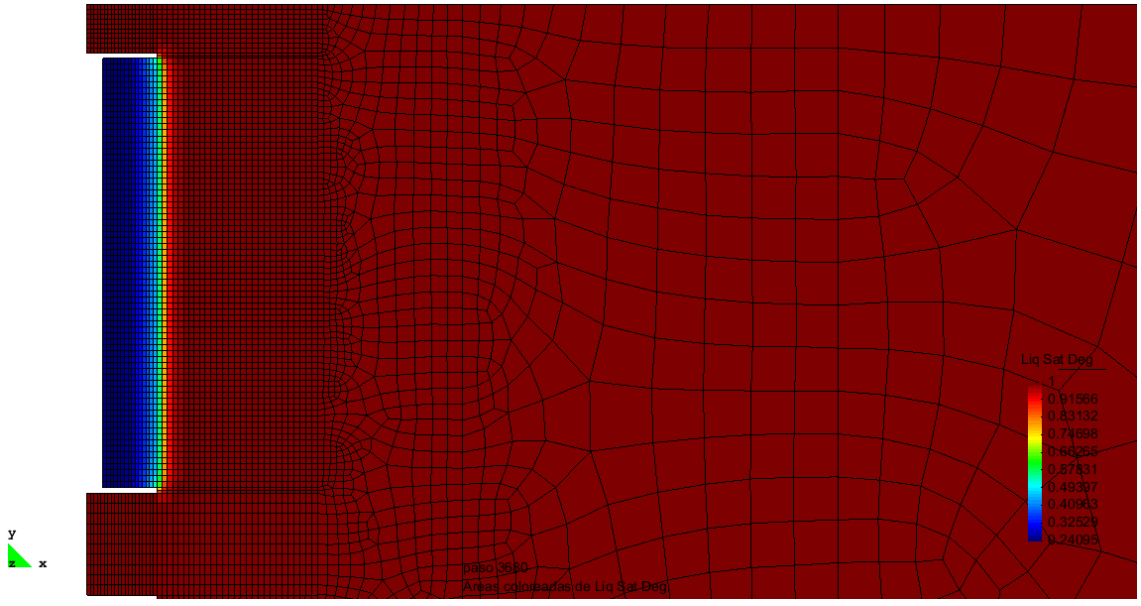

Figure C-12 Equivalue lines of degree of saturation at day 30.

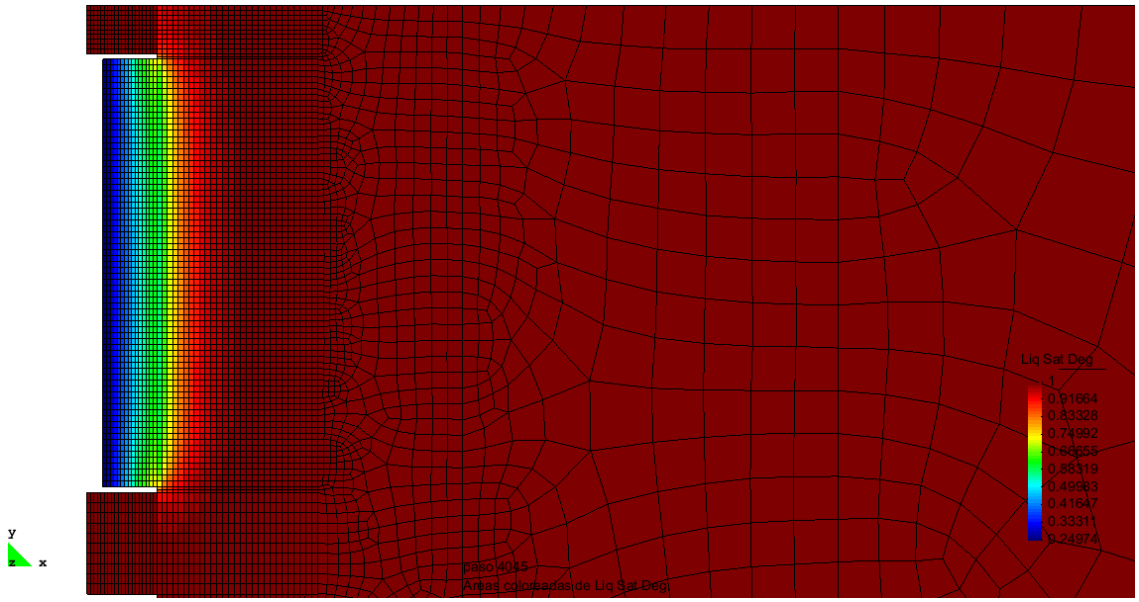

Figure C-13 Equivalue lines of degree of saturation at day 395.

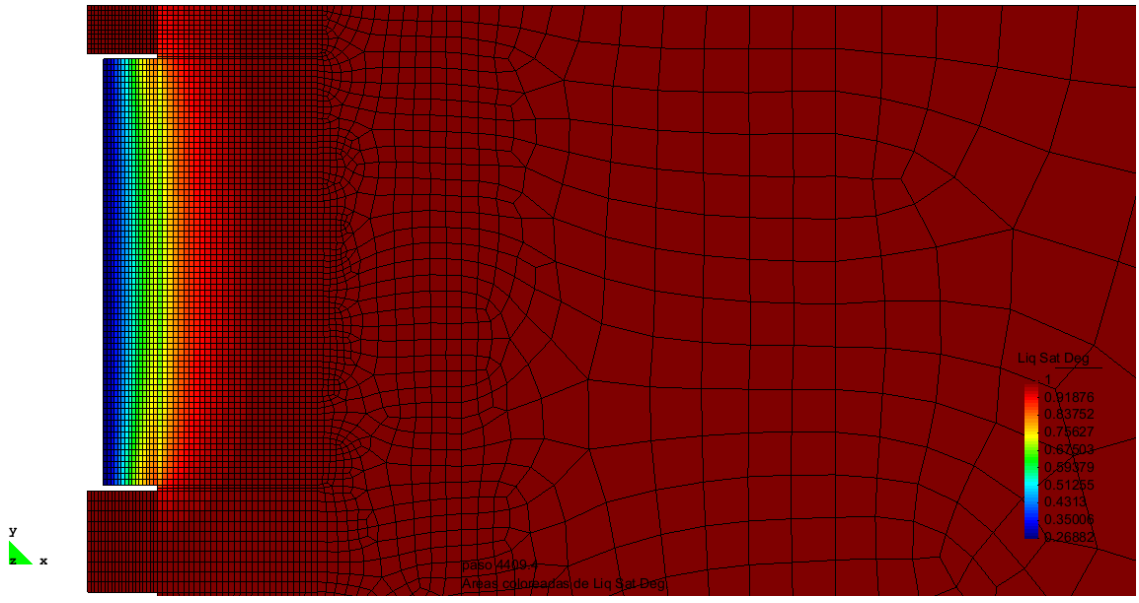

Figure C-14 Equivalue lines of degree of saturation at day 760.

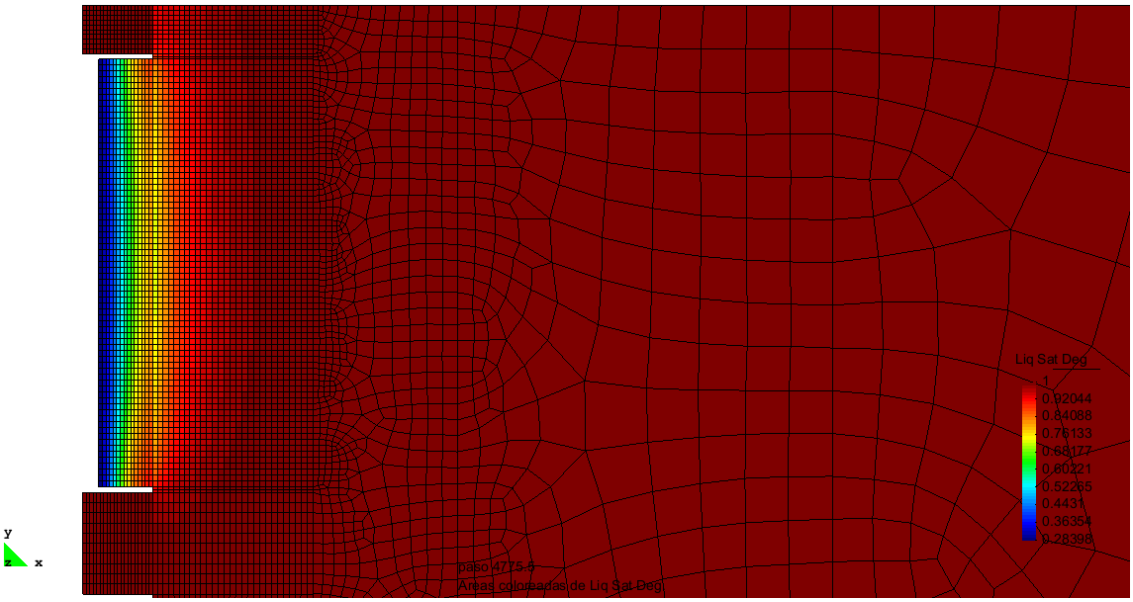

Figure C-15 Equivalue lines of degree of saturation at day 1125.

App. D Relative humidity

All simulation results in terms of Relative Humidity are given in this annexe. All distances are given in relation to the centre of the microtunnel. Time runs from bentonite emplacement.

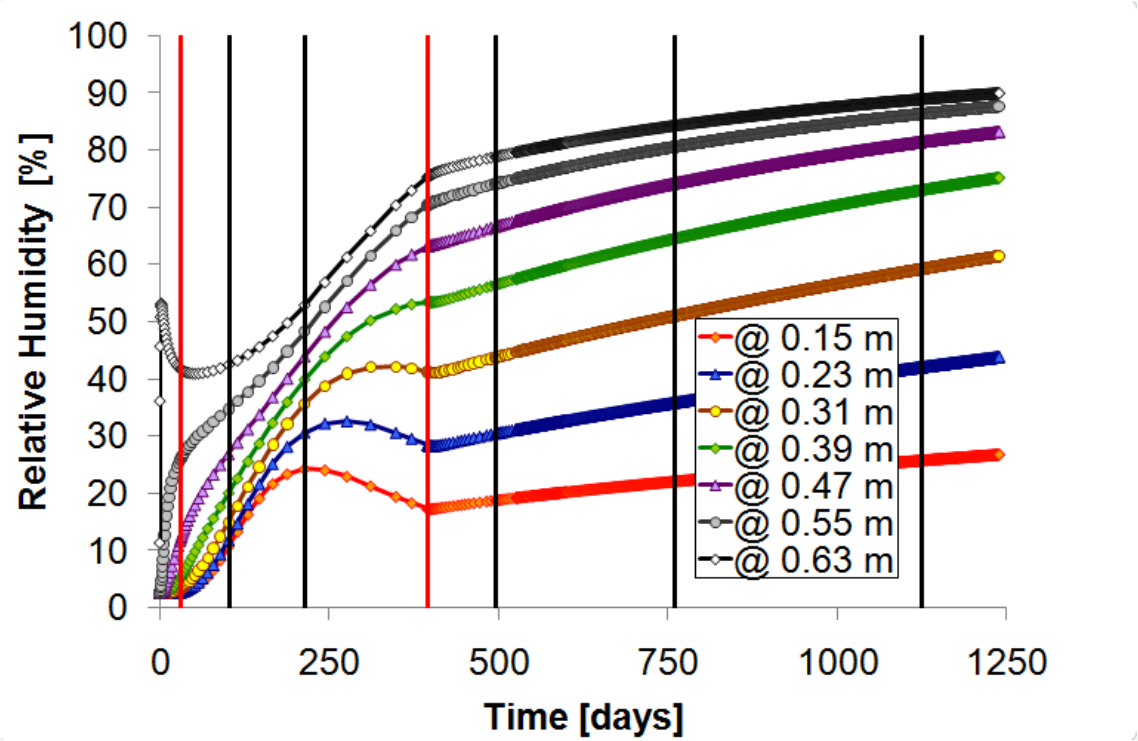

Figure D-1 Predicted evolution of the Relative Humidity in the bentonite barrier.

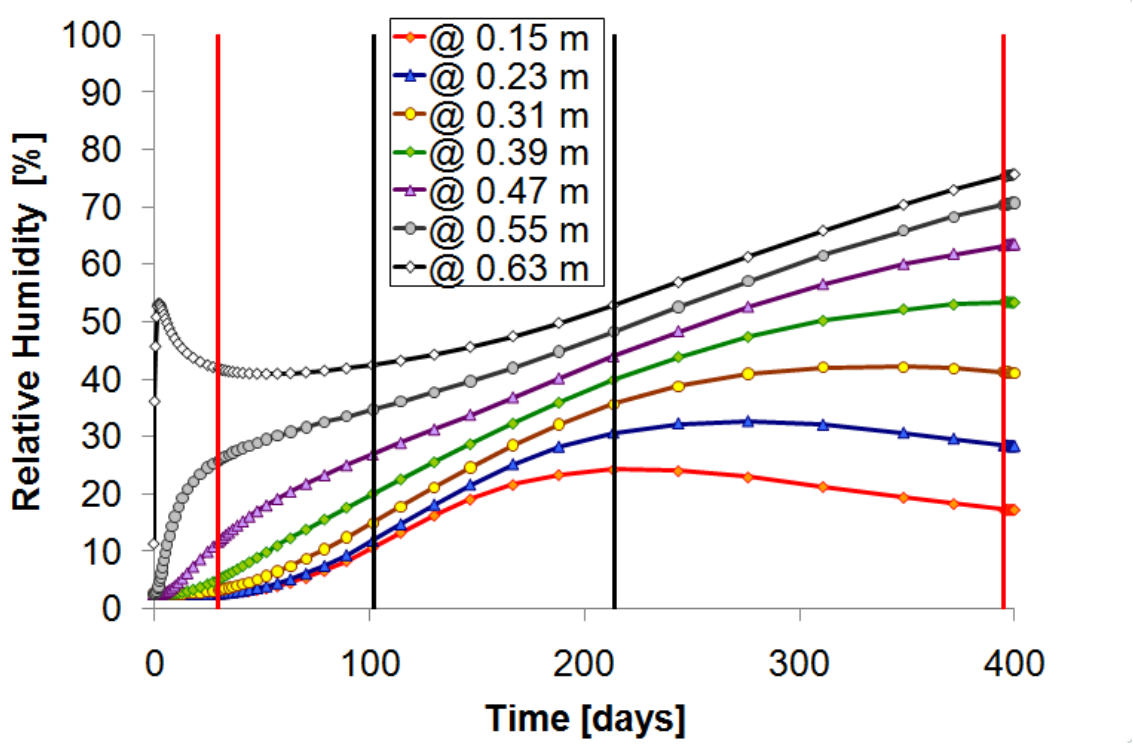

Figure D-2 Predicted evolution of the Relative Humidity in the bentonite barrier during the temperature increase period.

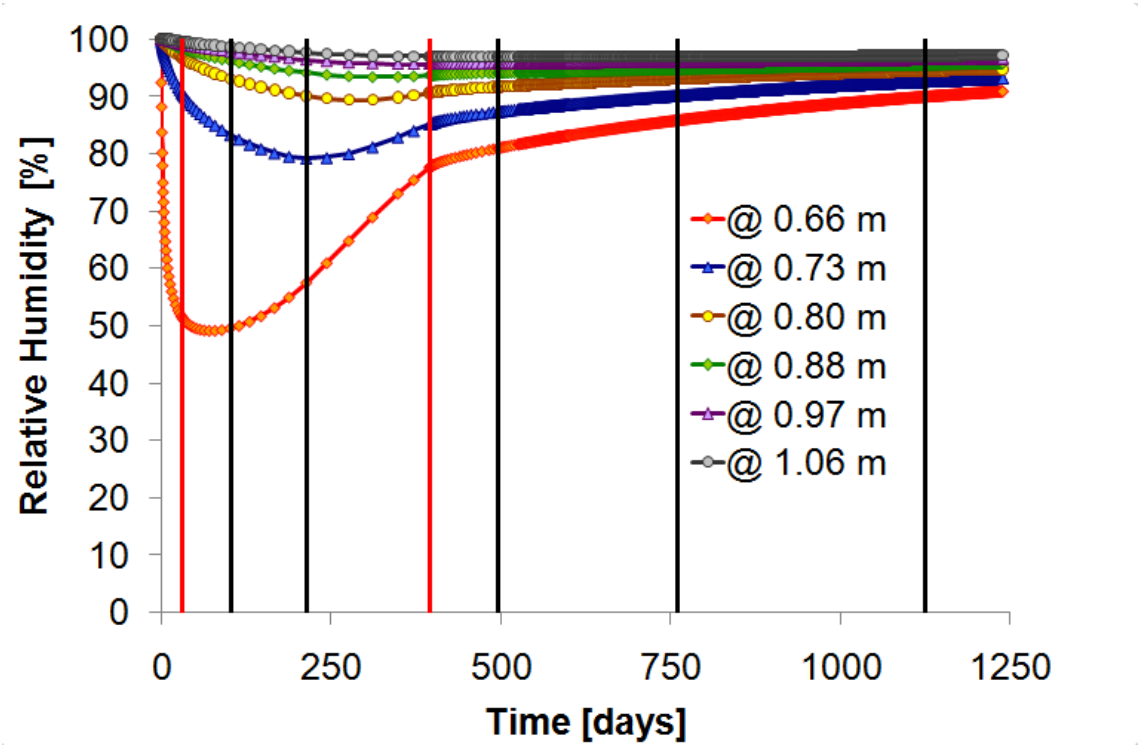

Figure D-3 Predicted evolution of the Relative Humidity in the first 40 cm of OC

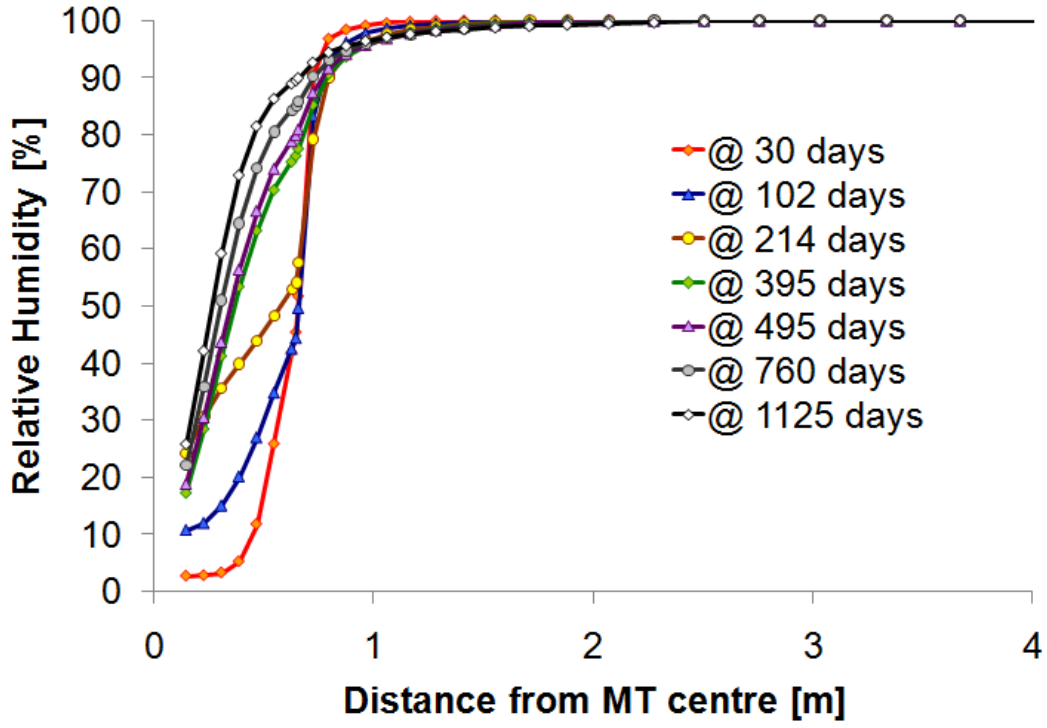

Figure D-4 Predicted profiles of Relative Humidity at different times along A1.

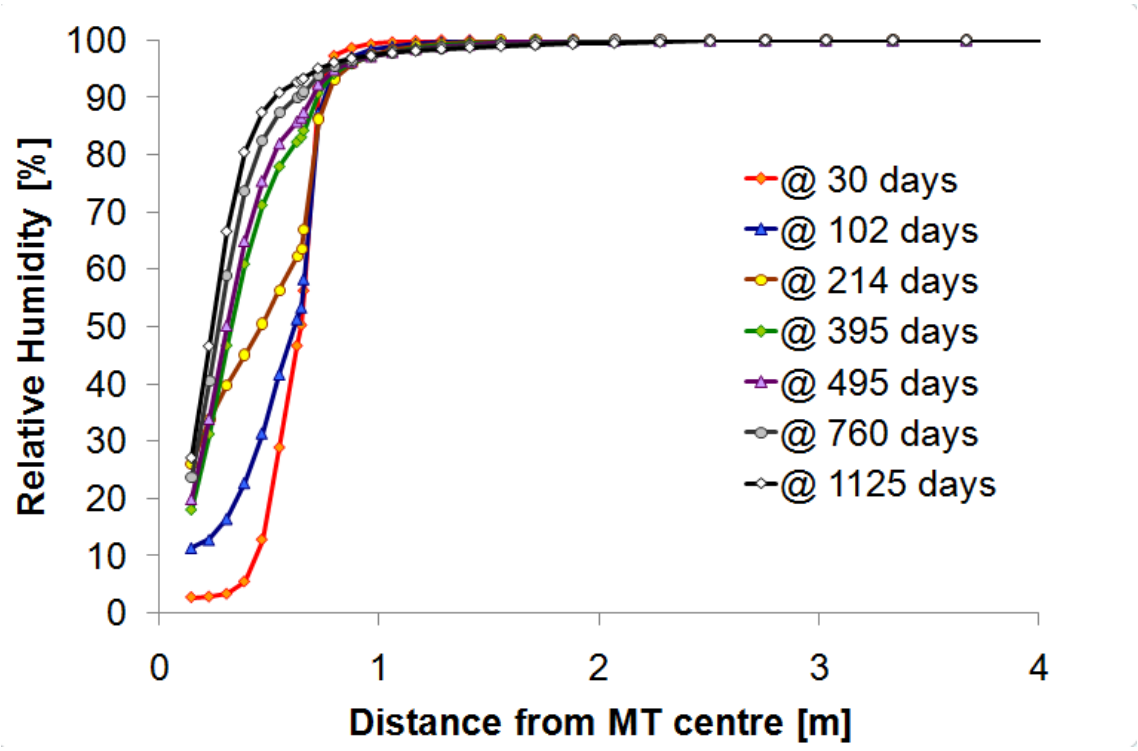

Figure D-5 Predicted profiles of Relative Humidity at different times along A2.

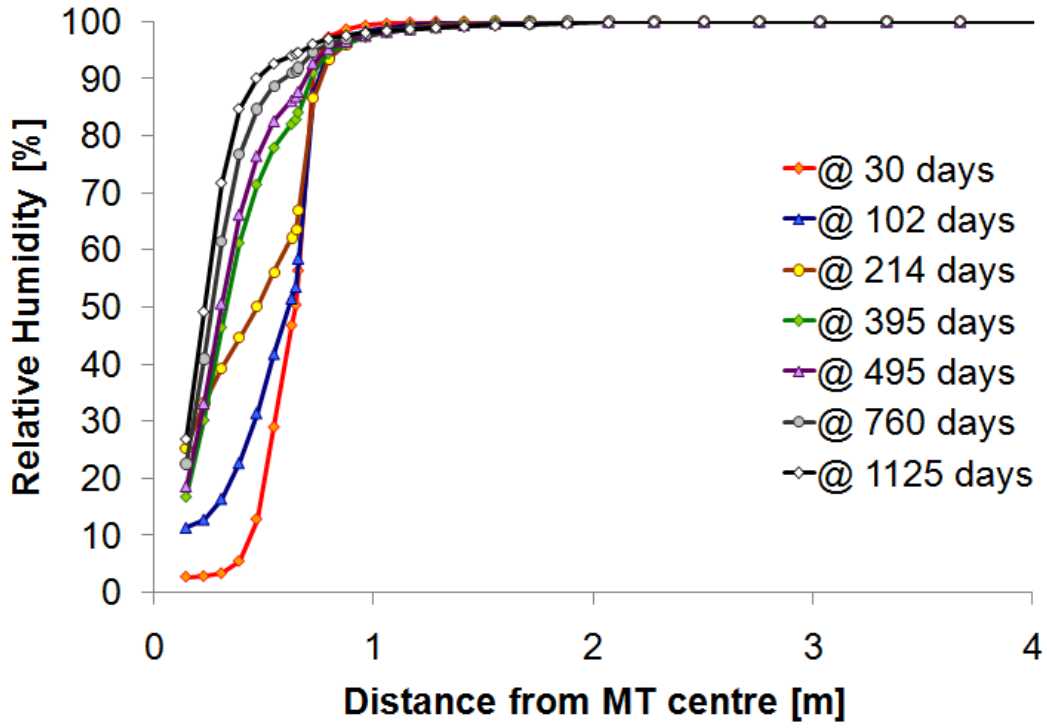

Figure D-6 Predicted profiles of Relative Humidity at different times along A3.

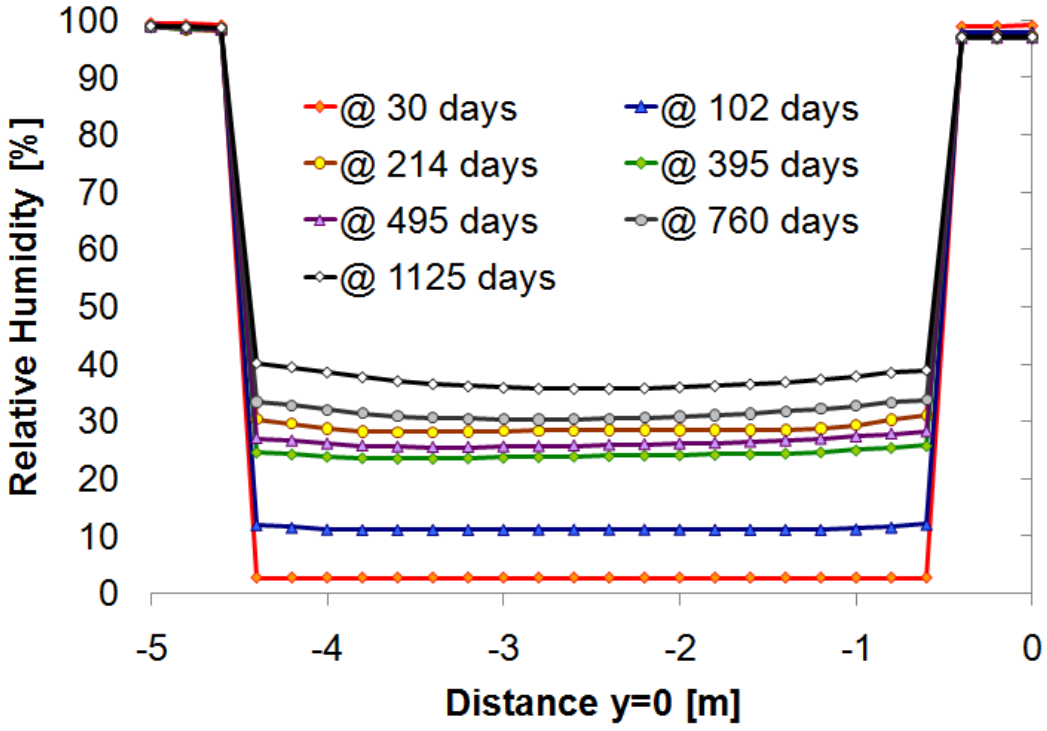

Figure D-7 Predicted profiles of Relative Humidity at different times along B1.

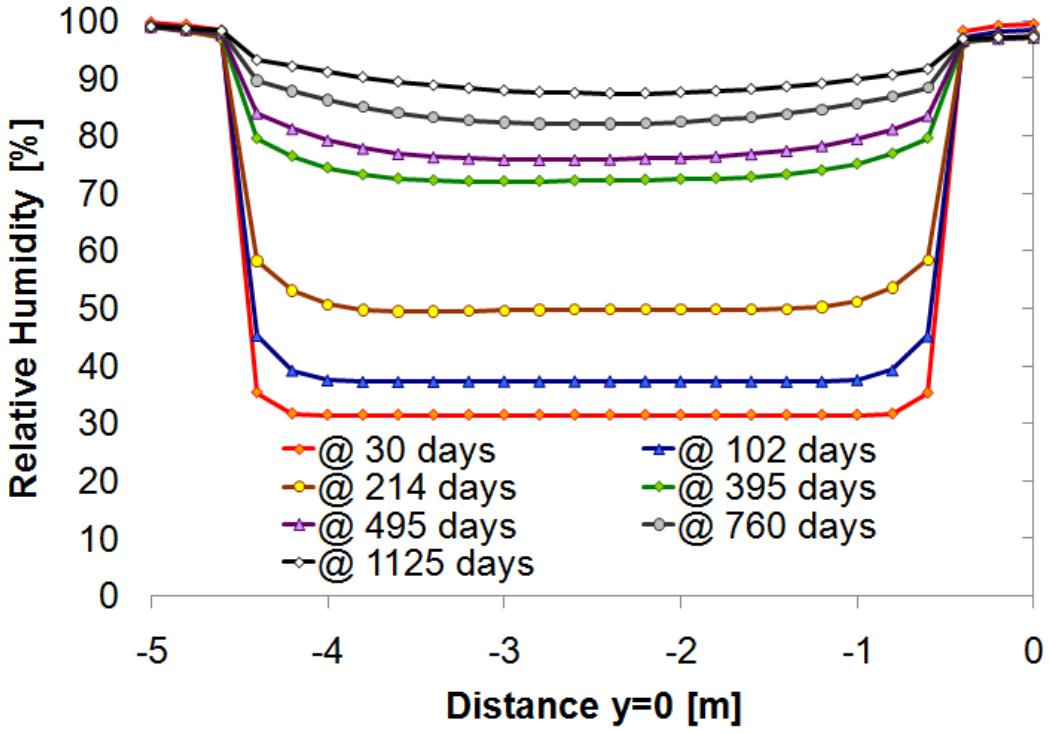

Figure D-8 Predicted profiles of Relative Humidity at different times along B2

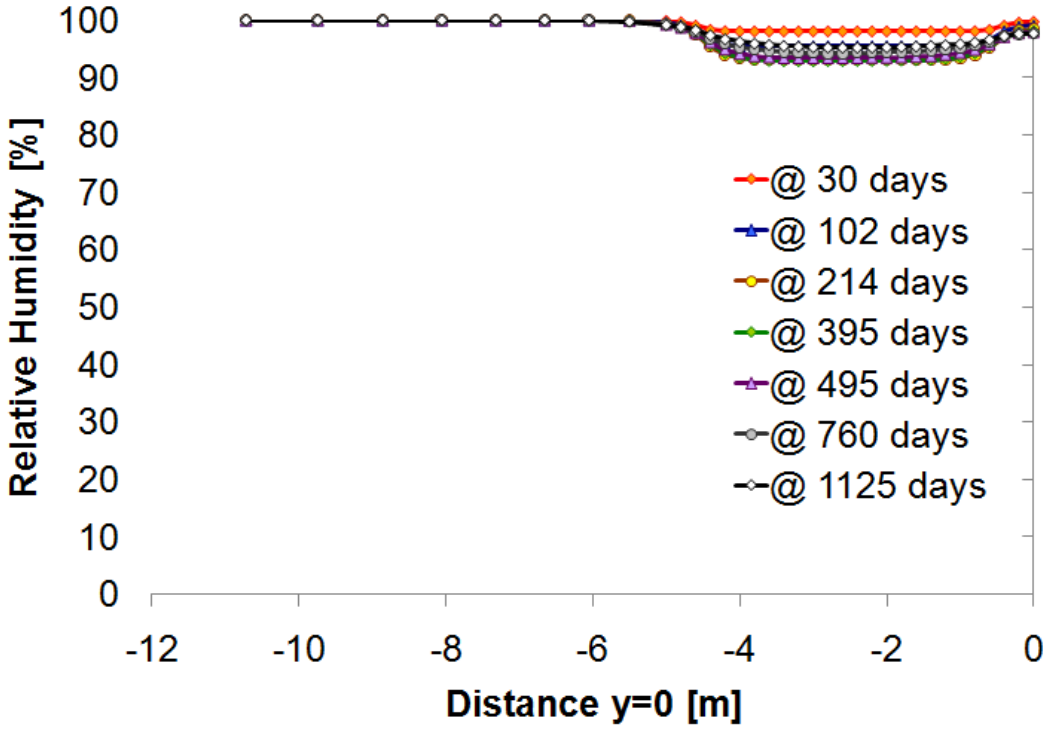

Figure D-9 Predicted profiles of Relative Humidity at different times along B3

App. E Liquid pressure

All simulation results in terms of liquid pressure are given in this annexe. All distances are given in relation to the centre of the microtunnel. Time runs from bentonite emplacement.

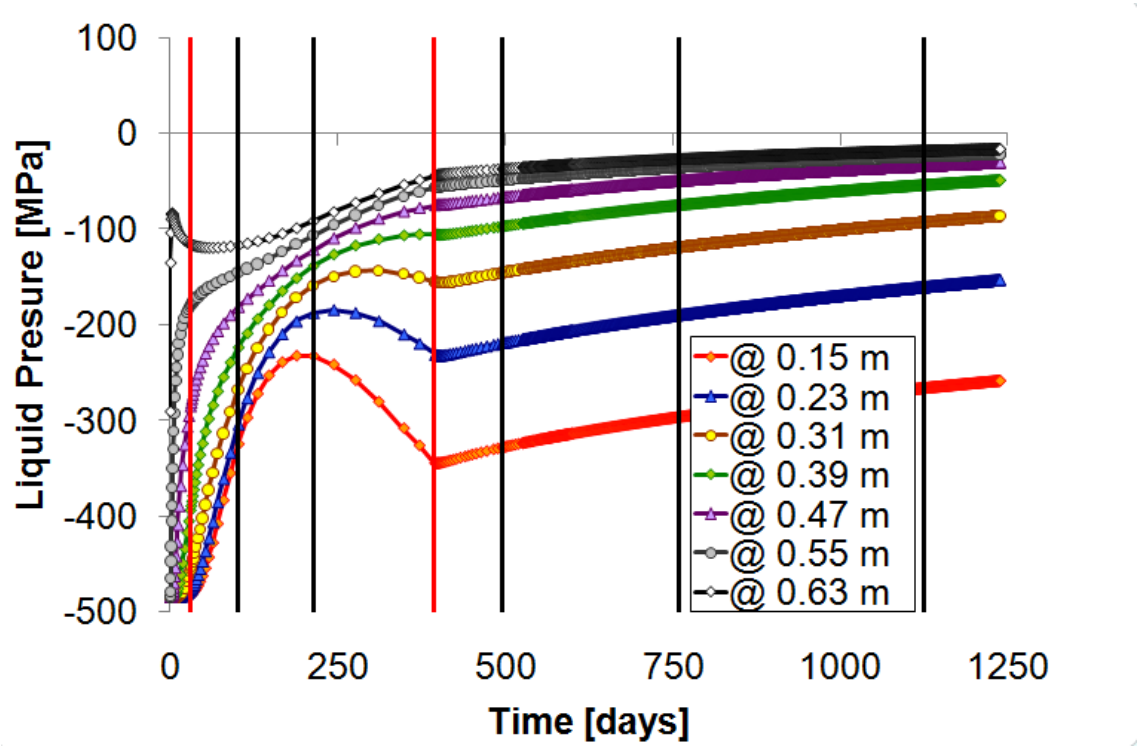

Figure E-1 Predicted evolution of the liquid pressure in the bentonite barrier.

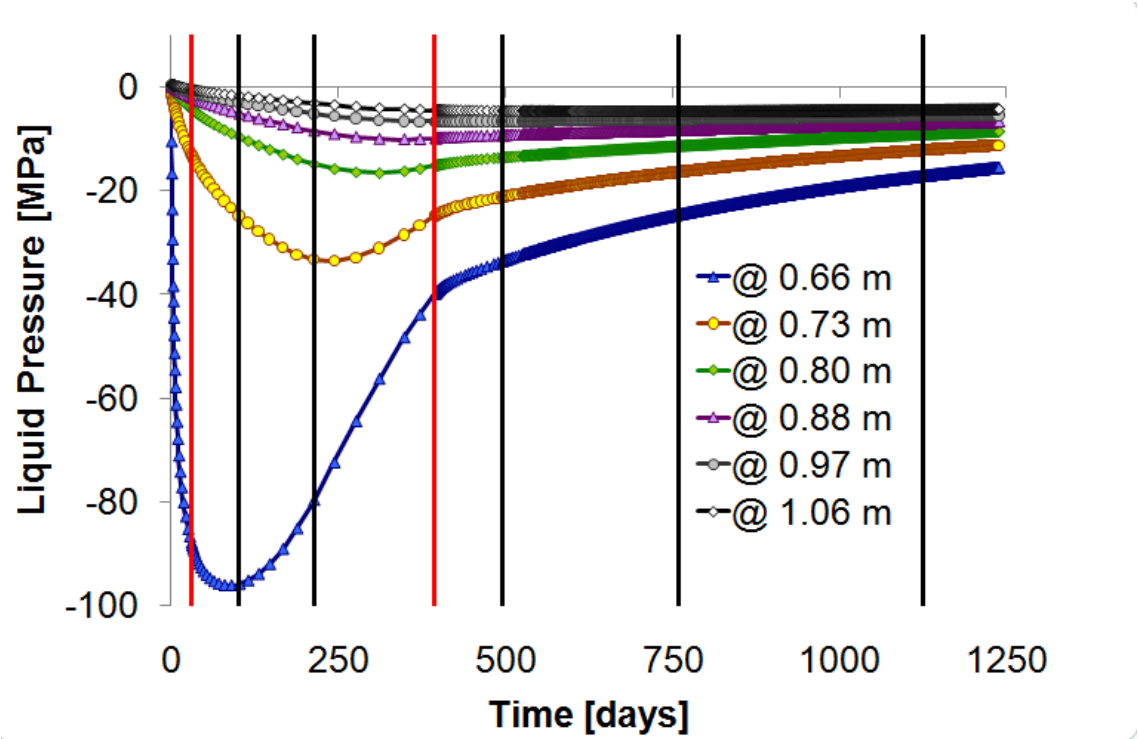

Figure E-2 Predicted evolution of the liquid pressure in the first 40 cm of OC.

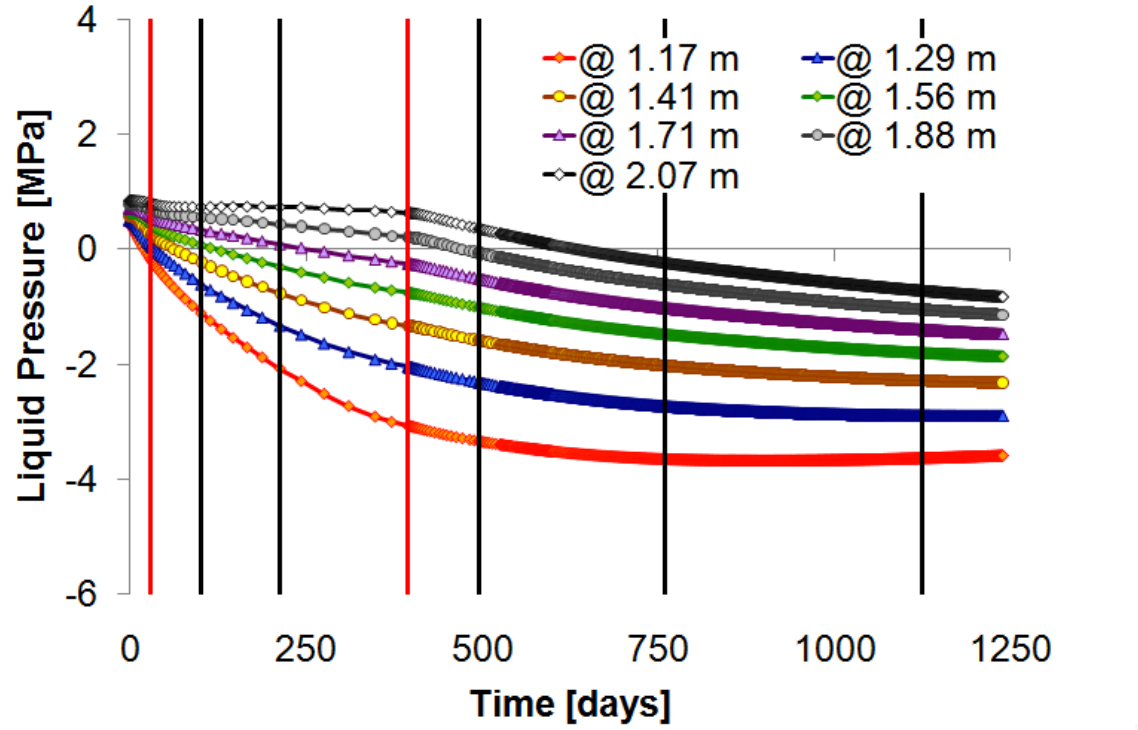

Figure E-3 Predicted evolution of the liquid pressure between 50 and 150cm from the microtunnel wall.

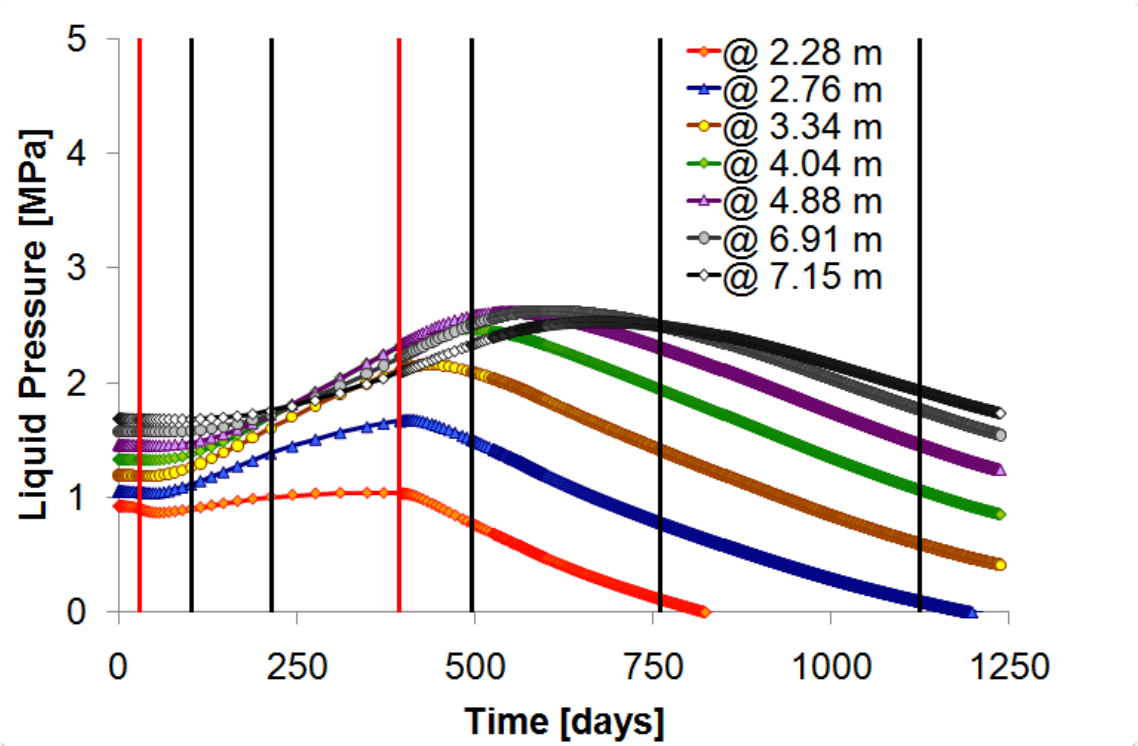

Figure E-4 Predicted evolution of the liquid pressure between 150 and 750cm from the microtunnel wall

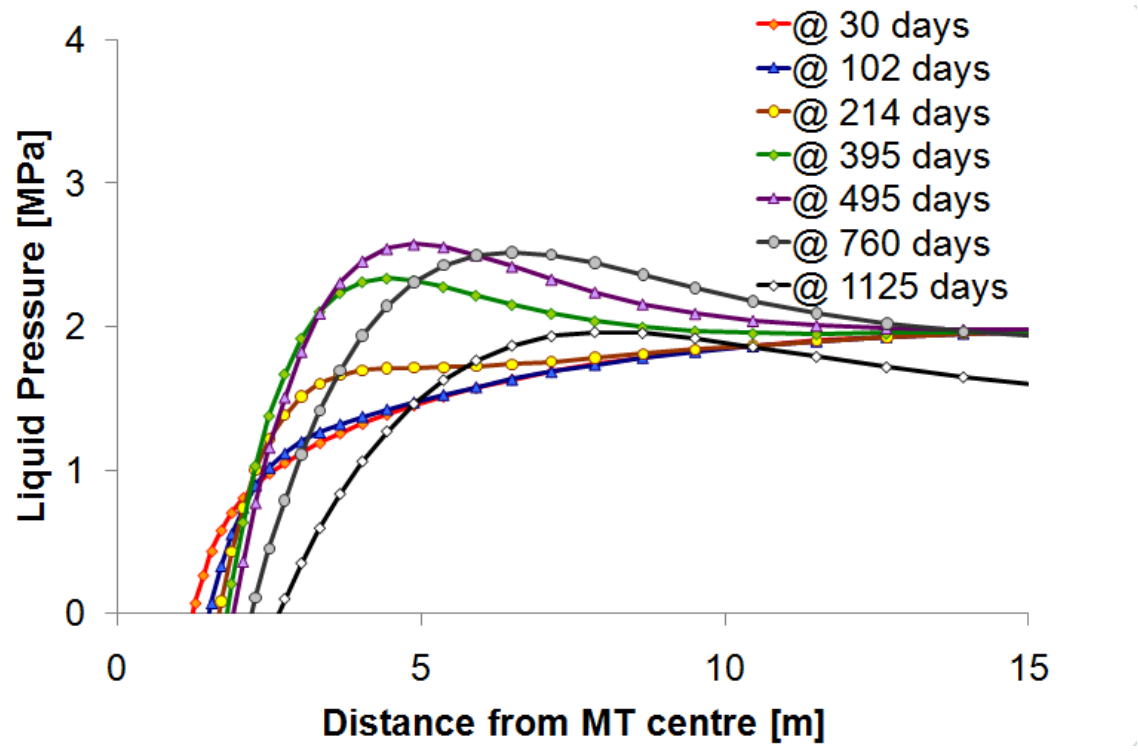

Figure E-5 Predicted profiles of liquid pressure at different times along A1

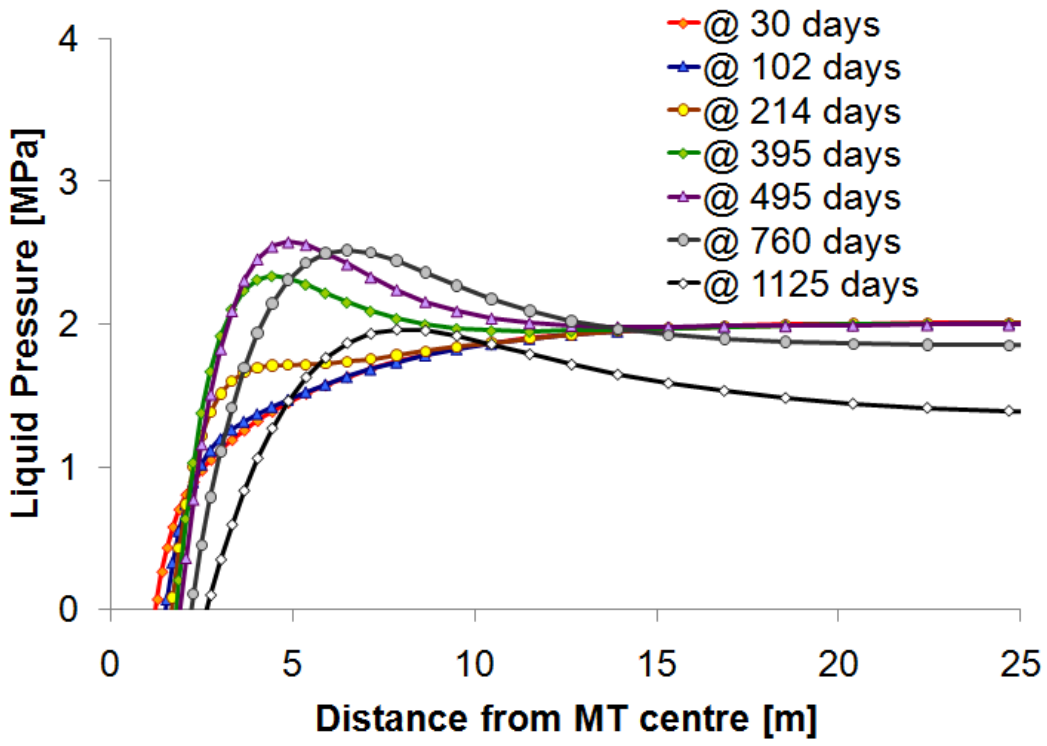

Figure E-6 Predicted profiles of liquid pressure at different times along A1

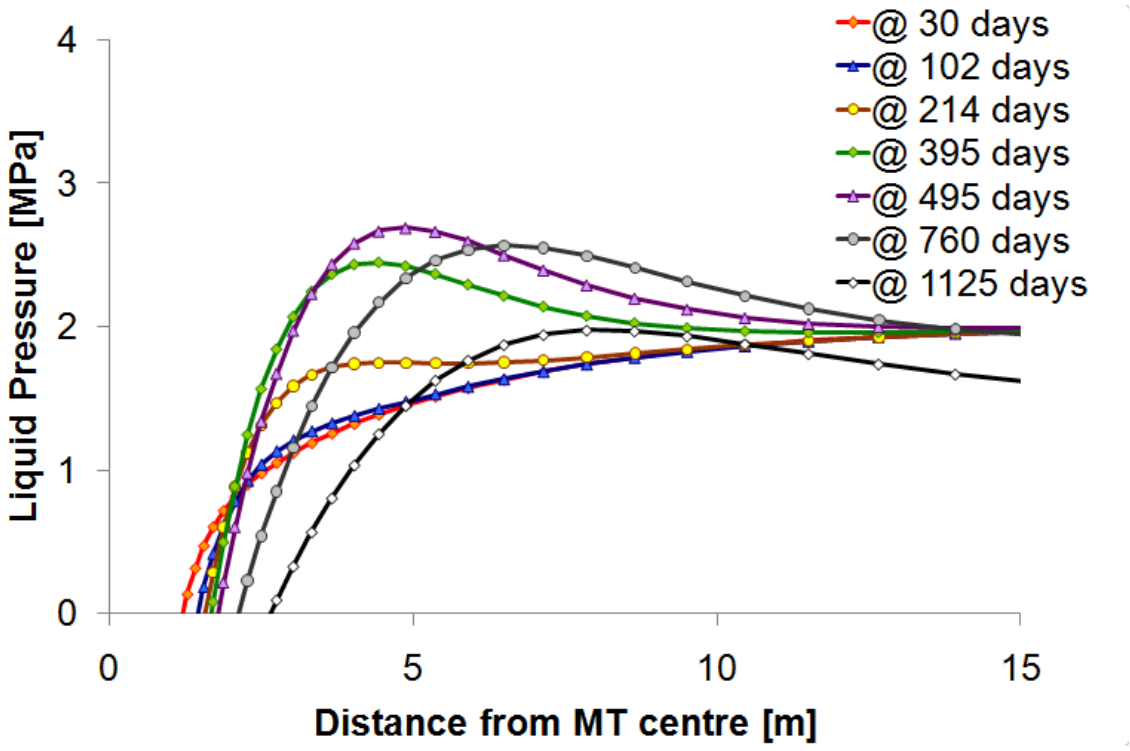

Figure E-7 Predicted profiles of liquid pressure at different times along A2

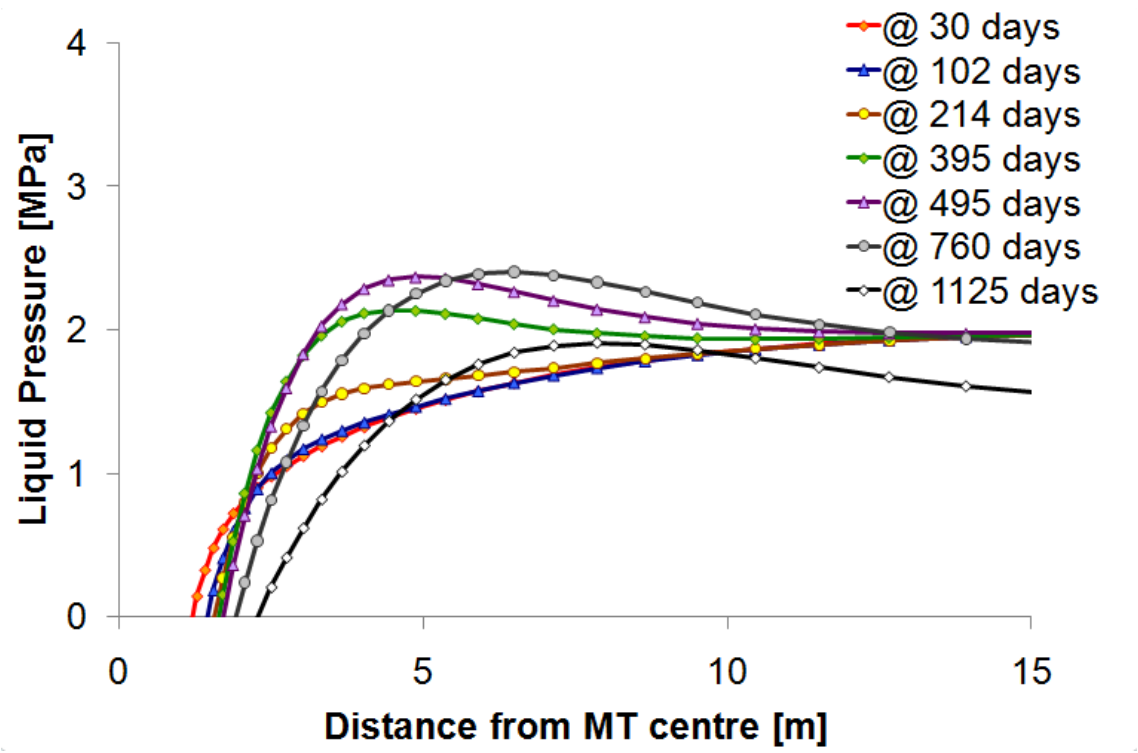

Figure E-8 Predicted profiles of liquid pressure at different times along A3

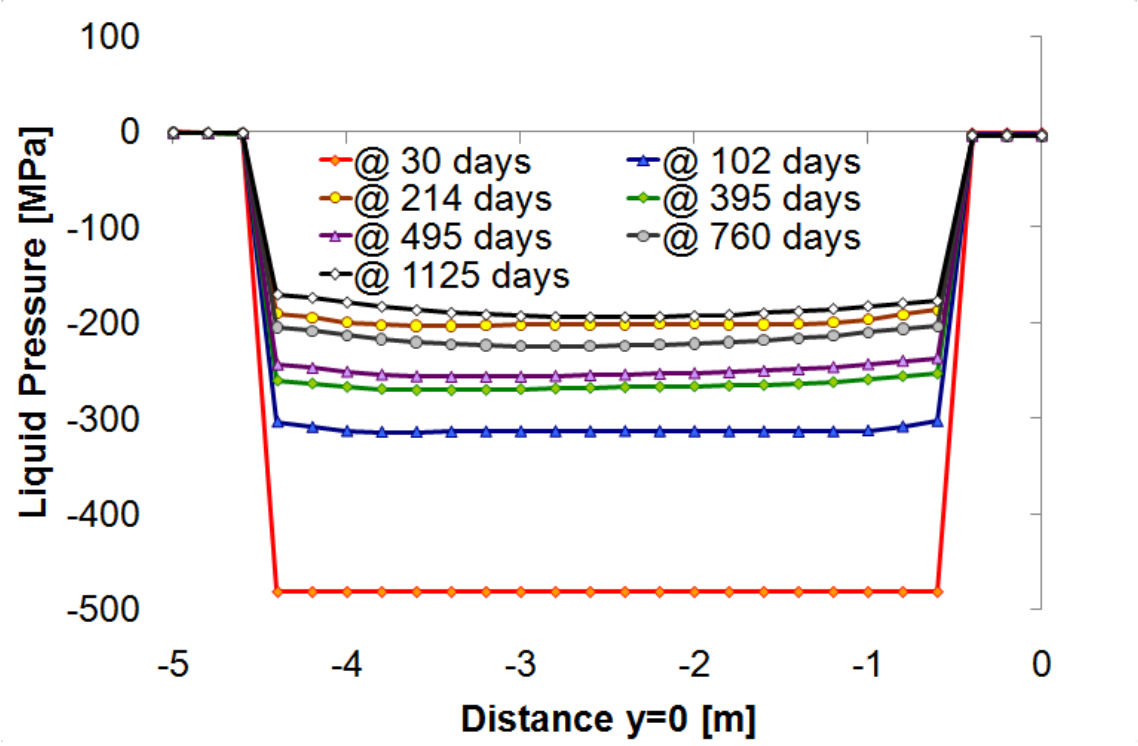

Figure E-9 Predicted profiles of liquid pressure at different times along B1

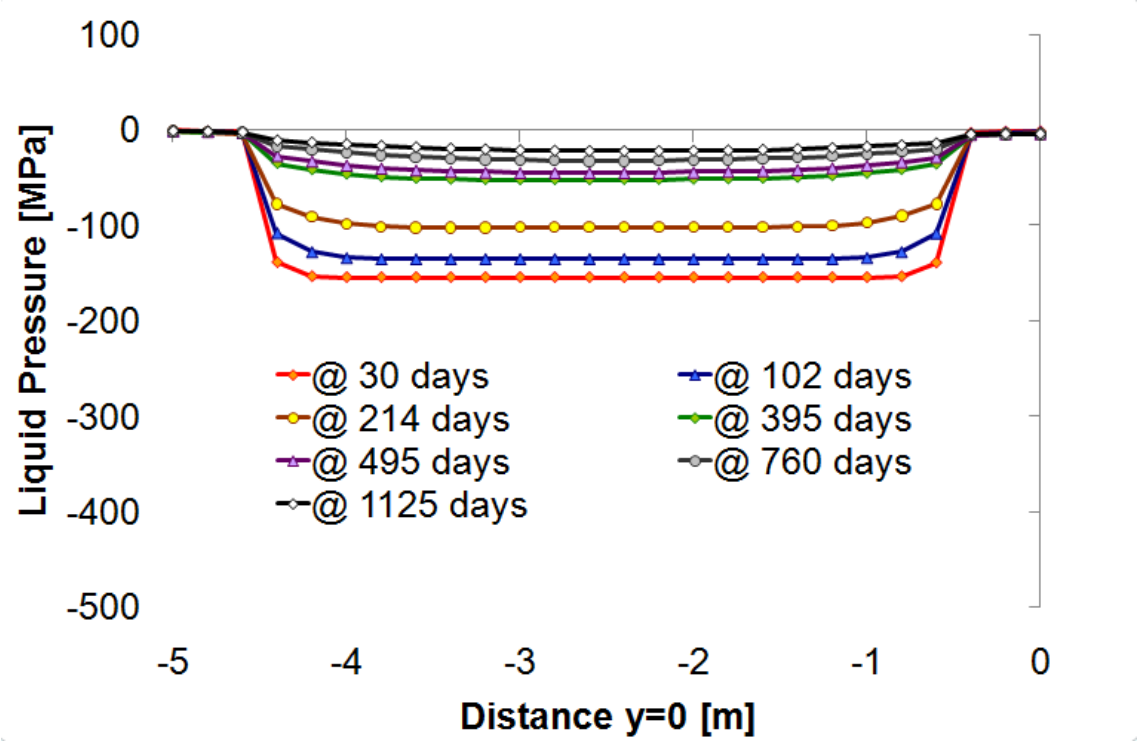

Figure E-10 Predicted profiles of liquid pressure at different times along B2

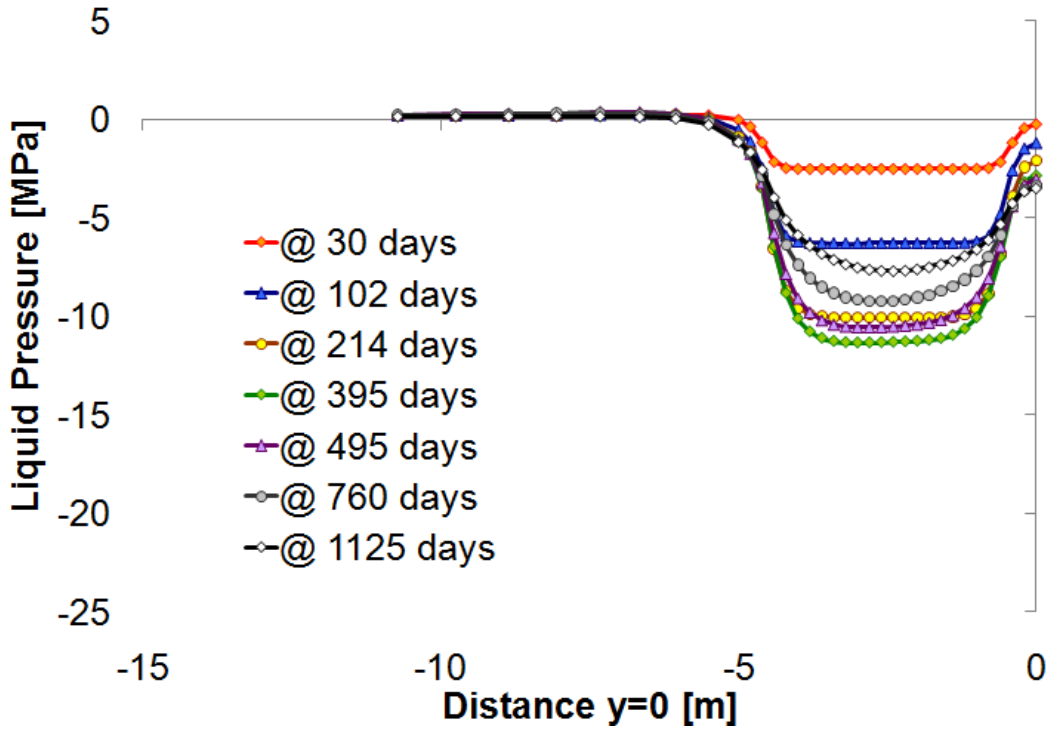

Figure E-11 Predicted profiles of liquid pressure at different times along B3

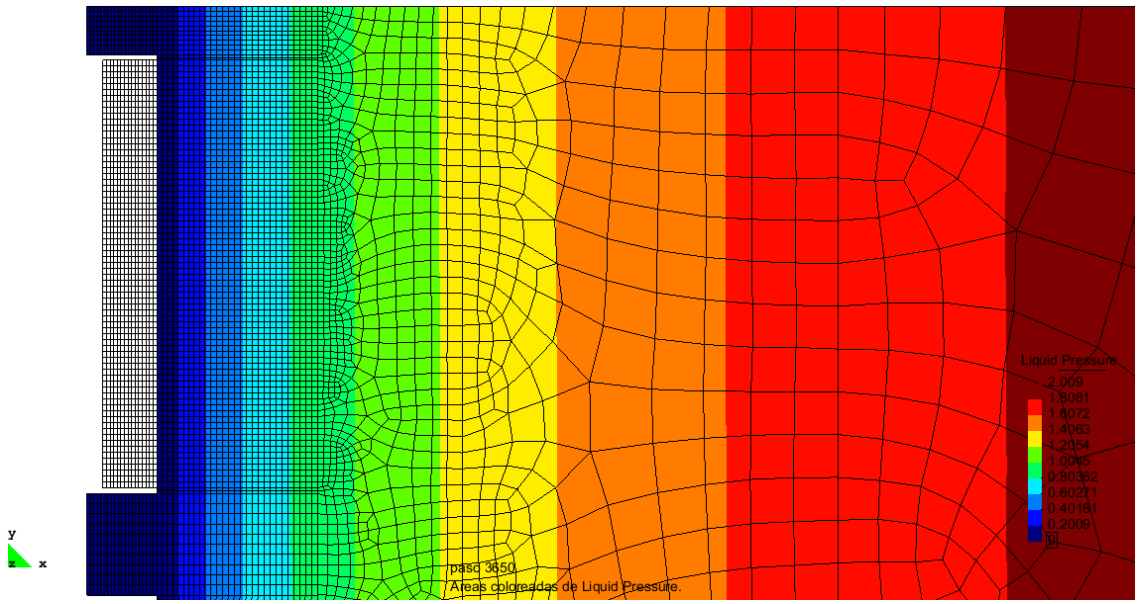

Figure E-12 Equivalue lines of liquid pressure at day 0

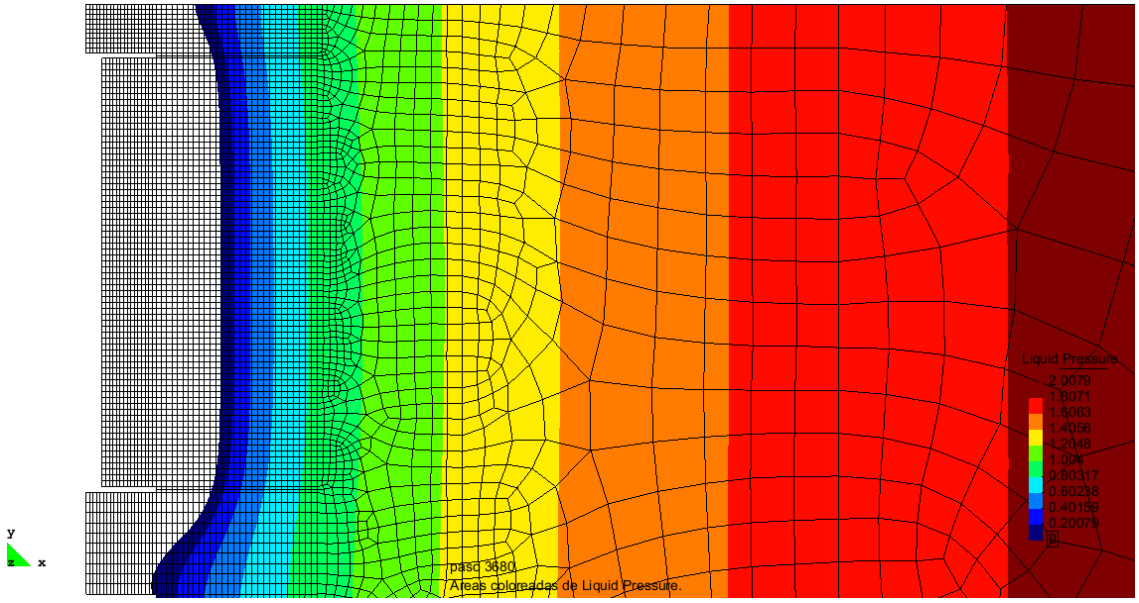

Figure E-13 Equivalue lines of liquid pressure at day 30

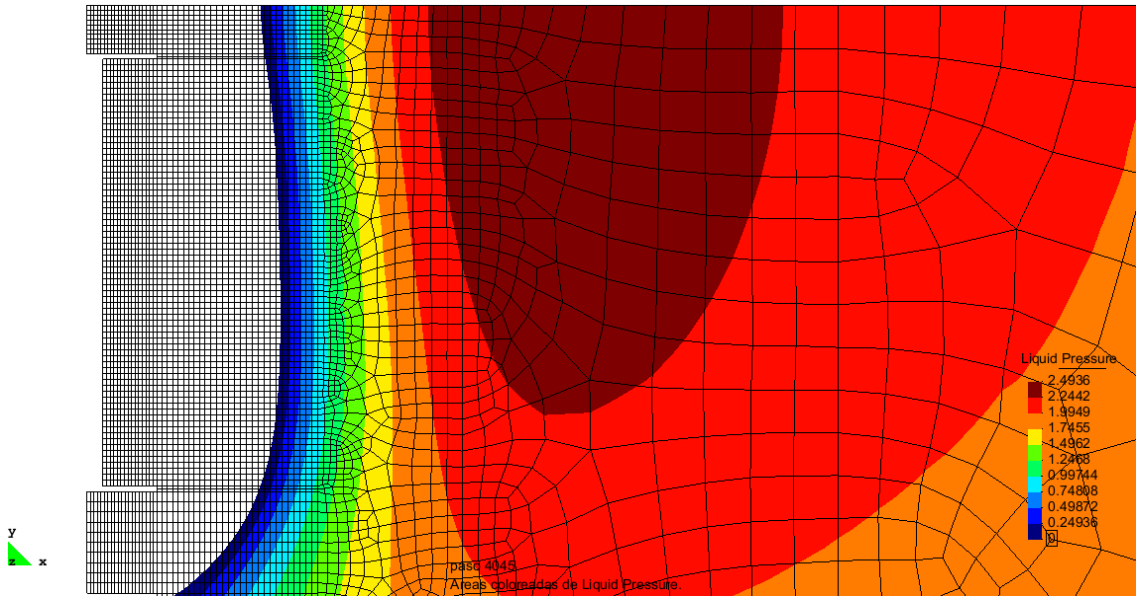

Figure E-14 Equivalue lines of liquid pressure at day 395

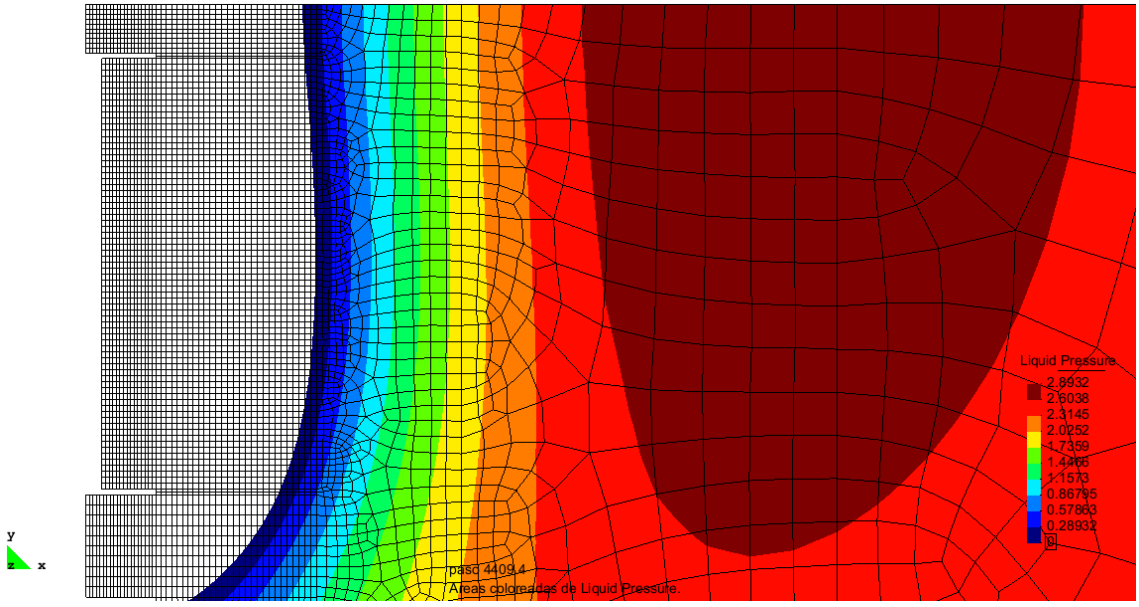

Figure E-15 Equivalue lines of liquid pressure at about day 760

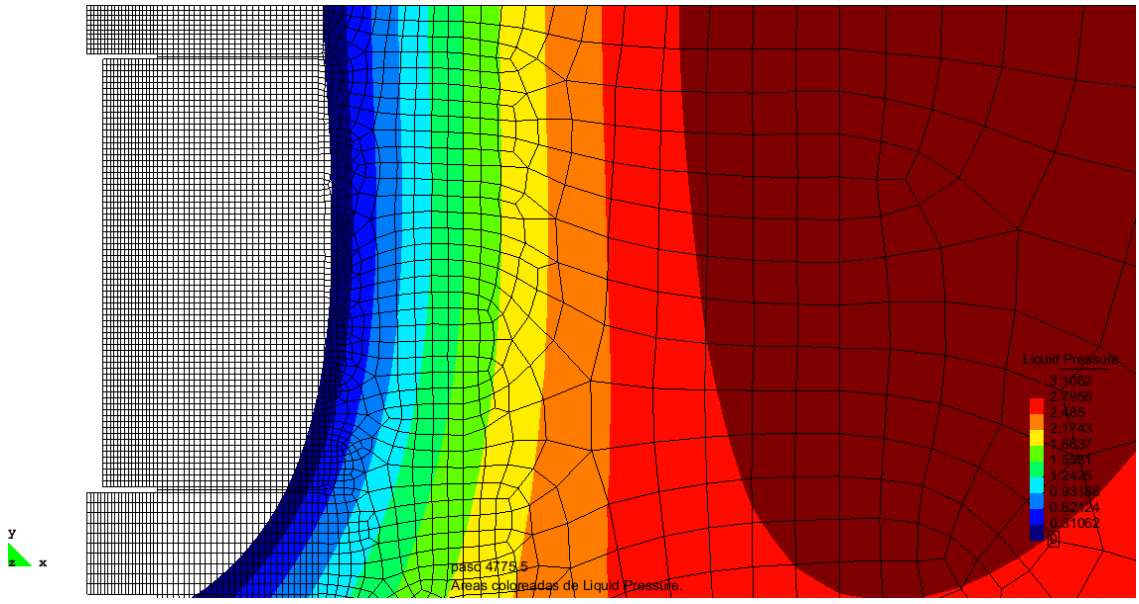

Figure E-16 Equivalue lines of liquid pressure at day 1125

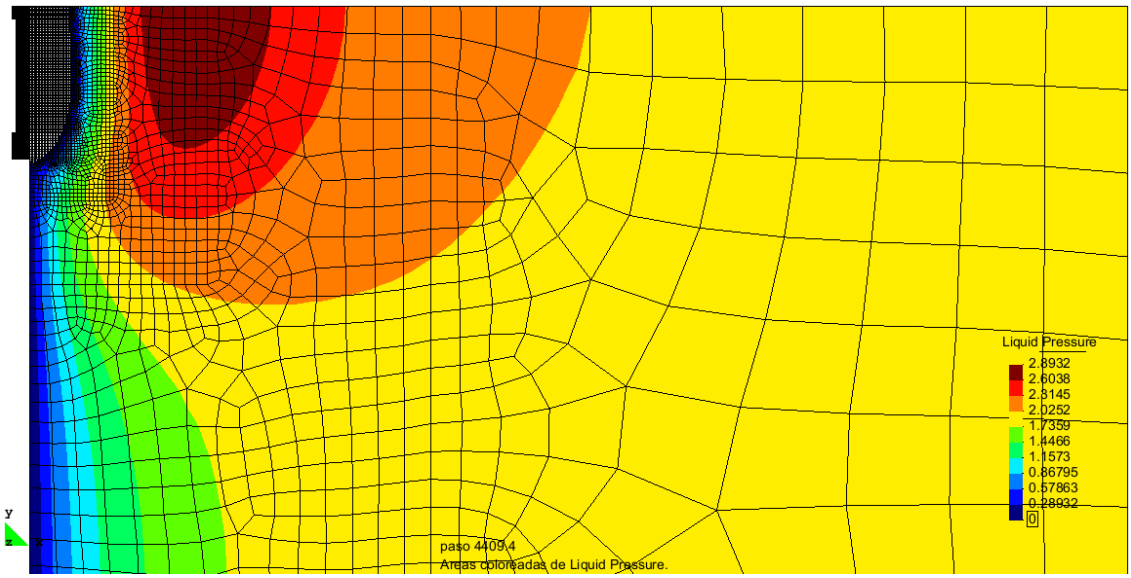

Figure E-17 Equivalue lines of liquid pressure at about day 760

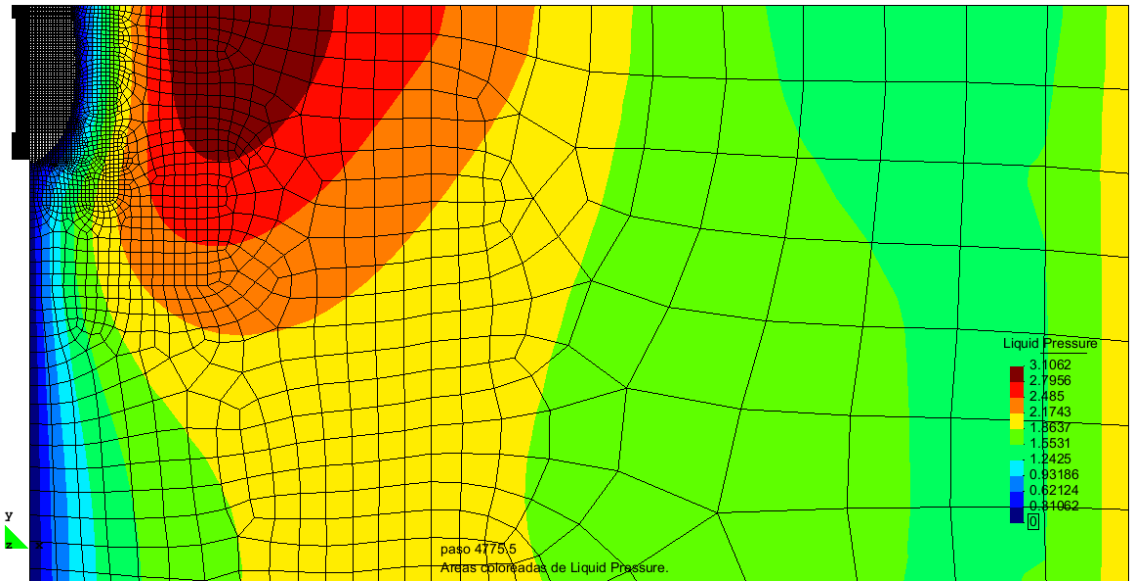

Figure E-18 Equivalue lines of liquid pressure at day 1125